Title

Exploring the potential of biogenic manganese oxides as water oxidation catalyst and investigating Mn oxidation mechanism using Electron Paramagnetic Resonance (EPR) spectroscopy

Author

Fu, Wen

Publication Date

2024

Peer reviewed|Thesis/dissertation

Exploring the Potential of Biogenic Manganese Oxides as Water Oxidation Catalyst and Investigating Mn Oxidation Mechanism Using Electron Paramagnetic Resonance (EPR) Spectroscopy

By

WEN FU

DISSERTATION

Submitted in partial satisfaction of the requirements for the degree of

DOCTOR OF PHILOSOPHY

in

Chemistry

in the

OFFICE OF GRADUATE STUDIES

of the

UNIVERSITY OF CALIFORNIA

DAVIS

Approved:

R. David Britt, Chair

William H. Casey

Marie C. Heffern

Committee in Charge

2024

Exploring the Potential of Biogenic Manganese Oxides as Water Oxidation Catalysts and Investigating Mn Oxidation Mechanism Using Electron Paramagnetic Resonance (EPR) Spectroscopy

Contents

Abstract

Water splitting is a promising but challenging solution to alleviate the urgent fuel crisis. While the hydrogen-evolution reaction provides the powerful hydrogen gas as a renewable energy source, the high energy barrier of the anodic oxygen-evolution reaction (OER) limits the overall water splitting efficiency. While heavy metal oxides have been found to be the highly efficient OER catalysts, nature employs the oxygen-evolving complex (OEC) in the photosystem II, which consists of a Mn_4O_5Ca cluster. It generates most of the O_2 in the world in a highly efficient and persistent manner. Inspired by the OEC cluster, in this dissertation, we synthesized biogenic manganese oxides ($BioMnO_x$) using a multicopper oxidase Mnx for OER catalysts. Chapter 1 will provide background information about the OER catalysts, the Mnx protein and Electron Paramagnetic Resonance (EPR) spectroscopy. Chapter 2 will explore the potential of the $BioMnO_x$ as OER catalysts and the structure-function relationship. Chapter 3 will investigate Co-doping effect of $BioMnO_x$ as well as the structural elucidation of Co-doped $BioMnO_x$ using X-ray Absorption Spectroscopy (XAS). On the mechanistic side of the story, Chapter 4 investigates the first row transition-metal ion-inhibition effect of Mnx. EPR spectroscopy has been proven to be a powerful tool to selectively probe the active sites and the metal binding sites of Mnx. Understanding the mechanism of the inhibition effect provides fundamental knowledge about the Mnx mechanism and provide information for formulating and optimizing $BioMnO_x$ synthesis. Chapter 5 extends the usage of EPR spectroscopy to other metalloprotein and inorganic systems.

Acknowledgments

First and foremost, I would really like to thank my advisor Dr. David Britt. He led me into the door and provided a great platform for me to learn, to concur and to discover. He provides not only tremendous support to my work, but also insights and critiques about my work, which is critical for me to think and move forward. I would like to express my greatest gratitude to the postdoc in the lab Lizhi Tao. Not only did she help me get started with my project, but she also instructed me how to approach scientific problems and how to think critically and professionally. Her academic professionalism and rigor also really impressed and inspired me.

I would also like to thank the Britt group for the great support and help over the years. I thank Guodong Rao, Khetpakorn Chakarawet and Gary Chow for providing comfort and support when I felt upset in research. I thank David Marchiori, Rick Saylor, and Derek Gagnon for leading me to the technical world, the helium liquefaction system. I thank Paul Stucky, Bryan Hunter, Aidin Balo, Troy Stich and Jarett Wilcoxen for providing great advice about my research. I would also like to thank Trisha Nguyen, David Villarreal and Liam Twomey for sharing ideas about research and everything.

I would like to thank Thomas Jaramillo and Joel Sanchez for allowing me to learn the electrochemistry and XPS techniques in the Jaramillo group in Stanford. I would also like to thank Jesus Velazquez, Forrest Hyler, Jessica Ortiz and Kingston Robinson for helping me with XAS experiments and ECSA measurement for my research. I would like to thank Drs. Ruchira Chatterjee and Yubing Lu at LBNL for the sincere help with my EXAFS fitting problems. I would like to thank Jeff Walton, Ping Yu and Derrick Kaseman for working

with me on the helium liquefaction system. These have been memorable experiences for me! I would like to thank all my friends for your companion and bringing me fun in my life!

Last but not the least, I would like to thank my significant other, Hui-Yuan Miao, for all her love and supports that my heart can hold. I would like to thank my parents and all my family for the unconditional support and love through my PhD and my whole life. I got my Ph.D. and move on to the next step of my life, did you see that, my dear grandparents?

The work was support by the National Science Foundation award number CHE-1665455 to R.D.B.

List of Figures

List of Tables

CHAPTER 1

Introduction to water oxidation catalysts and multicopper oxidase

1.1. Water Oxidation Catalysts (WOC)

The world's power consumption is expected to surge to 30 TW by 2050 and 50 TW by 2100. [1] Due to their high energy density, high accessibility, high controllability and mature industrialization processing techniques, fossil fuels have become our main energy source. However, as we exponentially expand our use of fossil fuels, the detrimental effects of fossil fuels have become a major concern. On the one hand, the combustion of fossil fuels generates toxic gases such as SO_2 that leads to significant environmental pollution and also endangers people's lives in many countries and the notorious global warming gas CO_2 that leads to inevitable global climate change. [2, 3] On the other hand, fossil fuels are the byproducts of photosynthesis that have been accumulating for millions or even billions of years. [4] The ever-increasing demand of fossil fuels conflicts with its nature of non-renewability, thus leading to an alarming call that we should find an alternative energy source that is carbon-neutral, and largely accessible, and environmentally friendly. A promising solution is water splitting to generate hydrogen fuel generation, the clean energy source. [5]

Upon applying electrical current to a hydrogen fuel-cell system, a water-splitting electrolysis can occur. Depending on the pH of the electrolyte, the water splitting can be mediated by either H^+ or OH^- (Figure 1.1). The overall net potential is -1.23 V. The stepwise reaction of water oxidation requires a large overpotential due to the high kinetic barrier of the reaction intermediates. [6] The major challenge of water electrolysis is the large overpotential caused by the high energy barrier of the OER, a process that involves the transfer of four electrons per molecule of O_2 generated. [7, 8]

In nature, water oxidation is conducted by the highly efficient Oxygen Evolution Complex (OEC) in the photosystem II (PSII). OEC will be briefly discussed in the next section. Synthetically, researchers have found that noble metal oxides are by-far the most efficient water oxidation catalysts. Platinum wire as the cathode coupled with IrO_2 as the anode generates a significantly-high-current-density system. [9] Besides, Rh, Ir and Ru oxides have been identified as highly active heterogeneous OER catalysts. [10, 11, 12]

Though noble metal oxides exhibit high current density and high OER efficiency, a global-scaled industrialization of these catalysts is still very challenging due to the extreme scarcity. [13] Thus, Earth-abundant element-based OER catalyst is a more promising solution to this concern. Most of the Earth-abundant elements that can form stable and active WOC are among the first row transition metal. [14] TiO_2 was proposed as a good photocatalyst but due to its large band gap (> 3 eV), the catalytic efficiency is limited and there was no significant progress. [15, 16] $BiVO_4$ has been identified as a promising photoanode material due to its lower band gap ($\sim$2.4 eV). [17] Though bulk oxides are not conductive due to their high band gaps, the titanium and vanadium oxides are moderate OER catalysts when in the form of thin films. In addition, α-Fe_2O_3 was identified as an efficient OER catalyst. [18] Though CuO, $Cu(OH)_2$ and ZnO have been shown as efficient OER catalysts, Cu- and Zn-oxide-based WOCs are not as efficient as Mn/Ni/Co-oxide-based OER catalysts. [19, 20, 21] NiO_x were also studied extensively as a promising OER catalyst. [22, 23]

While CoO_x has been shown to be a stable OER catalyst at high pH with positive potentials, [14] Kanan et al. electrodeposited Co^{2+} in phosphate buffer to acquire a highly active and stable CoPi catalyst that is stable at neutral pH (pH = 7). [24] This discovery has then inspired loads of research about the mechanism of the CoPi catalyst and the discovery of new cobalt-oxide-based OER catalysts. Co(IV) was shown to form during the electrolysis of CoPi and it was also shown that CoO_6 octahedra with O-O bond formation at the edge are the major structure for most of the Co-oxide-based catalysts. [25, 26, 27, 28] In addition to CoPi, other Co oxides such as Co_3O_4 [29, 30, 31], Co_4O_4 cubane [32] and Co-Mn layered hydroxide

[33] are also shown as extremely active OER catalysts. Note that Co_4O_4 cubane has similar structure to the OEC in PSII. The other promising candidate of first-row transition metal oxide OER catalysts are manganese oxides. Inspired by the fact that WOC in PSII is composed of mostly Mn, extensive research have been conducted to investigate the potential of manganese oxides as OER catalysts, which will be briefly summarized in the next section.

1.2. Oxygen Evolution Center (OEC) complex and MnO_x

Oxygenic photosynthesis, developed around 2.4 billion years ago, [34] converts the sunlight energy into chemical energy by organisms such as plants, algae and cyanobacteria. [35] Oxygenic photosynthesis is the main source of most of the oxygen content and supplies most of the biological energy necessary for the complex life on the Earth. [36] Among all the oxygenic photosynthesis machinery components, photosystem II (PSII) harvests the sunlight and catalyzes the water-oxidation reaction to produce dimolecular oxygen. The catalytic unit in the PSII is called the Oxygen Evolution Complex (OEC). [37] OEC is composed of a $CaMn_4O_5$ cluster with a $CaMn_3O_4$ cubane and a dangler Mn. [38, 39, 40] While X-ray crystallography alone cannot provide all the information about the structure, results from the X-ray absorption spectroscopy, [41, 42] EPR spectroscopy, [40, 43] FT-IR spectroscopy, [44, 45] mass spectrometry, [46] and computational methods [47] are combined to provide the complementary information about the location of the small molecules as well as the insights about reaction dynamics. [48] As a result, the "Kok cycle" of the OEC was proposed and confirmed to describe a mechanism of water oxidation with proton-coupled electron transfer (PCET) (Figure 1.3). [49, 50] In this mechanism, the tyrosine residue near the active site (Y161) is oxidized by P680 to form oxygen radical cation, which then catalyzes the oxidation of Mn clusters. [51] Depending on the oxidation states of Mn atoms, the OEC center is oxidized from S_0 to S_4, followed by release of dimolecular oxygen. While S_4 state is the least stable intermediate, the other paramagnetic Mn-cluster states have been extensively studied via EPR spectroscopy. [52, 53]

1.3. Current methods of synthesizing catalytic MnO_x

As Mn can adopt multiple metal oxidation states, [54] there are multiple types of manganese oxides and also additional ways to synthesize manganese-oxide catalysts include comproportionation reactions from reacting Mn^{2+} with permanganate and oxidizing Mn^{2+} from lower oxidation to higher using an external oxidant. Though aqueous manganese complexes are not stable during electrolysis under alkaline solution, [14] MnO_2 has been shown as a reasonably good OER catalyst in alkaline electrolyte solution. [55] Then, nano-sized Mn_2O_3 and layered Na-birnessite, with intercalation of divalent cations in particular, were shown as promising OER catalysts. [10, 56, 57, 58] It was proposed that surface-active Mn(III) sites are critical for water oxidation at neutral pH. [55, 59, 60] Besides different manganese-oxide compositions, particle sizes, methods of preparation, ion conductivity and carrier mobility within the material in combination determines the enhanced activity of manganese-oxide OER catalysts. As a result, the method to prepare manganese-oxide WOCs is especially critical for the catalytic activity.

One of the most common methods of synthesizing manganese-oxide single crystal or nanomaterials is hydrothermal synthesis, which crystallizes nanomaterials from high temperature aqueous solution at high pressure. [61] Various manganese oxides materials such as MnO_2 or Mn_2O_3 have been reliably synthesized using this method. [62, 63, 64, 65] The advantages of the hydrothermal synthesis are two folds. First, by varying the temperature and pressure, it allows the crystallization of the materials which may have vapor pressure similar to the melting point. Second, by accurately controlling the composition, a good-quality crystal can be obtained. [61] However, the disadvantages are obvious, due to their harsh synthetic conditions and high demand on the precision of the instruments.

An alternative common method for synthesizing manganese-oxide WOCs is electrodeposition. A three-electrode system is typically set up with an external potentiostat as the potential source to reduce the iR resistance. [66] Components of a three-electrode system

involves a working electrode, a reference electrode and a counter electrode. The working electrode in the water oxidation reaction regime is the manganese-oxide catalyst on a FTO/ITO plate, [67] while the counter electrode is commonly Pt metal, [67] or Ni foam [68], or any conductive materials that are too inert to undergo reduction reaction. [66] Ag/AgCl electrode is a common reference electrode, which provides a steady and well defined potential at 0.2225 V in 3.0 M KCl. [69] Electrodeposition has been proven to be an effective way of synthesizing MnO_x WOCs. [67,68,70] Some advantages of electrodeposition for electrocatalyst synthesis are its low cost and improved interfacial bonding between the coating material and substrate. [71] Another benefit is that it allows in-situ synthesis and catalysis of the thin film catalyst. However, one of the main drawback of this method is that the doping of some elements that do not have anodic reactions may not be efficient. For example, nitrate reduction has to be performed to rapidly raise the pH around the working electrode to facilitate La^{3+} and Mn^{2+}/Mn^{3+} co-deposition on the anodes. [72] While the result of this process can have beneficial effects on catalytic activity, the resulting product of the electrodeposition method is defect-prone and amorphous thin film. These properties also adds unpredictability to the resulting product. [73]

The most fundamental synthesis of manganese-oxide catalysts is chemical synthesis. According to the Pourbaix diagram, [14] an easier synthesis can be achieved under strong basic conditions. For example, MnO nanoparticle can be synthesized by reacting manganese acetate with NaOH solution for 12 hrs. [74] However, without further manipulation of the procedure and recipe, impurities and non-homogeneity of the shape and size can easily occur with this simple chemical synthesis.

While the majority of manganese-oxide syntheses require strong oxidants, [75,76,77] strongly basic conditions, [78] or an external electric potential to oxidize Mn(II), [79,80,81,82] researchers have developed green synthesis using plant or even plant extracts. [83,84] Mn-oxidizing microorganisms such as bacteria, [85,86,87,88,89] fungi, [90,91] and algae [92,93] are also used to synthesize manganese-oxides nanoparticles that can be utilized in various

fields. [94] While bio-mediated green synthesis of manganese-oxide nanoparticles has become a hot topic in different fields, the disadvantages of bio-mediated synthesis have become more and more obvious. First, it is much more difficult to control the synthesis conditions with bacteria as the reactants due to the sophisticated nature of the cell machinery. Second, bacteria can exert biological safety issue, which, in particular, will generate a significant amount of biohazard waste in a large-scale reaction. [94]

To solve this problem, the enzyme-catalyzed synthesis needs to be developed to synthesize manganese-oxide catalysts, whose characteristics can be easily manipulated and which can easily avoid the bio-safety issue. In this PhD dissertation, I propose to use an enzymatic pathway to synthesize manganese-oxide minerals under mild conditions and examine the OER activity of those for the application. On the other hand, mechanistic studies of the enzymatic Mn oxidation are also essential. Thus, in this PhD dissertation, I also present some research results of mechanistic investigation of the Mn-oxidizing enzyme, a.k.a. Mnx complex.

1.4. Mn-oxidizing bacteria

While the inorganic process of Mn(II) oxidation happens extremely slowly under ocean water condition in a highly energy-inefficient manner, the biological pathway can expedite this process by 5 orders of magnitude. [95] In nature, Mn-oxidizing bacteria and fungi are universal and responsible for this biological pathway in the global Mn cycle. Mn-oxidizing organisms are defined as a phylogenetically diverse group of microorganisms, which is categorized by the capacity to catalyze the oxidation of divalent, soluble Mn(II) to insoluble manganese oxides. [95] They accumulate Mn in the form of manganese oxides and can be found in deep sea manganese nodules, oxic/anoxic interfaces, manganese-rich surface films of shallow lakes and freshwater lake sediments and ferro-manganese deposits, and etc. [96, 97] Many presumable functions for bacteria to evolve and maintain the highly energy-consuming

Mn oxidation pathway have been proposed by investigators. For example, investigators speculated that Mn oxides can act as a electron acceptor for survival under anaerobic or low oxygen conditions. [98] Many species couple oxidation of the recalcitrant organic carbon, such as lignin, with reduction of MnO_x to provide energy in the nutrient-poor environment. [99] Researchers also found that accumulation of MnO_x can also react with reactive oxygen species (ROS) and thus prevent oxygen damage [100, 101, 102] or even radiation damage [103].

Mn(II)-oxidizing bacteria have been identified in a growing number of divergent phylogenetic lineages in the bacterial domain, such as Firmicutes, Proteobacteria and Actinobacteria [104]. Among the above Mn-oxidizing bacteria, some of the bacteria utilizes peroxides to oxidize Mn(II) indirectly. For example, a heme peroxide has been identified in two alphaproteobacteria species and the reactivity enhancement via addition of Ca^{2+} and H_2O_2 reveals that this calcium-binding enzyme undergoes a peroxide type of Mn oxidation mechanism. [105] Other bacteria encode multicopper oxidases (MCO) to directly oxidize Mn(II) to Mn(III) by one electron, coupled with oxygen reduction. For example, MnxG has been identified in *Bacillus* sp. strain SG-1. [106, 107] The structure and mechanism of Mn-oxidizing multicopper oxidases will be discussed in details in later sections.

1.5. Multicopper oxidases

Copper is an essential trace element to nearly all organisms. [108, 109] Since the Cu(III) active sites have not been observed in biological systems, most of the two-electron redox processes can be achieved with the Cu(I)/Cu(II) redox pair by maintaining either more than two copper centers or one copper and a redox-active cofactor. [108] The roles of coppers in the copper-containing enzymes involves electron transfer, oxidation of organic and inorganic substrates (such as tyrosinase [110]), dismutation of superoxide (such as peroxide dismutase [111]), transport of iron (such as human ceruloplasmin [112]) and reduction of inorganic small molecules (such as nitric oxide reductase [113]). Human ceruloplasmin is an essential cofactor protein in human blood to transport irons. [114] It has been shown that copper is essential for maintaining ceruloplasmin activity and maximizing the iron metabolism. [114]

Ceruloplasmins catalyze the oxidation from Fe(II) to Fe(III), which is then removed from the blood and stored in ferritin. [115]

Multicopper oxidase (MCO) is a large subdivision of the copper-containing enzymes, which oxidizes a wide range of organic or inorganic substrates with the simultaneous reduction of the dioxygen. [116] For example, laccases are able to catalyze direct oxidation of ortho- and para-diphenols, aminophenols, polyphenols, polyamines, and aryl diamines as well as some inorganic ions. [117, 118, 119, 120, 121, 122] The reduction potential needed for the oxidation of the substrate ranges from 420 mV to 790 mV. [117, 123] Among all the oxidation substrate for multicopper oxidases, the oxidation from Mn(II) to Mn(III) has a reduction potential of 1.5 V, which poises a large kinetic barrier for most of the enzymatic processes. However, the water-oxidation reaction at physiological conditions requires 1.23 V vs NHE, which would precede Mn(II) oxidation. Thus, to this end, the manganese oxidase is presumed to be highly regulated and thus understanding the structure and mechanism of manganese oxides is of critical significance. [106, 107, 124, 125, 126, 127]

The functions of the MCO are mostly achieved by majorly three types of coppers: Type I copper (T1Cu), Type II copper (T2Cu) and Type III copper (T3Cu). T1Cu, also known as the blue copper, is typically coordinated in a trigonal pyramidal geometry by one cysteine and two histidine side chains. The intense ligand-to-metal charge transfer transition gives the characteristic UV-vis peak at around 590 nm, which is often used to quantify the T1Cu-containing protein concentration. [128] T2Cu, also known as the "normal copper", is typically in square planar geometry, coordinated by histidine side chains and hydroxo groups. T3Cu is a binuclear copper site where two copper atoms are bridged by oxo or hydroxo groups. T3Cu is usually coupled with a T2Cu to form the trinuclear copper site (TNC), which serves as an electron sink in MCO to reduce the dioxygen to water (Figure 1.4). [117] Typical reactions for MCO involve the sequential one-electron oxidation of the substrate, electron transfer through side chains to TNC site, and the reduction of the oxygen to water.

1.6. MnxEFG complex

Manganese oxides widely exist on Earth's crust and surface and have been used for thousands of years in pigments, glass, battery and so on. [129] While abiotic manganese oxidation happens slowly in the seawater condition, biological manganese oxidation occurs much faster by 3 to 5 orders of magnitude. [130] A gene cluster, called *mnxG*, was discovered in marine Bacillus species to be responsible for the majority of the Mn(II) oxidation in the ocean. [106] Numerous attempts to purify an active Mn-oxidizing MCO enzyme were unsuccessful until 2012, [131] when the Tebo lab succeeded in heterologously producing an active manganese oxidase Mnx, from Bacillus sp. PL-12, a halotolerant organism isolated from marine sediments, [107, 132] but closely related to species from soil environments. Mnx is a complex of MnxG, a large (138 kDa) multicopper oxidase, tightly bound to small (12 kDa) accessory proteins, MnxE and MnxF, in the form of hexamers. [131, 133] MnxG has been shown to be catalytically active towards manganese oxidation, whereas MnxEF hexamer is found to be essential for preventing aggregation and stabilizing MnxG. [128] While MnxE and MnxF do not have close homologues, MnxG was found to be similar to the human ferroxidase ceruloplasmin. [106] MnxG has been found to have two T2Cu, one T1Cu and one T3Cu whereas MnxEF hexamer has three T2Cu that is different from the T2Cu in the MnxG. [128] Human ceruloplasmin, on the other hand, consists of two T1Cu, one T2Cu and one T3Cu. [134] However, besides the coppers consisting of the TNC site, the exact function of the extra T2Cu in the MnxG is still unknown. In addition to the Cu binding sites, MnxG also possesses two types of Mn(II) substrate binding sites as are identified by Electron Paramagnetic Resonance (EPR) spectroscopy: mononuclear Mn(II) site and a binuclear Mn(II) site. [81]

While, though the properties of the Mn(II) EPR signals, kinetics and inhibition effects can be probed, [135] the Mn(II) oxidation mechanism and the exact structure of the Mn binding sites still needs investigation. Many studies lean towards the one-electron oxidation mechanism, i.e. Mn(II) to Mn(III) and then to Mn(IV). [131, 136, 137] Detailed

spectroscopic and kinetic measurements [81, 136, 137, 138] led us to propose a mechanism for Mn(II) oxidation shown in Figure 1.2. Two Mn(II) ions bind to Mnx, inducing a conformational change that brings the two Mn(II) together via a hydroxide bridge, following deprotonation of Mn(II)-bound H_2O. [136] The Mn(III)/Mn(II) reduction potential is then lowered sufficiently to permit oxidation by the T1Cu, producing a doubly hydroxide-bridged binuclear Mn(III) intermediate. This intermediate disproportionates to oxo-bridged Mn(IV) and Mn(II), which recycles back to the Mn(II) substrate site. The oxo-bridged Mn(IV) then condenses to form MnO_2 nanoparticles. [137]

To explore the details of the structure of the active sites and the mechanism of Mnx complex, electron paramagnetic spectroscopy (EPR) is used to look at the paramagnetic Cu(II) species with spin 1/2 in the oxidized Mnx complex as well as the paramagnetic Mn(II) species with spin 5/2 to investigate the course of the reaction. The most critical advantages of EPR in this project involves:

1. EPR allows the detection of catalytic active sites, in this case Cu(II) protein binding sites and Mn(II) substrate binding sites, without the interference from other parts of the protein.

2. EPR gives the active-site structures at the molecular level while other protein structural characterization techniques are not applicable. So far, no molecular-level structures of the Mnx complex have been obtained via X-ray crystallography, TEM or NMR. [133]

3. EPR allows tracking of the electronic-structure change or metal coordination environment change in the active sites. These changes can be reflected by the changes in the g values or hyperfine patterns or hyperfine values.

4. Fast-freezing of the protein sample during a reaction course also provides a way to trap reactive paramagnetic intermediates, which can then be identified by EPR measurement. Knowing the information about the coordination environment and electronic structures of these intermediates is critical for investigating the mechanism of an enzymatic catalysis.

With the above advantages, EPR has been shown to be essential techniques for obtaining the structural and mechanistic information of metalloprotein as well as other inorganic or organic systems with paramagnetic centers. The Britt group, a.k.a. the CalEPR facility at the University of California-Davis, are home to six EPR instruments ranging from 9 to 263 GHz. In Chapter 4, I will mention some EPR studies related to Mnx complex while in Chapter 5, I will mention some of my collaboration work on various systems to show the power of EPR spectroscopy in Chemistry research. Below, I will briefly introduce the fundamentals of EPR spectroscopy.

1.7. Electron Paramagnetic Resonance (EPR)

1.7.1. Introduction to basics of spins. Each electron has a spin s = 1/2 with magnetic components of m_s = +1/2 and m_s = -1/2. Under a non-zero magnetic field, the electrons with different magnetic spin quantum numbers will align either parallel (m_s = +1/2) or antiparallel (m_s = -1/2) to the external magnetic field and the energy for each electron spin is defined as in Equation (1.1), where g_e is the electron's g-factor and μ_B is the Bohr magneton, which describes the magnetic moment of an electron due to its orbital or spin angular momentum.

$$E = m_s g_e \mu_B B_0 \tag{1.1}$$

This phenomenon is known as the Zeeman effect. Due to the Maxwell-Boltzmann distribution, the antiparallel spins with lower energy state have more spin population than the parallel spins under low thermodynamic temperature (e.g. 298 K). As a result, an antiparallel electron can change the m_s under the resonance condition by absorbing the photon of the energy as shown in Equation (1.2).

$$\Delta E = h\nu = g_e \mu_B B_0 \tag{1.2}$$

This is the foundation of Electron Paramagnetic Resonance (EPR) spectroscopy. Continuous-wave (CW) EPR is designed to sweep the external magnetic field at a fixed frequency and an absorption peak appears when the resonance condition is reached. X, K, Q, W and D band are commonly used as an alternative name for the microwave frequencies of around 9, 26, 45, 85 and 140 GHz. A typical outcome CW EPR spectrum is in the first derivative form due to the field modulation. Applying a small additional oscillating magnetic field and then using the phase-sensitive detection to filter the signal can result in an enhancement of the signal-to-noise ratio. The resulting spectrum is in the first derivative because of the lock-in detection mode. As an example for an EPR spectrum, a spin system with S = 1/2 has a spin transition at 340 mT with the microwave frequency of 9.5 GHz. This leads to an absorption peak and a first-derivative peak with field modulation (Figure 1.5).

1.7.2. Spin Hamiltonians. The above situation is a spin system of S = 1/2 with one electron. When two or more electron or nuclear spins are present, interactions between those spins and between spins and the magnetic field can happen. Spin Hamiltonians are used to describe and quantify the interactions. Examples of the spin Hamiltonians are electron Zeeman interaction, nuclear Zeeman interaction, hyperfine interaction, zero-field splitting and nuclear quadruple interaction.

The electron Zeeman (EZ) that describes the interaction between electron spin and the magnetic field can be represented by the spin Hamiltonian in Equation (1.3). Here, g is a dimensionless matrix and $\hat{S}$ is the total electron spin.

$$\hat{H}_{EZ} = \mu_B \vec{B}_0 g \hat{S} \tag{1.3}$$

In contrast to the EZ, the nuclear Zeeman interaction (NZ) describes the interaction between nuclear spin and the magnetic field. In Equation (1.4), μ_N is the nuclear magneton, g_N the nuclear g-value and $\hat{I}$ the total nuclear spin. The negative sign compared to EZ is due to the charge difference between the nucleus and the electron.

(1.4) $$\hat{H}_{NZ} = -\mu_N \vec{B}_0 g_N \hat{I}$$

The hyperfine interaction (HFI) spin Hamiltonian describes the interactions between electron spin and the nuclear spin, as shown in Equation (1.5). $\hat{S}$ and $\hat{I}$ are the electron spin and the nuclear spin while A is the matrix value for the hyperfine constant. A can be separated into isotropic component, A_{iso}, and dipolar component, A_{dip}. The Cu^{2+} system, for example, has a total spin S = 1/2 and shows the characteristic four-line hyperfine structure due to the nuclear spin I = 3/2 for both ^{63}Cu and ^{65}Cu.

(1.5) $$\hat{H}_{HFI} = \hat{S}A\hat{I}$$

Zero-field splitting (ZFS) values describes the dipolar interaction between electron spins for a spin system with S > 1/2, which breaks the degeneracy of the m_s levels at the zero magnetic field. The spin Hamiltonian of ZFS is shown in Equation (1.6) and Equation (1.7). A large ZFS is observed for Mn(II) spin system where the total electron spin S = 5/2 and the nuclear spin of ^{55}Mn, I = 5/2, complicates the EPR of the simple Mn(II) even more. [139]

(1.6) $$\hat{H}_{ZFS} = \hat{S}D\hat{S}$$

(1.7) $$\hat{H}_{ZFS} = D(\hat{S}_z^2 - 1/3(S(S+1) + E/D(\hat{S}_x^2 - \hat{S}_y^2)))$$

Other spin Hamiltonians include nuclear quadruple interaction (NQI), caused by the interaction between the electric quadruple moment and the electric field gradient of the nucleus in the spin system with I $\geq$ 1.

1.7.3. Cu(II) EPR. Because the Mnx is a multicopper oxidase that consists of T1Cu and T2Cu, here introduces the typical Cu(II) EPR. Cu(II) has an electronic configuration of d^9. In the aqueous environment, Cu(II) mainly adopts an axially elongated octahedral geometry, which results in the total electron spin S = 1/2. On the other hand, the two most stable isotopes for Cu both have nuclear spin I = 3/2, which leads to the same hyperfine structure. So in this case, the spin Hamiltonian can be represented in Equation (1.8). Due to the fact that EZ is much larger than NZ and NQI for Cu(II), the latter are typically neglected to the degree of approximation.

$$\hat{H}_{Total} = \hat{H}_{EZ} + \hat{H}_{HFI} = \mu_B \vec{B}_0 g \hat{S} + \hat{S} A \hat{I} \tag{1.8}$$

Figure 1.6 shows the EPR spectrum of Cu^{2+} in H_2O. The spectrum shows an axial powder form with $g_{\|} > g_{\perp}$ and $A_{\|} > A_{\perp}$, where $\|$ means parallel to the z direction and $\perp$ means parallel to the x, y plane. This axial powder form results from the Jahn-Teller distortion of d^9 electronic configuration where the direction parallel to the z direction is the unique axis. The quartet feature results from the hyperfine interaction between the unpaired electron from the d orbital and the nuclear spin of the copper.

1.7.4. Mnx Cu(II) EPR. The EPR spectrum of 25 μM of as-isolated Mnx EFG is shown in Figure 1.7. The simulation was performed using EasySpin software package. [140, 141] The EPR spectrum shows three types of copper, T1Cu and two types of T2Cu. EPR spectrum of the MnxEF hexamer alone shows the signal for only the T2Cu-B, revealing that T2Cu-B exists in MnxEF and also inferring that T2Cu-A exists in MnxG. [142] No T3Cu signal is shown on EPR because the dinuclear T3Cu site is antiferromagnetically coupled and thus EPR silent. T1Cu is buried in the signals of the T2Cu and cannot resolve well under either X band or Q band EPR spectra though the peak at 590 nm and the mutagenesis study on the T1Cu-binding residue H140A reveals the presence of T1Cu. [128] In Chapter 4, I will

show that the addition of Co^{2+} to the as-isolated Mnx selectively removes the T2Cu-A, thus exposing the T1Cu signal on Q band EPR.

Using sodium dithionite can make all Cu sites EPR silent due to the formation of diamagnetic Cu(I) with an electronic configuration of d^{10}. This creates the reduced version of the Mnx, called red-Mnx, which does not undergo manganese oxidation under anaerobic environment. The benefits of the red-Mnx are: 1. It allows us to focus on the EPR signal of the substrate ion, such as Mn(II), without the interference of Cu(II) signals at the center field; 2. The non-reactive nature of red-Mnx helps us investigate the structure of the Mn(II) substrate binding sites; 3. Upon re-exposing to the oxygen, the red-Mnx will be oxidized and resume the oxidase activity. In this case, by freeze-quenching the reaction mixture with liquid nitrogen, a Mn(III) intermediate can be trapped and investigated. Thus, the red-Mnx can facilitate the investigation of the binding site structure and properties as well as the manganese oxidation mechanism.

1.7.5. Spin quantification of Cu(II). The intensity of the peak-to-peak amplitude is reflective of the quantity of the Cu(II) spins. In reality, the slight variation of the individual Cu(II) spin environment can cause variations in the g and A tensors, which causes broadening of the peak. As a result, the Cu(II) spins can be quantified by integrating the absorption spectrum. [143] Previously, the number of the Cu(II) in Mnx was estimated based on the comparison of the integral with that of a standard Cu(II) spectrum. [128]

Here, I present the spin quantification of a series of known concentrations of Cu(II) in H_2O as a standard curve for Cu(II) quantification in the sample (Figure 1.8). The EPR spectra of different known concentrations of Cu(II) in H_2O are taken under 15 K and 40 dB where Cu(II) signal is checked to be unsaturated. The first derivative plots were then baseline-corrected and integrated to acquire the absorption spectra. The integral of the absorption spectra was then calibrated with Q values to get the final spin quantification value. As shown in Figure 1.8, the EPR signal and the corresponding absorption spectra increase linearly in the intensity when the concentration increases. In Figure 1.8C, the linear

relationship between the measured Cu(II) concentration and the theoretical concentration is illustrated and then compared with that acquired from ICP-MS, a technique that measures the amount of total Cu in the sample.

The two standard curves show reasonable accuracy of Cu(II) concentration with high R-square values. The two standard curves both give a slope less than 1, indicating that the actual Cu(II) concentration is slightly lower than the expected Cu(II) concentration. One reason that EPR curve has a lower slope than ICP-MS is that some of the Cu(II) becomes EPR silent probably due to dimerization. In many cases in biology, dimerization of the two monomeric copper means degradation of a copper active site or the loss of function. Thus, to this end, compared to ICP-MS, quantitative EPR is a great tool to quantify the mononuclear Cu(II) spins, which are essential for the enzymatic activity of copper-containing proteins.

1.7.6. Cu(II) in different buffer systems. Many copper-containing enzymes are studied in different buffer systems such as HEPES and Tris buffer because their pKa is close to the physiological pH. However, the solubility of copper in different buffer systems are different. With the Cu(II) concentration standard curve determined via EPR, a brief investigation of the Cu(II) in six buffers can be determined. 100 μM of $CuSO_4$ was made in different buffers at pH 7.8 and the precipitate was filtered out with 3 kDa microfilter. The concentration standard curve determined in Section 1.7.5 was used to determine the actual concentration of soluble Cu(II) in the buffer. As shown in Figure 1.9, Cu(II) in phosphate, HEPES and MOPS buffers do not form soluble Cu-buffer complex while Cu(II) forms stable complexes in Tris, Imidazole and TES buffers. These results alert us that when working with copper-containing proteins, the buffer choice is critical due to the potential precipitation.

In aqueous acid:

Anode:	$2\ H_2O\ (l)$	→	$O_2\ (g) + 4\ H^+ + 4\ e^-$	$E^0 = -1.23\ V$
Cathode:	$4\ H^+ + 4\ e^-$	→	$2\ H_2\ (g)$	$E^0 = -0.00\ V$
Total:	$2\ H_2O\ (l)$	→	$O_2\ (g) + 2\ H_2\ (g)$	$E^0 = -1.23\ V$

In aqueous base:

Anode:	$4\ OH^-$	→	$O_2\ (g) + 2\ H_2O\ (l) + 4\ e^-$	$E^0 = -0.40\ V$
Cathode:	$4\ H_2O\ (l) + 4\ e^-$	→	$2\ H_2\ (g) + 4\ OH^-$	$E^0 = -0.83\ V$
Total:	$2\ H_2O\ (l)$	→	$O_2\ (g) + 2\ H_2\ (g)$	$E^0 = -1.23\ V$

FIGURE 1.1. Scheme of water splitting half reactions at low and high pHs. Regenerated with permission from Hunter, et al. [2]

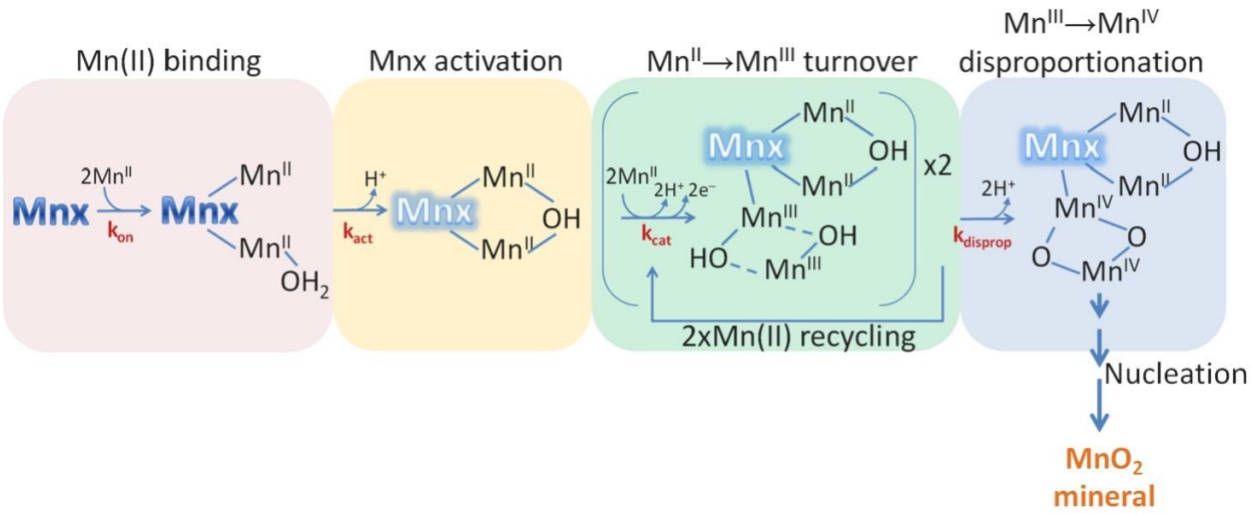

FIGURE 1.2. Proposed Mnx mechanism of Mn(II) oxidation and MnO_2 formation: Two Mn(II) bind at the Mnx substrate site (Mn(II) binding step), and form a hydroxide-bridged activated complex, [Mn(II),Mn(II)](OH), following a protein conformation change and Mn(II)-OH_2 deprotonation (Mnx activation step). Electron transfer and Mn(III) translocation leaves [Mn(II),Mn(III)](OH), and turnover produces a dihydroxide-bridged Mn(III) intermediate, [Mn(III),Mn(III)]$(OH)_2$ Mn(II) → Mn(III) turnover step). Two of these intermediates subsequently disproportionate to two Mn(II) ions, which are recycled, and a dioxo-bridged Mn(IV) product, [Mn(IV),Mn(IV)]$(O)_2$ (Mn(III) → Mn(IV) disproportionation step), which then condenses into MnO_2 nanoparticles(nucleation step).

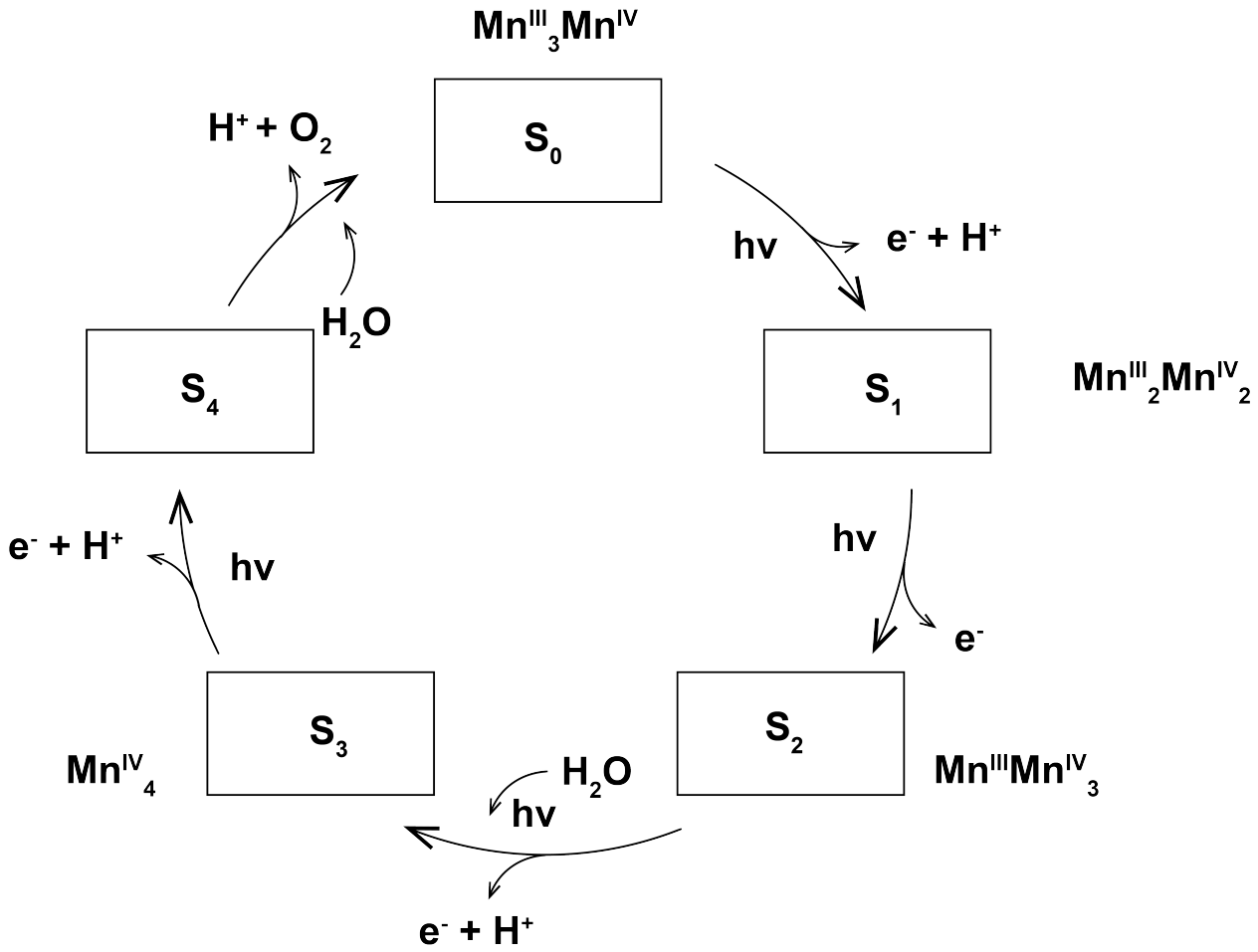

FIGURE 1.3. Simplified Kok cycle.

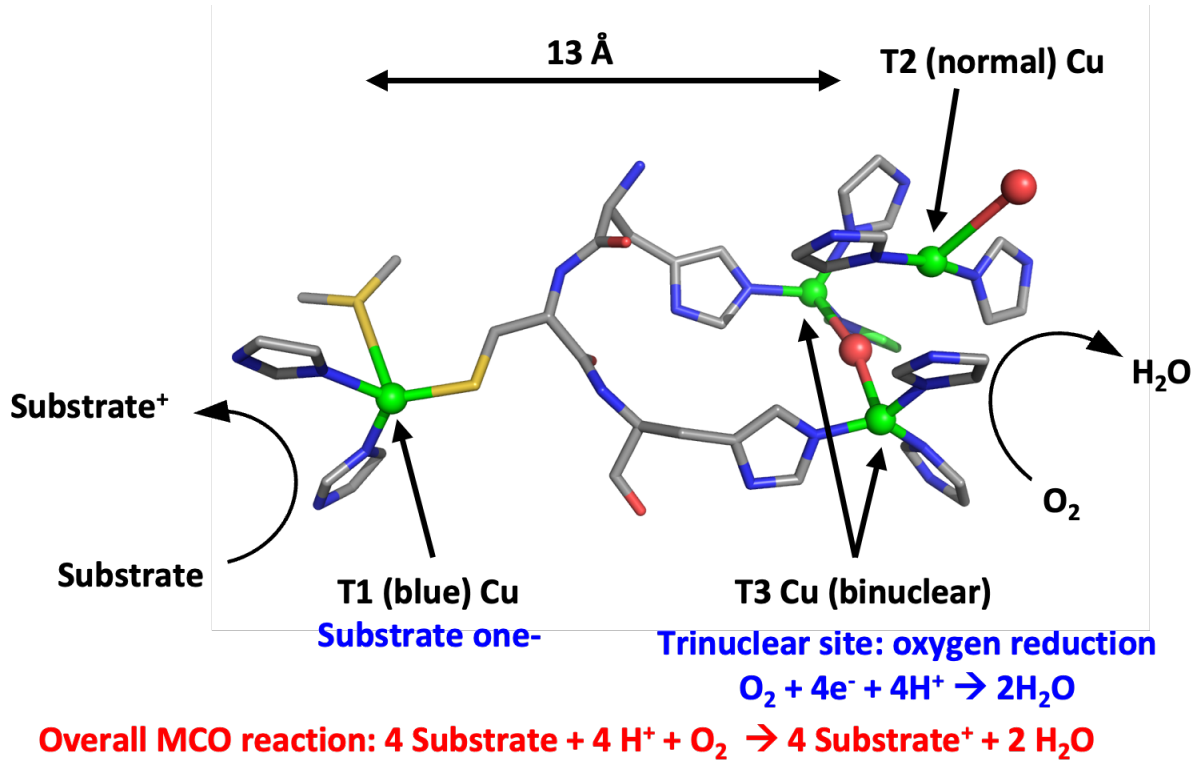

FIGURE 1.4. The copper actives sites of the human ceruloplasmin (PDB: 4enz) [134]

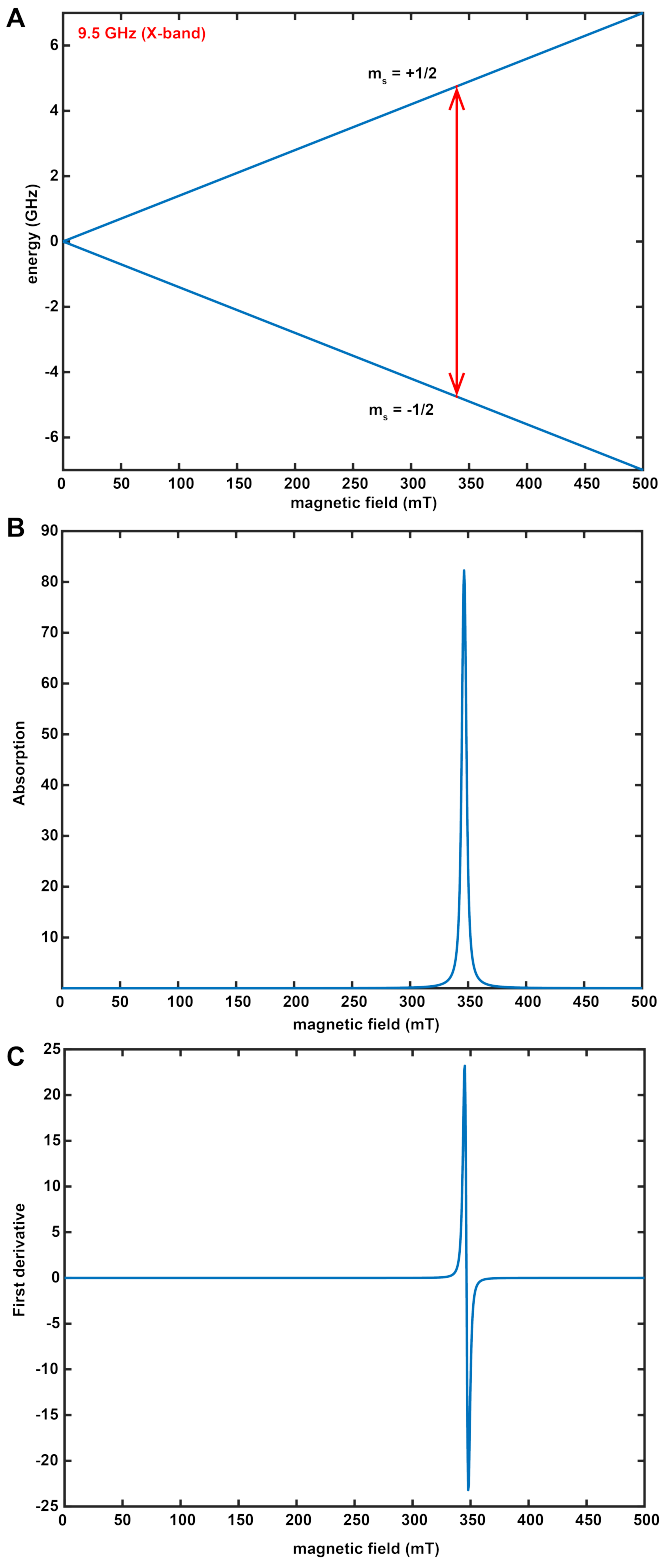

FIGURE 1.5. X-band CW EPR spectral simulation for S = 1/2 system.

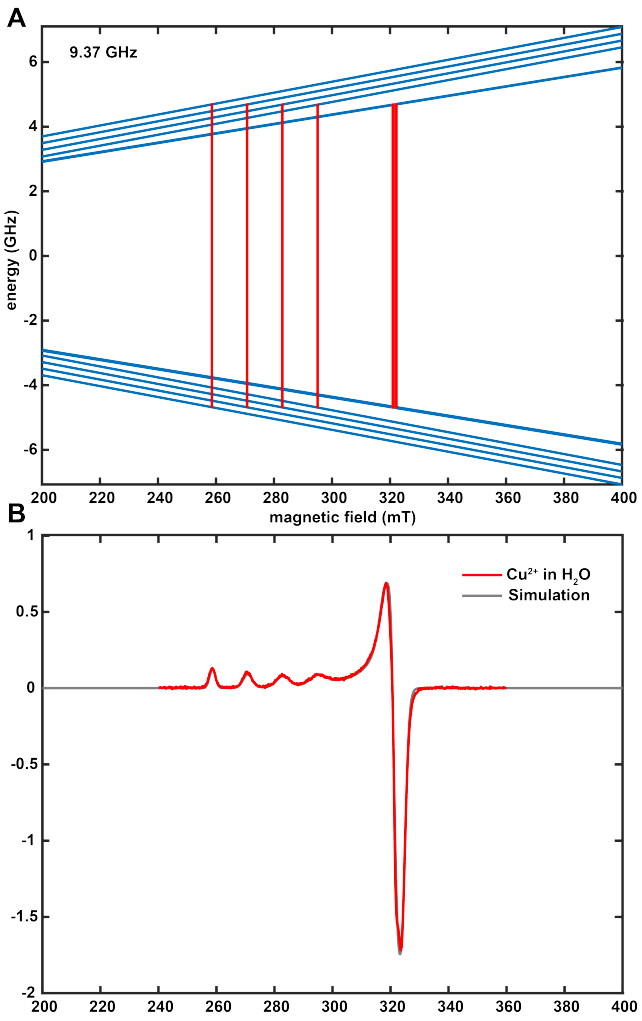

FIGURE 1.6. X-band CW EPR spectral simulation for Cu^{2+} in water.

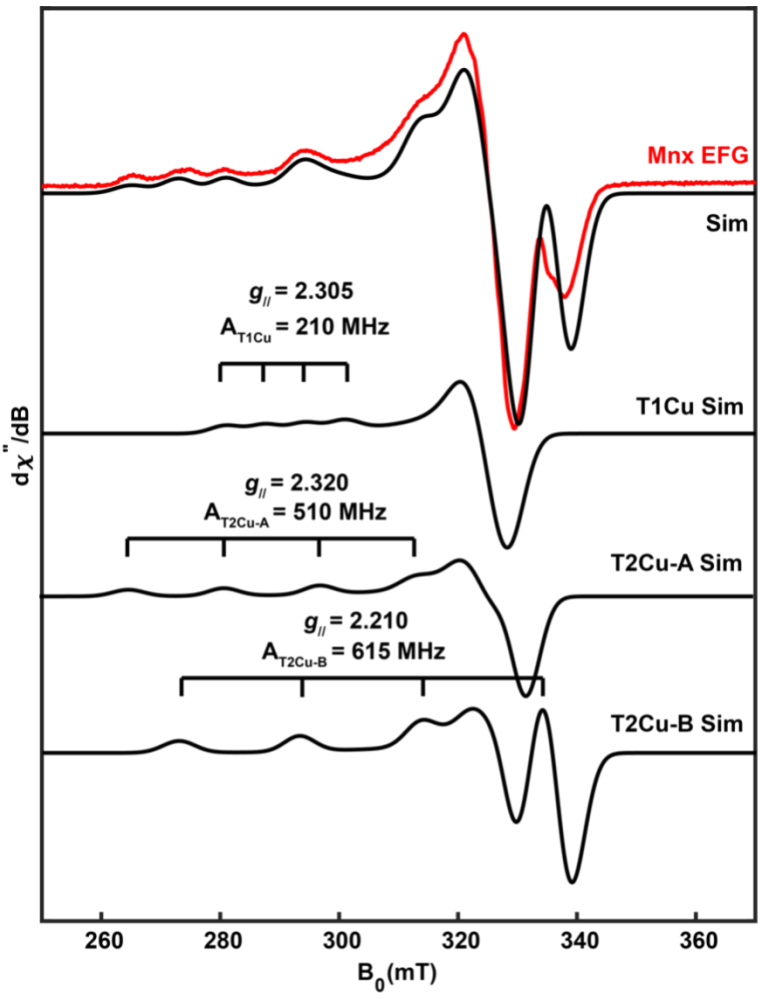

FIGURE 1.7. X-band CW EPR spectrum (Red) and simulation (Black) of Mnx.

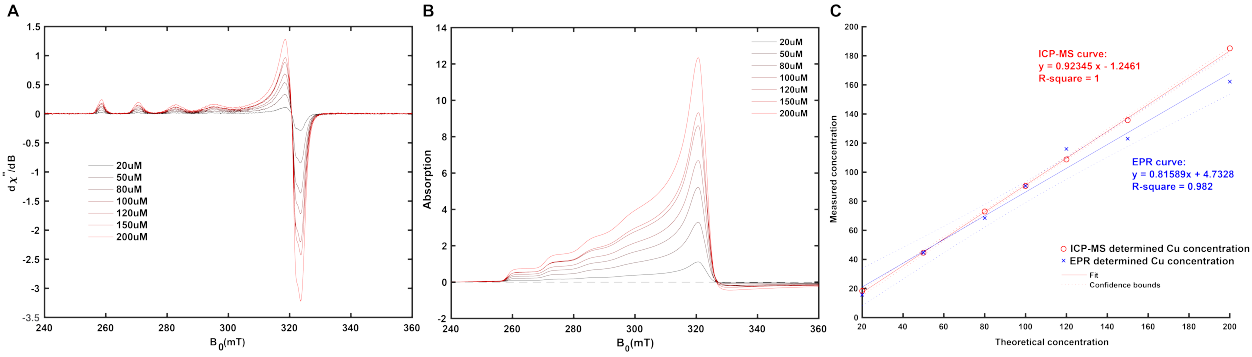

FIGURE 1.8. Cu(II) spin quantification with known concentration of Cu(II). C shows two standard curves with ICP-MS and EPR.

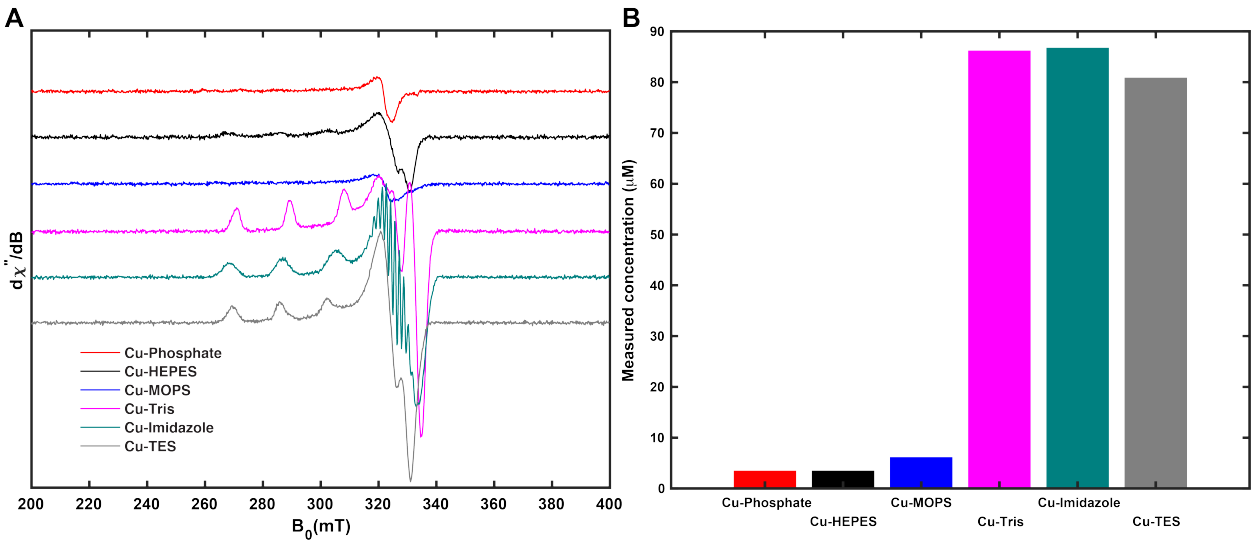

FIGURE 1.9. Cu(II) EPR spectra (A) and spin quantification (B) of 100 μM Cu_{2+} in different buffer systems at pH 7.5.

CHAPTER 2

The biogenic manganese oxides by MnxEFG for water oxidation

2.1. Abstract

Solar energy provides one major pathway to addressing global energy problems. Inspired by photosynthesis, non-biological solar energy systems are designed to both absorb light and "split water" to generate hydrogen fuel. However, during this process, the oxygen evolution reaction (OER) at the anode has a high kinetic barrier and overpotential, which reduces the overall efficiency. To improve the efficiency of OER, intensive efforts have been put forward developing promising OER catalysts. Inspired by the highly efficient oxygen-evolving complex (OEC) in photosystem II in Nature, manganese-oxide catalysts have garnered intensive attention due to the availability and minimal toxicity. However, the synthesis of most manganese-oxide catalysts requires strong oxidants, external high electric potentials, or highly basic conditions, which makes large-scale production energy-consuming and less efficient. In this study, we present a natural and clean process for synthesizing manganese-oxide catalysts using an oceanic bacterial manganese oxidase named MnxG. The biogenic manganese oxides, as generated under different conditions, have different morphologies and crystalline structures and are as effective or even more effective than synthetic Mn birnessites. Spectroscopic analyses, including XAS, XPS and EPR, suggest that the monoclinic-birnessite component, together with surface Mn(III) species, plays a crucial role in the OER activity of biogenic MnO_x(Figure 2.1).

The content in this chapter is reproduced from a manuscript submitted to ACS Catalysis, under review.

2.2. Introduction

Clean and affordable renewable energy sources are greatly needed to reduce our dependence on fossil fuels. Research in this area is currently under intensive investigation. [5, 7, 144, 145] Amongst the various energy sources available, sunlight provides a large amount of clean energy. [1] In nature, solar energy is efficiently converted to chemical energy via photosynthesis. [146] A route to exploiting this capability in non-biological solar energy systems such as the "Artificial Leaf" have been explored in order to harness solar energy and "split water" to generate hydrogen fuel. [147] However, a major challenge in such artificial systems is the large overpotential caused by the high energy barrier of the anodic oxygen evolution reaction (OER), a process that involves the transfer of four electrons per molecule of O_2 generated. [7, 148] To improve the efficiency of O_2 evolution, intensive efforts have been put forward to develop promising OER catalysts. [2] Noble metal oxides including IrO_2 and RuO_2 were identified as highly efficient water oxidation catalysts. However, due to their high cost and toxicity, large-scale water oxidation would not be feasible. [2, 149, 150] As a result, attention was shifted toward abundant, efficient, and low-cost first-row transition metal oxides such as cobalt phosphate (CoPi) and $NiFeO_x$. [7, 24, 151] In Nature, the highly efficient Mn_4O_5Ca oxygen-evolving complex (OEC) of photosystem II produces the majority of oxygen gas in the atmosphere. [152] The OEC complex consists of a cubane-like Mn_3O_4Ca structure with a μ-oxo ligand connecting to a dangling Mn atom. [39] Although the oxygen evolution mechanism of the OEC remains elusive, the structural similarity of manganese oxides to the OEC has inspired a significant amount of research on manganese oxide-based catalysts. [37, 39, 78, 153, 154, 155] For example, one of the commonly studied manganese oxide-based OER catalysts is layered birnessite, which consists of an edge-sharing lattice of octahedral manganese oxide units and interstitial alkaline metal cations between layers to balance the negative charges created by defects. [58, 68, 153, 156]

While the majority of manganese oxide syntheses require strong oxidants, [75, 76, 77] strongly basic conditions, [78] or an external electric potential to oxidize Mn(II), [68, 79,

80, 82] most naturally existing manganese oxide minerals are synthesized through enzymatic pathways under mild conditions. Abiotic oxidation of soluble Mn(II) to Mn(III) and Mn(IV) oxides occurs very slowly in seawater (pH 8.16). [130, 157] However, aerobic biological manganese oxidation can expedite this process by three to five orders of magnitude. [158] Within the marine Bacillus bacteria, a multicopper oxidase (MCO), MnxG, has been found to enzymatically generate manganese oxides. [81, 106] In 2013, MnxG was first expressed and purified in a form of a protein complex named Mnx, where the MnxG (138 kDa) subunit is combined with three MnxE (∼12 kDa each) and three MnxF (∼12 kDa each) accessory protein subunits. [131, 133] Since then, the structure and mechanism of Mnx have been intensively investigated via electron paramagnetic resonance (EPR) spectroscopy. [81, 128, 135, 138] The product of the Mn oxidation of Mnx was also characterized as defected layered Mn(III,IV) oxides (denoted by $BioMnO_x$ or biogenic MnO_x) with a tunable rod-shaped morphology. [159, 160] However, the potential of $BioMnO_x$ as OER catalysts has yet to be explored. Here, we employ the Mnx enzyme to synthesize biogenic manganese-oxide catalysts (denoted by $BioMnO_x$). We investigate the efficacy of $BioMnO_x$ as a catalyst for OER under near-neutral pH conditions. By utilizing a combination of microscopy and spectroscopy techniques, including SEM, XPS, XAS, and EPR, we established the structure-function relationship between biogenic MnO_x and OER activity. This work provides valuable insights into the development of efficient OER catalysts that can be produced using a gentle and sustainable process.

2.3. Experimental procedures

General procedures and materials. Milli-Q water (18 MΩ-cm resistivity) was used to make solutions and rinse the electrodes and glassware. For the sample preparation, $MnSO_4 \cdot H_2O$ (MW 169.01 g/mol) was used as Mn^{2+}(aq) source. Mn_2O_3 powder (MW 157.87 g/mol) was used as a reference Mn(III) oxide. Sodium pyrophosphate (NaPP, MW 265.90 g/mol) was used as Mn(III) chelator. All chemicals were purchased from Sigma Aldrich

unless otherwise noted. Unless noted otherwise, all standard manganese oxides and cobalt oxides were purchased from Sigma Aldrich.

Synthetic birnessite synthesis. Synthetic birnessite was synthesized using a modified protocol previously reported. [161] First, $MnCl_2 \cdot 4H_2O$ solution (MW 197.91 g/mol, 3.166 g in 32 mL H_2O) was added dropwise to NaOH solution (MW 40 g/mol, 11 g in 36 mL H_2O), followed by vigorously stirring to obtain $Mn(OH)_2$ as a pink precipitate. Then $KMnO_4$ solution (MW 158.034 g/mol, 1g in 32 mL H_2O) was then added dropwise to the above mixture to yield a dark grey precipitate. After stirring for an hour, the mixture was heated at 55 ℃for 24 hours. Then the supernatant was discarded and the remaining suspension was centrifuged for 20 minutes at 27500 xg. The resulting pellet was collected, washed five times with 1 M NaCl and then washed ten times with Milli-Q water to remove excessive salts and bases. Finally, the synthetic birnessite powder was collected by lyophilization and characterized by powder X-ray diffraction (pXRD). The synthetic birnessite was used as one of the X-ray Absorption Near Edge Structure (XANES) spectroscopy standards for Mn K-edge XANES Linear Combination Fitting (LCF) analysis.

MnxEFG protein complex overexpression and purification. Mnx protein complex (Mnx E_3F_3G, ∼211 kDa, denoted as MnxEFG) was overexpressed in Escherichia coli BL21 (DE3) using the pASK/IBA3plus vector (IBA Lifesciences, Germany) containing the mnxEFG gene construct and Strep-tag II. The protein was purified via Strep-tag affinity chromatography (IBA Lifesciences, Germany) and size exclusion chromatography with a HiLoad 16/600 Superdex 200 pg (GE Healthcare, IL, USA) column as described previously [128]. The eluted protein was dialyzed to remove excess Cu^{2+} and stored in the storage buffer containing 20 mM HEPES, 20 mM KCl and 20% v/v ethylene glycol. The MnxEFG protein complex was then ready for aerobic Mn oxidation experiments.

Aerobic Mn oxidation experiments and biogenic MnO_x (BioMnO_x-I, -II, -III, or -IV) sample preparation. Biogenic MnO_x was synthesized via aerobic oxidation of

Mn^{2+}(aq) by MnxEFG. 10 μL of 100 μM MnxEFG solution (final concentration = 20 nM) was added to 50 mL of buffer (10 mM HEPES, 50 mM NaCl, pH = 7.8) in a 50 mL conical polypropylene centrifuge tube under ambient conditions and was allowed to equilibrate. Varying amount of $MnSO_4$ solution was added and then the tube was gently inverted for 6 – 8 times to ensure thorough mixing (Table 2.2). The reaction was then incubated for 2 hours with the tube loosely capped to ensure sufficient oxygen supply. Following incubation, the reaction mixture was centrifuged at 12000 rpm for 30 min, and the resulting pellets were washed with Milli-Q water 5 times followed by gentle centrifugation (6000 rpm for 2 min). After washing, the precipitate was resuspended, added dropwise to the petri dish and dried on the bench for 2 - 3 days. The resulting dried pellets were collected. The resulting biogenic manganese oxides were classified as $BioMnO_x$-I, -II, -III, or -IV (Table 2.2) based on the initial amount of $MnSO_4$ and the duration of incubation.

Electrodeposited monoclinic birnessite (monoclinic birnessite) sample preparation. The monoclinic birnessite sample was prepared using a protocol modified from existing literature. [57, 68] Electrodeposition was performed on a Princeton Applied Research (Oak Ridge, TN, USA) Model 263 A potentiostat/galvanostat, and was analyzed using the PowerStep software package. in a three-electrode system. The three-electrode system contains a fluorine-doped tin-oxide-coated glass (FTO; Sigma Aldrich, MO, USA) working electrode, a nickel foam (MTI Corp., CA, USA) counter electrode, and an Ag/AgCl in 3 M NaCl (0.203 V vs NHE; BASi, IN, USA) reference electrode. Na-birnessite was electrodeposited onto a 10 cm × 9 cm FTO plate submerged in the electrolyte (2 mM $MnSO_4$ and 50 mM NaCl). During electrodeposition, a 1.0 V potential (vs. NHE) was applied for 300 s, followed by the application of a 1.2 V potential (vs. NHE) until a total charge of 27 C (300 mC/cm^2) was transferred. The electrodeposited FTO plate was then washed 3 times with Milli-Q water and dried under air for 3 days. The monoclinic birnessite powder was then obtained by gently scraping the film with a clean razor.

Electrochemical measurements. Linear sweep voltammetry (LSV) and Chronoamperometry (CA) were conducted on Princeton Applied Research Model 263 A potentiostat/galvanostat in a three-electrode system. The reference electrode used was Ag/AgCl (3 M NaCl), the counter electrode was nickel foam, and the working electrode was prepared by drop-casting 12 μg Mn oxide sample from a sonicated suspension in Milli-Q water onto 1 cm^2 of FTO, followed by drying on the bench overnight (Figure 2.7). The LSV was measured from 0 V to 1.5 V (vs Ag/AgCl) and CA was taken at an overpotential of 800 mV for 1000 s. All LSV and CA measurements were conducted under stirring in 15 mL 0.5 M sodium phosphate buffer (pH 7.8). For all electrochemical measurements, LSV and CV curves were measured at the beginning to charge the double layer and to remove the air-oxidized surface layer and a second LSV and then CA were taken and recorded as electrochemical data.

Electrochemically active surface area measurements (ECSA). The ECSA was calculated from the measurements of cyclic voltammetry at different scan rates. The potential range from 350 mV to 515 mV, was chosen to minimize the faradaic current response. CV was conducted within the stirring solution in this range with the scan rate of 300, 200, 100, 50, 20 and 10 mV/s. At each potential vertex, the working electrode was held at the vertex potential for 10 s to allow double-layer charging. The slope of the resulting current vs scan rate plot is equal to the double layer capacitance, C_{DL}, which is then equal to the ECSA multiplied by specific capacitance, Cs [162]: (Equation 2.1).

$$Slope = C_{DL} = (ECSA) * C_s \tag{2.1}$$

Powder X-ray Diffraction (pXRD). pXRD patterns were measured on a Bruker D8 ADVANCE Eco instrument using Cu K_α irradiation (λ = 0.154 nm). The sample was ground and filtered with a 100-mesh sieve to obtain a fine powder, then mounted via ethanol solvent smear onto the SiO_2 zero-background plate. pXRD measurement was performed

with 2θ from 5°to 75°in 3421 steps. The pattern was background-corrected, K_2-stripped and peak-matched using Crystallographic Open Database (COD).

Scanning Electron Microscopy (SEM). SEM was performed with Thermo Fisher Quattro S at Advanced Materials Characterization and Testing Laboratory (AMCaT) at the University of California-Davis. SEM samples were prepared by drying a droplet of suspension sample on a silicon wafer. The surface morphology of the sample was examined using an Everhart-Thornley detector (ETD) with acceleration voltage of 5 kV and spot size of 2.5 Å.

X-ray photoelectron spectroscopy (XPS). High-resolution XPS of cobalt, manganese, and oxygen (PHI 5000 VersaProbe, Physical Electronics, Enzo, Chigasaki, Japan) was obtained with an Al K_α source. All measurement were performed on the carbon tape and calibrated to the adventitious carbon 1s peak at 284.8 eV.

Electron Paramagnetic Resonance (EPR) spectroscopy. Manganese oxide powder was grounded and filtered through a 100-mesh sieve. Fine manganese oxide powder (0.3 mg) was suspended in 200 μL sodium pyrophosphate solution (20 mM NaPP and 20% ethylene glycol) by vortex mixing and sonication. The mixture was centrifuged at 13300 rpm (20000 xg) for 30 s. The supernatant was then pipetted into an X-band EPR tube and frozen in liquid nitrogen. X-band continuous-wave (CW) EPR spectra were recorded using a EleXsys E500 spectrometer (Bruker, Billerica, MA). Cryogenic temperature were achieved and controlled using an ESR900 liquid helium cryostat in conjunction with a temperature controller (Oxford Instruments ITC503) and gas flow controller. Parallel-mode EPR experiments (B0 $\parallel$ B1) were performed with a dual-mode resonator (ER4116DM). All CW EPR data were collected under slow-passage, non-saturating conditions. Spectrometer settings were as follows: conversion time = 40 ms, modulation amplitude = 0.8 mT, and modulation frequency = 100 kHz; other settings are given in the corresponding figure captions.

X-ray Absorption Spectroscopy (XAS) and data analysis. All XAS scans were taken at the Stanford Synchrotron Radiation Lightsource (SSRL) at the SLAC National

Accelerator Laboratory. Powder and thin film samples were taken in either beamline stations 4-3 or 2-2. Energy calibration of the beam was performed using elemental Mn for Mn K-edge. The fluorescence data were collected using a Lytle detector or Ge detector and then averaged together to increase the signal-to-noise ratio. X-ray Absorption Near Edge Structure (XANES) data were analyzed using the Athena package within the Demeter XAS-processing software. Scans of each sample were aligned and averaged to generate a merged spectrum. All of the Mn K-edge XAS spectra were calibrated by setting the third peak of the Mn foil spectrum in the reference channel to the edge energy of Mn, 6539 eV. The average oxidation states (AOS) of Mn in manganese oxides samples were estimated following the method described by Wong, et al. [163] The standard curve for AOS was plotted based on the edge energies of Mn foil, MnO, Mn_2O_3, β-MnO_2 and $KMnO_4$. The XAS spectra of MnO, Mn_3O_4, Mn_2O_3, β-MnO_2, δ-MnO_2 and synthetic birnessite were collected and used as standard components for Mn K-edge Linear Combination Fitting (LCF). All fitting components were forced to be positive contributions, but the percentage sum was not forced to 1 to allow the presence of the unknown composition. The R-factor was reported to examine the quality of fitting (Equation 2.2).

$$\frac{\sum(data - fit)^2}{\sum data^2} \tag{2.2}$$

2.4. Results and Discussion

2.4.1. Synthesis of biogenic MnO_x with diverse morphologies and crystalline structures. As shown in Figure 2.2, the biogenic MnO_x samples with diverse morphologies and crystalline structures were synthesized by varying the ratio of Mn(II) to Mnx protein (denoted as Mn(II)/Mnx) and the mineralization time. When the ratio of Mn(II)/Mnx was as low as 10,000, and mineralization allowed to continue for 0.5 h, the biogenic MnO_x show a uniform "cabbage-like" morphology (BioMnO_x-I, Figure 2.2B). Increasing the ratio of Mn(II)/Mnx to 50,000 and the length of mineralization to 2 h, the morphology of the

biogenic MnO_x became sets of short-ordered "rods" with the length of ~100 nm and the diameter of ~20 nm (BioMnO_x-II, Figure 2.2B). When the ratio of Mn(II)/Mnx was increased to 100,000, long-ordered "rod-net" (BioMnO_x-III, Figure 2.2B) biogenic MnO_x formed, with the diameter of the rods ~10 nm. Powder X-ray diffraction (pXRD) patterns (Figure 2.2C) of these three types of biogenic MnO_x show weak and broad peaks, indicating that the samples with a short ageing time ($\leq$ 2 h) are amorphous and lack of long-range ordering. Further increasing the ratio of Mn(II)/Mnx to as high as 4,200,000 and extending the mineralization time to as long as ~72 h, the biogenic MnO_x crystallized to form the "fiber-like" MnO_x solids (BioMnO_x-IV, Figure 2.2B). The pXRD pattern of BioMnO_x-IV showing long-range ordered crystalline structures contains manganite (84.28%, COD cif: 9009774) and groutite (15.72%, COD cif: 9011546), both of which are polymorphs of Mn(III)O(OH) (see Figure 2.8). [164] In addition, as a standard control, monoclinic birnessite (COD: 9001270) was also synthesized via electrodeposition method (see Experimental procedure for details), [57] with its characteristic pXRD peaks at 12°, 26°and 38°(Figure 2.2C).

Based on the different morphologies and crystalline structures of biogenic MnO_x, we propose the following biogenic MnO_x growth mechanism. The initially generated MnO_x solids coat around the Mnx protein complex (Note: the diameter of Mnx protein complex is ~10 nm. [133]) by forming the "cabbage-like" MnO_x morphology (BioMnO_x-I). When more Mn(II) in the aqueous solution (corresponding to higher ratio of Mn(II)/Mnx) is available, the cabbage-shape MnO_x further grows along one direction by forming rods (BioMnO_x-II) or rod-net structures (BioMnO_x-III), or eventually crystallizing into the fiber-like manganite/ groutite structures (BioMnO_x-IV).

2.4.2. OER activities of biogenic MnO_x. With the above sets of biogenic MnO_x with diverse morphologies and structures synthesized, we employed them as electrocatalysts for water-oxidation reaction. [68,160] Both linear-sweep voltammetric (LSV) and chronoamperometric (CA) studies were performed. As shown in Figure 2.3, all these biogenic MnO_x show activities for anodic O_2 evolution, i.e., employing smaller overpotentials (η < 880 mV

at 0.1 mA·cm^{-2}, Normal Hydrogen Electrode which is used through this paper.) than that of the bare FTO electrode ($\eta > 930$ mV at 0.1 mA·cm^{-2} vs NHE, Figure 2.3A), and showing higher CA current density at 1.6 V (vs NHE) (Figure 2.3B). We note that MnOx with varying morphologies have also been reported to show varying OER activities. [165, 166] Especially, while the amorphous BioMnO$_x$-III exhibits comparable activity ($\eta \approx 760$ mV) for O_2 evolution to the standard monoclinic birnessite, the BioMnO$_x$-II shows a much higher activity for O_2 evolution, with η ca. 700 mV, i.e., 60 mV smaller than that of monoclinic birnessite. In addition, the CA current density of BioMnO$_x$-II at 1.6 V (vs NHE) was stabilized at 5.8 A· g^{-1}·cm^{-2}, which is 2 A·g^{-1}·cm^{-2} higher than that of monoclinic birnessite (Figure 2.3B). The BioMnO$_x$-II also exhibits a higher electrochemically active surface area (ECSA) than the monoclinic birnessite (Figure 2.9).

2.4.3. Mn K-edge XANES of biogenic MnO$_x$. We employed X-ray absorption spectroscopy (XAS) to investigate the bulk structural composition of biogenic MnO$_x$, due to the non-crystallinity property of BioMnO$_x$-II and III. Linear combination fitting (LCF) analysis on the Mn K-edge XANES region (Figure 2.10) was performed by employing a set of standard manganese oxides (Figure 2.11), including monoclinic birnessite, synthetic birnessite (Figure 2.12), δ-MnO_2, β-MnO_2 (cif: 1514117), Mn_2O_3 (cif: 1514103), Mn_3O_4 (cif: 1514104) and MnO (cif: 1010393). As shown in Figure 2.4, BioMnO$_x$-II consists of 75.1% monoclinic birnessite, as well as 12.77% feitknechtite [167] and 12.13% triclinic birnessite; meanwhile, BioMnO$_x$-III consists of 42.4% monoclinic birnessite, as well as 23.54% feitknechtite, 22.36% triclinic birnessite, and 11% Mn_2O_3. LCF analysis suggests that monoclinic birnessite is the major component for both BioMnO$_x$-II and BioMnO$_x$-III, which could be the reason that these two samples show at least comparable OER activity to monoclinic birnessite. To be noted, for BioMnO$_x$-I, monoclinic birnessite is also the major component (54.9%, Figure 2.4). However, a homogenous suspension of BioMnO$_x$-I was difficult to achieve (different from the other samples), which could affect the attachment of the suspension onto the FTO

electrode. Therefore, the low activity of BioMnO$_x$-I (Figure 2.3) we measured may not correspond to the actual catalytic activity (vide infra). In the following sections, we will not correlate the structure/surface properties of BioMnO$_x$-I with the measured activity, and will focus on understanding the key to the activity of BioMnO$_x$-II and BioMnO$_x$-III. In addition, for BioMnO$_x$-IV, consistent with pXRD analysis (vide supra), LCF analysis suggests it contains manganite (67.3%) and groutite (32.7%), [168] both of which show lower activity than monoclinic birnessite (Figures 2.4, 2.13& 2.14). This explains the low OER activity of BioMnO$_x$-IV (Figure 2.3).

2.4.4. Spectroscopic characterization of surface Mn. To understand the origin of the higher comparable activity of BioMnO$_x$-II and BioMnO$_x$-III, as compared to the standard monoclinic birnessite, respectively, we employed XPS and EPR spectroscopies to characterize the surface Mn oxidation states of biogenic MnO$_x$.

Figure 2.5A and 2.5B show the Mn3s and Mn2p XPS spectra of the BioMnO$_x$ catalysts, respectively. Three XPS spectroscopic features are related to the surface Mn oxidation state: 1) the energy splitting (ΔEMn3s) in Mn3s spectra: the lower ΔE_{Mn3s}, the higher oxidation state of surface Mn [169] 2) Mn 2p3/2 binding energy: high binding energy of Mn2p suggests high oxidation state of surface Mn species [170]; 3) the energy splitting (ΔEMn_{2p}) between the Mn 2p1/2 and the satellite peak (the broad peak as indicated in Figure 2.5A): the lower ΔE_{Mn2p}, the lower oxidation state of surface Mn species [169]. Therefore, as summarized in Table 2.1, the oxidation state of Mn of BioMnO$_x$-IV is the lowest (III, see Table 2.1), as the XPS spectra show the lowest Mn 2p3/2 binding energy (641.8 eV), the smallest ΔE_{Mn2p} (9.9 eV) and the largest ΔE_{Mn3s} (5.5 eV). This is consistent with its crystalline structures containing manganite and groutite, both of which are polymorphs of Mn(III)O(OH). In addition, the surface of BioMnO$_x$-II and BioMnO$_x$-III consists of a mixture of Mn(III) and Mn(IV) species, with ΔE_{Mn3s} and ΔE_{Mn2p} ca. 5.1 eV and 11.0 eV, respectively, while monoclinic birnessite contains more surface Mn(IV) by showing lower ΔE_{Mn3s} (4.6 eV) and larger ΔE_{Mn2p} (11.5 eV).

We further employed X-band parallel mode continuous-wave (CW) EPR spectroscopy to probe the surface Mn(III) species, as it has been attributed as the key for OER activities in previous studies. [171] Five- or six-coordinate Mn(III) ions ($3d^4$) are typically high-spin with a total spin of S = 2. For such integer spin system, transitions between the $M_s = |\pm 2>$ spin manifold of S = 2 integer spin system (e.g., Mn(III) [172, 173] and Fe(II) [174, 175]) can be detected by using parallel polarization (B0 ∥ B1). Here, for probing surface Mn(III), pyrophosphate (PP) was employed as the chelator to the surface Mn(III) of the $BioMnO_x$ samples. As shown in Figure 2.6, EPR spectra of $BioMnO_x$-I, $BioMnO_x$-II and $BioMnO_x$-III show a sextet centered at 80 mT ($g_{eff} = 8.20$) with ^{55}Mn (I = 5/2) hyperfine splitting of 140 MHz, which is typical signal of Mn(III)PP. [138, 176] This suggests the Mn(III) species at the surface of $BioMnO_x$-I, $BioMnO_x$-II and $BioMnO_x$-III, which is consistent with above XPS analysis. In contrast, no Mn(III)PP signal was observed for the crystallized samples of $BioMnO_x$-IV, monoclinic birnessite and the Mn_2O_3 standard, suggesting no labile Mn(III) species at the surface.

Both XPS and EPR analysis suggest that the surface the labile surface Mn(III) species contributes to the higher and comparable OER activity of $BioMnO_x$-II and $BioMnO_x$-III, as compared to the standard monoclinic birnessite.

2.5. Conclusion

In this work, we show that efficient OER manganese-oxide catalysts can be synthesized through a mild and tunable biological method. High OER activity of the biogenic MnO_x is achieved as compared to synthetic birnessite. Spectroscopic analysis suggests that the monoclinic-birnessite component, along with the surface Mn(III) species, is potentially crucial for the activity of biogenic MnO_x. This work provides valuable insights into the development of efficient OER catalysts that can be produced using a gentle and sustainable process.

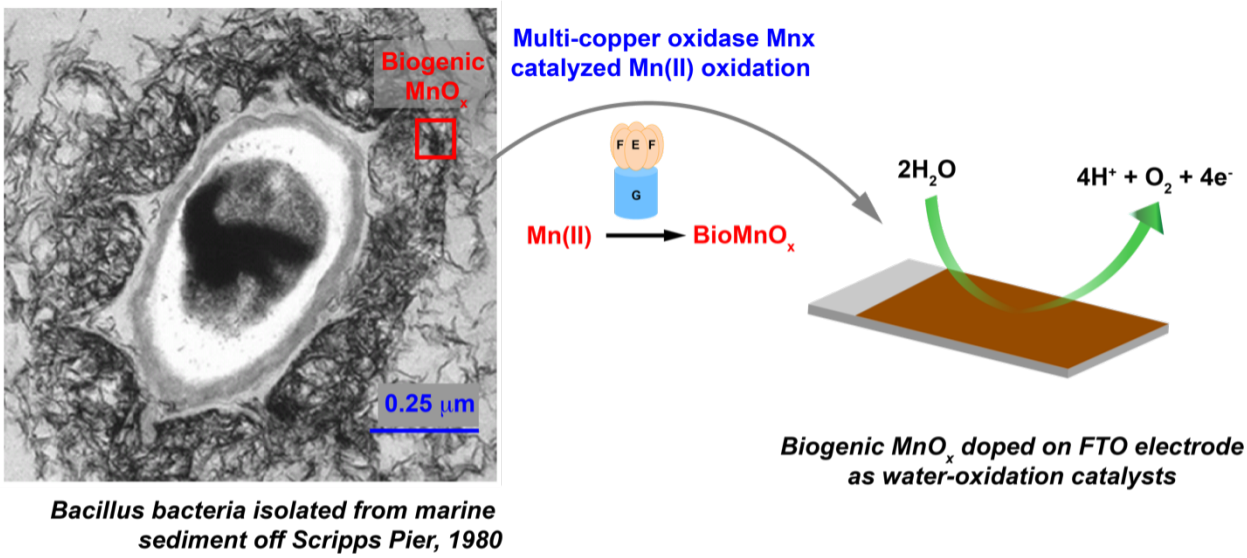

FIGURE 2.1. Overview of investigating water oxidation potential of the biogenic MnO_x ($BioMnO_x$).

Catalysts	Mn oxidation state	Mn $2p_{3/2}$ binding energy (eV)	ΔMn_{2p} splitting (eV)	ΔMn_{3s} splitting (eV)	References
	II	640.7	6.3	5.9	Oku, et al. [177]
	II	640.9	-	6.1	Foord, et al. [178]
	II	641.7	-	5.5	Carver, et al. [179]
	II	640.9	-	5.6	Nelson, et al. [180]
	II	-	6.0	6.0	Gorlin, et al. [181]
	II	-	6.0	6.0	Gorlin, et al. [169]
MnO	II	-	-	6.1	Ilton, et al. [182]
	II	-	-	5.7	Namgung, et al. [164]
	II	-	-	5.7	Cerrato, et al. [183]
	2.0	-	-	6.2	Galakhov, et al. [184]
	II	-	-	5.2	Lee, et al. [185]

	II	640.8	-	5.8	Junta and Hochella [170]
	II	-	-	5.8	Murray, et al. [186]
Mn_3O_4	II,III	641.4	10.5	5.3	Oku, et al. [177]
	II,III	641.0	-	5.6	Nelson, et al. [180]
	II,III	-	10.5	6.0	Gorlin, et al. [181]
	II,III	-	10.3	5.8	Gorlin, et al. [169]
	II,III	-	-	5.6	Murray, et al. [186]
	II,III	-	-	5.2	Lee, et al. [185]
	2.66	-	-	5.6	Galakhov, et al. [184]
	2.68-2.85	641.5	-	5.45	Han, et al. [187]
Mn_2O_3	III(α)	641.9	10.0	5.2	Oku, et al. [177]
	III(γ)	641.7	-	5.2	Oku, et al. [177]
	III	641.8	-	5.5	Foord, et al. [178]
	III	641.8	-	5.4	Carver, et al. [179]
	III	641.2	-	5.4	Nelson, el al. [180]
	III	-	10.0	5.1	Gorlin, et al. [181]
	III	-	10.0	5.1	Gorlin, et al. [169]
	III	-	-	5.5	Namgung, et al. [164]
	III	-	-	5.2-5.3	Cerrato, et al. [183]
MnOOH	III(γ)	641.7	-	4.6	Oku, et al. [177]
	III	-	-	5.4	Ilton, et al. [182]
	III(γ)	-	-	5.3	Murray, et al. [186]
	III(γ)	641.7	-	5.4	Junta and Hochella [170]
Mn_5O_8	II,IV	-	-	4.9	Murray, et al. [186]
	II,IV	-	-	4.6	Lee, et al. [185]

	3.89(α)	-	-	4.5	Sun, et al. [188]
	3.66(β)	-	-	4.7	Sun, et al. [188]
	3.78(γ)	-	-	4.6	Sun, et al. [188]
	IV(β)	642.2	11.2	4.7	Oku, et al. [177]
	IV	642.5	-	4.5	Foord, et al. [178]
	IV	642.4	-	-	Carver, et al. [179]
	IV	641.9	-	4.5	Nelson, et al. [180]
MnO_2	IV	-	11.8	4.5	Gorlin, et al. [181]
	IV	-	11.8	4.5	Gorlin, et al. [169]
	IV	-	11.8	4.5	Pinaud, et al. [57]
	IV	-	-	4.4	Ilton, et al. [182]
	IV(β)	-	-	4.9	Namgung, et al. [164]
	IV	-	-	4.6	Murray, et al. [186]
	IV	642.0	-	4.5	Junta and Hochella [170]
	IV	-	-	4.5	Cerrato, et al. [183]
Li_2MnO_3	4.0	-	-	4.5	Galakhov, et al. [184]
$Na_{0.31}MnO_{1.9}$ nanofiber	3.32	642.4	-	5.1	Li, et al. [22]
$La_{1-x}Sr_xMnO_3$	3.0-3.3	-	-	~5.3	Galakhov, et al. [184]
Mn(III,IV) oxides	III,IV	-	-	5.0-5.1	Cerrato, et al. [183]
$BioMnO_x$-I	II-IV	642.8	11.8	5.3	This study
$BioMnO_x$-II	III,IV	642.0	11.0	5.1	This study
$BioMnO_x$-III	III,IV	642.0	11.2	5.3	This study

$BioMnO_x$-IV	III	641.9	9.9	5.5	This study
Monoclinic birnessite	III,IV	642.2	11.5	4.6	This study

TABLE 2.1. Literature summary of Mn 2p and Mn 3s XPS experimental parameter values of manganese oxides with oxidation states between II and IV.

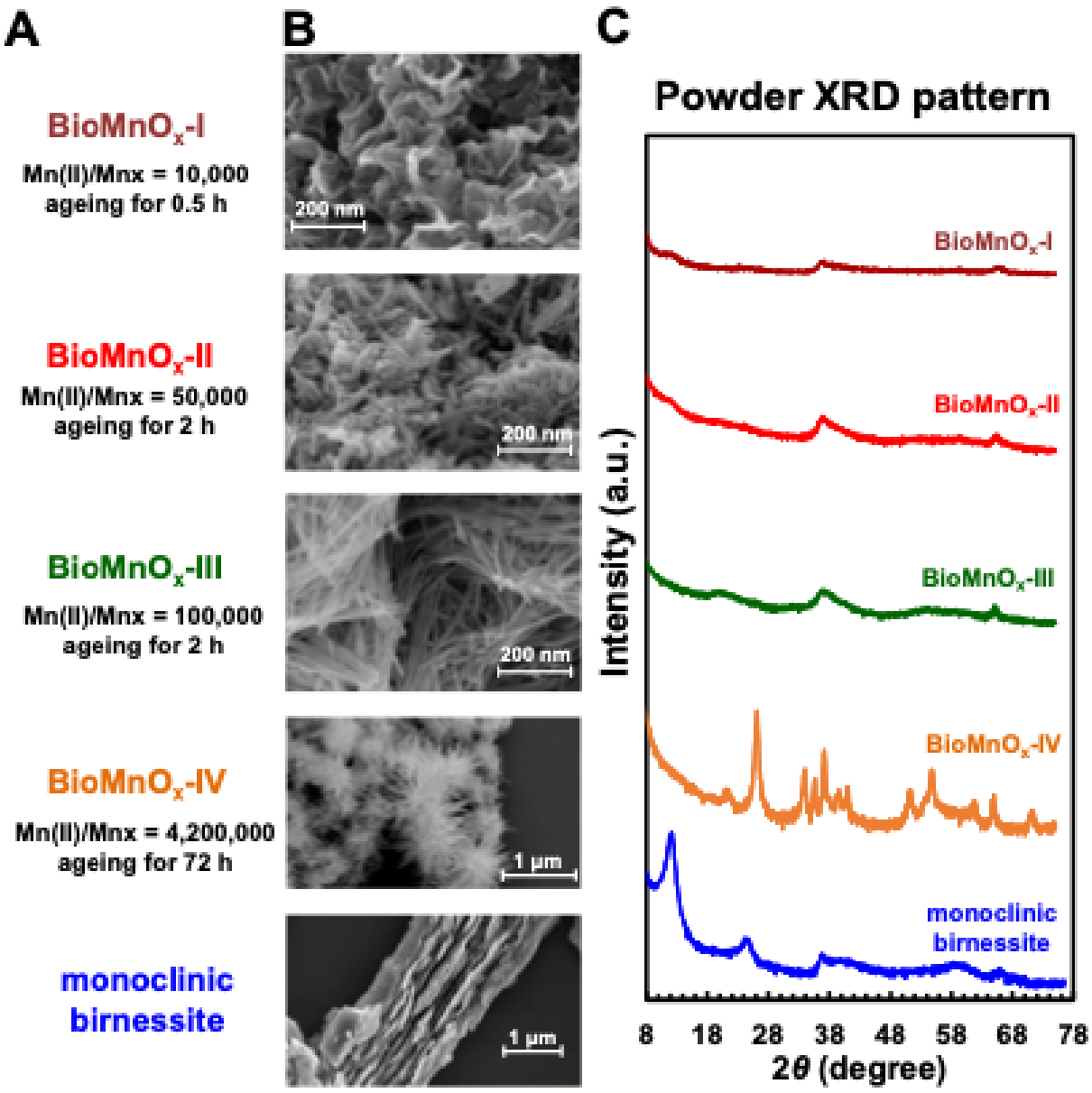

FIGURE 2.2. Panel A: recipes for $BioMnO_x$ samples. Panel B: Scanning electron micrographs (SEM) of $BioMnO_x$-I, -II, -III, and -IV, and monoclinic birnessite with scale bars. The length and width of $BioMnO_x$-II and -III are denoted. Panel C: pXRD spectra of $BioMnO_x$ and monoclinic birnessite. The pXRD patterns are background-subtracted and Kα2-stripped.

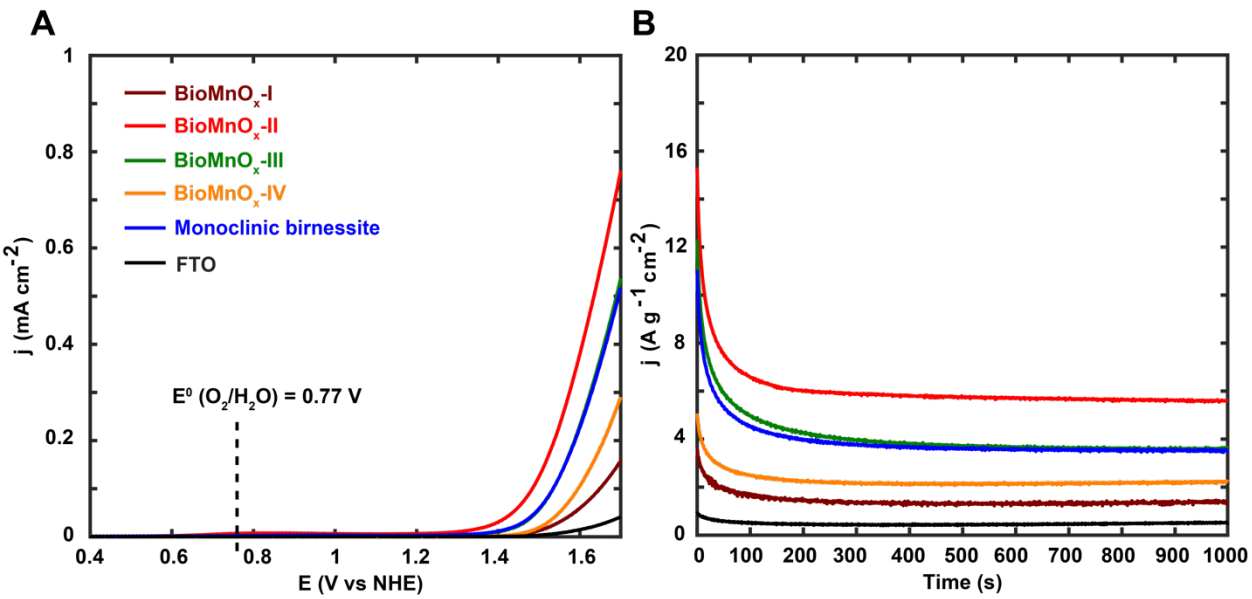

FIGURE 2.3. Linear sweep voltammagrams (A) and chronoamperometry (B) of BioMnO$_x$-I, -II, -III, and -IV, monoclinic birnessite and bare FTO plate as a control (black). LSV was taken with a scan rate of 10 mV/s. CA was measured at 1.6 V (vs NHE, $\eta = 830$ mV). The electrolyte is 0.5 M NaPi (pH 7.8).

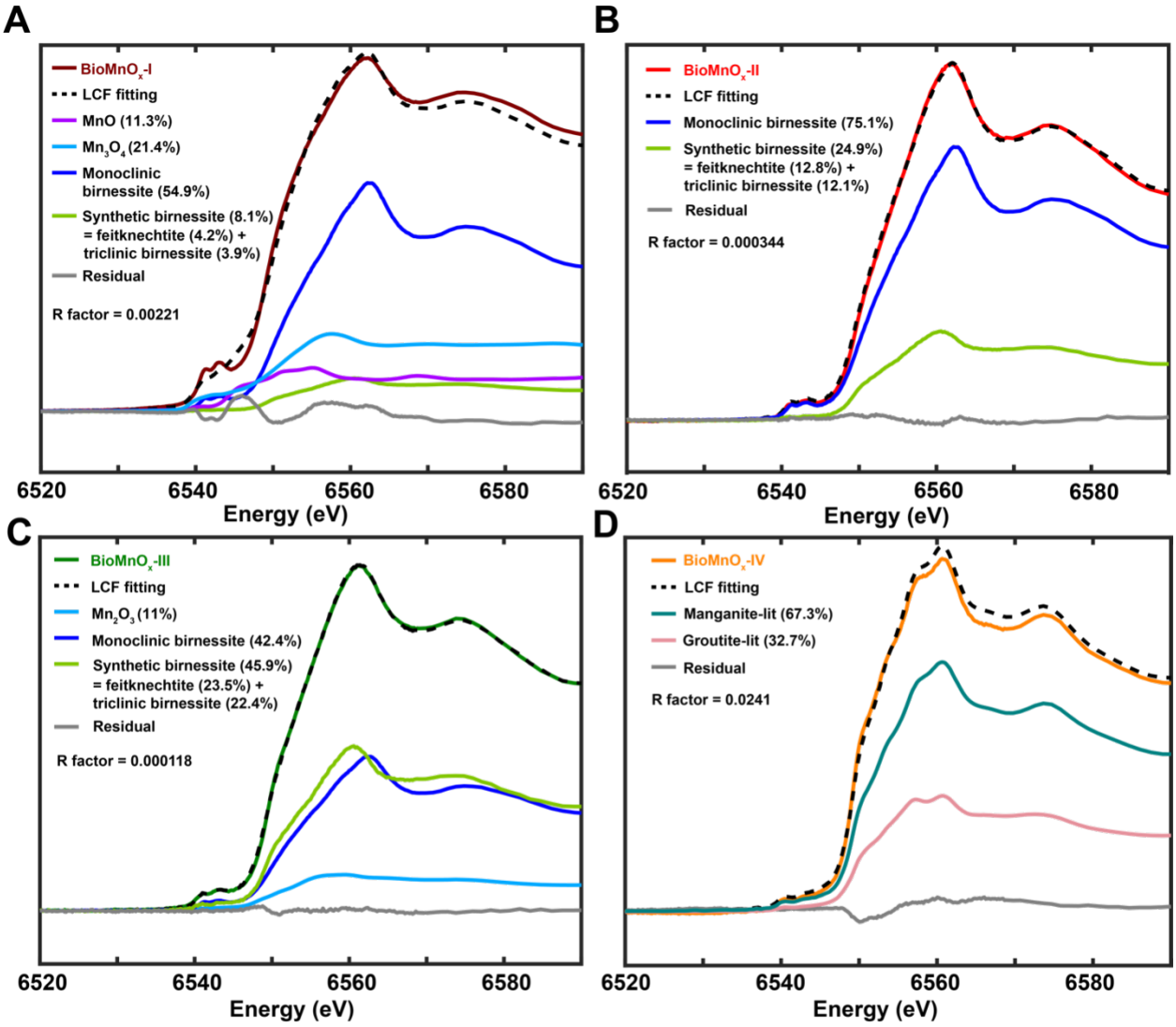

FIGURE 2.4. Mn K-edge XANES linear combination fitting (LCF) spectra of BioMnO$_x$-I to -IV (A–D). The synthetic birnessite with 51.3% of feitknechtite and 48.7% of triclinic birnessite is used as an LCF standard and the percentage of each component is indicated (Figure 2.13). Manganite-lit and groutite-lit are the manganite and groutite Mn K-edge XANES spectra downloaded from the literature. [168]

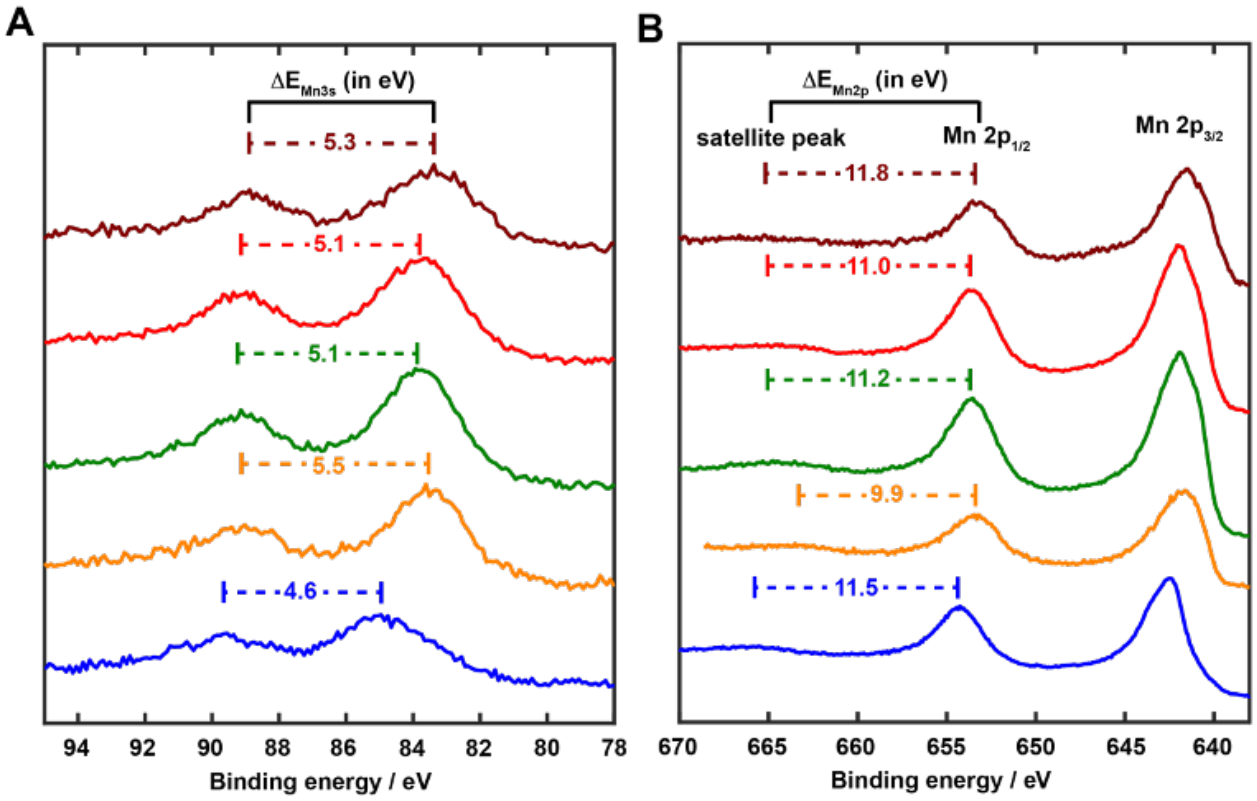

FIGURE 2.5. (A) Mn3s XPS and (B) Mn2p XPS of BioMnO$_x$ and monoclinic birnessite. As a control experiment, the EPR spectra of the standard Mn(III) oxide

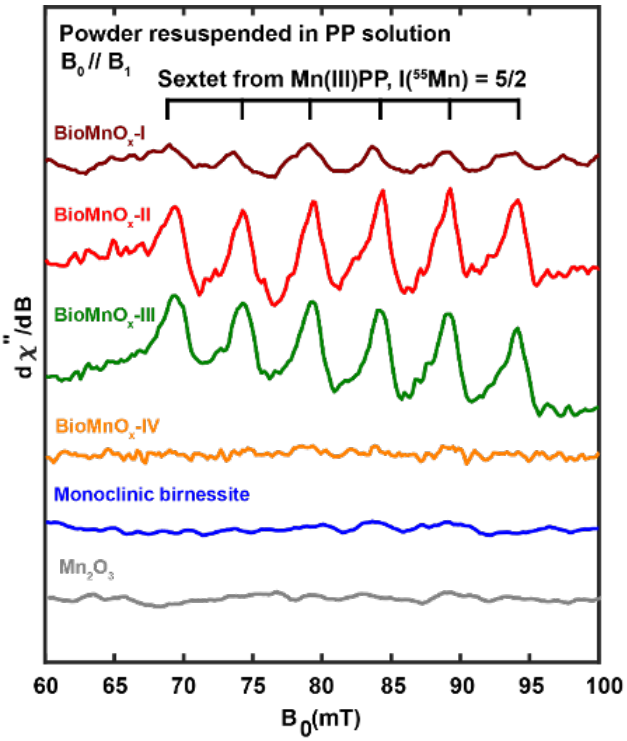

FIGURE 2.6. X-band (9.37 GHz) parallel-mode EPR spectra of $BioMnO_x$ and monoclinic birnessite. As a control experiment, the EPR spectra of the standard Mn(III) oxide (Mn_2O_3) was measured and shown in the gray trace. EPR Experimental parameters: temperature = 8 K; microwave frequency = 9.371 GHz; microwave power = 10 mW; conversion time = 40 ms; modulation amplitude = 0.8 mT; modulation frequency = 100 kHz.

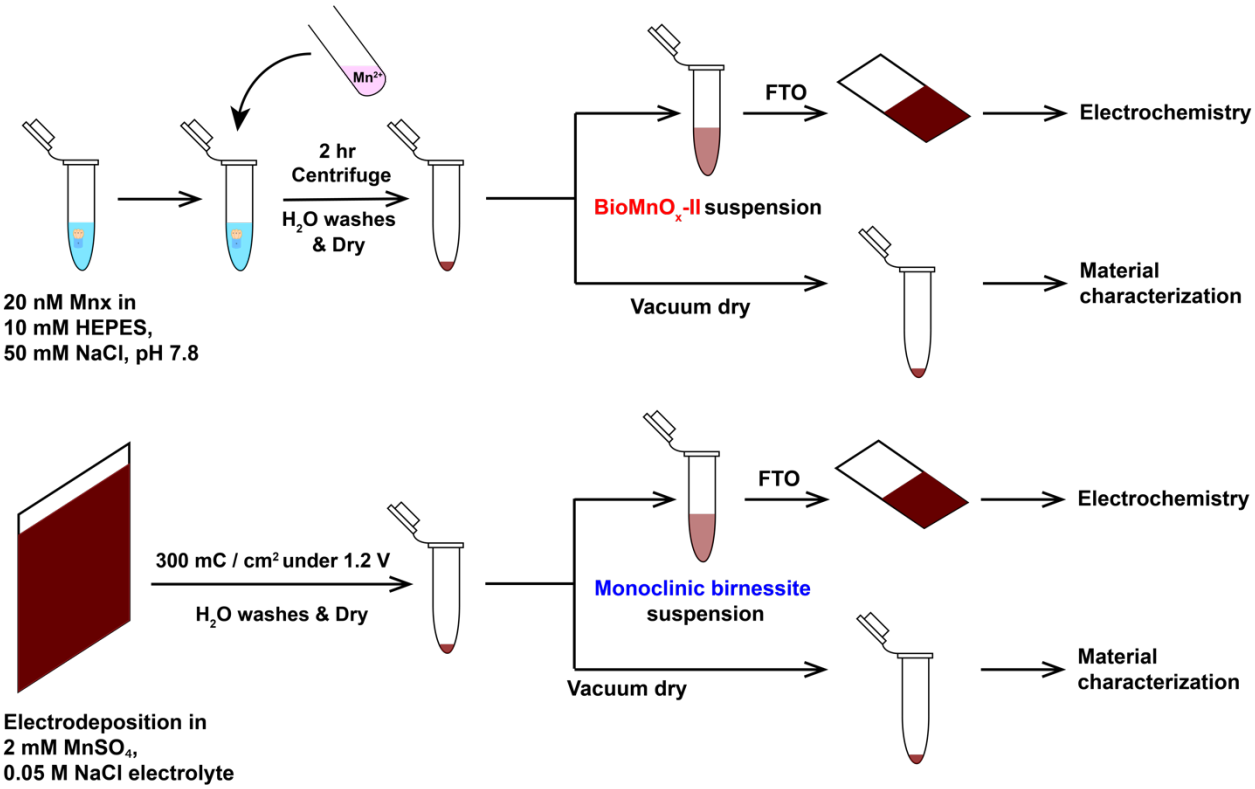

FIGURE 2.7. Biogenic manganese oxide sample (e.g. $BioMnO_x$-II sample) and monoclinic birnessite preparation schemes. The dried powder samples were used in material characterization experiments while the samples dropcast onto the FTO glass slide were used in electrochemical measurements.

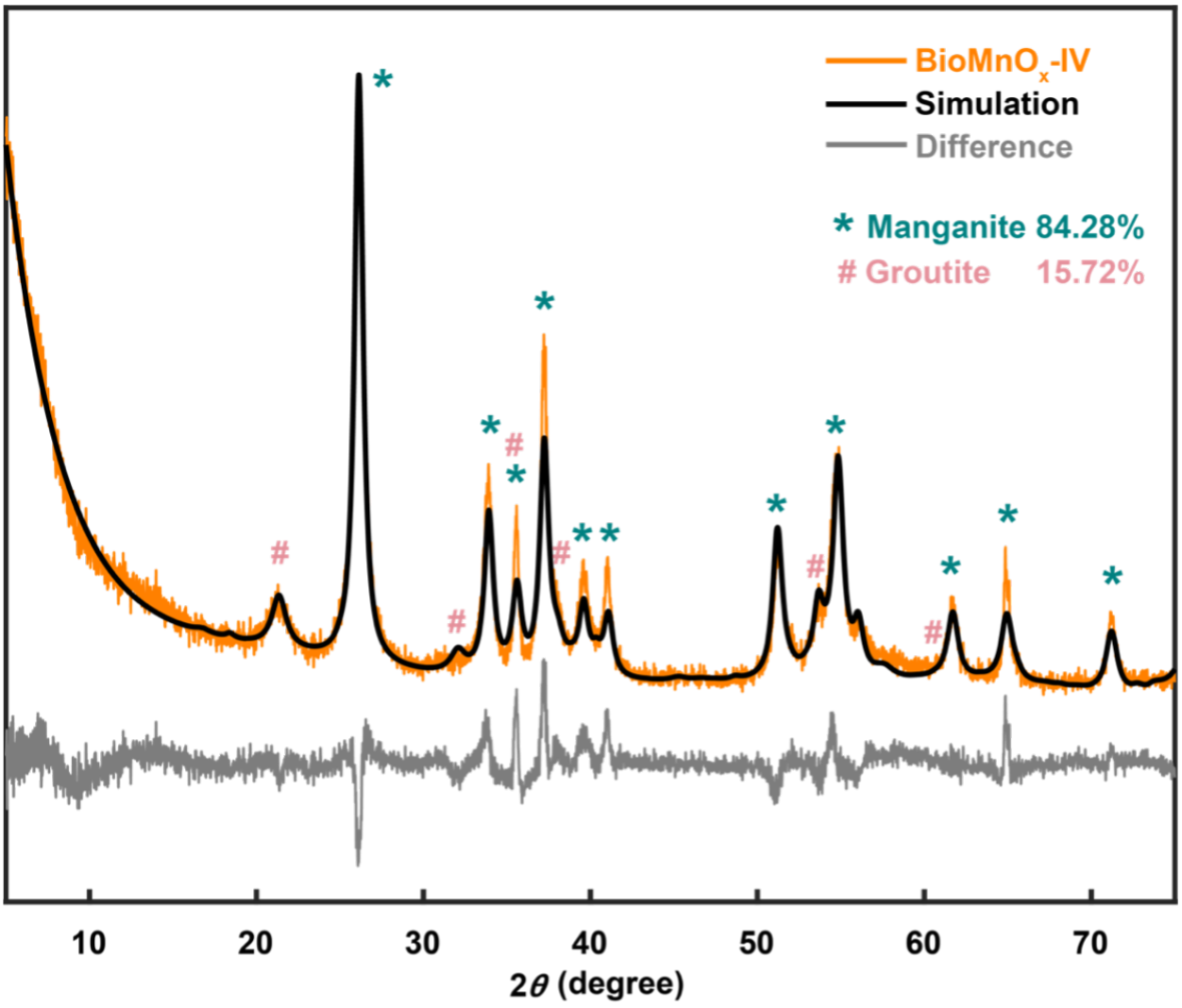

FIGURE 2.8. PXRD pattern of BioMnO$_x$-IV (in orange) and simulation (in black) using Rietveld refinement via TOPAS6.

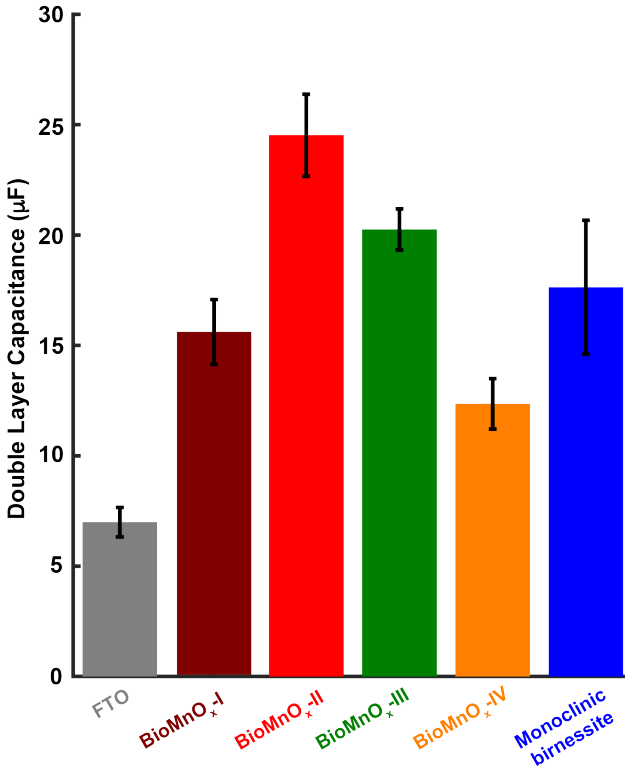

FIGURE 2.9. Electrochemically active surface area (ECSA) of $BioMnO_x$ and monoclinic birnessite. The error bar is calculated and shown for each sample based on the standard deviation.

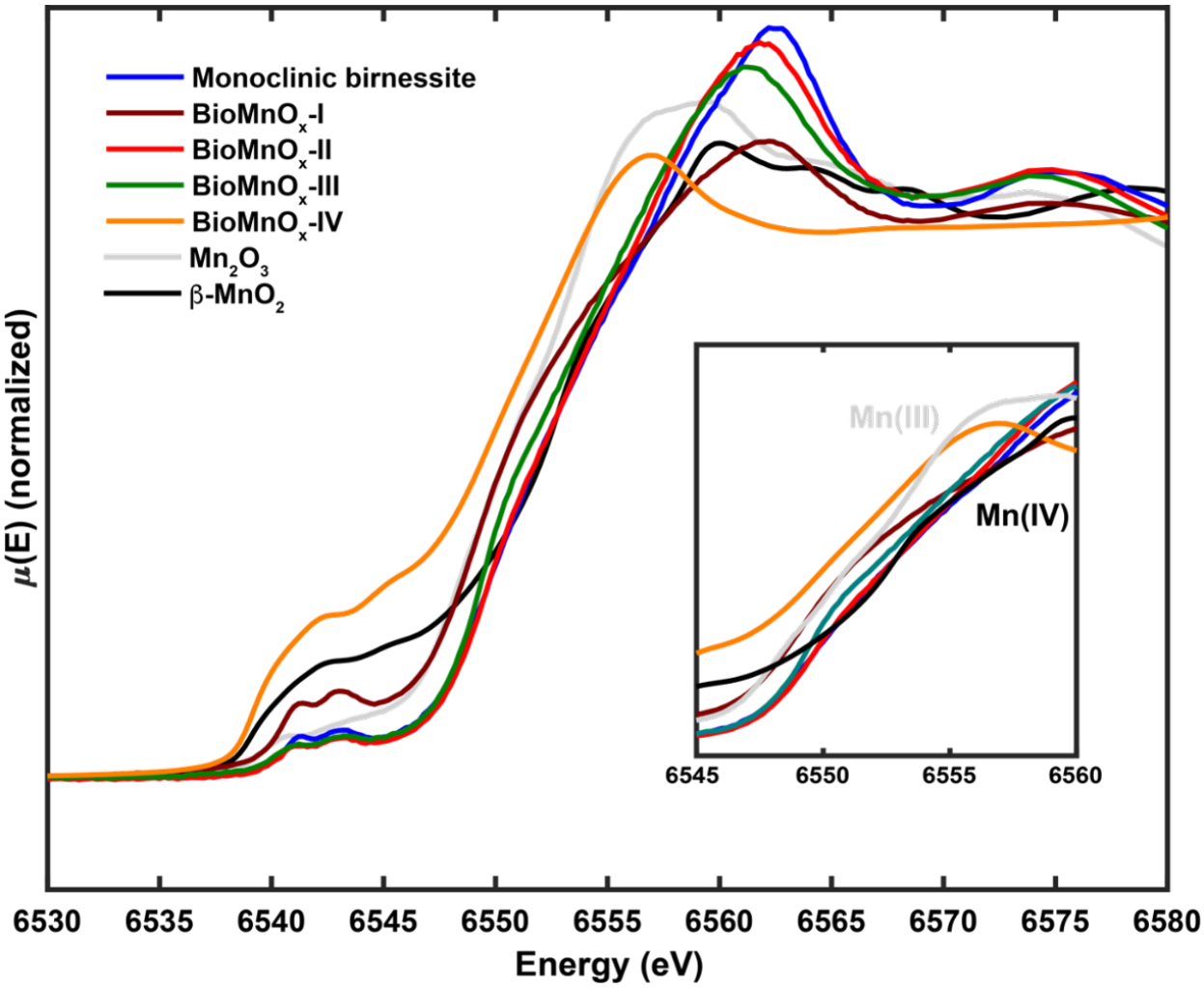

FIGURE 2.10. Normalized Mn K-edge XANES spectra of $BioMnO_x$

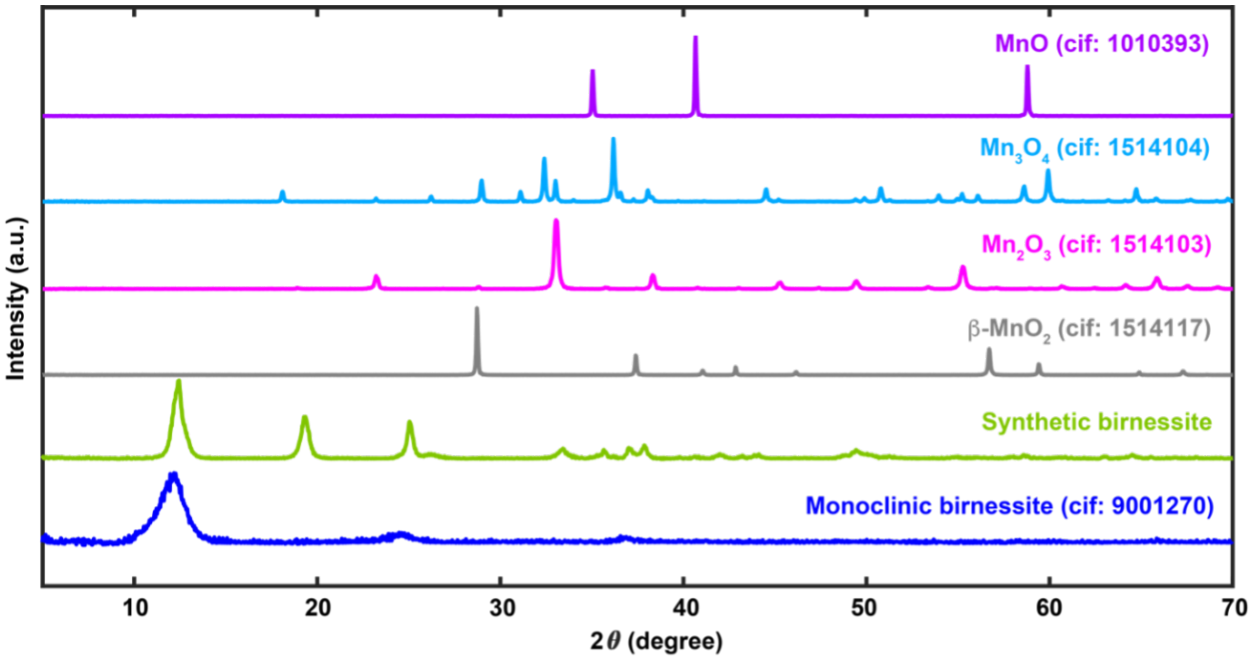

FIGURE 2.11. PXRD spectra of manganese oxide standards

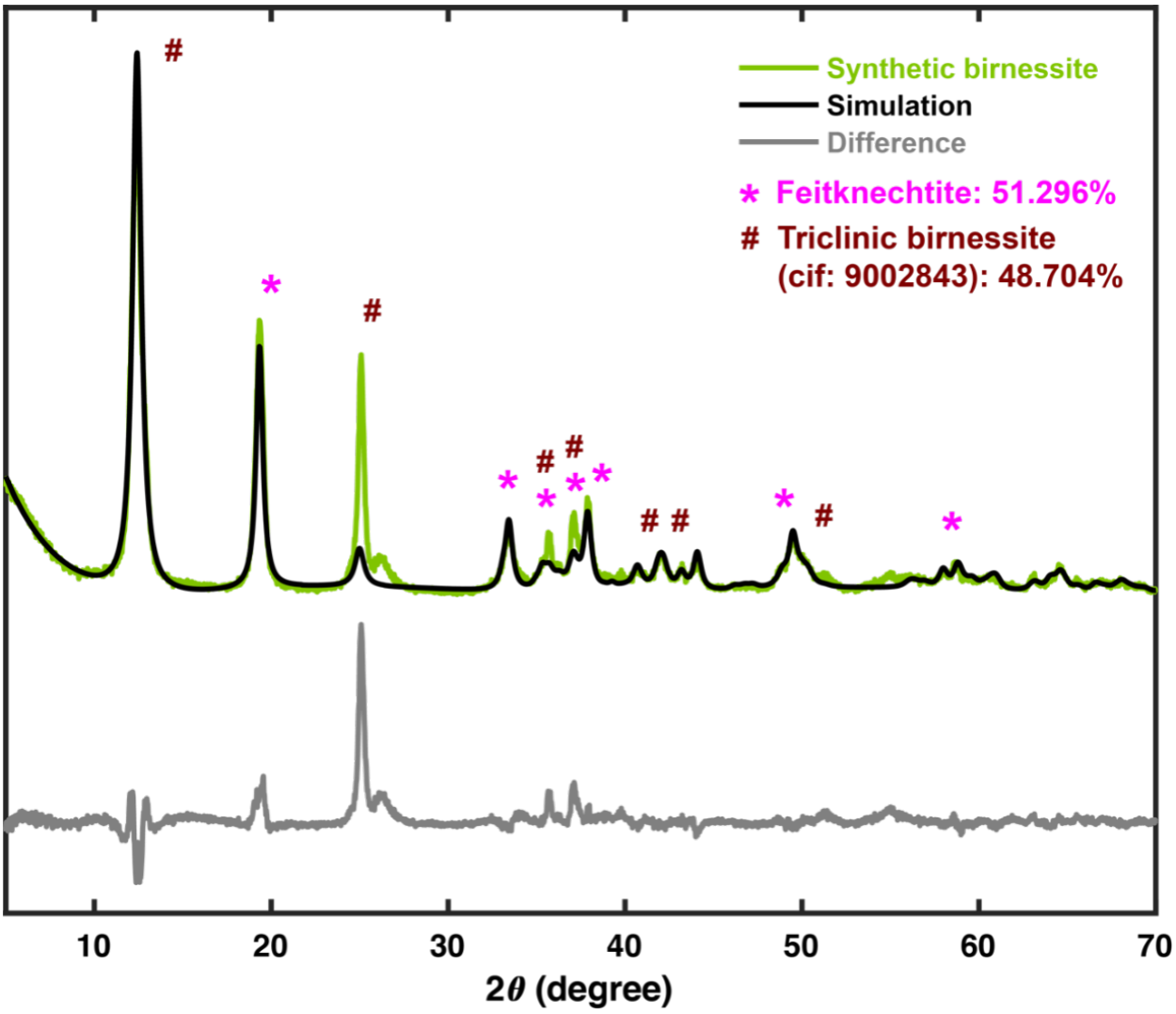

FIGURE 2.12. PXRD pattern and Rietveld refinement of synthetic birnessite standard. Feitknechtite crystallographic coordinates are obtained from Post, et al. (2023) [167]

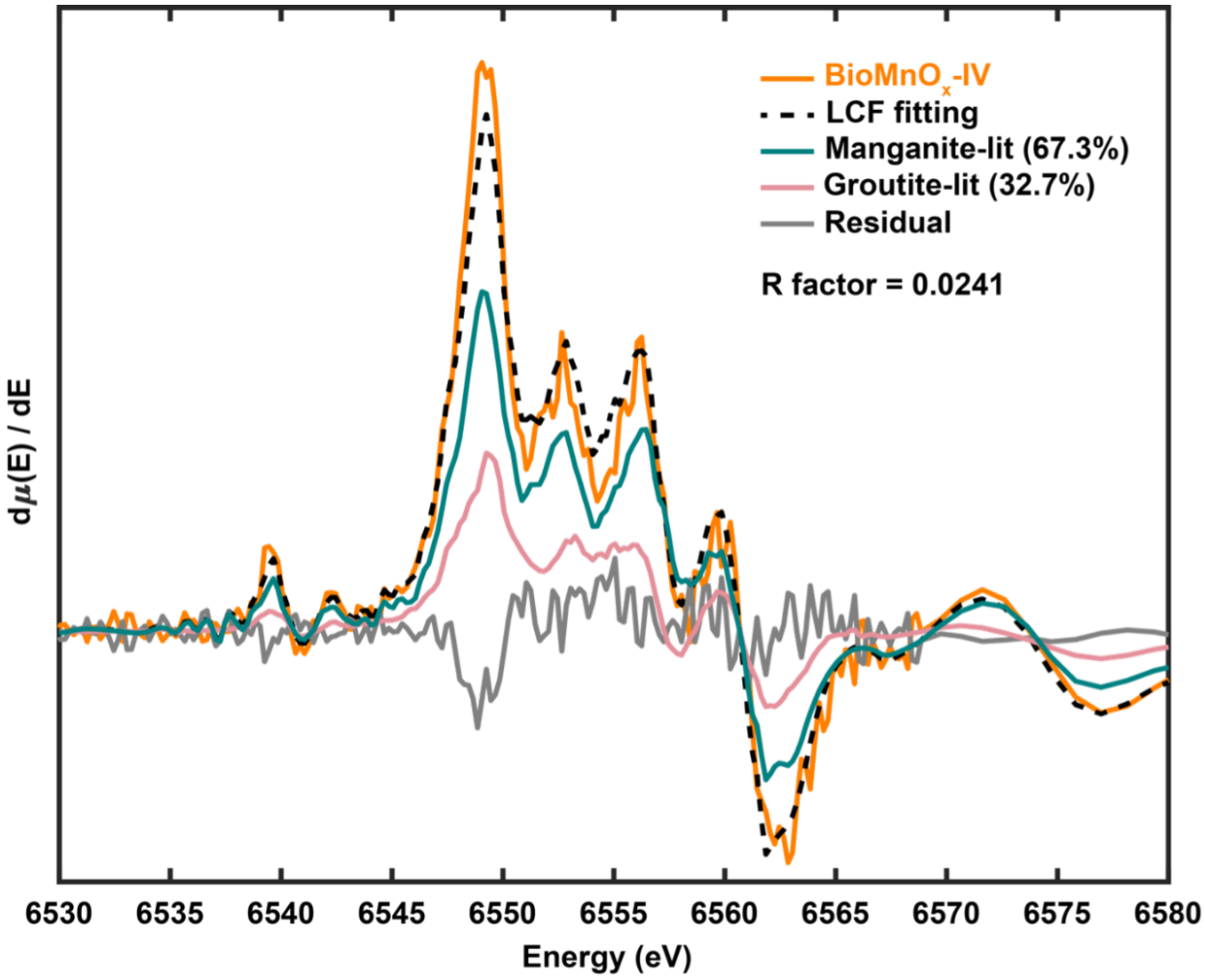

FIGURE 2.13. First derivative LCF of BioMnO$_x$-IV. Manganite-lit and groutite-lit are manganite and groutite XANES spectra from the literature. [168] The first derivative spectrum of BioMnO$_x$-IV was fitted with the first derivative spectra of manganite-lit and groutite-lit curves because manganite-lit and groutite-lit can be better distinguished in first derivative plots.

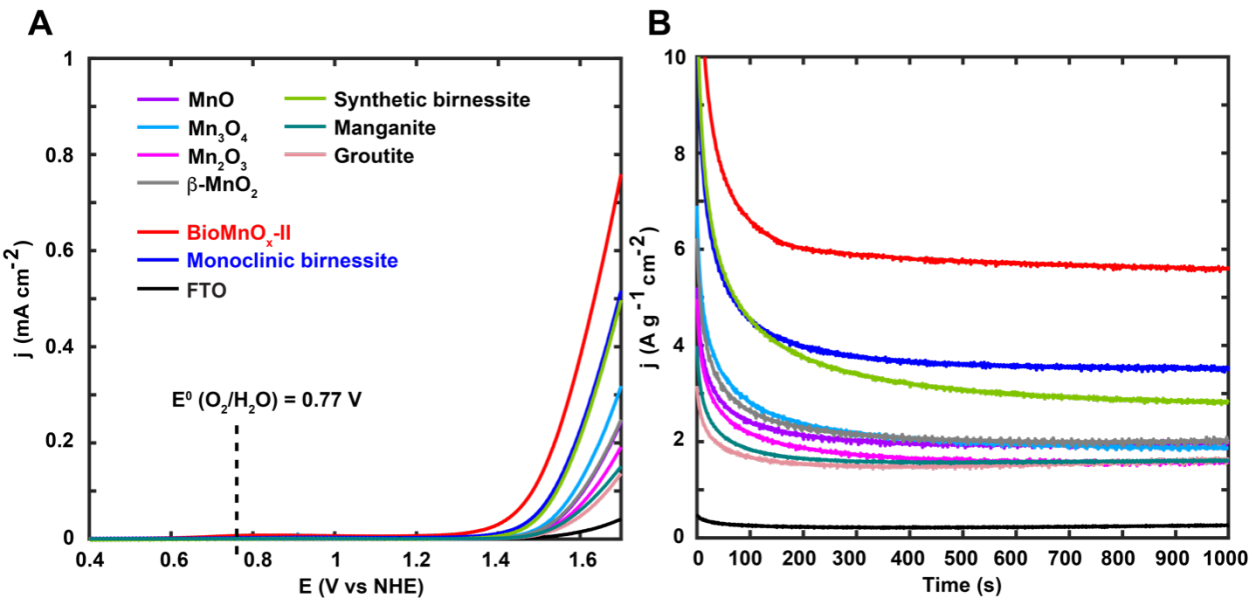

FIGURE 2.14. LSV (A) and CA (B) of selected manganese oxide standards and BioMnO$_x$-II. LSV was taken with a scanning rate of 10 mV/s. CA was measured at 1.6 V (vs NHE, $\eta = 830$ mV). The electrolyte is 0.5 M NaPi (pH 7.8). Manganite and groutite samples were grounded powders of the minerals obtained from Caland Mine, Atikokan, Ontario, Canada and from Cayuna Iron Range, Minnesota, USA, respectively.

Reaction	Sample	MnxEFG concentration (nM)	Amount of $Mn^{2+}_{(aq)}$ added	$Mn^{2+}_{(aq)}$/MnxEFG ratio	Incubation time
I	$BioMnO_x$-I	20	100 μL 0.1 M	10,000	30 min
II	$BioMnO_x$-II	20	100 μL 0.1 M	50,000	2 hr
III	$BioMnO_x$-III	20	100 μL 0.1 M	100,000	2 hr
IV	$BioMnO_x$-IV	20	100 μL 0.1 M	4,200,000	72 hr

TABLE 2.2. Reaction conditions for the synthesis of $BioMnO_x$-I, -II, -III, and -IV.

CHAPTER 3

Co-doped biogenic manganese oxides as water oxidation catalysts

3.1. Abstract

In chapter 2, we showed that $BioMnO_x$ exhibits significantly higher OER activity than electrodeposited birnessite (monoclinic birnessite). We now explored the effect of cobalt doping on the OER activity of $BioMnO_x$ and monoclinic birnessite, a naturally occurring phase of manganese oxide, and show that the Co doping significantly enhances the OER activity of $BioMnO_x$, almost comparable to the OER activity of CoPi, but does not have the same effect on the monoclinic birnessite. In addition, we explored the Co local environment by XAS to rationalize the mechanism of Co doping and to explain the enhancement of the OER activity. Finally, by using the EXAFS curve fitting, we found that Co is intercalated into the manganese-oxide layer after the electrolysis and thus we rationalize that CoPi is not likely to form during the electrolysis.

The content in this chapter is not published.

3.2. Introduction

Heavy metal oxides including IrO_2 and RuO_2 were identified as highly efficient water oxidation catalysts but due to their high cost and toxicity, large-scale water oxidation would not be feasible. [2, 189, 190] As a result, attention is shifted toward abundant, efficient, and low-cost first-row transition metal oxides such as cobalt phosphate (CoPi) and $NiFeO_x$. [7, 24, 151] CoPi has been shown to be efficient, self-repairing, and operative at neutral pH, making it a promising OER catalyst with the potential of large-scale operations. [24, 191] Structurally, CoPi forms an edge-sharing CoO_6 octahedron, similar to the structure of CoOOH. [28] It has been shown that doping manganese oxides with alkaline metals or first-row transition metals improved OER activity. [81, 156, 192, 193, 194] Similarly, we also investigated the effects of cobalt doping on the biogenic MnO_x and birnessite. Bulk and surface structural characterizations were performed to investigate the underlying mechanism of the enhanced activity and Co-doping effect.

3.3. Experimental procedures

Due to its extraordinary electrocatalytic behavior and well-characterized structure of $BioMnO_x$-II, for this chapter, all Co-doped biogenic MnO_x refer to Co-doped $BioMnO_x$-II (Co-$BioMnO_x$-II). For the preparation and material characterization methods with respect to MnO_x, refer to Chapter 2 at Section 2.3.

3.3.1. Material synthesis.

Co-doped biogenic MnO_x (Co-$BioMnO_x$-II) sample preparation. 0.7 – 1.5 mg of MnO_x was suspended in Milli-Q water (833 μL H_2O per mg of MnO_x). The mixture was sonicated to acquire homogeneous suspension and 10 mol% of $Co^{2+}{}_{(aq)}$ was added and thoroughly mixed. The molar percentage was calculated based on the molecular weight of the MnO_2. The mixture was incubated on the bench for 18 h. The mixture was then centrifuged at 6000 rpm for 1 min, washed 5 times with Milli-Q water, and dried under vacuum at room temperature. The preparation of the resulting powder, denoted by Co-$BioMnO_x$-II, is

illustrated in Figure 3.8. Other transition metal-doped manganese oxides were prepared via the same procedure, with Co^{2+} replaced by either Ni^{2+} or Fe^{2+}.

Co-doped monoclinic birnessite (Co-monoclinic birnessite) sample preparation. Co-doped monoclinic birnessite sample was prepared using the same protocol as Co-BioMnO_x-II in order to maintain consistency. 0.7 – 1.5 mg of monoclinic birnessite was suspended in Milli-Q water (833 μL H_2O per mg monoclinic birnessite) and homogenized via sonication. 10 mol% of $Co^{2+}{}_{(aq)}$ was added and thoroughly mixed. The molar percentage was calculated based on the molecular weight of MnO_2. The mixture was incubated on the bench for 18 h, then centrifuged (6000 rpm for 1 min), and washed 5 times with Milli-Q water. The precipitate was dried under vacuum at room temperature. The resulting powder was denoted as Co-monoclinic birnessite. The Co-monoclinic birnessite sample preparation is illustrated in Figure 3.8.

Cobalt phosphate catalyst (CoPi) sample preparation. The cobalt phosphate catalyst sample was prepared using a previously-described method for electrodeposition of bulk K-CoPi. [24] The CoPi catalyst was electrodeposited onto a 10 cm × 9 cm FTO plate submerged in the electrolyte (0.5 mM $Co(NO_3)_2$ solution in 0.1 M potassium phosphate, KPi, pH 7.0). During electrodeposition, a 1.25 V potential (vs. NHE) was applied until 180 C ($\sim$2 C/cm^2) of charge was passed. The electrodeposited FTO plate was rinsed 5 times with Milli-Q water and dried on the bench, after which CoPi powder was obtained by gently scraping the film with a clean razor. The resulting powder, denoted CoPi, was collected. The CoPi sample preparation is illustrated in Figure 3.8.

CoOOH synthesis. CoOOH was synthesized following the previously published procedure. [195] Pink β-$Co(OH)_2$ powder was heated under a flow of oxygen at 125 °C for 24 hours with stirring to allow thorough mixing. We note that heating the reaction mixture above 130 °C can lead to black Co_3O_4 formation. The resulting brown CoOOH powder was characterized by pXRD. The CoOOH was used as one of the XANES standards for the Co K-edge LCF.

3.3.2. Material characterization.

Electrochemically active surface area measurements (ECSA). The ECSA was calculated from the measurements of cyclic voltammetry at different scan rates. The potential range from 350 mV to 515 mV, was chosen to minimize the faradaic current response. CV was conducted within the stirring solution in this range with the scan rate of 300, 200, 100, 50, 20 and 10 mV/s. At each potential vertex, the working electrode was held at the vertex potential for 10 s to allow double-layer charging. The slope of the resulting current vs scan rate plot is equal to the double layer capacitance, C_{DL}, which is then equal to the ECSA multiplied by specific capacitance, C_{s}, (Equation 3.1). [162]

$$Slope = C_{DL} = (ECSA) * C_s \tag{3.1}$$

Scanning Electron Microscopy (SEM) and Energy-Dispersive X-ray Spectroscopy (EDS). SEM was performed with Thermo Fisher Quattro S at Advanced Materials Characterization and Testing Laboratory (AMCaT) at the University of California-Davis. SEM samples were prepared by drying a droplet of suspension sample on a silicon wafer. The surface morphology of the sample was examined using an Everhart-Thornley detector (ETD) with acceleration voltage of 5 kV and spot size of 2.5 Å. High resolution SEM was performed in Stanford Nano Shared Facilities (SNSF) with FEI Magellan 400 XHR instrument. EDS was performed with Thermo Fisher FEI Scios Dual Beam FIB/SEM located in the Center for Nano-MicroManufacturing (CNM2). The above SEM sample was used for EDS measurements. 10 keV energy of electron beam was used to cover the range for K series and L series of Mn and Co elements.

Inductively Coupled Plasma-Mass Spectrometry (ICP-MS). ICP-MS was performed in UC Davis Interdisciplinary Center for Inductively-Coupled Plasma Mass Spectrometry (UCD/ICPMS). MnO_x (∼5 mg) sample was digested and fully dissolved by adding 3% HNO_3 and 30% H_2O_2 and heating at 95 °C. Extra portion of concentrated HNO_3 and heating was applied to the

biogenic MnO_x samples to remove the white precipitate, assumed to be organic or proteinaceous, after general digestion. Standard curves for manganese and cobalt elements were made by using the Laboratory Control Sample and the Initial Calibration Verification and based on the standard curves, the concentrations (in ppm) of manganese and cobalt in the samples were determined.

X-ray Absorption Spectroscopy (XAS) and data analysis. All XAS scans were taken at the Stanford Synchrotron Radiation Lightsource (SSRL) at the SLAC National Accelerator Laboratory. Powder and thin film samples were taken in either beamline stations 4-3 or 2-2. Energy calibration of the beam was performed using elemental Mn, for Mn K-edge, and elemental Co, for Co K-edge. The fluorescence data were collected using a Lytle detector or Ge detector and then averaged together to increase the signal-to-noise ratio. Thin film samples were prepared by dropcasting 120 μg of the corresponding sample on a 1 cm x 1 cm area of FTO glass. The resulting thin film samples were dried under Ar prior to XAS measurement. For the post-electrochemistry ex-situ thin film samples, we conducted the same electrochemistry experiment series, LSV–CV–LSV–CA, on the as-deposited thin films, which were then dried and stored under Ar until XAS measurement. For XAS measurement of the thin film samples, the samples were stabilized by Kapton tape on the sample holder and fluorescence data was collected using a Ge detector. Two different spots and three scans per spot were taken for each sample as replicates to get a better consistency and signal-to-noise ratio. The Co foil data were collected in the reference channel for edge calibration.

Extended X-ray Absorption Fine Structure (EXAFS) analysis. The EXAFS analysis was performed on both powder samples and thin film samples. All the EXAFS curve fitting was performed over R-space using Artemis and the IFEFFIT software. Powder samples were fitted with the window of $3 \leq k \leq 11$ and $0 \leq R \leq 6$. Shell-by-shell R-space fitting was performed by introducing one or two shells at a time. The R-factor was used to describe the quality of the fit (Equation 2.2). The FEFF calculation was done in the

Demeter 0.9.26 to determine the ab initio amplitudes $f_i(k)$ and phases $\delta_i(k)$, which are then used in the EXAFS equation (Equation 3.2):

$$\chi(k) = S_0^2 \sum_i \frac{N_i f_i(k)}{kD_i^2} \exp(\frac{-2D_i}{\lambda_i(k)}) \exp(-2k^2\sigma_i^2) sin(2kD_i + \delta_i(k)) \tag{3.2}$$

EXAFS is a technique that measures the number and type of neighboring atoms (scatterers) and the distance between the central atom (absorber) and the scatterers. In the EXAFS equation, $f_i(k)$ is the parameterized scattering factor of the scatterers, which is proportional to the possibility of elastic scattering from the scatterers. $\lambda_i(k)$ is the inelastic free mean path, which describes the inelastic losses due to excitation of the scatterers. $\delta_i(k)$ is the phase change due to the presence of both absorber and scatterer. $f_i(k)$, $\lambda_i(k)$ and δ_i are the three terms that are dependent on the type of scatterer. S_0^2 is the amplitude reduction factor due to the shake-up/off processes of the absorber. N_i, D_i and σ_i are the degeneracy of the absorber-scatterer path, the half of total path length of a path and the static and thermal disorder factor of the path.

In this chapter, Mn and Co K-edge EXAFS spectra were taken and analyzed. All of the Mn K-edge XAS spectra were calibrated by setting the first peak of the Mn foil spectrum to the edge energy of Mn, 6539 eV. The S_0^2 value of Co is set to be 0.85. All of the Co K-edge XAS spectra were calibrated by setting the third peak of the Co foil spectrum in the reference channel to the edge energy of Co, 7709 eV. The S_0^2 value of Co is set to be 0.75.

3.4. Results and Discussion

3.4.1. The introduction of a second transition metal ion. Although biogenic MnO_x, especially BioMnO_x-II and BioMnO_x-III, exhibit a good OER activity (vide supra), the overall activity of MnO_x is still low, because the activity-related bond strength of M-OH for Mn is the highest among the first-row transition metals. [7] Therefore, we introduced a second transition metal ion (Fe^{2+}, Co^{2+} or Ni^{2+}) onto the surface of biogenic MnO_x, in

order to improve the OER activity. Here, BioMnO$_x$-II was chosen for doping the second metal ion at the surface (denoted as M-BioMnO$_x$-II, M = Fe, Co, or Ni), since it shows the highest OER activity among all the BioMnO$_x$ samples. As shown in Figure 3.9, the introduction of either Fe^{2+} or Ni^{2+} did not improve the OER activity of BioMnO$_x$. In contrast, the Co-BioMnO$_x$-II shows significant higher OER activity than that of BioMnO$_x$-II, with the overpotential at 0.1 mA/cm^2 ca. 630 mV and the CA current density at 1.6 V (vs NHE) was stabilized at 18 A$\cdot$ g$^{-1}\cdot$ cm^{-2}, which is almost three times of the corresponding current density of BioMnO$_x$-II. We also synthesized the well-known CoPi catalyst for comparison. [24] We noted that Co-BioMnO$_x$-II shows comparable overpotential and ~80% CA current density to that of CoPi. This suggests that the OER activity of Co-BioMnO$_x$-II is comparable to that of CoPi. In addition, a Co-doped monoclinic birnessite sample (denoted as Co-monoclinic birnessite) was also synthesized as a control. While the introduction of the Co metal ion onto the surface of monoclinic birnessite improved the OER activity, the overall activity is much lower than that of Co-BioMnO$_x$-II or CoPi (Figure 3.1). To understand the origin of such high OER activity of Co-BioMnO$_x$-II catalysts, in the following sections, we employed multiple spectroscopies, including XANES, XPS, EXAFS, etc, to characterize the Co-BioMnO$_x$-II, especially the potentially active Co species.

3.4.2. Structural characterization of biogenic MnO$_x$. From Chapter 2, we found that the structural composition of BioMnO$_x$-II is 75.1% monoclinic birnessite and 24.9% synthetic birnessite, which then contains 12.8% feitknechtite and 12.1% triclinic birnessite. In this section, we first try to get comprehensive structural information about BioMnO$_x$, including the characterization of the oxidation state in the bulk BioMnO$_x$. Building from this, we will analyze the structural composition and build the structure-function relationship of Co-doped BioMnO$_x$-II.

In terms of the Mn oxidation state, the average oxidation state was determined from the linear relationship between oxidation states of the standard samples (Figures 2.10& 3.10–3.11) and their corresponding edge energy of the XANES spectra (Table 3.1). [163, 196]

We further employed Mn K-edge EXAFS analysis to obtain the fine structural information of manganese oxide lattice in the MnO_x (Table 3.2 and Figures 3.13– 3.17). As shown in Figure 3.12A, Fourier transforms of Mn K-edge EXAFS of BioMnO$_x$-II and monoclinic birnessite show four regions of peaks within 6 Å distance: first shell Mn-O (∼1.5 Å), first shell Mn-Mn (∼2.5 Å), interlayer Mn-O/Na or long-ranged Mn-O (3–4 Å), and long-ranged Mn-Mn path above 4 Å. EXAFS fitting of BioMnO$_x$-II was performed by using varying structural models, including monoclinic birnessite, triclinic birnessite and feitknechtite as suggested via the XANES LCF analysis (vide supra, Section 2.4.3). Figure 3.12 shows that the feitknechtite model yields the best fit with BioMnO$_x$-II (Figures 3.14– 3.16). For the control sample monoclinic birnessite, a good fitting was obtained by using the corresponding structural model of monoclinic birnessite (Figure 3.12 and Figure 3.17).

3.4.3. Characterization of Mn species of Co-BioMnO$_x$-II. Shown in Figure 3.18, the EDS analysis suggests that the percentage of surface Co/Mn species for Co-BioMnO$_x$-II and Co-monoclinic birnessite is ca. 5.7% and 5.9%, respectively. High-resolution SEM (Figure 3.19) and pXRD patterns (Figure 3.20) of Co-BioMnO$_x$-II show the similar short-ordered rods morphology and amorphous structure to those of BioMnO$_x$-II. This suggests that the introduction of ca. 5.7% Co did not affect the morphology and crystalline structure of BioMnO$_x$-II (as well as monoclinic birnessite). However, LCF analysis on the Mn K-edge XANES region of Co-BioMnO$_x$-II and Co-monoclinic birnessite show changes of bulk structural composition upon Co doping (Figure 3.2). As shown in Figure 3.2 and Table 3.3, Co-BioMnO$_x$-II contains more feitknechtite (24.7%) and triclinic birnessite (23.3%), but less monoclinic birnessite (49.2%), as compared to BioMnO$_x$-II. This composition is similar to that of BioMnO$_x$-III (Figure 2.4), suggesting that biogenic MnO_x also evolved (most likely monoclinic birnessite converted to feitknechtite [159, 197] and triclinic birnessite [157]) during the 18 h Co^{2+}-incubating process (Figure 3.8). For monoclinic birnessite, upon Co doping, 12.9% Mn_2O_3 and 12.6% Mn_3O_4 was formed. In terms of the Mn oxidation state, the average oxidation state was determined from the linear relationship between oxidation states

of the standard samples (Figures 2.10 & 3.10 & 3.11) and their corresponding edge energy of the XANES spectra. [163, 196] As shown in Figure 3.2E and Table 3.4, upon doping with Co^{2+}, the overall bulk Mn oxidation state decreased from 3.64 to 3.55 for $BioMnO_x$-II, and from 3.67 to 3.62 for monoclinic birnessite. This is consistent with the red-shift of the Mn3s binding energies of both Co-$BioMnO_x$-II and Co-monoclinic birnessite, indicating that the oxidation states of surface Mn decrease upon Co doping (Figure 3.2F). This suggests that during the Co^{2+} doping process, Co^{2+} could be oxidized by Mn(IV) species, resulting in the low average oxidation states of Mn. Given that the enhanced activity should come from Co species, [7] in the following sections, we focus on the characterization of Co species to understand the mechanism of enhanced OER activity of Co-$BioMnO_x$-II and active structure of the catalyst.

3.4.4. Characterization of Co species of Co-$BioMnO_x$-II. While there are not many differences (similar Co binding energies and peak shapes) of Co 2p XPS through three samples of Co-$BioMnO_x$-II, Co-monoclinic birnessite and CoPi (Figure 3.21), we employed Co K-edge XANES spectroscopy to determine the average oxidation state of Co, which is between +2 and +3 (Figure 3.3). The average oxidation state of Co in the sample of Co-$BioMnO_x$-II is similar to CoPi, but much lower than that of Co-monoclinic birnessite, suggesting more Co(III) in Co-monoclinic birnessite. This is consistent with the XPS analysis in section 2.4.3 that shows monoclinic birnessite contains more surface Mn(IV), which could oxidize more Co(II) to form Co(III). We further employed Mn and Co K-edge EXAFS analysis to probe the local coordination environment of Co in the MnO_x (Tables 3.5 and 3.6. We first used Fourier transforms of Mn K-edge EXAFS analysis to obtain the fine structural information of manganese oxide lattice. As shown in Figure 3.4A&C, Fourier transforms of Mn K-edge EXAFS of $BioMnO_x$-II and monoclinic birnessite show four regions of peaks within 6 Å distance: first shell Mn-O (∼1.5 Å), first shell Mn-Mn (∼2.5 Å), interlayer Mn-O/Na or long-ranged Mn-O (3–4 Å), and long-ranged Mn-Mn path above 4 Å. EXAFS fitting of $BioMnO_x$-II was performed by using varying structural models, including

monoclinic birnessite, triclinic birnessite and feitknechtite as suggested via the XANES LCF analysis (vide supra, Section 2.4.3). Figure 3.4 shows that the feitknechtite model yields the best fit with BioMnO$_x$-II (Figures 3.14 - 3.16). For the control sample monoclinic birnessite, a good fitting was obtained by using the corresponding structural model of monoclinic birnessite (Figure 3.4C and Figure 3.17). Upon doping with Co, we did not observe much structural changes to the manganese-oxide lattice (Figures 3.22&Figure 3.23). Especially, the ratio between the first two prominent peaks remains the same for both Co-BioMnO$_x$-II and Co-monoclinic birnessite (Figure 3.4). With the fine structural information of manganese oxide lattice in hand, Co K-edge EXAFS fitting was performed by constructing a Co/MnO$_x$ model, i.e., replacing a Mn site in monoclinic birnessite or feitknechtite model with Co (Figure 3.5AB), followed by data refinement. Here, we first focus on the structural analysis of the "before-OER" samples, i.e., the as-synthesized powder sample. Fourier transforms of Co K-edge EXAFS of Co-BioMnO$_x$-II and Co-monoclinic birnessite show four regions of peaks within 6 Å distance: first shell Co-O (∼1.5 Å), first shell Co-Mn (∼2.5 Å), interlayer Co-O/Na or long-ranged Co-O (3–4 Å), and long-ranged Co-Mn path above 4 Å (Figure 3.5A&B), and the ratio of the first shell Co-O and Co-Mn/Co is similar in both samples, suggesting that Co is fully coordinated to the second shell. The long-ranged Co-Mn/Co peaks at 4.6 Å and 5.2 Å share similar peak shape and relative intensity to the corresponding Mn K-edge spectra of Co-monoclinic birnessite and Co-BioMnO$_x$-II, suggesting that Co is doped inside of the manganese oxide lattice in both samples. By using the Co-feitknechtite model, an excellent fit was obtained for Co-BioMnO$_x$-II (Figures 3.5A & 3.25). For Co-monoclinic birnessite samples, a good fit was obtained for the first two peaks by varying the coordination numbers of first shell Co-O and Co-Mn paths (Figures 3.5B & 3.26). The fitted coordination number of five to six suggests a fully-coordinated octahedral geometry (Table 3.6). In contrast, long-ranged Co-O and Co-Mn paths are not well described by the fit, indicating an ill-defined conformation change around the Co (Figure 3.26). As a fitting standard, the fit to CoPi data were obtained by utilizing a CoOOH model (Figure 3.5C)

and a good fit of CoPi spectrum after electrolysis was obtained using the scattering paths suggested by Kanan et al (Figure 3.28). [28] Based on above results, 1) the lower average oxidation state of Co species in Co-BioMnO$_x$-II; 2) the active Co-feitknechtite structure, both are essential to the OER activity enhancement of BioMnO$_x$-II with Co doping.

3.4.5. Comparison of Co-BioMnO$_x$ and CoPi. Although the Co-feitknechtite structure of Co-BioMnO$_x$-II that we attribute as the essential for the enhanced OER activity is different from the CoOOH model for CoPi (Figure 3.5), we do not know if any similar CoPi species was formed during or after the electrolysis. The CoPi-like structure could potentially form via CoO$_x$ aggregates with the Co ions released from the manganese oxide lattice. If there are any, it could also contribute to the OER activity. To answer this question, we also performed Co K-edge EXAFS fitting for the samples after OER reaction to see if there are any Co local structural changes. As shown in Figure 3.5, after electrolysis, the Co–O and Co–Mn/Co peak intensity ratio increases for Co-BioMnO$_x$-II (but remains unchanged for Co-monoclinic birnessite and CoPi), which infers that Mn defect sites were generated and O vacancies were filled around Co after electrolysis (Figure 3.5). The long-ranged Co-Mn distance also decreases after electrolysis (Table 3.6). However, an excellent fit (R-factor of 0.0025 and a reduced χ^2 of 17.19) was still obtained for Co-BioMnO$_x$-II after electrolysis by using the Co-feitknechtite model (Figure 3.5). This suggests that the Co-feitknechtite structure is not dramatically changed during electrolysis. For comparison, we also employed CoOOH model to fit the spectrum of Co-BioMnO$_x$-II after electrolysis with the R-factor of 0.0134 and a reduced χ^2 of 44.15, which is not as good as Co-feitknechtite fitting (Figures 3.30 & 3.31). Especially, the fitting pattern of the Co–O peaks from 3 Å to 4 Å does not match well. To compare those two model fits, we performed Hamilton test to compare the goodness of fits in relation with the number of free parameters (Equation 3.3). The p value from the Hamilton test is 0.03, which is smaller than 0.05, indicating that Co-feitknechtite model fit is statistically significantly better than CoOOH model fit. The discrepancy between the two model fits is mainly reflected by the poor fitting pattern of the Co–O peaks from 3 Å to 4

Å (Figure 3.31). To this extent, we claim that there is no distinguishable amount of CoPi structure formed after electrochemical process, thus inferring that CoPi does not significantly contribute to the OER activity of Co-BioMnO$_x$-II. Based on above analysis, it is less likely that the CoPi-like active species formed during/after electrolysis when Co-BioMnO$_x$-II is used as the catalyst. This further confirm our analysis that the Co-feitknechtite structure is the active site contributing to the enhanced OER activity.

$$p = \frac{\int_0^r t^{(a-1)}(1-t)^{(b-1)}dt}{\int_0^1 t^{(a-1)}(1-t)^{(b-1)}dt} \tag{3.3}$$

3.4.6. EXAFS analysis for CoPi question (NM analysis). In order to investigate deeply whether CoPi is formed during the electrolysis, it is sufficient to answer the question: after electrolysis, the second coordination sphere about the central Co atom consists of mainly Mn atoms instead of Co atoms. However, due to the proximity of the atomic number of Co and Mn, differentiation between two atoms in EXAFS model fitting is not absolutely accurate. Thus, we rely on the statistics to determine how likely the second coordination sphere metals are Co versus other first row transition metals. Besides the metal identity, we also included the coordination number as another variable to consider the situation of under-coordination. This analysis is denoted as Coordination number-Metal identity (NM) analysis from now on.

We build models based on CoOOH model compound, keeping the central atom as the Co atom while varying the identity of the second coordination sphere metal to V, Cr, Mn, Fe, Co, Ni, Cu and Zn (Figure 3.6).

The reasons why the CoOOH model is chosen to be the base model are as follows. The first reason is that based on the Co K-edge XANES spectra, after the electrolysis, most of the doped Co in the Co-BioMnO$_x$-II are in the Co(III) form, which has low-spin d^6 electronic configuration that gives rise to a relatively isotropic coordination environment.

The second reason is that Co-Feitknechtite model, the better fit model of Co-BioMnO_x-II, and Co-monoclinic birnessite model both share some structural similarity with CoOOH model. Thus, CoOOH model is a reasonably simplified model for the after-electrolysis thin film samples. For each M-CoOOH model, an independent FEFF calculation was performed to calculate the corresponding $f_i(k)$, $\lambda_i(k)$, and $\delta_i(k)$ in the EXAFS equation of the metal M (Equation 3.2). Then for each model, a curve fitting was performed on the R-space EXAFS spectra of CoOOH, CoPi thin film (TF) sample, Co-monoclinic birnessite TF sample and Co-BioMnO_x-II TF sample with the fixed fitting window of $3 \leq k \leq 10$ and $0 \leq R \leq 3$. For each curve fitting, first shell Co-O path (1.90 Å) and Co-M path (2.85 Å) were included with fixed coordination numbers of 6 and N respectively (N = 3, 3.5, 4, 4.5, 5, 5.5, 6, 6.5 and 7). The five guess parameters were ΔE (same value for both paths) and Δr and σ^2 for each paths. The curve fitting was performed in R space and on all three k weights.

To make the thin film samples, 120 μg of Co-monoclinic birnessite, Co-MnO_x and CoPi samples were dropcast onto the 1 cm x 1 cm of the FTO electrode plate. After a series of electrochemistry processes (LSV→CV→LSV→CA), the thin film samples were immediately transferred to the argon environment to dry and store until the XAS measurements under helium environment to prevent any post-electrochemistry structural modifications by the air. Most parts of the samples are assumed to be solvent accessible and thus the structural change in the bulk is reflective of the surface structural change.

For each of the fitting with the M-OOH model and a fixed coordination number, an R-factor is acquired to describe the goodness of this fit. The resulting R-factor for each fit was recorded and the map of R-factors with respect to the coordination number and metal identity was drawn in Figure 3.7. The x-axis is the coordination number N from 3 to 7, the y-axis is the identity of the metal M and the number at each cross point represents the R-factor of the curve fit with the corresponding M-CoOOH model FEFF calculation and fixed coordination number N. The color bar was based on the logarithm scale of 10 colors with the colored regions the lowest R-factors for each sample, which reflects the tendency of the first

shell local coordination environment of the Co center. The colored region shows the best fit regions. As is shown in the Figure 3.7, the colored region of CoOOH is located at Co centered around a high coordination number, which indicates that CoOOH favors highly coordinated Co-CoOOH model. This result is consistent with the CoOOH crystal structure. The colored region on the map of CoPi TF sample shows that the coordination environment of Co center is similar to Co-CoOOH except the coordination number is lower. The previous study shows that the coordination number of the neighboring Co for the bulk K-CoPi thin film sample is 4.5 while that for the surface K-CoPi thin film sample is 3.4. [28] The coordination number determined in our method is slightly higher than their bulk thin film sample due to the twice electrochemistry processes that further completes the coordination environment around Co center. Thus, the results from the CoPi map also confirms with the previous literature. On the other hand, the Co-monoclinic birnessite map shows that the colored region is focused on the Mn with high coordination numbers, which illustrates that after electrolysis, Co-monoclinic birnessite forms a Mn-CoOOH structure with a full coordination environment. On the other hand, the colored region on the Co-BioMnO_x-II map shows that there are two subdomains located around Mn with N around 5 and Co with N around 6.5. This difference reveals that after electrochemistry, Co-BioMnO_x-II has two major Co species, a Mn-CoOOH structure with a low coordination number and a CoOOH-like structure. The assignment from the Co-monoclinic birnessite map confirms with the XANES LCF analysis and the previous hypothesis that Co introduces conformational change into the monoclinic birnessite manganese oxide lattice and then is buried by the crystalline manganese oxide while the lower coordinated Mn-CoOOH structure of Co-BioMnO_x-II confirms that Co is simply doped into manganese oxide layer to fill the cavity while keeping the relatively defected layered structure. However, in this analysis, CoOOH is shown to appear in the after-electrolysis Co-BioMnO_x-II sample, inferring that CoOOH might contribute to the enhanced OER activity of Co-BioMnO_x-II. This CoOOH-like structure might result from the release of Co from the highly flexible Co binding sites.

This methodology can help differentiate two metals in the second coordination sphere with close atomic number, which was commonly considered highly unlikely. However, detailed mathematical and statistical proof about the validity of this analysis needs to be conducted based on EXAFS fitting on the standard M-CoOOH model compound. Besides that, this analysis considers only the models with the same metal identity and thus more analysis needs to be performed such as Mn/Co-CoOOH model fitting with different Mn fractions.

3.5. Comments and future directions

Co is a powerful element for water oxidation reactions. Simply applying current to an electrolyte with Co^{2+} ions with any of the major anions, such as PO_4^{3-} will generate the highly efficient CoO_x-based OER catalysts. Any Co-containing system risks forming CoO_x, which contributes non-negligibly to the overall water oxidation, during the electrolysis process. Thus, in order to be rigorous of the newly developed Co-containing systems, including low-concentration Co-doping systems, one needs to check the possible presence of CoO_x during electrolysis.

However, proving that there is no CoO_x formed in situ is extremely challenging, especially in the mixed first-row transition-metal oxides, such as Co-BioMnO_x. Because the atomic number of Co is close to that of Mn, distinguishing Co from Mn needs X-ray techniques with atomic resolution to analyze the characteristic absorption energy of inner shell electrons or electron paramagnetic resonance (EPR) spectroscopy to examine the spin behavior of the material. Upon careful design, in-situ measurement of EPR can be used to monitor the formation of Co(IV) during electrolysis. [25]

In this chapter, we analyzed the statistical probability of having CoPi formed during electrolysis in the Co-BioMnO_x system using EXAFS. While EXAFS is a bulk technique, a thin film electrode on FTO can be made to reduce the bulk volume. Upon EXAFS fitting analysis, the Co coordination environment before and after electrolysis is revealed. The logic is that if we show that Co is inside of the MnO_x lattice, in the similar environment

both before and after electrolysis, then there is little chance for Co to form CoO_x during electrolysis and then return back to the doped state, due to possible high energy barrier of this transformation. More likely, the CoO_x formed during electrolysis would remain after electrolysis. As a result, the fact the after-electrolysis thin film sample has a similar Co-feitknechtite local structure than before-electrolysis sample indicates that Co is likely to remain as Co-MnO_x during the electrolysis and thus CoO_x is less likely to form during the electrolysis.

However, this is only a deduction based on the statistical results, but not a solid evidence. Thus, in order to acquire the real picture of how the catalysts behave under electrolysis, high-resolution techniques need to be used for in-situ measurement. Some ideas would be in-situ EPR experiments with low concentration of Co doping thin film samples and *in-operando* XPS experiments to look at the surface of the material.

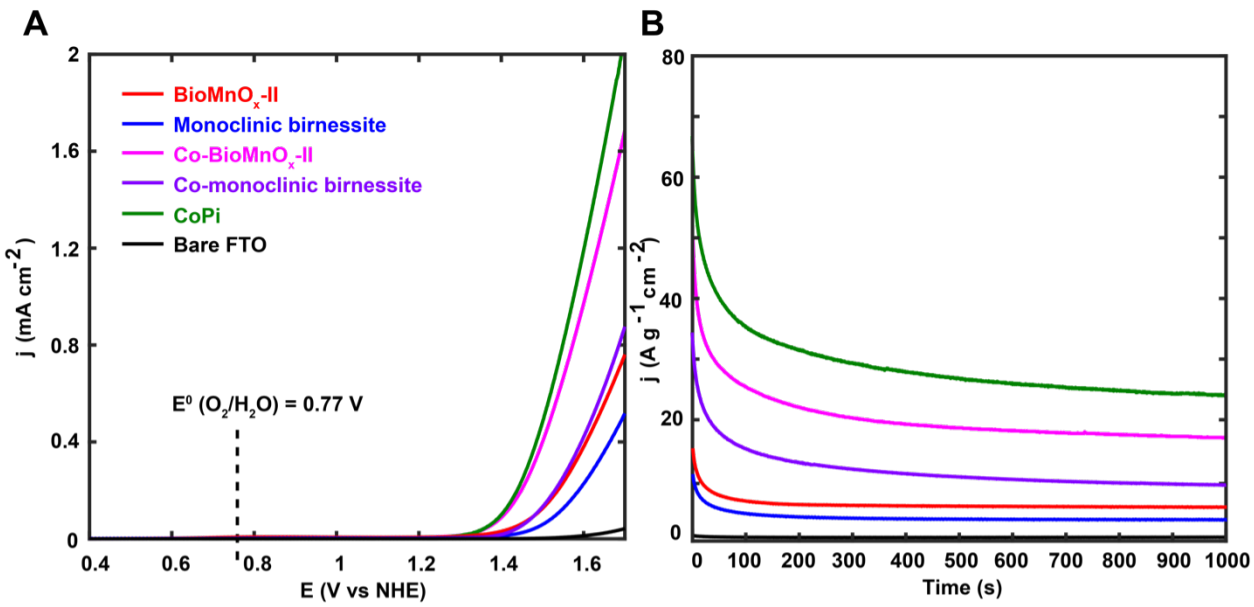

FIGURE 3.1. Linear sweep voltammagrams (A) and chronoamperometry (B) of Co-BioMnO$_x$-II (magenta trace) compared to Co-monoclinic birnessite (purple trace) and CoPi (green trace) catalysts. LSV was taken with a scan rate of 10 mV/s. CA was measured at 1.6 V (vs NHE, $\eta = 830$ mV). The electrolyte is 0.5 M NaPi (pH 7.8).

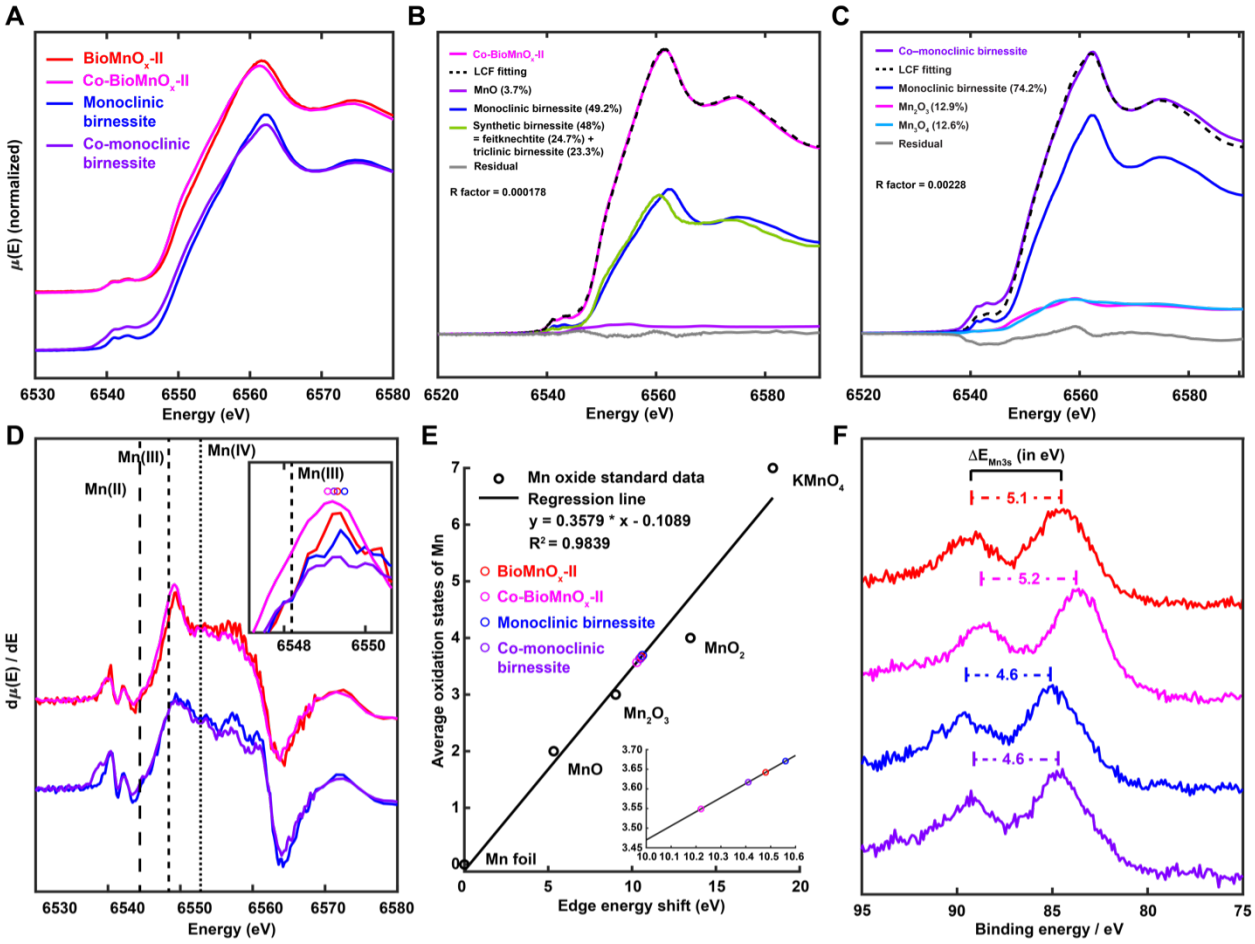

FIGURE 3.2. Mn K-edge XANES normalized spectra of $BioMnO_x$-II, monoclinic birnessite and their corresponding Co-doped samples (A), Mn K-edge XANES LCF for Co-$BioMnO_x$-II (B) and Co-monoclinic birnessite (C), Mn K-edge XANES first derivative plot (D), the standardization curve of Mn oxidation state vs edge energy shift (E), and Mn3s XPS (F)

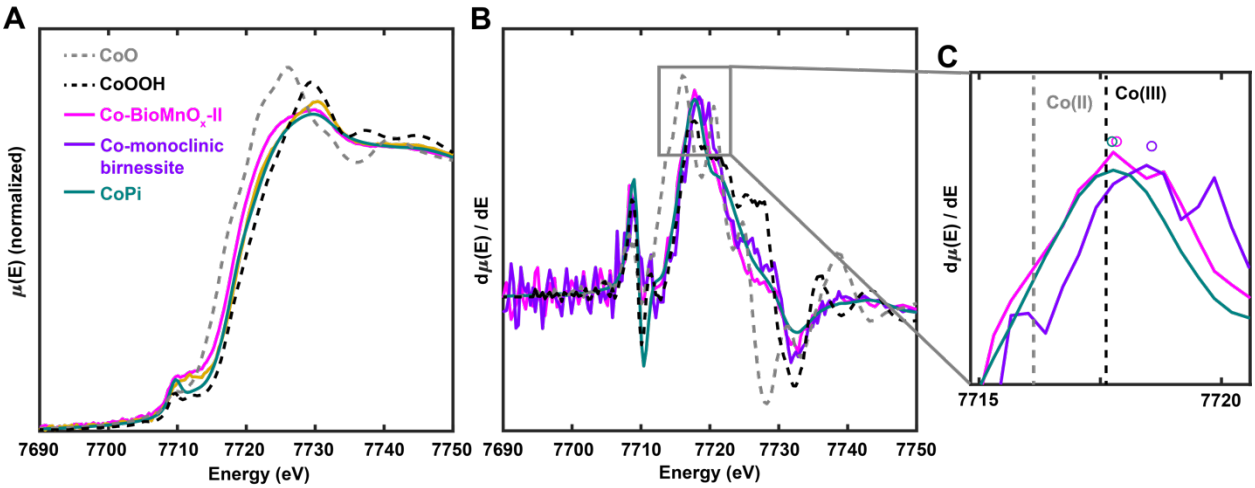

FIGURE 3.3. The Co K-edge XANES spectra (A) and first-derivative plot (B) of Co-BioMnO$_x$-II compared with Co-monoclinic birnessite and CoPi with a zoom-in first-derivative plot (C) showing the position of the first intense peak.

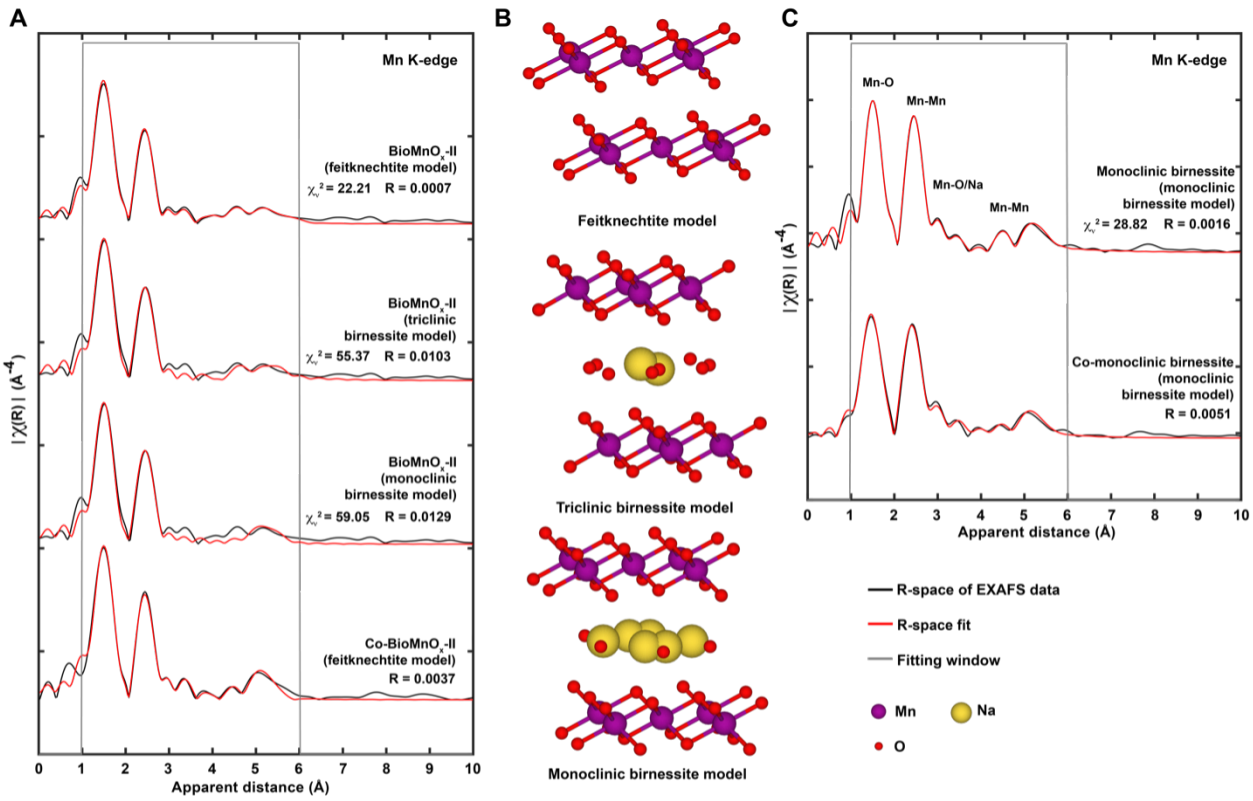

FIGURE 3.4. Mn K-edge EXAFS fitting spectra for BioMnO$_x$-II samples (A) and monoclinic birnessite samples (C). Feitknechtite, triclinic birnessite and monoclinic birnessite models are shown in B. The curve fitting was performed within the R = 1–6 Å window marked with the grey line and the model used for the curve fitting is shown in the parenthesis. Reduced chi-square values (χ_ν^2) and R-factor (R) are used to describe the goodness of the curve fitting.

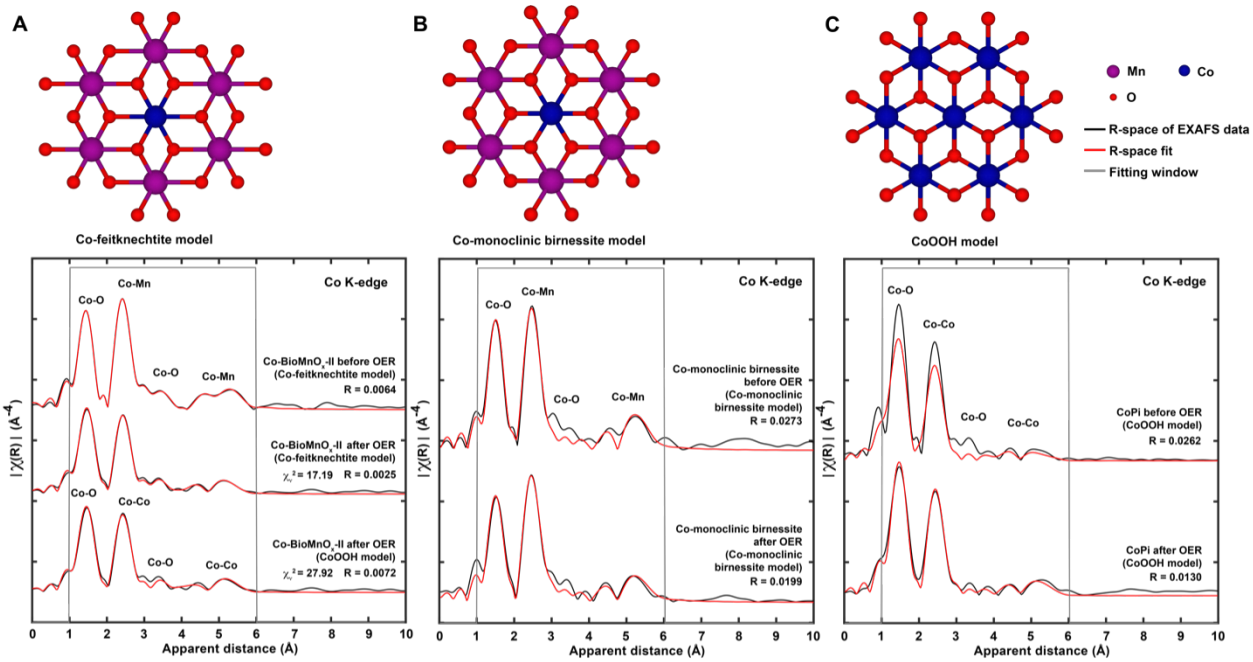

FIGURE 3.5. Co K-edge EXAFS fitting spectra for Co-BioMnO$_x$-II (A), Co-monoclinic birnessite (B) and CoPi (C). Co-feiknechtite, Co-monoclinic birnessite, and CoOOH models are used to fit Co-BioMnO$_x$-II, Co-mononclinic birnessite and CoPi respectively. Before OER and after OER refers to the as-prepared powder samples and the thin film after electrolysis respectively. The curve fitting was performed within the R = 1–6 Å window marked with the grey line and the model used for the curve fitting is shown in the parenthesis. Reduced chi-square values (χ_ν^2) and R-factor (R) are used to describe the goodness of the curve fitting.

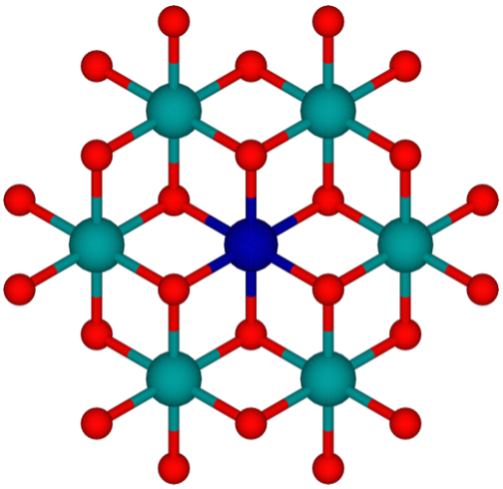

FIGURE 3.6. Models for the NM analysis. The blue sphere represents the central Co atom. The green spheres represents the second coordination sphere atoms. Depending on the identity of the atoms, eight models are created with V, Cr, Mn, Fe, Co, Ni, Cu and Zn. The red spheres represent the oxygen atoms.

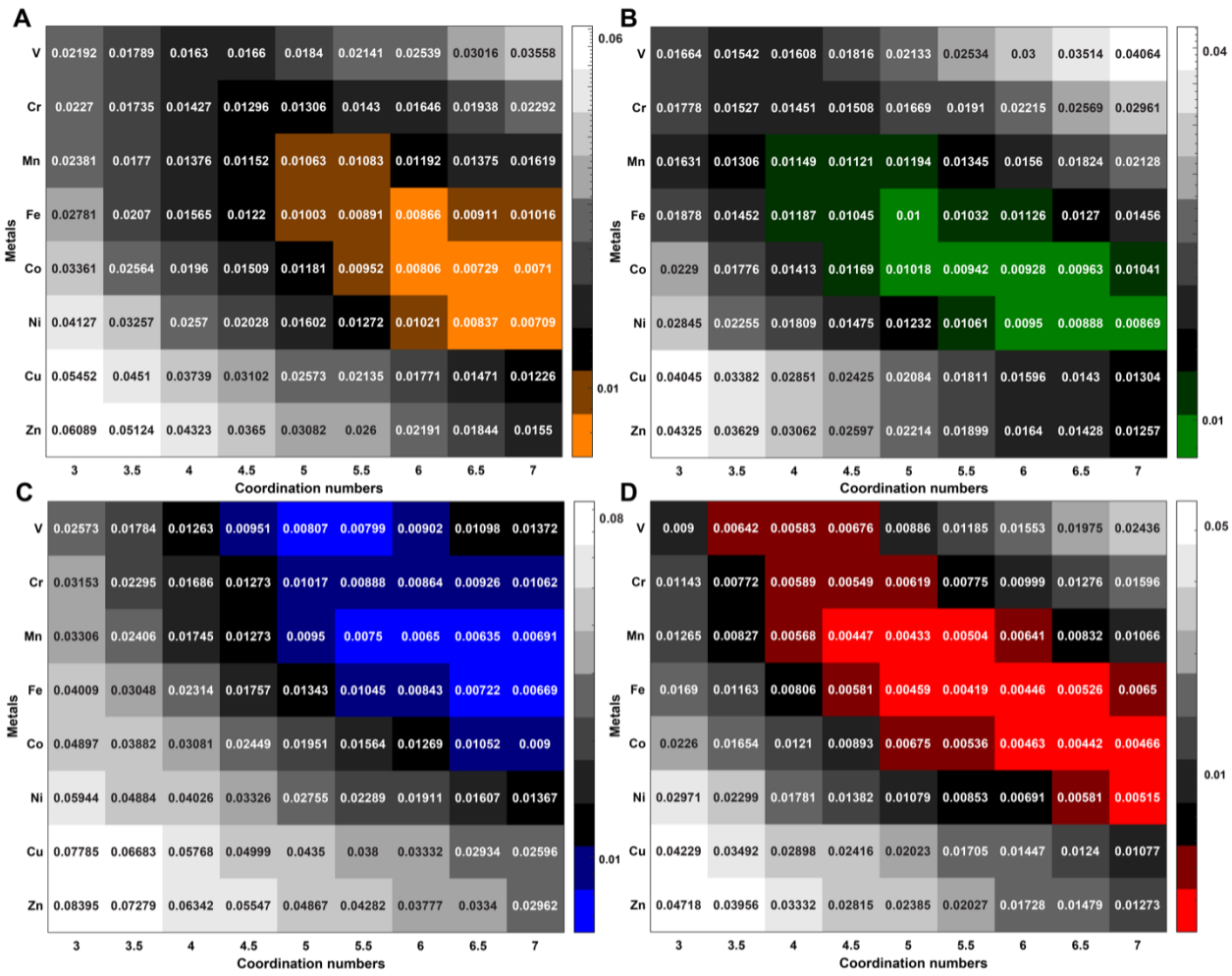

FIGURE 3.7. The resulting R-factor maps of NM analysis. A, B, C, and D represent the R-factor maps for CoOOH sample, after-electrolysis CoPi sample, after-electrolysis Co-monoclinic birnessite sample, and after-electrolysis Co-BioMnO_x-II sample.

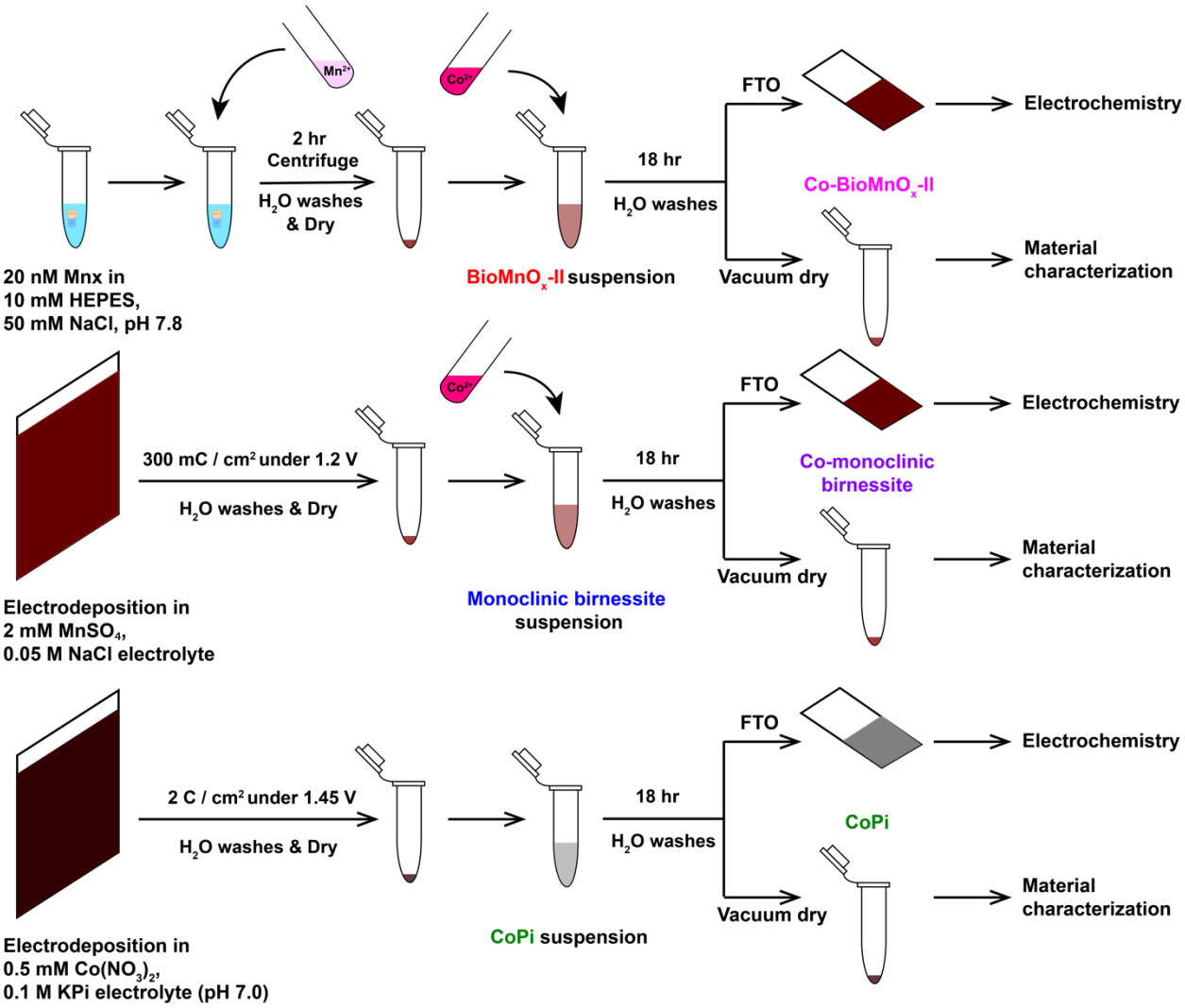

FIGURE 3.8. Co-BioMnO$_x$-II, Co-monoclinic birnessite and CoPi sample preparation schemes. The dried powder samples were used in material characterization experiments while the samples dropcast onto the FTO glass slide were used in electrochemical measurements.

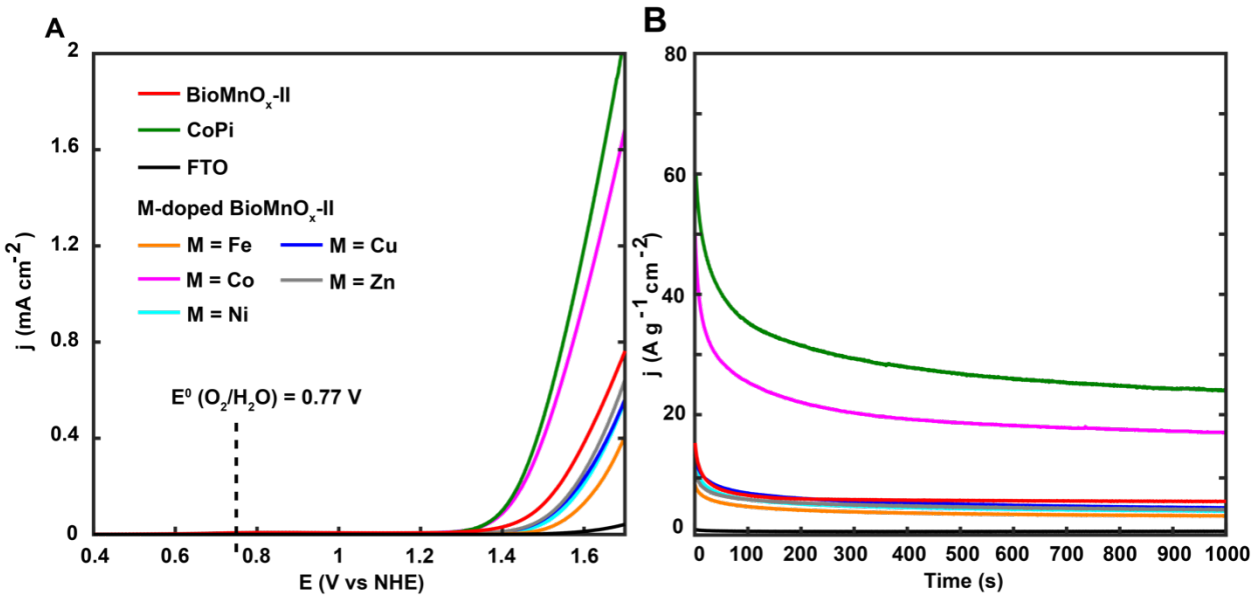

FIGURE 3.9. LSV (A) and CA (B) of M-doped BioMnO$_x$-II. All doped metal ions were added in the aqueous M^{2+} form. LSV was taken with scanning rate of 10 mV/s. CA was measured at 1.6 V (vs NHE, $\eta = 830$ mV). The electrolyte is 0.5 M NaPi (pH 7.8).

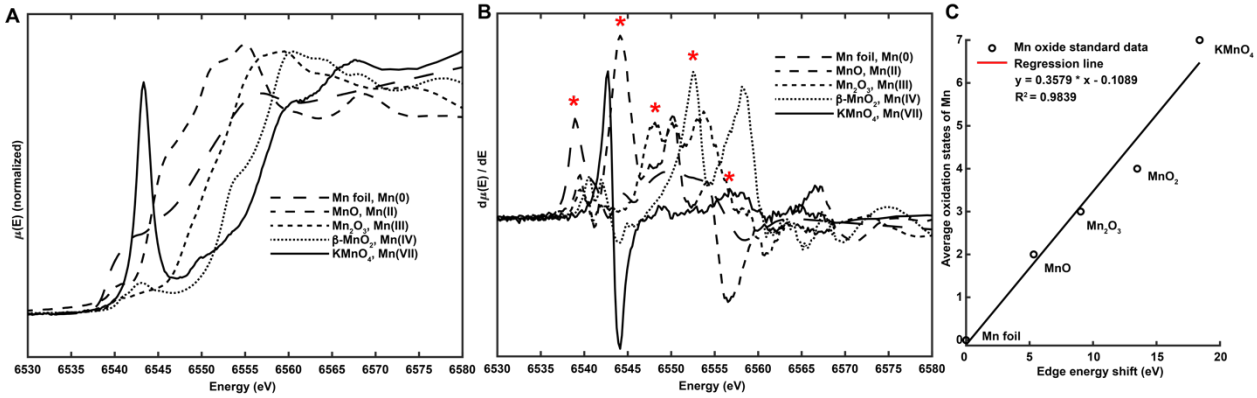

FIGURE 3.10. Normalized Mn K-edge XANES spectra (A), first derivative plot (B) and the oxidation state calibration curve (C) of manganese oxide standards. All spectra were calibrated based on the Mn foil spectra in the reference channel. The first peak at the edge in the first derivative spectrum (labeled in * on the right plot) is chosen for the determination of the Mn oxidation states.

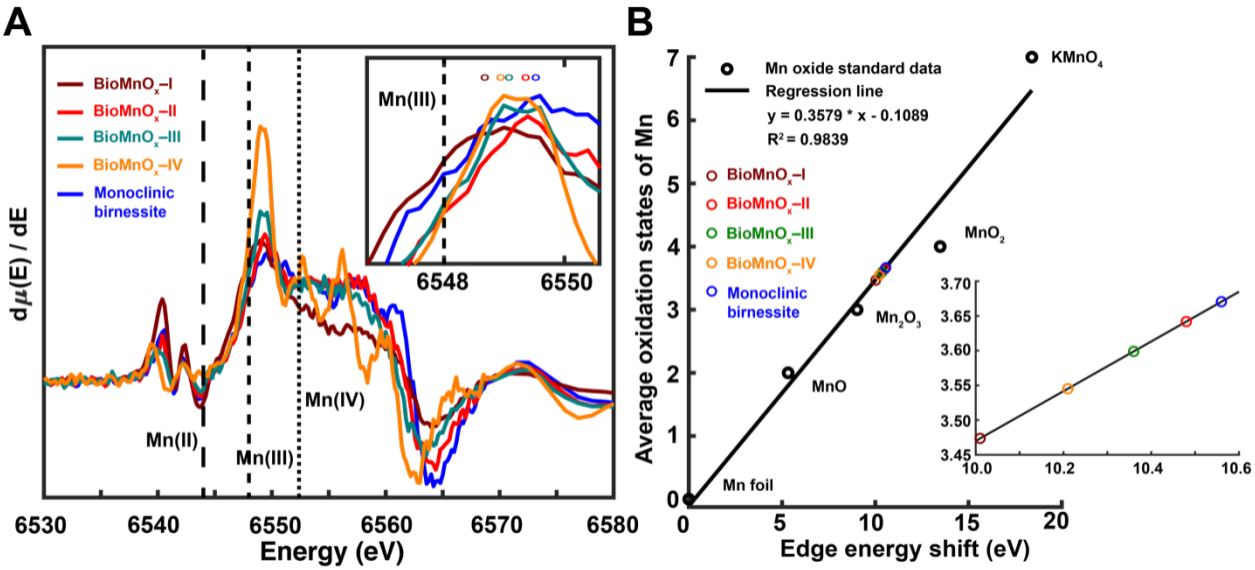

FIGURE 3.11. First derivative plot of Mn K-edge XANES spectra for $BioMnO_x$ and monoclinic birnessite (A) and the determination of oxidation states (B). The inset in A shows the position of the first peak at the edge in the first derivative spectrum. The inset in B shows the enlarged view of the $BioMnO_x$ peak position region. The normalized Mn K-edge XANES spectra for $BioMnO_x$ and monoclinic birnessite are shown in Figure 2.10.

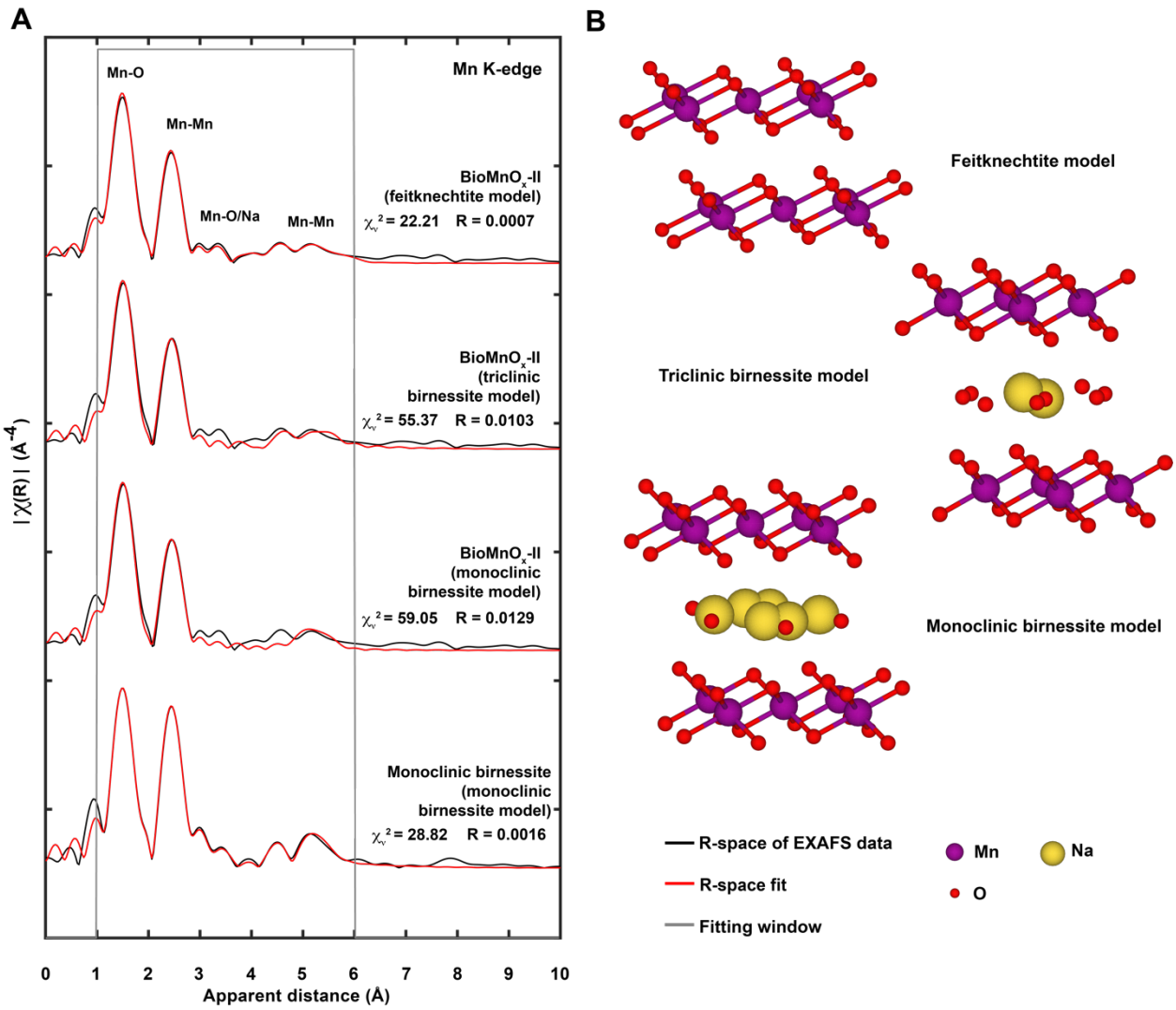

FIGURE 3.12. Mn K-edge EXAFS fitting spectra for BioMnO$_x$-II samples and monoclinic birnessite samples (A). Feitknechtite, triclinic birnessite and monoclinic birnessite models are shown in B. The curve fitting was performed within the R = 1–6 Å window marked with the grey line and the model used for the curve fitting is shown in the parenthesis. Reduced chi-square values (χ_ν^2) and R-factor (R) are used to describe the goodness of the curve fitting.

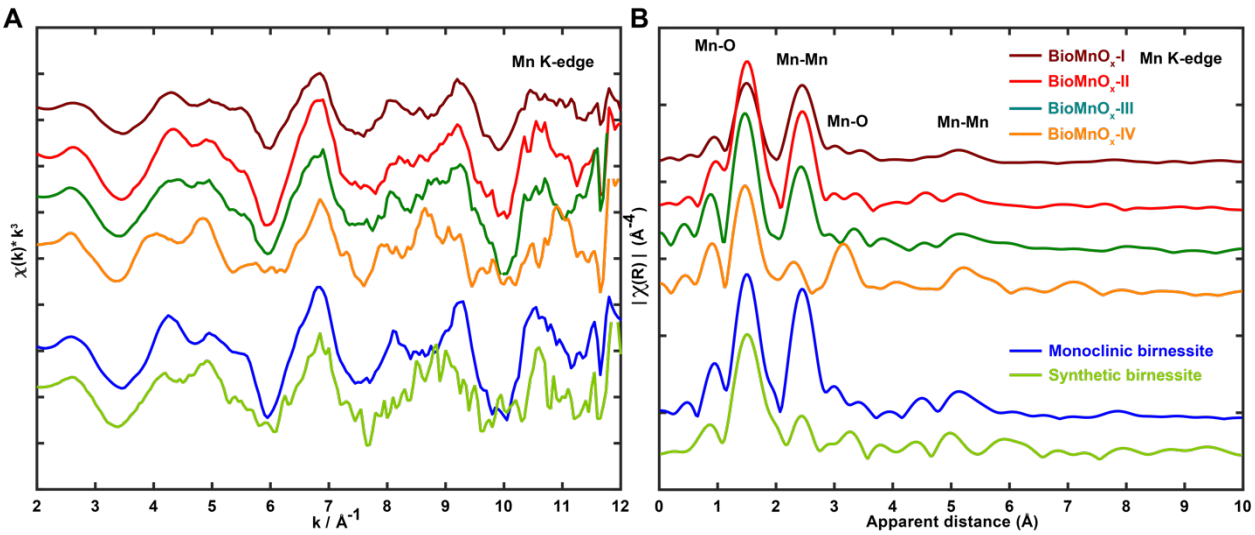

FIGURE 3.13. k^3-weighted EXAFS spectra (A) and Fourier transforms (B) of Mn K-edge. All of the curves have been equally scaled down and translated for display purposes.

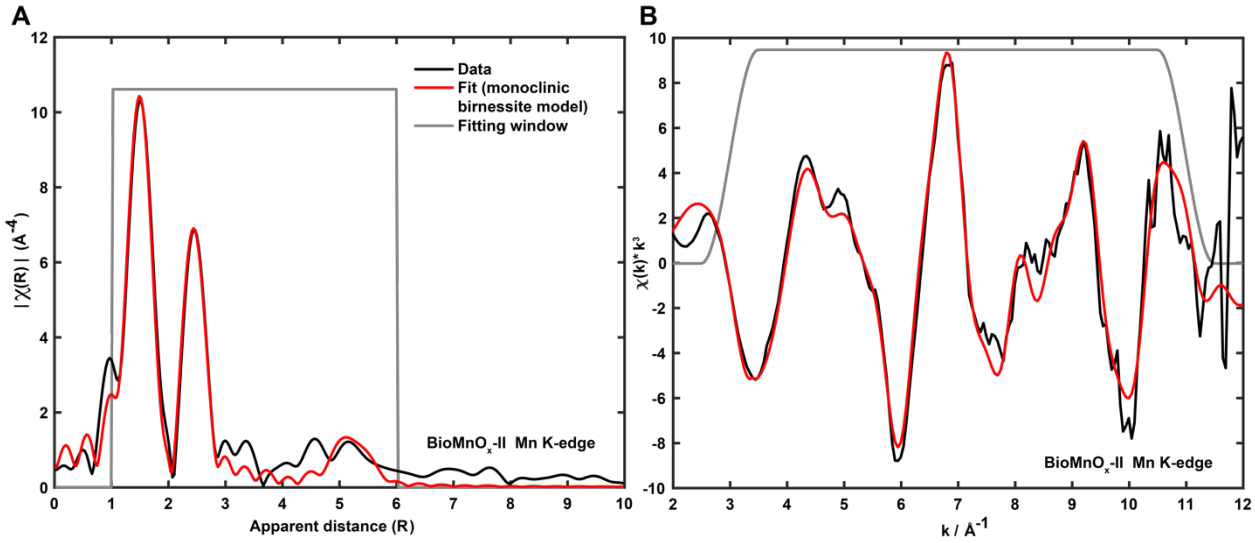

FIGURE 3.14. Mn K-edge curve fitting in R-space and k-space of $BioMnO_x$-II with monoclinic birnessite model.

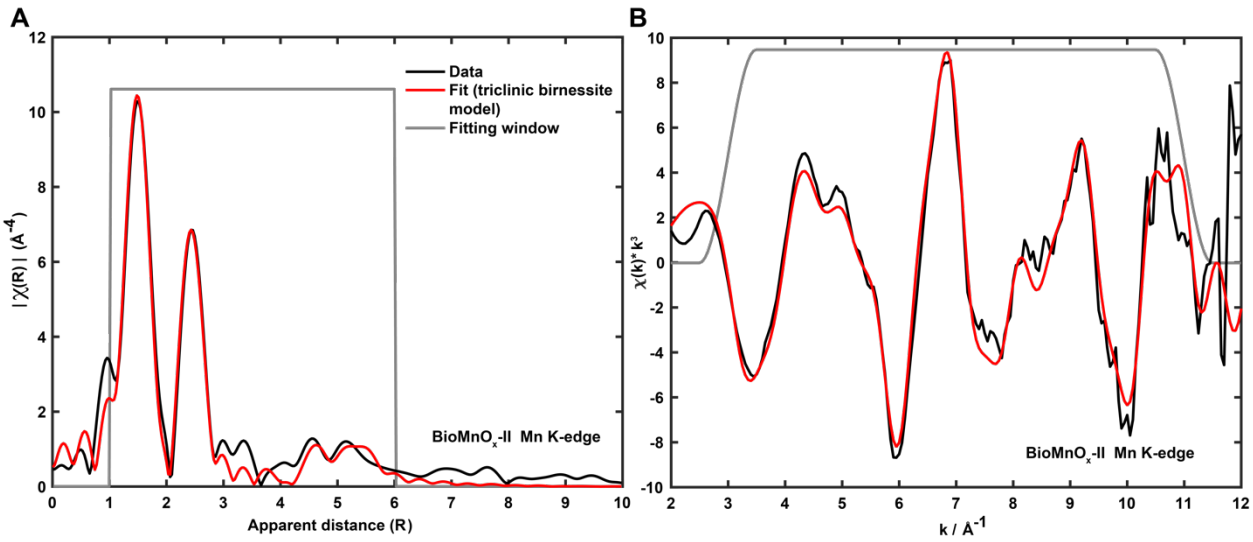

FIGURE 3.15. Mn K-edge curve fitting in R-space and k-space of BioMnO$_x$-II with triclinic birnessite model.

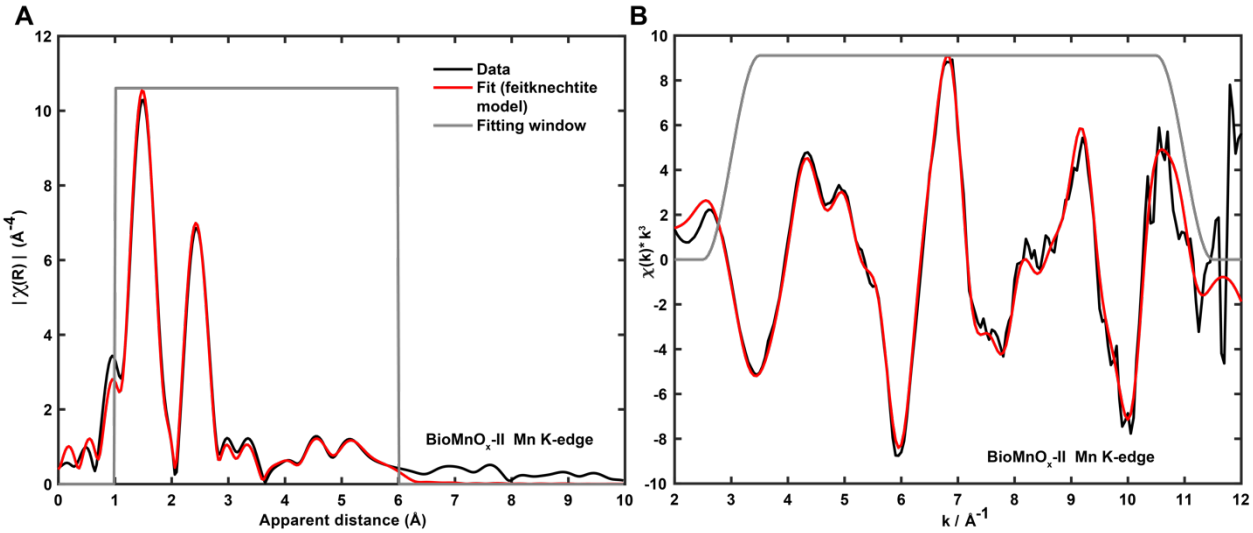

FIGURE 3.16. Mn K-edge curve fitting in R-space and k-space of BioMnO$_x$-II with feitknechtite model.

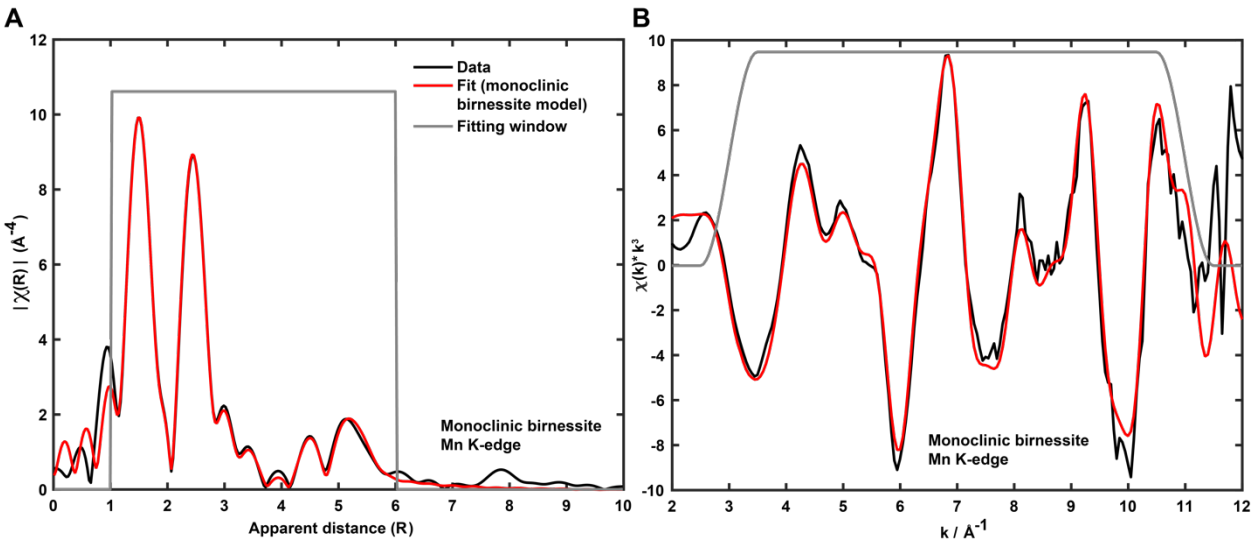

FIGURE 3.17. Mn K-edge curve fitting in R-space and k-space of monoclinic birnessite with monoclinic birnessite model.

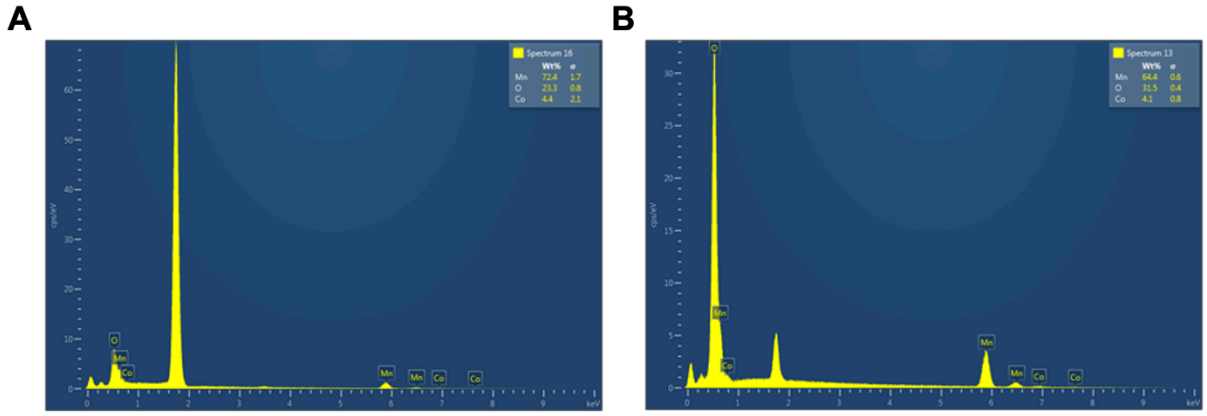

FIGURE 3.18. EDS point spectra of Co-BioMnO$_x$-II (A) and Co-monoclinic birnessite (B). The Co/Mn percentage was calculated based on the weight percentage normalized by molecular weight. The Co/Mn percentage is 5.7% for Co-BioMnO$_x$-II and 5.9% for Co-monoclinic birnessite.

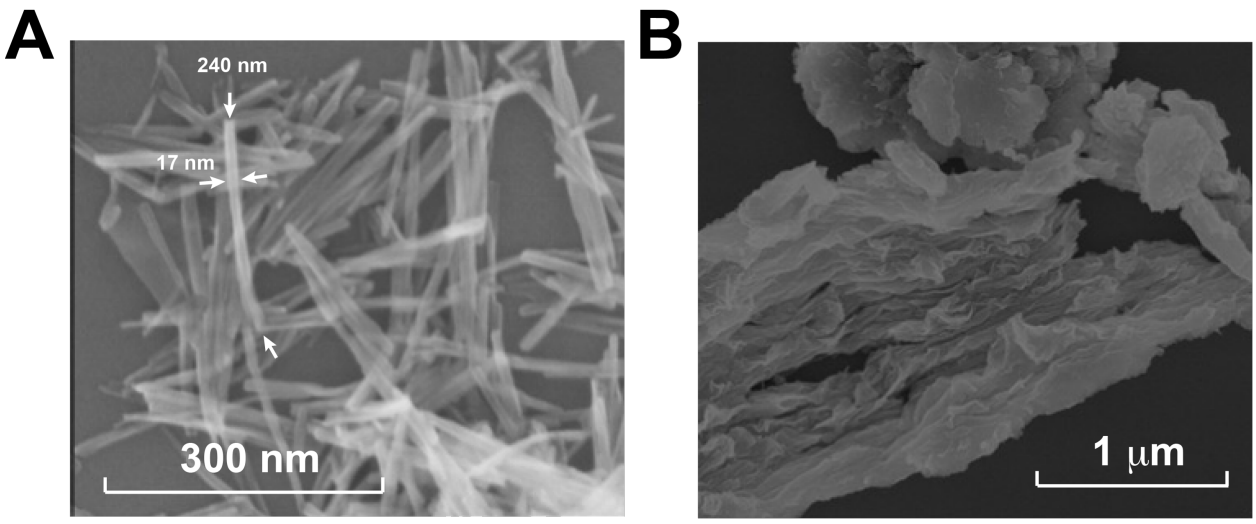

FIGURE 3.19. High-resolution SEM graphs of Co-BioMnO$_x$-II (A) and Co-monoclinic birnessite (B). The scale bar of Co-BioMnO$_x$-II is 300 nm and that of Co-monoclinic birnessite is 1 μm. The high-resolution SEM was taken in the Stanford Nano Shared Facilities (SNSF).

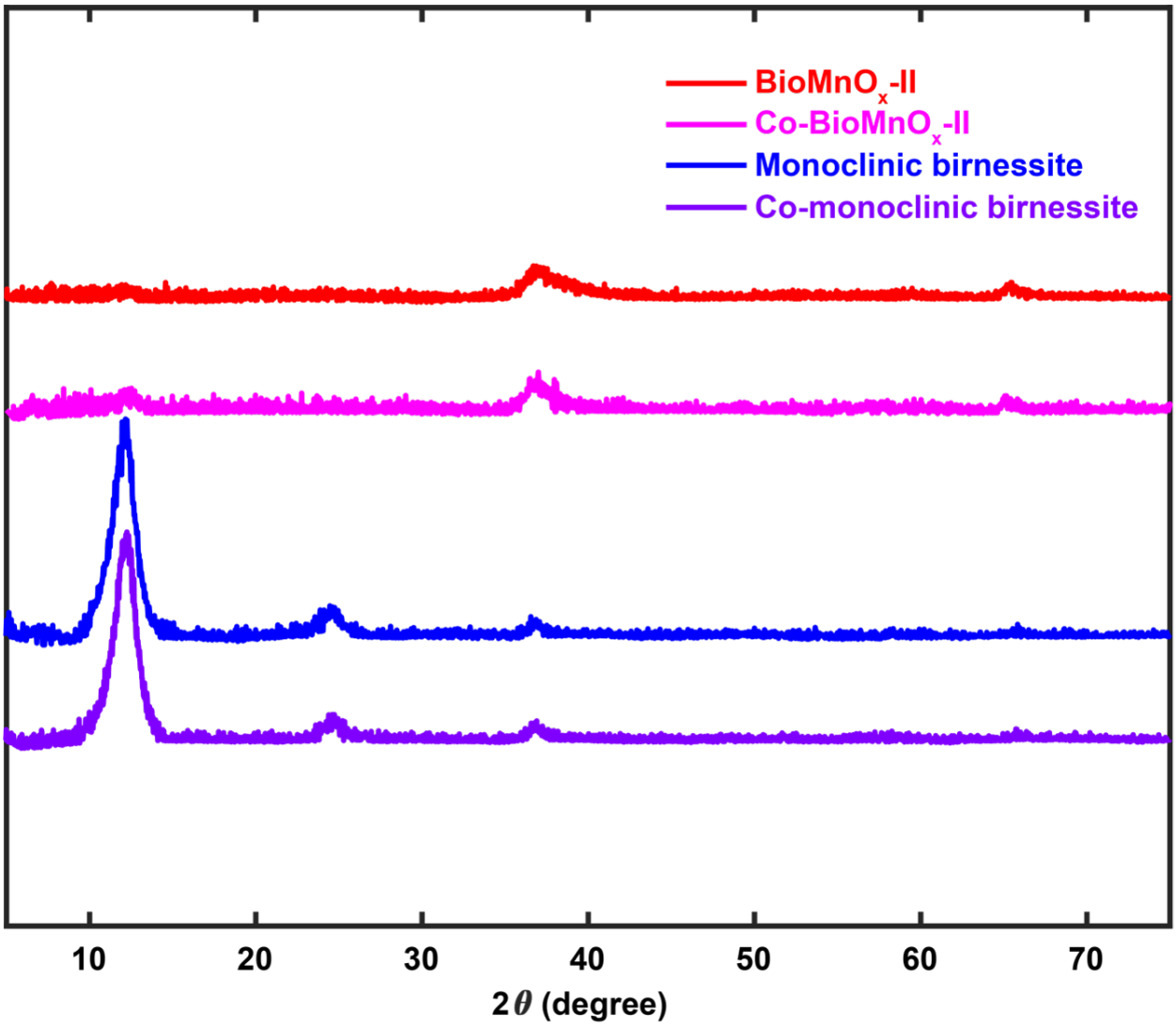

FIGURE 3.20. PXRD pattern of Co-BioMnO$_x$-II and Co-monoclinic birnessite in comparison with BioMnO$_x$-II and monoclinic birnessite.

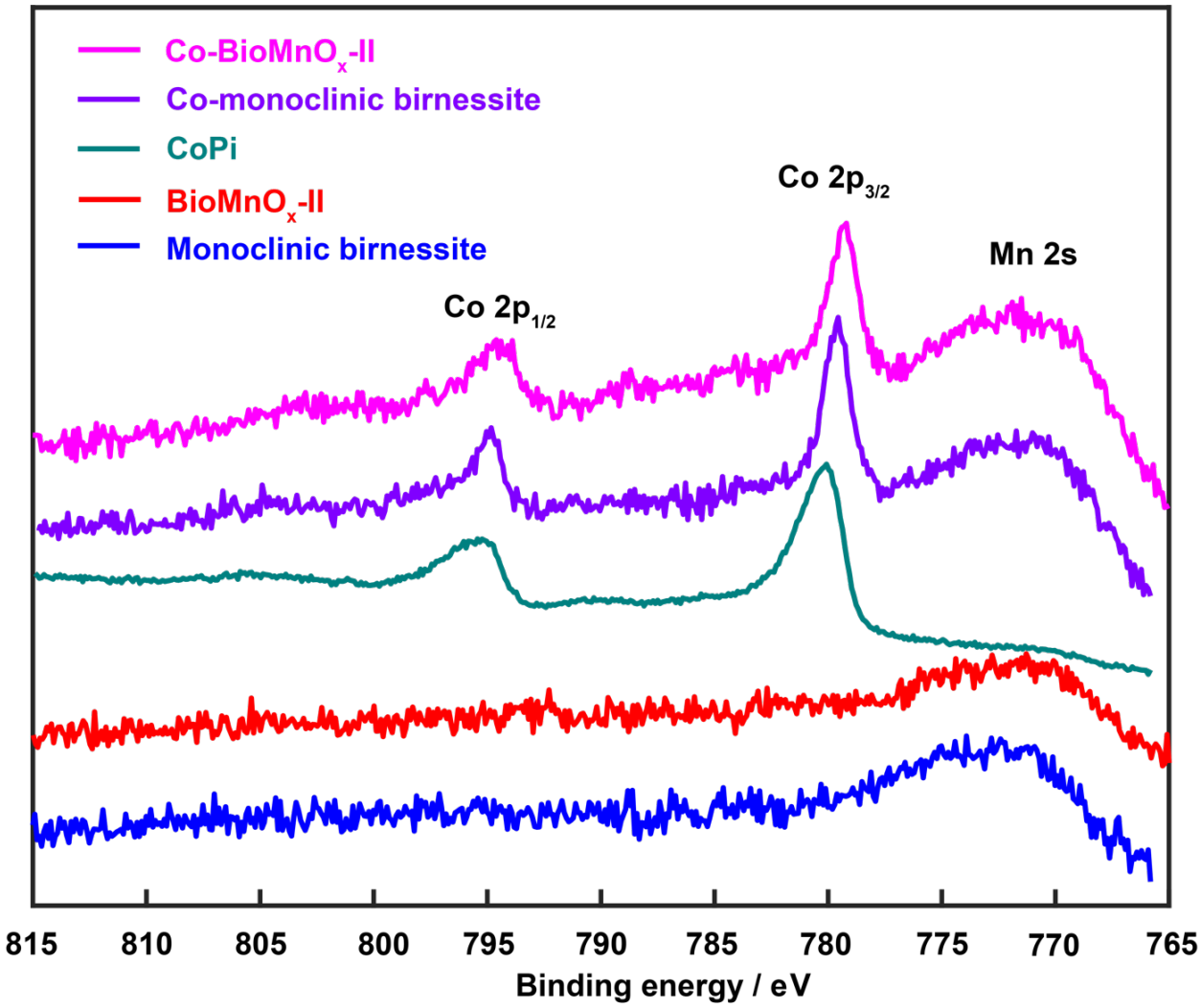

FIGURE 3.21. Co 2p XPS spectra of Co-BioMnO$_x$-II, Co-monoclinic birnessite, and CoPi.

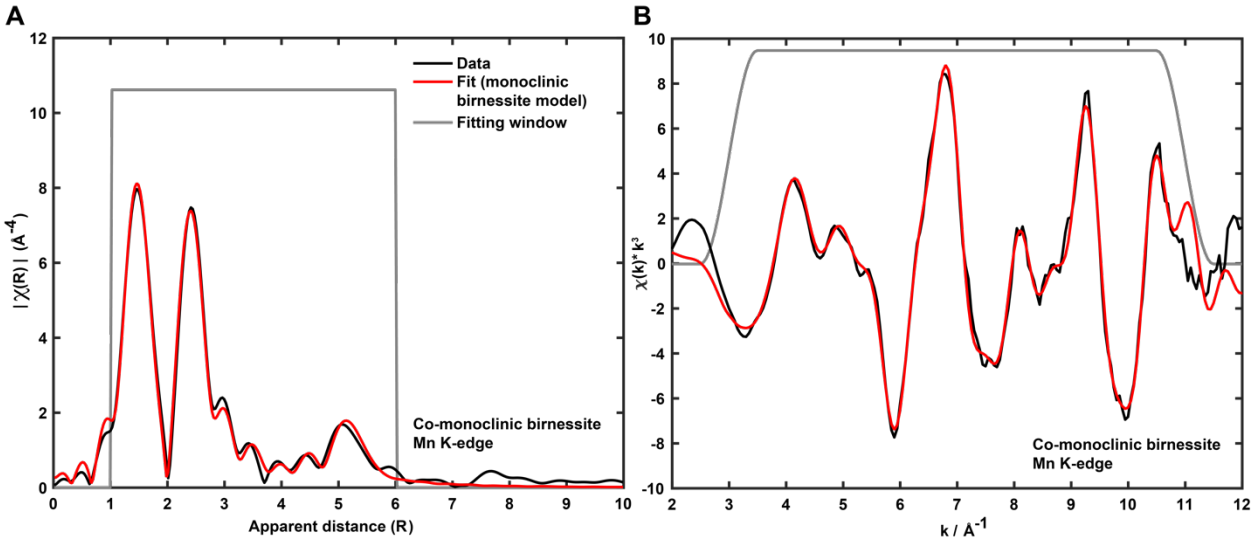

FIGURE 3.22. Mn K-edge curve fitting in R-space and k-space of Co-monoclinic birnessite with monoclinic birnessite model.

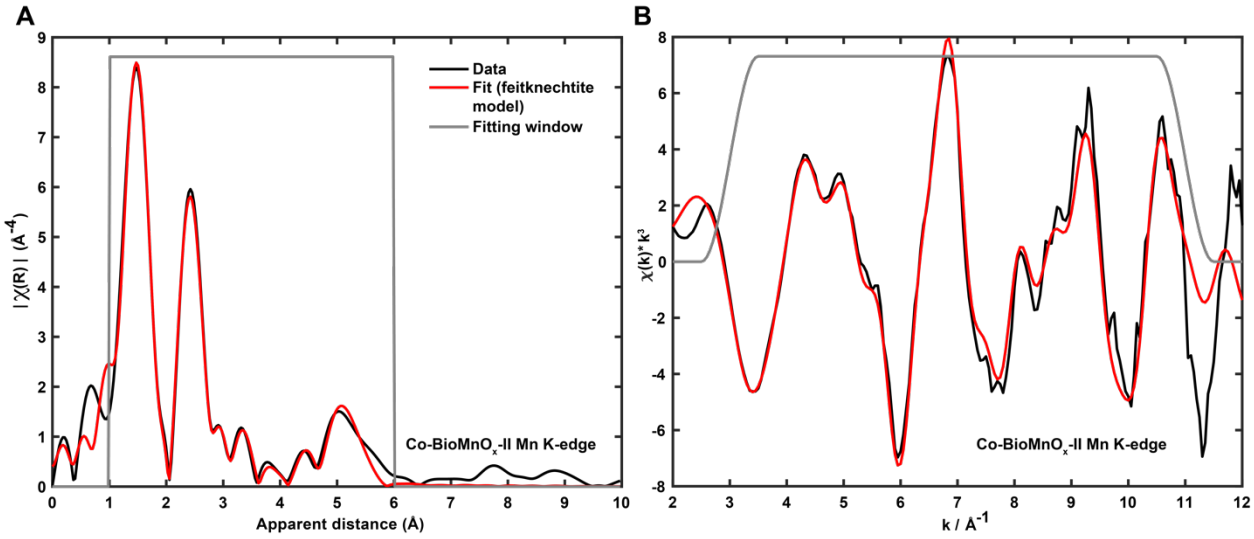

FIGURE 3.23. Mn K-edge curve fitting in R-space and k-space of Co-BioMnO$_x$-II with feitknechtite model.

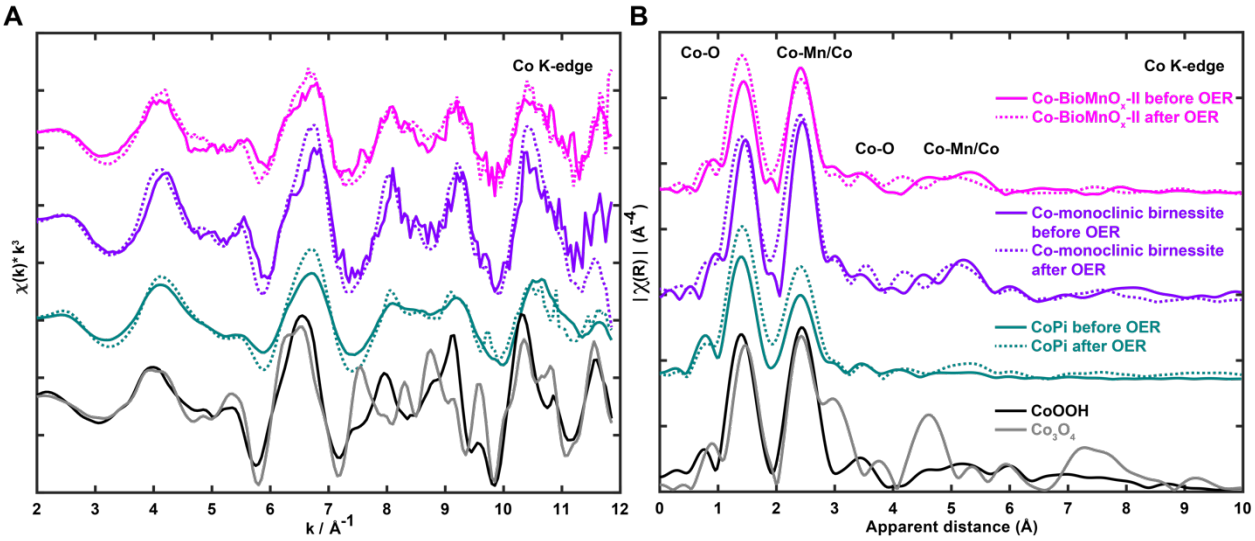

FIGURE 3.24. k^3-weighted EXAFS spectra (A) and Fourier transforms (B) of Co K-edge. All of the curves have been equally scaled down and translated for display purposes.

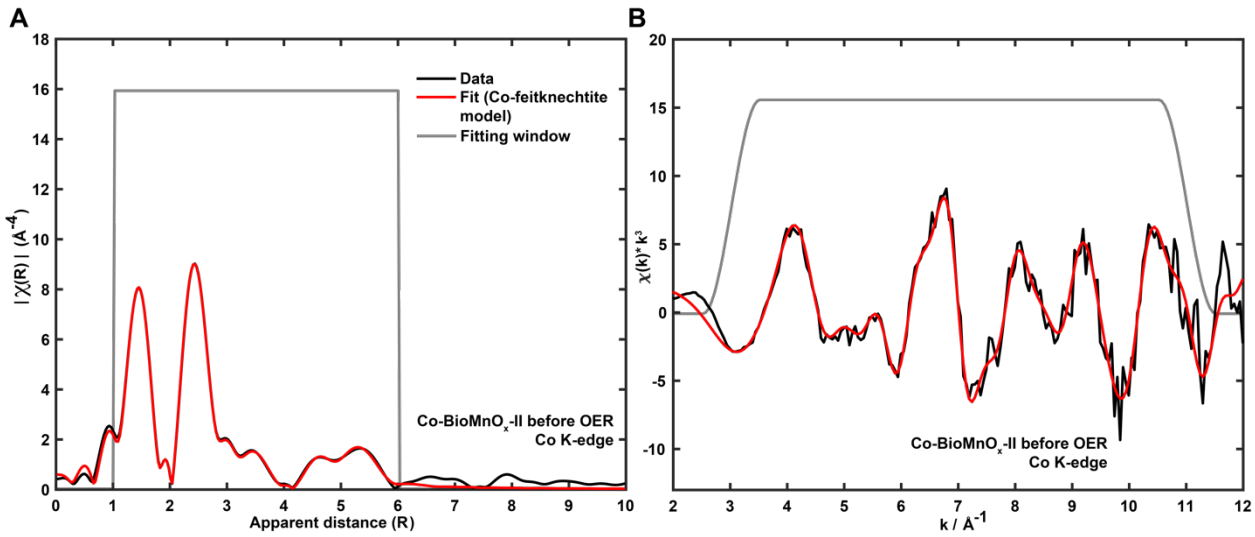

FIGURE 3.25. Co K-edge curve fitting in R-space and k-space of Co-BioMnO_x-II before OER with Co-feitknechtite model.

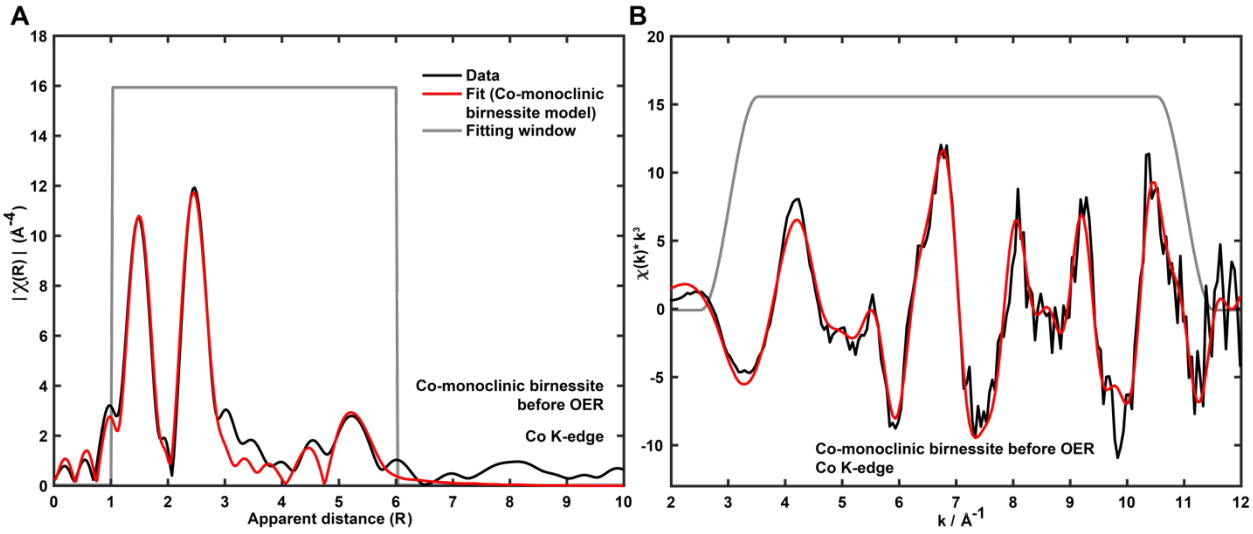

FIGURE 3.26. Co K-edge curve fitting in R-space and k-space of Co-monoclinic birnessite before OER with Co-monoclinic birnessite model.

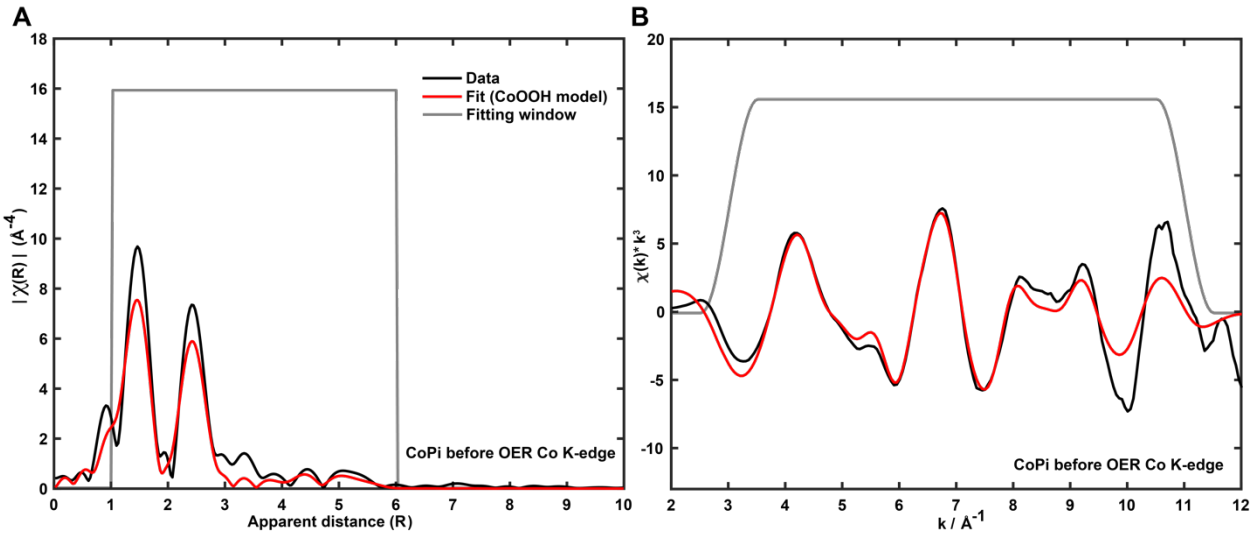

FIGURE 3.27. Co K-edge curve fitting in R-space and k-space of CoPi before OER with CoOOH model.

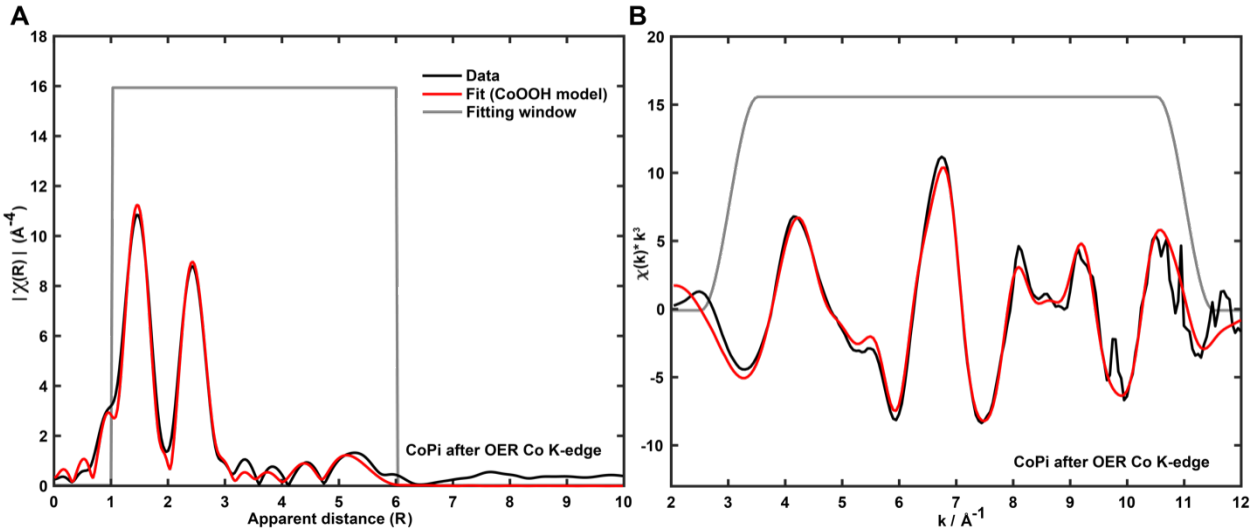

FIGURE 3.28. Co K-edge curve fitting in R-space and k-space of CoPi after OER with CoOOH model.

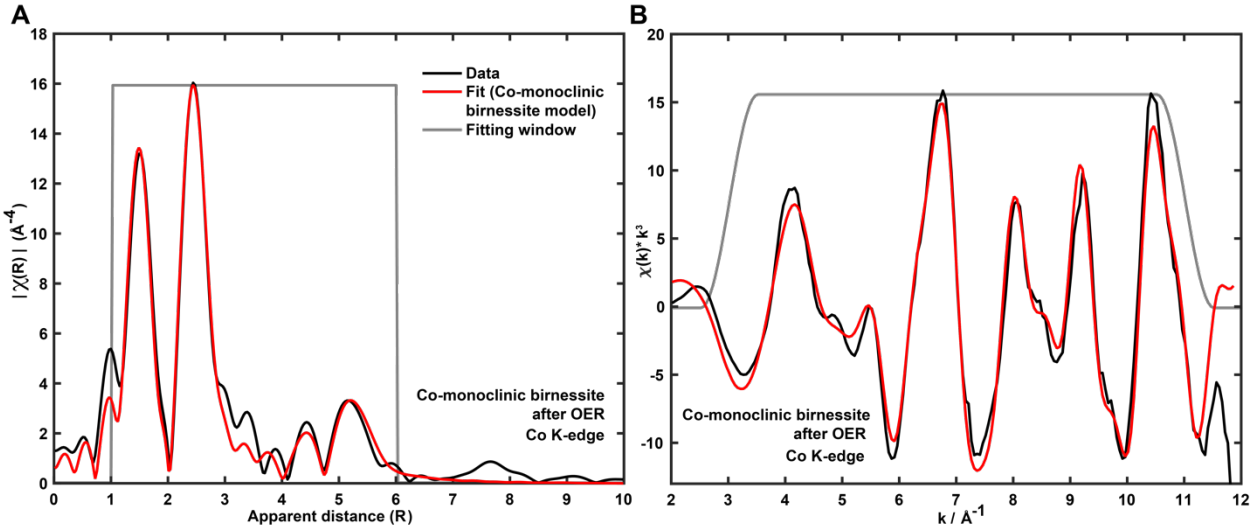

FIGURE 3.29. Co K-edge curve fitting in R-space and k-space of Co-monoclinic birnessite after OER with Co-monoclinic birnessite model.

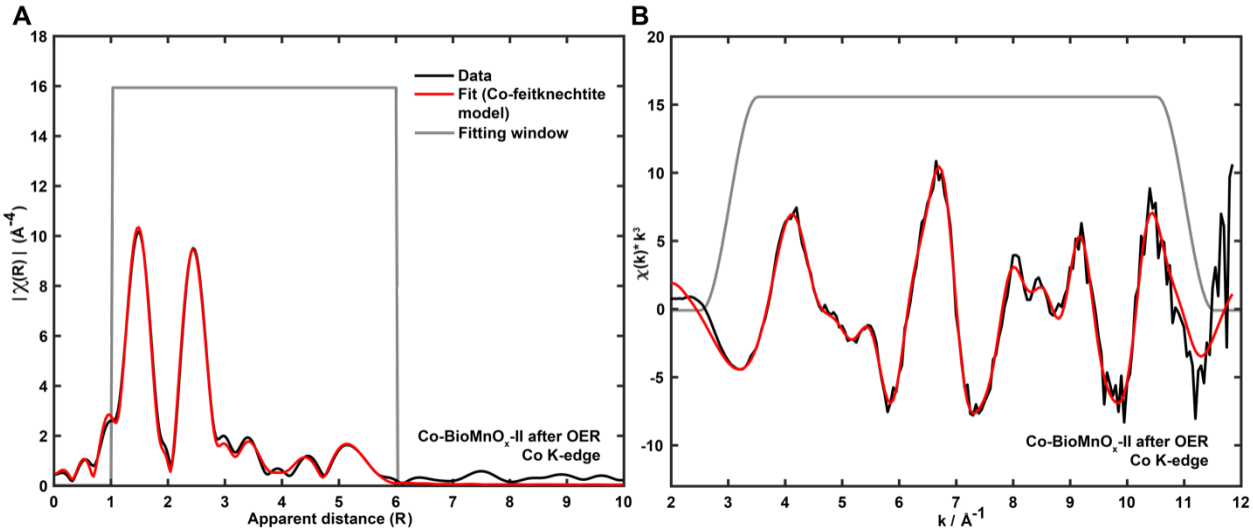

FIGURE 3.30. Co K-edge curve fitting in R-space and k-space Co-BioMnO$_x$-II after OER with Co-feitknechtite model.

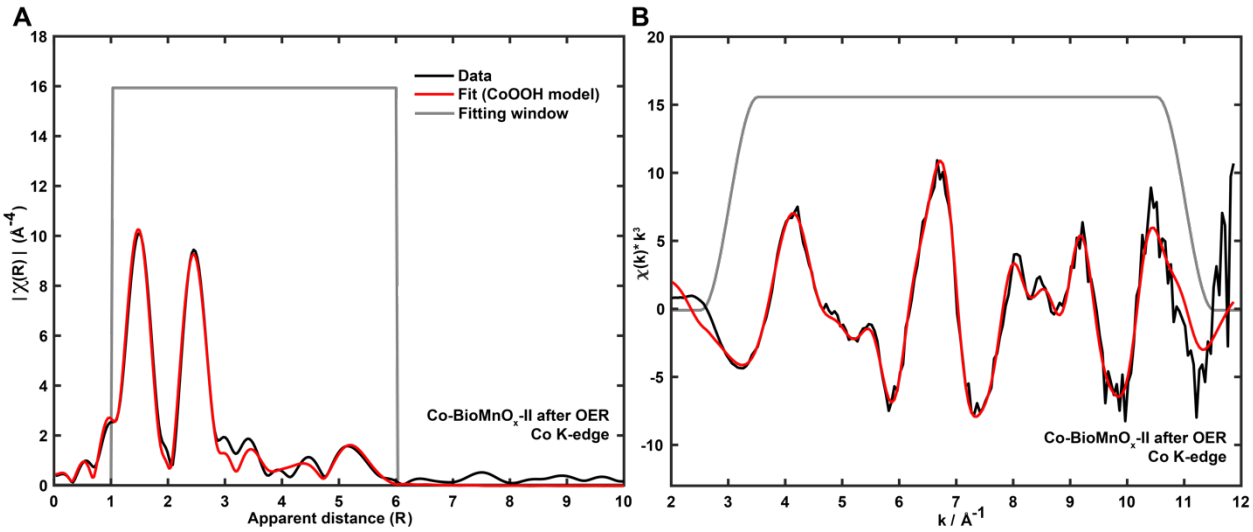

FIGURE 3.31. Co K-edge curve fitting in R-space and k-space of Co-BioMnO$_x$-II after OER with CoOOH model.

Mn oxides compounds	Energy shift $E - E_0$ (eV) in this study	Oxidation states calculated in this study	Oxidation states (energy shift) in previous study
Mn foil	0	0	0
MnO	5.21	2	2 (6 eV) [196], 2 (6.4 eV) [198]
Mn_2O_3	9.14	3	3 (9 eV) [196]
β-MnO_2	13.32	4	4 (14 eV) [196]
$KMnO_4$	18.40	7	-
Mn_3O_4	7.93	2.73	2.68-2.85 [187],2.66 [199], 2.68 [200]
δ-MnO_2	11.93	4.16	3.53-3.98 [201],4.02 [200], 3.7-3.9 [161]
Triclinic birnessite	9.93	3.45*	3.4-3.57 [182], 3.57 [161, 200]
Monoclinic birnessite	10.56	3.67	3.8 (12.6 eV) [196], 3.6-3.76 [202], 3.58-3.84 [203]
$BioMnO_x$-I	10.01	3.47	
$BioMnO_x$-II	10.48	3.64	3.32-3.62 [159], 3.9 [159], 3.85 [204], 3.9 [200]
$BioMnO_x$-III	10.36	3.60	
$BioMnO_x$-IV	10.21	3.55	

TABLE 3.1. Oxidation states of manganese in selected manganese oxides. Mn foil, MnO, Mn_2O_3, δ-MnO_2, and $KMnO_4$ are used for plotting the standard curve of oxidation states vs edge energy. *In this study, triclinic birnessite is synthesized as a mixture with feitknechtite, see Figure 2.12 for detailed information.

Sample	Path	R_{eff}(Å)	R(Å)	σ^2(Å^{-2})	N	ΔE_0 (eV)	R_f (%)	χ_ν^2
$BioMnO_x$-II (monoclinic birnessite model)	Mn-O	1.918	1.899 (0.0045)	0.0028 (0.0008)	4.28 (0.26)	4.952 (0.590)	1.285	59.05
	Mn-Mn	2.850	3.029 (0.0232)	0.0105 (0.0050)	**2**			
	Mn-Mn	2.954	2.861 (0.0072)	0.0062 (0.0012)	**4**			
	Mn-Mn (MS)	5.907	5.771 (0.0192)	0.0104 (0.0022)	**8**			
$BioMnO_x$-II (triclinic birnessite model)	Mn-O	1.935	1.899 (0.0042)	0.0026 (0.0007)	4.27 (0.25)	9.864 (0.547)	1.028	55.37
	Mn-Mn	2.848	3.013 (0.0289)	0.0135 (0.0074)	**2**			
	Mn-Mn	2.953	2.858 (0.0084)	0.0067 (0.0012)	**4**			
	Mn-Mn	5.174	5.343 (0.0258)	0.0062 (0.0032)	**4**			
	Mn-Mn (MS)	5.697	5.765 (0.0172)	0.0039 (0.0019)	**4**			
$BioMnO_x$-II (feitknechtite model)	Mn-O	1.916	1.901 (0.0062)	0.0023 (0.0004)	**4**	-2.438 (1.210)	0.073	22.21
	Mn-O	2.254	2.269 (0.0772)	0.0330 (0.0137)	**2**			

	Mn-Mn	2.891	2.882 (0.0129)	0.0059 (0.0009)	**4***			
	Mn-Mn	3.175	3.083 (0.0237)	0.0068 (0.0028)	**2***			
	Mn-O	3.666	3.788 (0.0712)	0.0223 (0.0155)	**4**			
	Mn-O	3.963	4.256 (0.0616)	0.0121 (0.0115)	**4**			
	Mn-O	4.515	4.641 (0.0682)	0.0089 (0.0089)	**4**			
	Mn-Mn	5.176	5.000 (0.0362)	0.0109 (0.0043)	**4**			
	Mn-Mn	5.640	5.567 (0.0804)	0.0152 (0.0120)	**6**			
	Mn-Mn (MS)	5.781	5.833 (0.0621)	0.0115 (0.0085)	**4**			
	Mn-Mn	6.233	6.350 (0.0772)	0.0109 (0.0097)	**4**			
Monoclinic birnessite (monoclinic birnessite model)	Mn-O	1.918	1.889 (0.0030)	0.0016 (0.0004)	**4**	-0.192 (0.521)	0.165	28.82
	Mn-O	1.968	1.732 (0.0093)	0.0126 (0.0025)	**2**			
	Mn-Mn	2.850	2.843 (0.0039)	0.0015 (0.0004)	**2**			
	Mn-Mn	2.954	2.806 (0.0170)	0.0202 (0.0019)	**4**			

Mn-Na	3.861	3.763	0.0065	**4**
		(0.0162)	(0.0018)	
Mn-Na	4.068	4.000	0.0068	**4**
		(0.0189)	(0.0021)	
Mn-Mn	5.174	5.256	0.0056	**8**
		(0.0093)	(0.0015)	
Mn-Mn (MS)	5.907	5.708	0.0067	**4**
		(0.0145)	(0.0008)	

TABLE 3.2. EXAFS fitting parameter values of the Mn K-edge spectra for $BioMnO_x$-II, monoclinic birnessite. *The coordination numbers of these two paths of the feitknechtite model are reversed compared to the FEFF calculation to give the best fit.

Catalysts	Monoclinic birnessite	Feitknechtite	Triclinic birnessite	Other components				
				Manganite	Groutite	MnO	Mn_3O_4	Mn_2O_3
$BioMnO_x$-I	54.9%	4.2%	3.9%	-	-	11.3%	21.4%	-
$BioMnO_x$-II	75.1%	12.8%	12.1%	-	-	-	-	-
$BioMnO_x$-III	42.4%	23.5%	22.4%	-	-	-	-	11%
$BioMnO_x$-IV	-	-	-	67.3%	32.7%	-	-	-
Co-$BioMnO_x$-II	49.2%	24.7%	23.3%	-	-	-	-	3.7%
Co-monoclinic birnessite	74.2%	12.9%	12.6%	-	-	-	-	-

TABLE 3.3. Summary of Mn K-edge XANES LCF component percentage values.

Mn oxides compounds	Energy shift $E - E_0$ (eV) in this study	Oxidation states calculated in this study	Oxidation states (energy shift) in previous study
Monoclinic birnessite	10.56	3.67	3.8 (12.6 eV) [196], 3.6-3.76 [202], 3.58-3.84 [203]
$BioMnO_x$-I	10.01	3.47	
$BioMnO_x$-II	10.48	3.64	3.32-3.62 [159], 3.9 [159], 3.85 [204], 3.9 [200]
$BioMnO_x$-III	10.36	3.60	
$BioMnO_x$-IV	10.21	3.55	
Co-$BioMnO_x$-II	10.22	3.55	
Co-monoclinic birnessite	10.41	3.62	3.48-3.77 [156], 3.65-3.71 [205]

TABLE 3.4. Table 3.1 extension. Oxidation states of manganese in selected manganese oxides and Co-doped manganese oxides.

Sample	Path	R_{eff}(Å)	R(Å)	σ^2(Å^{-2})	N	ΔE_0 (eV)	R_f (%)	χ_ν^2
	Mn-O	1.916	1.901	0.0041	4	-1.647	0.373	55.95
			(0.0004)	(0.0004)		(0.855)		
	Mn-O	2.254	2.274	0.0268	**2**			
BioMnO$_x$-II			(0.0386)	(0.0065)				
(feitknechtite	Mn-	2.891	2.882	0.0071	**4***			
model)	Mn		(0.0085)	(0.0006)				
	Mn-	3.175	3.104	0.0072	**2***			
	Mn		(0.0136)	(0.0015)				
	Mn-O	3.666	3.750	0.0145	**4**			
			(0.0404)	(0.0062)				
	Mn-O	3.963	4.180	0.0261	**4**			
			(0.0842)	(0.0172)				
	Mn-	5.176	4.952	0.0195	**4**			
	Mn		(0.0458)	(0.0067)				
	Mn-	5.640	5.542	0.0089	**6**			
	Mn		(0.0231)	(0.0033)				
	Mn-	5.781	5.791	0.0170	**4**			
	Mn		(0.0507)	(0.0095)				
	(MS)							
	Mn-O	1.918	1.886	0.0031	**4**	-6.303	0.511	135.96
			(0.0061)	(0.0004)		(1.353)		
	Mn-O	1.968	2.259	0.0222	**2**			
Monoclinic birnessite			(0.0484)	(0.0067)				
(monoclinic birnessite	Mn-	2.850	3.160	0.0180	**2**			
model)	Mn		(0.0528)	(0.0065)				

Mn-	2.954	2.848	0.0060	**4**
Mn		(0.0067)	(0.0006)	
Mn-Na	3.861	3.753	0.0027	**4**
		(0.0199)	(0.0018)	
Mn-Na	4.068	3.971	0.0039	**4**
		(0.0264)	(0.0022)	
Mn-	5.174	5.275	0.0087	**8**
Mn		(0.0363)	(0.0034)	
Mn-	5.907	5.718	0.0073	**4**
Mn		(0.0201)	(0.0012)	
(MS)				

TABLE 3.5. Extension of Table 3.2. Fitting parameter values of the Mn K-edge spectra for Co-BioMnO_x-II, Co-monoclinic birnessite. *The coordination numbers of these two paths of the feitknechtite model are reversed compared to the FEFF calculation to give the best fit.

Sample	Path	R_{eff}(Å)	R(Å)	σ^2(Å^{-2})	N	ΔE_0 (eV)	R_f (%)	χ_ν^2
Co-monoclinic birnessite before OER (Co-monoclinic birnessite model)	Co-O	1.918	1.916 (0.0079)	0.0030 (0.0015)	5.16 (0.62)	1.993 (0.936)	2.733	35.36
	Co-Mn	2.850	2.840 (0.0081)	0.0049 (0.0016)	5.60 (1.00)			
	Co-Mn	4.997	4.899 (0.0610)	0.0098 (0.0079)	**4**			
	Co-Mn (MS)	5.907	5.760 (0.0199)	0.0050 (0.0020)	**8**			
Co-monoclinic birnessite after OER (Co-monoclinic birnessite model)	Co-O	1.918	1.912 (0.0066)	0.0025 (0.0013)	6.14 (0.69)	-0.339 (0.878)	1.994	408.34
	Co-Mn	2.850	2.841 (0.0065)	0.0034 (0.0012)	6.30 (0.93)			
	Co-Mn	4.997	4.907 (0.0424)	0.0063 (0.0051)	**4**			
	Co-Mn (MS)	5.907	5.774 (0.0178)	0.0040 (0.0017)	**8**			
CoPi before OER (CoOOH model)	Co-O	1.897	1.899 (0.0105)	0.0076 (0.0008)	**6**	-1.731 (1.117)	2.619	2254.54
	Co-Co	2.851	2.818 (0.0132)	0.0117 (0.0012)	**6**			
	Co-Co	4.938	4.811 (0.0790)	0.0190 (0.0119)	**6**			
	Co-Co (MS)	5.702	5.753 (0.0743)	0.0226 (0.0106)	**12**			

CoPi after OER (CoOOH model)	Co-O	1.897	1.898 (0.0052)	0.0037 (0.0004)	**6**	-2.304 (0.682)	1.301	212.13
	Co-Co	2.851	2.825 (0.0063)	0.0082 (0.0006)	**6**			
	Co-O	3.813	3.922 (0.0740)	0.0278 (0.0164)	**6**			
	Co-Co	4.938	4.867 (0.0474)	0.0161 (0.0067)	**6**			
	Co-Co (MS)	5.702	5.750 (0.0255)	0.0145 (0.0031)	**12**			
Co-BioMnO$_x$-II before OER (Co-feitknechtite model)	Co-O	1.916	1.902 (0.0037)	0.0038 (0.0002)	**4**	-7.764 (0.592)	0.064	3.75
	Co-O	2.254	2.540 (0.0158)	0.0065 (0.0017)	**2**			
	Co-Mn	2.891	2.815 (0.0038)	0.0046 (0.0002)	**4***			
	Co-Mn	3.175	3.107 (0.0648)	0.0276 (0.0074)	**2***			
	Co-O	3.666	3.787 (0.0121)	0.0025 (0.0014)	**4**			
	Co-O	3.963	4.049 (0.0157)	0.0032 (0.0018)	**4**			
	Co-O	4.515	4.521 (0.0315)	0.0103 (0.0047)	**4**			
	Co-Mn	5.176	5.314 (0.0140)	0.0050 (0.0013)	**4**			

	Co-Mn	5.781	5.718	0.0045	**4**			
	(MS)		(0.0111)	(0.0008)				
	Co-Mn	6.233	6.278	0.0064	**4**			
			(0.0213)	(0.0024)				
	Mn-O	1.916	1.908	0.0037	5.49	-4.514	0.255	17.19
			(0.0042)	(0.0006)	(0.26)	(0.644)		
Co-BioMnO$_x$-II after OER (Co-feitknechtite model)	Co-Mn	2.891	2.840	0.0046	**4***			
			(0.0040)	(0.0004)				
	Co-Mn	3.175	2.956	0.0243	**2***			
			(0.0471)	(0.0130)				
	Co-O	3.666	3.793	0.0031	**4**			
			(0.0184)	(0.0022)				
	Co-O	3.963	4.060	0.0047	**6***			
			(0.0193)	(0.0021)				
	Co-Mn	5.176	4.908	0.0100	**4**			
			(0.0226)	(0.0027)				
	Co-Mn	5.640	5.510	0.0125	**6**			
			(0.0392)	(0.0053)				
	Co-Mn	5.781	5.782	0.0082	**4**			
	(MS)		(0.0232)	(0.0028)				
	Co-O	1.897	1.908	0.0045	**6**	-2.787	1.339	44.15
Co-BioMnO$_x$-II after OER (CoOOH model)			(0.0051)	(0.0004)		(0.666)		
	Co-Co	2.851	2.831	0.0077	**6**			
			(0.0056)	(0.0005)				
	Co-O	3.813	3.989	0.0201	**6**			
			(0.0636)	(0.0114)				

Co-Co	4.938	4.876	0.0147	**6**
		(0.0394)	(0.0052)	
Co-Co	5.702	5.765	0.0124	**12**
(MS)		(0.0188)	(0.0021)	

TABLE 3.6. EXAFS fitting parameter values of the Co K-edge spectra for Co-BioMnO_x-II, Co-monoclinic birnessite and CoPi. *This path, which corresponds to the interlayer Co-O path, has a coordination number of 4 in the FEFF calculation but in this situation, 6 gives the best fit.

CHAPTER 4

First-row transition-metal inhibition of Mnx protein

4.1. Abstract

The manganese oxidase complex, Mnx, from Bacillus sp. PL-12 contains a multicopper oxidase (MCO) and oxidizes dissolved Mn(II) to form insoluble manganese oxide (MnO_2) mineral. Previous kinetic and spectroscopic analyses have shown that the enzyme's mechanism proceeds through an activation step that facilitates formation of a series of binuclear Mn complexes in the oxidation states II, III, and IV on the path to MnO_2 formation. We now demonstrate that the enzyme is inhibited by first-row transition metals in the order of the Irving-Williams series. Zn(II) strongly ($K_i \sim 1.5\ \mu M$) inhibits both activation and turnover steps, as well as the rate of Mn(II) binding. The combined Zn(II) and Mn(II) concentration dependence establishes that the inhibition is non-competitive. This result is supported by electron paramagnetic resonance (EPR) spectroscopy, which reveals unaltered Mnx-bound Mn(II) EPR signals, both mono- and binuclear, in the presence of Zn(II). We infer that inhibitory metals bind at a site separate from the substrate sites and block the conformation change required to activate the enzyme, a case of allosteric inhibition. The likely biological role of this inhibitory site is discussed in the context of Bacillus spore physiology. While Cu(II) inhibits Mnx strongly, in accord with the Irving-Williams series, it increases Mnx activation at low concentrations, suggesting that weakly bound Cu, in addition to the four canonical MCO-Cu, may support enzyme activity, perhaps as an electron-transfer agent.

The content in this chapter is in part reproduced from Journal of Inorganic Biochemistry, 224, 111547. doi: https://doi.org/10.1016/j.jinorgbio.2021.111547 [135]

4.2. Introduction

Manganese biomineralization by manganese-oxidizing microorganisms is the dominant route of manganese-oxide mineral deposition on Earth, and a key pathway of the global Mn cycle. Mn-oxidizing microorganisms oxidize Mn(II) either directly through multicopper oxidases or indirectly through peroxides, which was discussed in Section 1.4 The MCO enzyme family relies on at least four copper cofactors to couple oxidation of a wide variety of substrates, both organic and inorganic, at a type 1 copper center (T1-Cu) with reduction of O_2 to water at a trinuclear copper center. [117, 206] Mnx is a complex of MnxG, a large (138 kDa) multicopper oxidase, tightly bound to three copies each of small (12 kDa) accessory proteins, MnxE and MnxF. [131, 133] While MnxE and MnxF do not have close homologues, MnxG was found to be similar to the human ferroxidase ceruloplasmin. However, unlike ceruloplasmin, MnxG catalyzes two successive and energetically difficult one-electron oxidation steps, and produces MnO_2 biomineral as a final product, representing a new subclass of Mn(II)-mineralizing MCO enzymes. A proposed mechanism was illustrated in Section 1.6.

This MnxG catalyzes the oxidation of Mn(II) to Mn(III), which then disproportionate to Mn(IV)O_2 nanoparticulate and Mn(II). In the environment, further transformation and abiotic partial reduction of the resulting biogenic MnO_2 nanoparticulate product leads to a variety of Mn(III,IV) oxides [158,161,207,208,209,210,211,212] — highly reactive mineral phases that are capable of scavenging and oxidizing not only organics, but also many trace metals, including toxic metals. [159, 213, 214, 215, 216, 217] Indeed, numerous studies have explored how incubation of Mn-oxidizing bacteria with different metals affects the structure and composition of the biogenic manganese oxides product, [160, 210, 218, 219, 220, 221, 222,223,224,225] and technologies are being pursued to use bacterially produced manganese oxide to clean contaminated waters. [89,213,226,227,228,229,230,231] However, how the presence of other metals interferes with the enzymatic mechanism of Mn oxidation remained unknown in the absence of a purified enzyme from an Mn-oxidizing organism. Each step of the proposed Mnx enzymatic mechanism in Figure 1.2 can potentially be influenced by

other metals. Studies with whole cells have demonstrated that different metals can get incorporated into the MnO_2, [210, 218, 219, 220, 222, 223, 232] presumably by affecting condensation of the primary enzymatic product into the mineral structure. However, other metals could also bind directly to the enzyme, competing with Mn(II) for Mnx binding sites, or interfering with the Mn(II) oxidation by disrupting formation of hydroxo- and oxo-bridges, or slowing down the enzyme conformation change. In this study, we address the question of how first-row transition metals affect Mn(II) oxidation by Mnx. Zn(II) powerfully inhibits all stages of Mnx catalysis, and does so non-competitively, a conclusion supported by EPR spectroscopy, which shows that Zn(II) has no effect on the Mnx-bound Mn(II) signals. Thus, Zn(II) binds at an inhibitory site, separate from the substrate site. Other divalent metals inhibit the reaction according to the Irving-Williams order (Co(II) < Ni(II) < Cu(II) > Zn(II) [233, 234]). Cu(II), however, stimulates the enzyme at low concentrations, playing an additional role in catalysis. We propose a mechanism accounting for inhibition and offer hypotheses on the role of Zn(II) inhibition in the physiology of Mn-oxidizing Bacillus spores.

4.3. Results

4.3.1. Inhibition of Mnx reaction by Zn(II). MnO_2 production by Mnx was noticeably slowed by quite low (0.2 μM) concentrations of Zn(II), although the growth of the MnO_2 absorption band remained sigmoidal as the Zn(II) concentration increased (Figure 4.1).

The enzymatic traces are sigmoidal, a slow induction phase being followed by linear growth. They were fit with the activation equation (Equation 4.1) [235]:

$$[MnO_2] = V_{(s-s)}(x - x_0) - V_{(s-s)}/k_{cat}(1 - e^{(-k_{cat}(x-x_0))}) \tag{4.1}$$

To account for the observed x_0 and k_{act} dependences on Zn(II), a general mechanism of an activatable enzyme in the presence of an inhibitor can be invoked (Figure 4.2). [235]

In our case we assume that (1) conversion to the active Mnx conformation (Mnx* in green in Figure 1.2) is triggered by substrate binding only; (2) Zn(II) binding to activated Mnx is negligible; (3) binding of Zn(II) to Mnx is unaffected by the presence of Mn(II) (red boxes in Figure 1.2); and (4) Zn-bound Mnx is not activated by Mn(II) so that the activation rate constant in the presence of Zn(II) approaches zero ($k_{act}' \rightarrow 0$) with increasing Zn.

Fitting the lag time x_0 vs Zn(II) concentration and k_{act} vs Zn(II) concentration yields approximately the same K_i(Zn) with a value of $\sim$1.5 μM. Steady-state turnover of Mn(II) also shows a rapid decline with increasing Zn(II) concentration. Also, the Dixon plot with the reciprocals of the steady-state rate against Zn(II) concentration shows the straight line feature with an intersection point on the x-axis. Thus, the Zn(II) inhibition kinetics studies converge to a conclusion that Zn(II) is non-competitively inhibiting the Mnx reaction.

4.3.2. EPR characterization of Mn binding site in the Mnx. We tested the hypothesis that inhibition is due to Zn(II) competition for the Mn(II) binding sites on Mnx (similar to Zn(II) inhibition of Fe(II) oxidation in MCOs ceruloplasmin 213 and Fet3p 214) using EPR spectroscopy. Mnx-bound mononuclear and dinuclear Mn(II) EPR signals (designated as "class ii" and "class iii", respectively) were previously detected when Mn(II) is added to Mnx, the mixture likely reflecting weaker Mn(II) binding to a second site. [81] These signals should be suppressed if Zn(II) binds competitively with Mn(II), but the addition of Zn(II) had no effect on either signal, even after oxygen was added to the mixture to initiate the reaction. Thus, the EPR evidence strongly indicates noncompetitive binding of Zn(II) inhibitor.

The experiments above all indicate that Zn(II) does not compete with Mn(II) substrate binding sites, but binds to a separate site, hindering Mn(II) binding, enzyme activation step, and inhibiting Mn(II) oxidation. Zn(II) strongly inhibits the reaction, affecting each stage of the Mnx catalysis: Mn(II) binding, Mnx activation, and turnover. Our kinetic experiments, supported by EPR studies, demonstrate that Zn(II) does not compete with Mn(II) for binding at the substrate site (Figure 4.3). The inhibition constant for Zn(II),

~1.5 μM, does not vary with Mn(II) concentration, and is consistent with the data at each step of the enzymatic reaction. Analysis of turnover rates with the Dixon plot also confirms the noncompetitive nature of Zn(II) inhibition. We propose an allosteric mechanism, in which Zn(II) binding stabilizes Mnx in its inactive form. This binding thereby prevents the conformation change that otherwise triggers enzyme activation and couples the two Mnx-bound Mn(II) for efficient electron transfer. Without activation, the turnover of uncoupled Mn(II) species proceeds very slowly.

4.4. EPR characterization of Co(II) inhibition

4.4.1. Mnx inhibition by Co(II), Ni(II), and Cu(II). Inhibition of Mn-oxidation activity of Mnx by Co(II), Ni(II), and Cu(II) was also tested, at a single Mn(II) concentration of 50 μM and over a range of inhibiting metals concentrations. Previous studies with Mn(II)-oxidizing spore extract pointed to the possibility that Co(II) can be oxidized enzymatically by Mn-oxidizing organisms since Co(III) oxides were found to co-precipitate together with Mn oxides.215 However, we showed conclusively that Co(II) is not a substrate of Mn-oxidizing factor in Bacillus species, but is oxidized indirectly by the enzymatically generated, highly reactive MnO_2 nanoparticles. [236] Indeed, we confirmed here that incubating Co(II) with Mnx for a prolonged amount of time does not lead to any visible oxidative reaction, while in the presence of Mn(II), the addition of Co(II) modifies the colloidal MnO_2 with a broad feature around 600 nm (Figure 4.4), likely due to Co (III) oxides, or Co(III) incorporated within MnO_2 structure, as has been reported previously. [219, 220, 237, 238]

Extrapolations to the x-axis for the Dixon plots of Mnx inhibited by Zn(II), Ni(II), and Co(II) result in K_i values of 1.1 μM, 22 μM and 50 μM, indicating that Ni(II) and Co(II) are weaker Mnx inhibitors than Zn(II). For Cu(II), The rise and fall of k_{act} and $V_{s\text{-}s}$ implies that there are two Cu(II) binding sites. The second site is inhibitory, while the first is stimulatory. We considered the possibility that Zn(II) inhibition might be explained by its displacing Cu(II) at the stimulatory site. In that event, addition of Cu(II) to reverse such displacement should diminish Zn(II) inhibition. However, addition of Cu(II) at an

activating concentration of 0.5 μM had essentially no effect on the inhibition of Mnx by Zn(II) (Figure 4.5). Thus, the inhibitory site is clearly separate from the Cu(II)-activation site.

In addition to Zn(II), other essential divalent metals Co(II), Ni(II), and Cu(II) inhibit Mnx, with inhibition rate constants all in the micromolar range. The inhibition trend among these metals falls within Irving–Williams series, the pattern that describes competition of the metals for binding to amino acid residues on proteins. [233]

4.4.2. Investigation of the Co(II) inhibition mechanism using EPR spectroscopy.

With the conclusions drawn by the kinetic experiments, the mechanism of Co(II), Ni(II), and Zn(II) inhibition is investigated via EPR. Since the active sites of Mnx are copper, the addition of Cu(II) to the Mnx solution will create complexity to the EPR spectra. Due to this complexity, we put less emphasis on the Cu(II) inhibition.

As was mentioned above, EPR spectroscopy shows that Zn(II) addition could not modify the manganese binding sites (Figure 4.3), and thus we investigated whether Cu binding sites can be affected by the addition of Co(II), Ni(II) and Zn(II). Multicopper oxidases consist of three types of copper sites: type 1 (T1) or blue copper sites (coordinated in a trigonal pyramidal geometry with one cysteine and two histidine), type 2 (T2) or normal copper sites (square planar geometry, normally bound to histidine residues and hydroxo ligands), and type 3 (T3) copper sites (dinuclear copper sites bridged by a hydroxide in the resting state).176 The EPR signals of different copper sites in the Mnx have been separated and identified. [128] There are two distinct T2Cu sites, T2Cu-A and T2Cu-B with g = [2.055 2.055 2.320], ^{63}Cu A = [54 54 510] MHz corresponding to T2Cu-A and g = [2.046 2.046 2.210], ^{63}Cu A = [54 54 615] MHz corresponding to T2Cu-B, known to be located in the MnxEF hexamer. T1Cu signal obtains a g = [2.050 2.065 2.305] and ^{63}Cu A = [45 45 210] MHz. The ratio of T2Cu-A, T2Cu-B, and T1Cu is determined as 2:3:1. Due to the spin superexchange of the dinuclear Cu, T3Cu is EPR silent. The simulation of the Mnx is

illustrated in Figure 4.6. T2Cu-A was shown to locate in MnxEF while T2Cu-B and T1Cu are located in the MnxG subunit. [128]

The addition of Co(II), Ni(II), or Zn(II) selectively reduces the signal of the T2Cu-A in the MnxG subunit (Figure 4.7). However, no direct evidence shows that the metal ions are replacing the T2Cu-A. Quantitatively, by integrating the area of the absorption EPR spectrum, Zn(II) removes the least amount of T2Cu-A while Co(II) removes the most. Q-band EPR spectrum of Mnx with Co^{2+} addition confirms the absence of T2Cu-A (Figure 4.8). The T1Cu signal is also exposed, which confirmed the T1Cu assignment and simulation by Tao, et al. (2017). [128]

We then examined the UV-vis spectrum of Mnx protein with the addition of Co(II). The addition of Co(II) to Mnx without the substrate Mn(II) generates a broad feature around 500 nm and 600 nm and the peak increases linearly with the concentration of Co(II) added (Figure 4.9). Because Co(II) cannot be oxidized by Mnx alone and the subtraction of Mnx + Co(II) spectra cancels out the contribution from T1Cu, instead of Co(III) signal, the broad feature at 500 nm and 600 nm is likely to be the Mnx-bound Co(II).

The addition of Co^{2+} results in the increase in the characteristic low field Co^{2+} EPR signal and the peak-to-peak intensity increases linearly (Figure 4.10). Because Co(II) adopts a d^7 electronic configuration and in this case Co(II) is most likely bound to H_2O or N-residues on the Mnx, which are weak field ligands, Co(II) has a high spin S = 3/2. The broad peak at $g_{eff} \approx 5$ ($B_0 \approx 150$ mT) is characteristic of the Co^{2+} aqua complex and the broad feature is due to the nuclear spin I = 7/2 of Co. [25] However, no clear evidence from EPR shows that Co^{2+} is bound to Mnx.

Since the T2Cu-A, located in the MnxG catalytic subunit, was removed by the addition of Co^{2+}, we were then curious about how this affects the Mn oxidation. With the nearly complete elimination of T2Cu-A in MnxG with Co^{2+}, the MnxG is still turning over the Mn oxidation within 2 minutes (Figure 4.11A). Notably, there is a T2Cu-A recovery at the end of Mn oxidation from around 5 mins to 10 mins (Figure 4.11B). One hypothesis to explain

this peak is that the T2Cu-A released from the Cu binding site is forming a Cu-HEPES complex that may have a peak at the same position. However, even though the broadness of T2Cu-B peak and the peak at ∼288 mT indicate that Cu-HEPES complex is formed, the T2Cu-A peak does not correspond to the Cu-HEPES. The effect of buffer exchange is also explored. Buffer exchange (BE) refers to performing five washes with the protein storage buffer (20 mM HEPES, 20 mM NaCl, 20% EG, pH 7.8) in order to remove any free and unbound ions. Even though the buffer exchange decreases both the T2Cu-A and T2Cu-B signals, after buffer exchange, the T2Cu-A signal appears more evidently (Figure 4.12).

The evidence of the appearance of the peak at 265 mT infers that T2Cu-A is recovered upon Mn oxidation, even though the second peak at ∼280 mT is not evident. The recovery of T2Cu-A peak is more evident after buffer exchange probably due to the removal of extra Co^{2+} (Figure 4.13). Note that buffer exchange alone does not induce the recovery of the T2Cu-A peak. One hypothesis is that Mn oxidation at low Co^{2+} concentration may trigger the rearrangement of the Cu(II) in the MnxG to optimize the Mn oxidation process. Because T2Cu-B is reduced upon buffer exchange, some Cu^{2+} may still bind to MnxEFG non-specifically and these Cu^{2+} can be rearranged to bind in the T2Cu-A site to facilitate the electron transfer and Mn oxidation.

In addition, the Co^{2+} signal is reduced as the Mn oxidation proceeds, which is another evidence of the oxidation of Co^{2+} by the nascent MnO_2. The slight downfield shift of Co peak upon the addition of Mn^{2+} is possibly due to the binding of Co^{2+} to MnxG (Figure 4.13).

4.4.3. Comments on the future direction. We have initially explored the Co^{2+} inhibition of MnxEFG and found that Co^{2+}, Ni^{2+} and Zn^{2+} can specifically remove T2Cu-A in MnxG in order of strongest to weakest. This is seemingly contradictory to the kinetic study where Zn^{2+} is found to be the strongest inhibitor of the series. A closer look at the Co2+ inhibition mechanism may involve:

1.quantifying the Cu^{2+} in the MnxEFG after buffer exchange to check if there are two binding sites as proposed in Tao et. al. (2017) and to further understand the role of T2Cu-A. [128]

2. looking for an alternative buffer system that does not form precipitate with Cu^{2+}. In addition, we also explored the effect of Co2+ on MnxEFG with the Mn oxidation and found that T2Cu-A might be recovered from the removal by Co^{2+}.

Thus some future directions may involve:

1.Measuring the Mn oxidation reaction rate with Co^{2+} and comparing with that without Co^{2+} to confirm the non-competitive inhibition proposed by kinetics studies.

2.Measuring the high-frequency EPR spectra to further separate the T2Cu-A from other Cu signals, which will be a direct evidence of whether the recovered signal is T2Cu-A or other Cu complexes.

3.Optimizing the EPR conditions to examine the hyperfine and any g value shift in order to capture any Mnx-bound Co^{2+} signals. The further exploration of the Co^{2+} effect on MnxEFG helps extend our knowledge of MnxG and multicopper oxidase and the mechanism of Mn oxidation by MnxG.

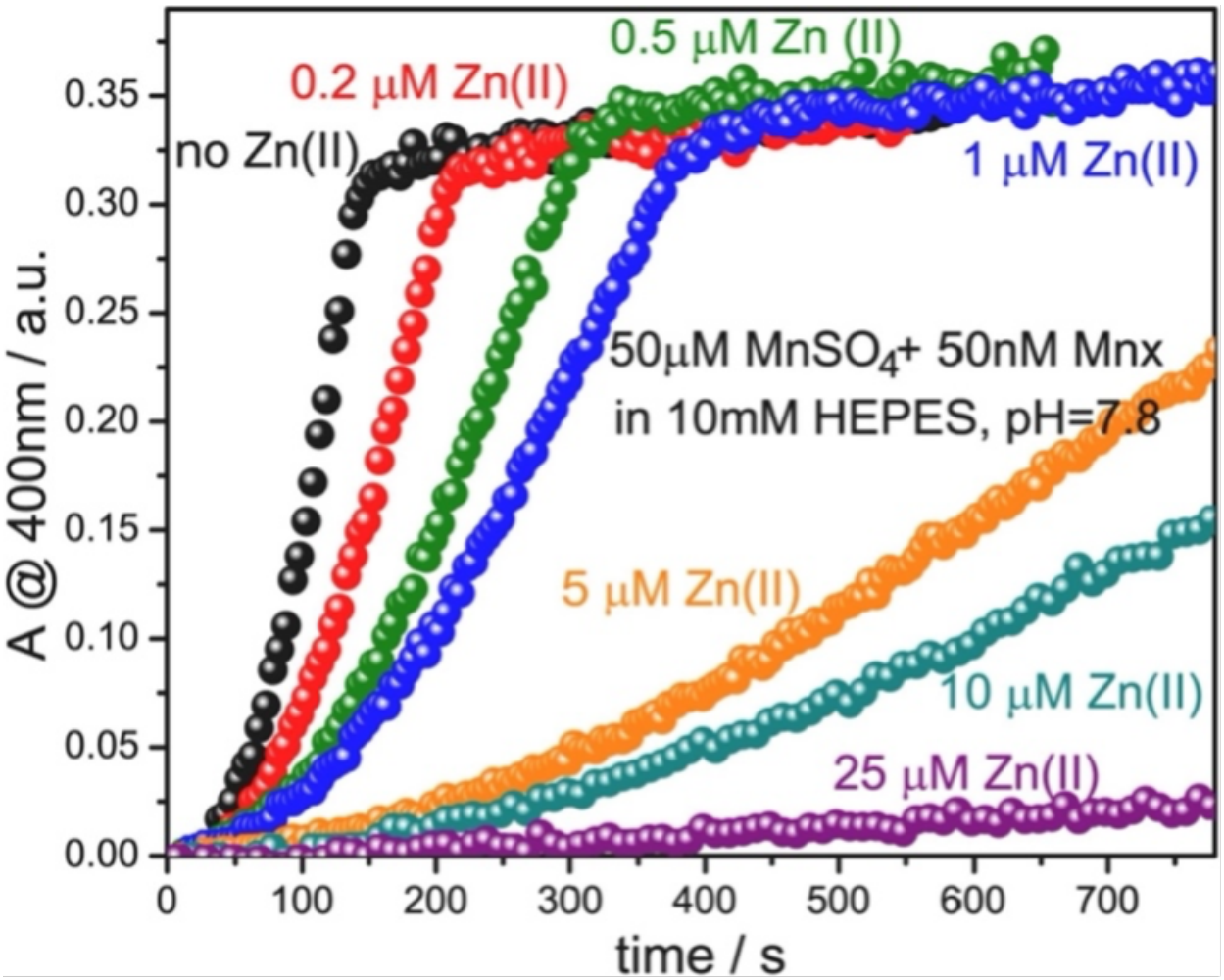

FIGURE 4.1. Progress curves taken at 400 nm during Mnx-catalyzed oxidation of 50 μM $MnSO_4$ in the presence of indicated concentrations of Zn(II), in 10 mM HEPES, pH 7.8.

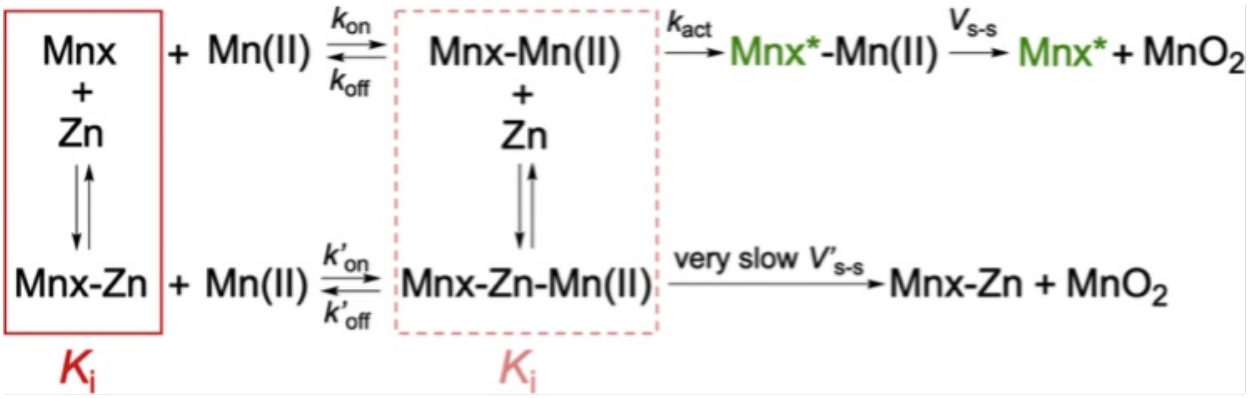

FIGURE 4.2. Kinetic mechanism of Zn inhibition.

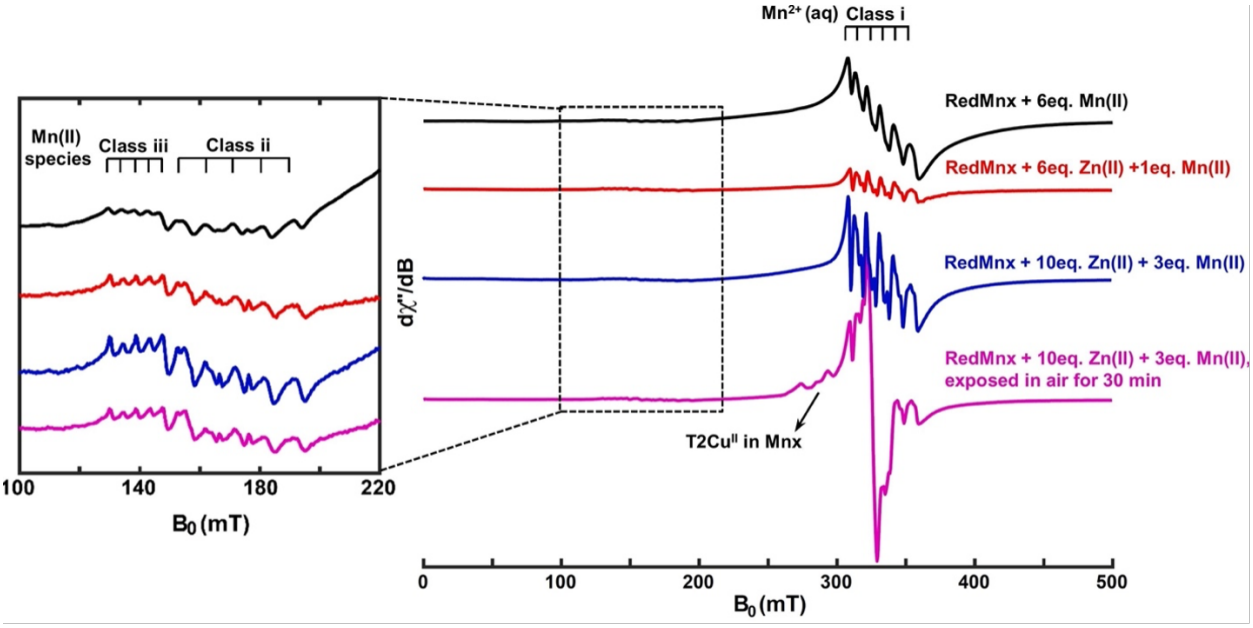

FIGURE 4.3. X-band CW EPR spectra of Mnx with Zn(II).

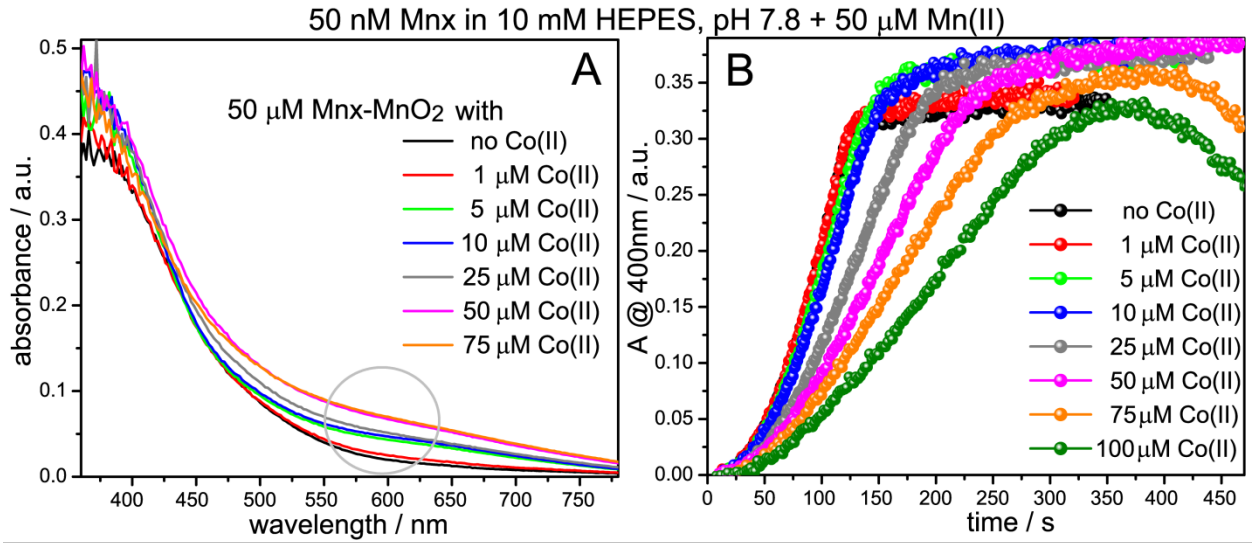

FIGURE 4.4. UV-vis spectra of Mnx with Co(II). (A) MnO_2 final spectrum obtained in the presence of different amount of Co(II), added as $CoCl_2$ to inhibit oxidation of 50 μM $MnSO_4$ by 50nM Mnx in HEPES buffer, pH 7.8. Addition of Co(II) results in modification of colloidal MnO_2, manifested as a broad feature around 600 nm. (B) Progress curves taken at 400 nm during Mnx-catalyzed oxidation of 50 μM $MnSO_4$4 in the presence of indicated amount of Co(II). With 75 μM and 100 μM Co(II), the manganese oxide product precipitated.

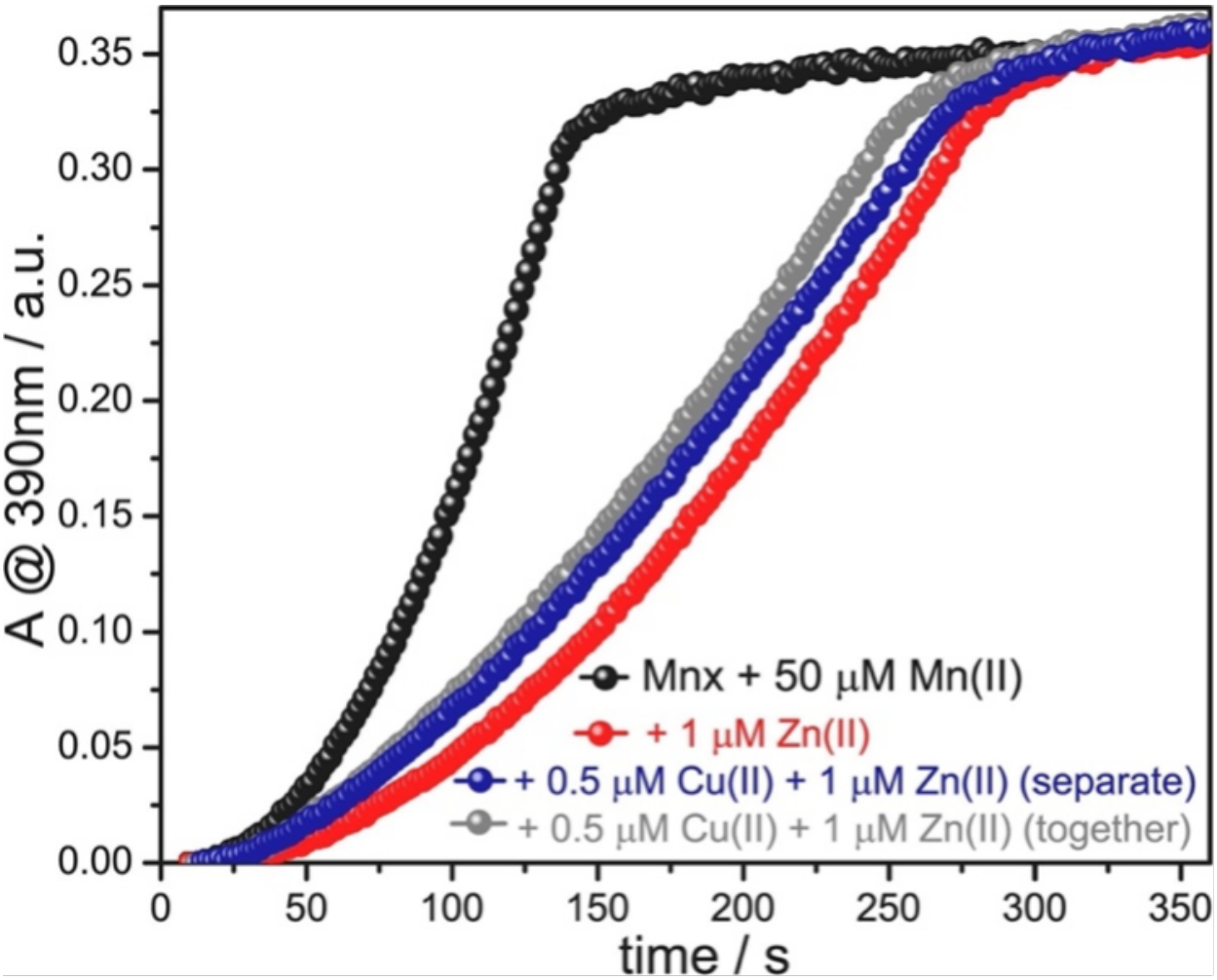

FIGURE 4.5. Progress curves of MnO_2 product formation taken at 390 nm during oxidation of 50 μM $MnSO_4$ by 50 nM Mnx in 10 mM HEPES at pH 7.8, in the presence of 1 μM $ZnSO_4$ and 0.5 μM $CuSO_4$, added separately or together, as indicated.

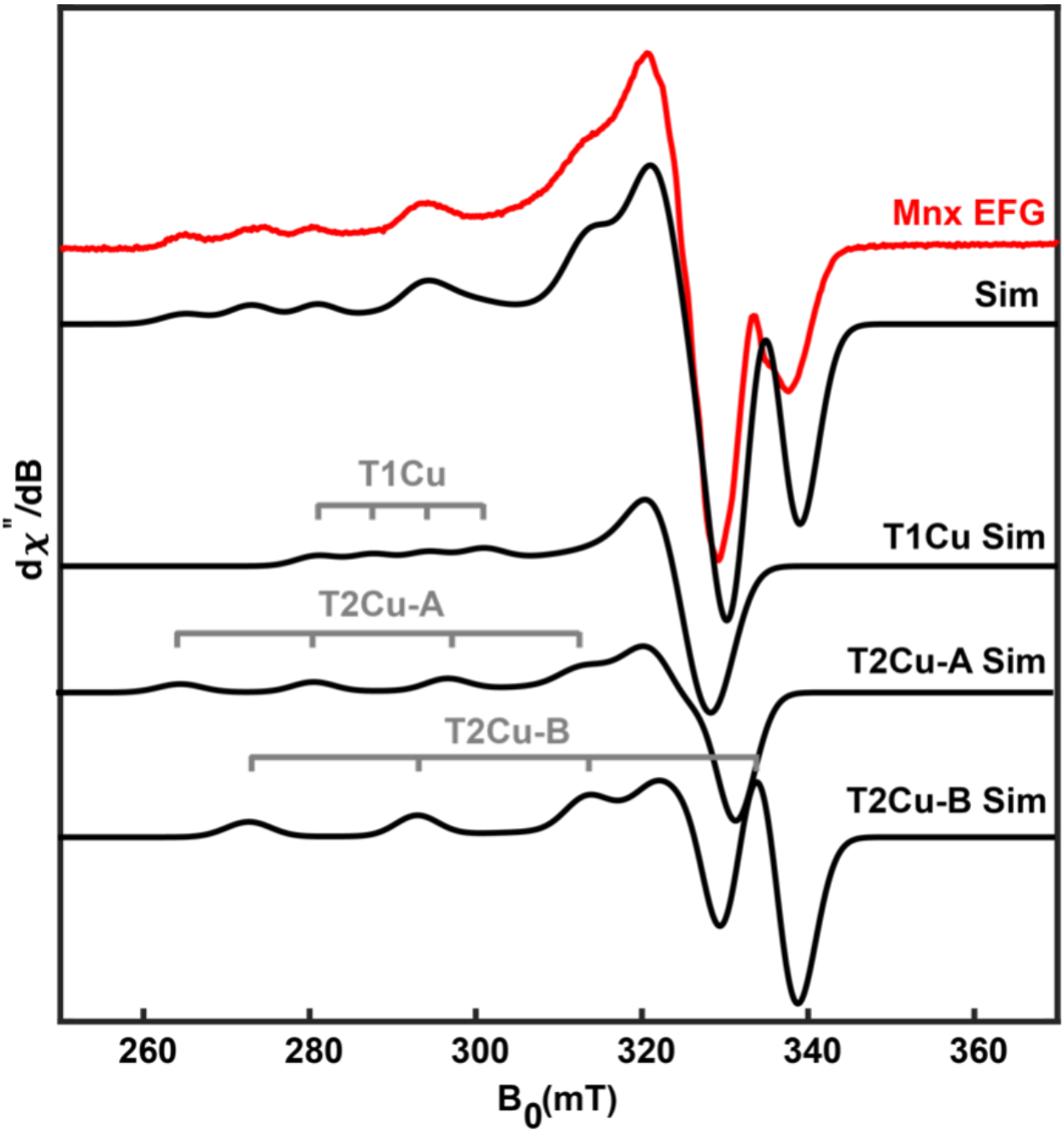

FIGURE 4.6. Mnx X-band CW EPR spectrum. The simulations are illustrated in black traces while the data is illustrated in the red trace. Gray lines show the ^{63}Cu hyperfine. Experimental parameters: temperature = 15 K; microwave frequency = 9.38 GHz; microwave power = 0.02 mW (no saturation); conversion time = 100 ms; modulation amplitude = 0.8 mT; and modulation frequency = 100 kHz.

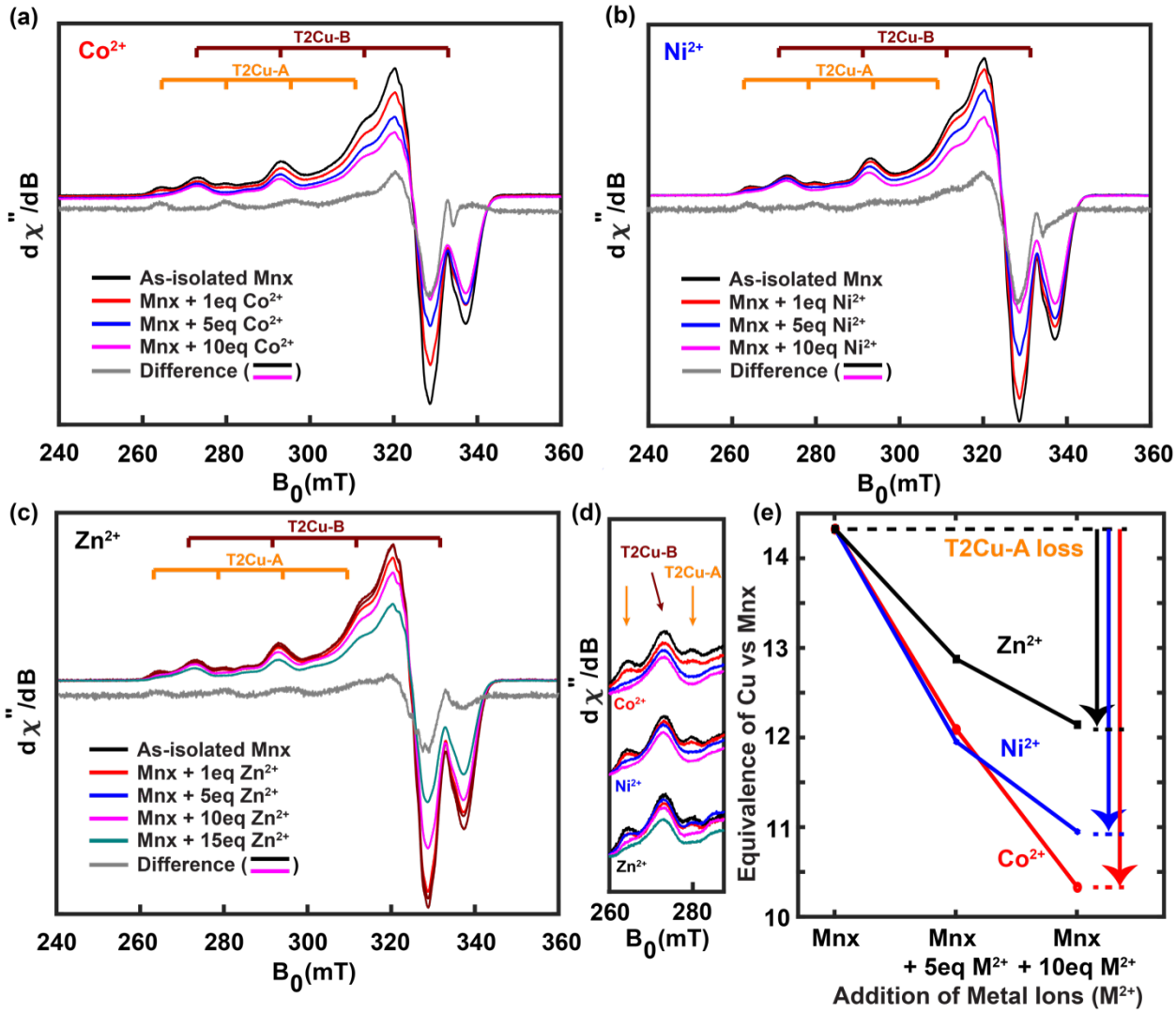

FIGURE 4.7. EPR spectra of Mnx with the addition of (a) Co^{2+}, (b) Ni^{2+}, and (c) Zn^{2+}. The difference spectrum between the as-isolated Mnx (black trace) and the Mnx + 10 equiv. of M^{2+} (magenta trace). The brown indicators show the ^{63}Cu hyperfine of T2Cu-B while the orange indicators show the ^{63}Cu hyperfine of T2Cu-A. The zoom-in spectra are shown in (d) with B_0 from 260 mT to 284 mT. (e) shows the Cu equivalences in Mnx upon addition of M^{2+}. The intensity of all spectra was normalized with the resonator Q value and the square root of the power. Experimental parameters: temperature = 15 K; microwave frequency = 9.38 GHz; microwave power = 0.02 mW (no saturation); conversion time = 100 ms; modulation amplitude = 0.8 mT; and modulation frequency = 100 kHz.

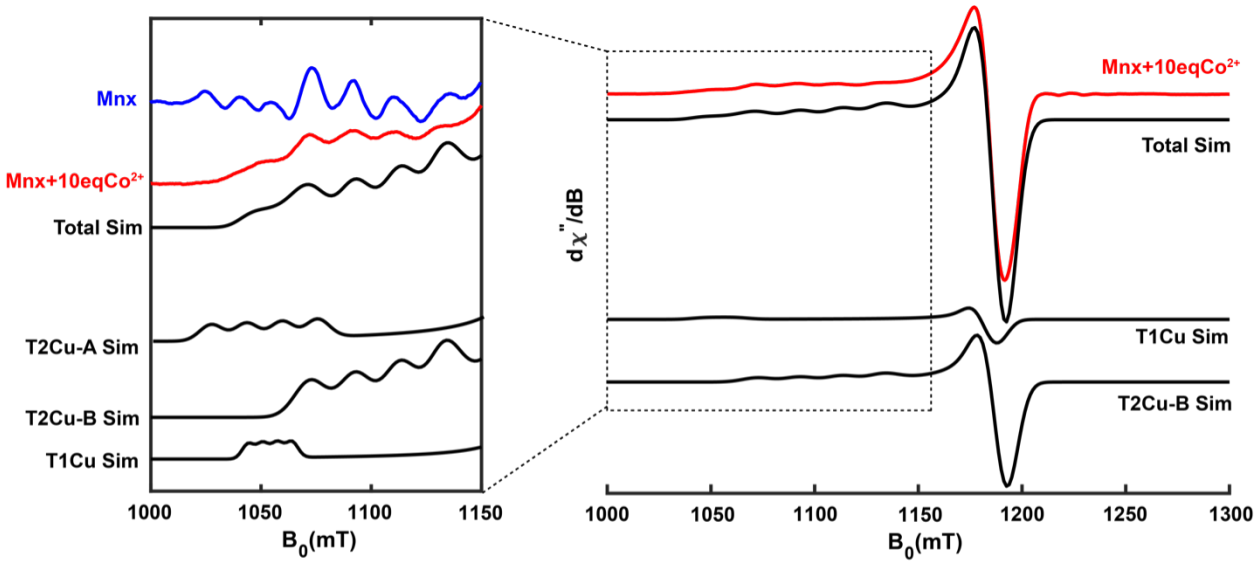

FIGURE 4.8. Q-band (34.322 GHz) pseudo-modulated (modulation amplitude, 7.5 mT) electron spin-echo (ESE) detected field swept EPR spectrum of Mnx with 10 eq. of Co^{2+} (red trace) at 30 K, microwave frequency = 34.322 GHz, $\pi/2$ = 12 ns, and τ = 300 ns.

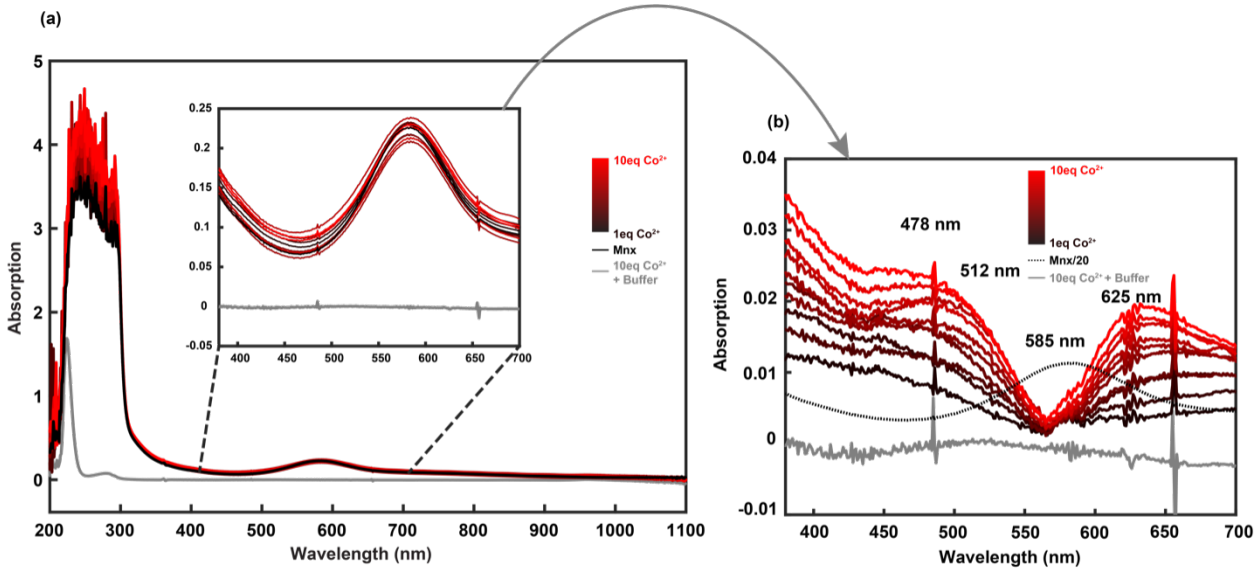

FIGURE 4.9. UV-vis spectra of Mnx with 1 – 10 equiv. of Co(II). (a) UV-vis spectrum of 25 μM Mnx with 1 – 10 equiv. Co(II), added as $CoCl_2$, without the presence of Mn(II) to investigate the Mnx-Co(II) complex. (b) difference spectrum ranging from 380 to 700 nm obtained by subtracting the Mnx spectrum from the Mnx + Co(II) spectrum.

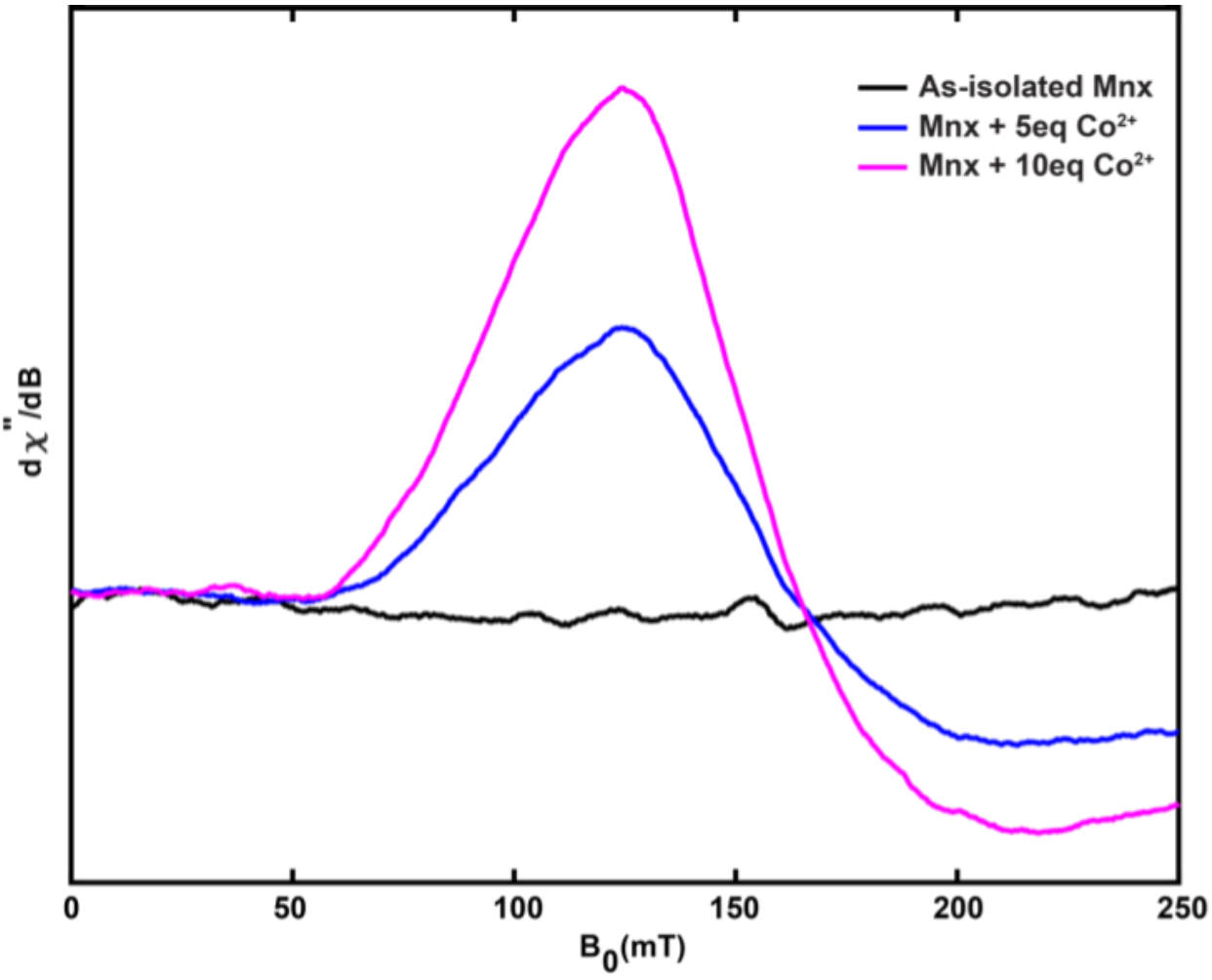

FIGURE 4.10. X-band CW EPR spectrum of Mnx and Mnx + Co^{2+} samples. Experimental parameters: temperature = 15 K; microwave frequency = 9.38 GHz; microwave power = 0.02 mW (no saturation); conversion time = 100 ms; modulation amplitude = 0.8 mT; and modulation frequency = 100 kHz.

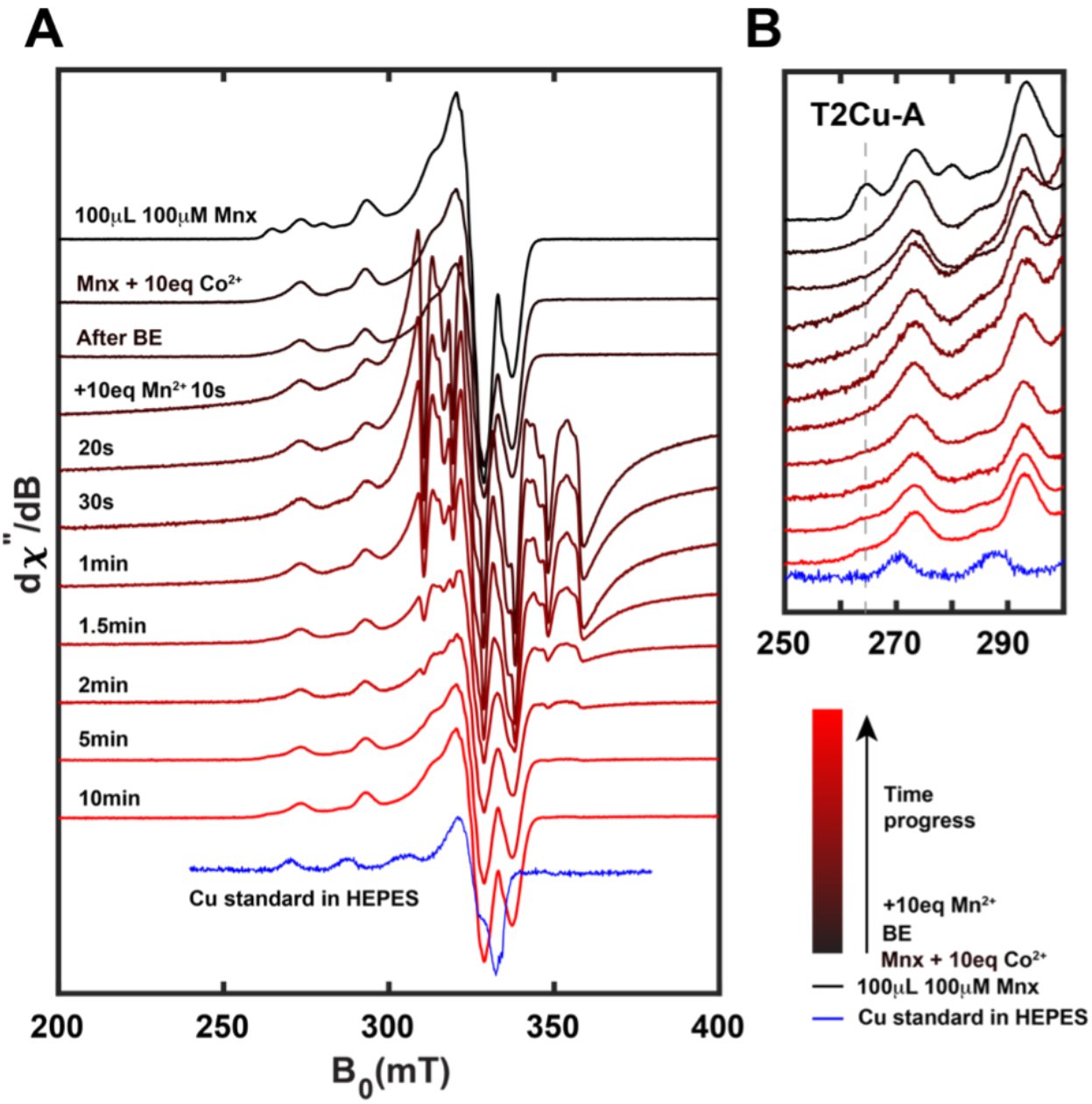

FIGURE 4.11. X-band CW EPR spectra of Mnx with 10 equiv. of Co^{2+} and 1 – 10 equiv. of Mn^{2+} (A) and the inlet from 250 mT to 300 mT (B). The gradient of red color represents the amount of Mn^{2+} added. BE represents buffer exchange with the HEPES buffer. Experimental parameters: temperature = 15 K; microwave frequency = 9.38 GHz; microwave power = 0.02 mW (no saturation); conversion time = 100 ms; modulation amplitude = 0.8 mT; and modulation frequency = 100 kHz

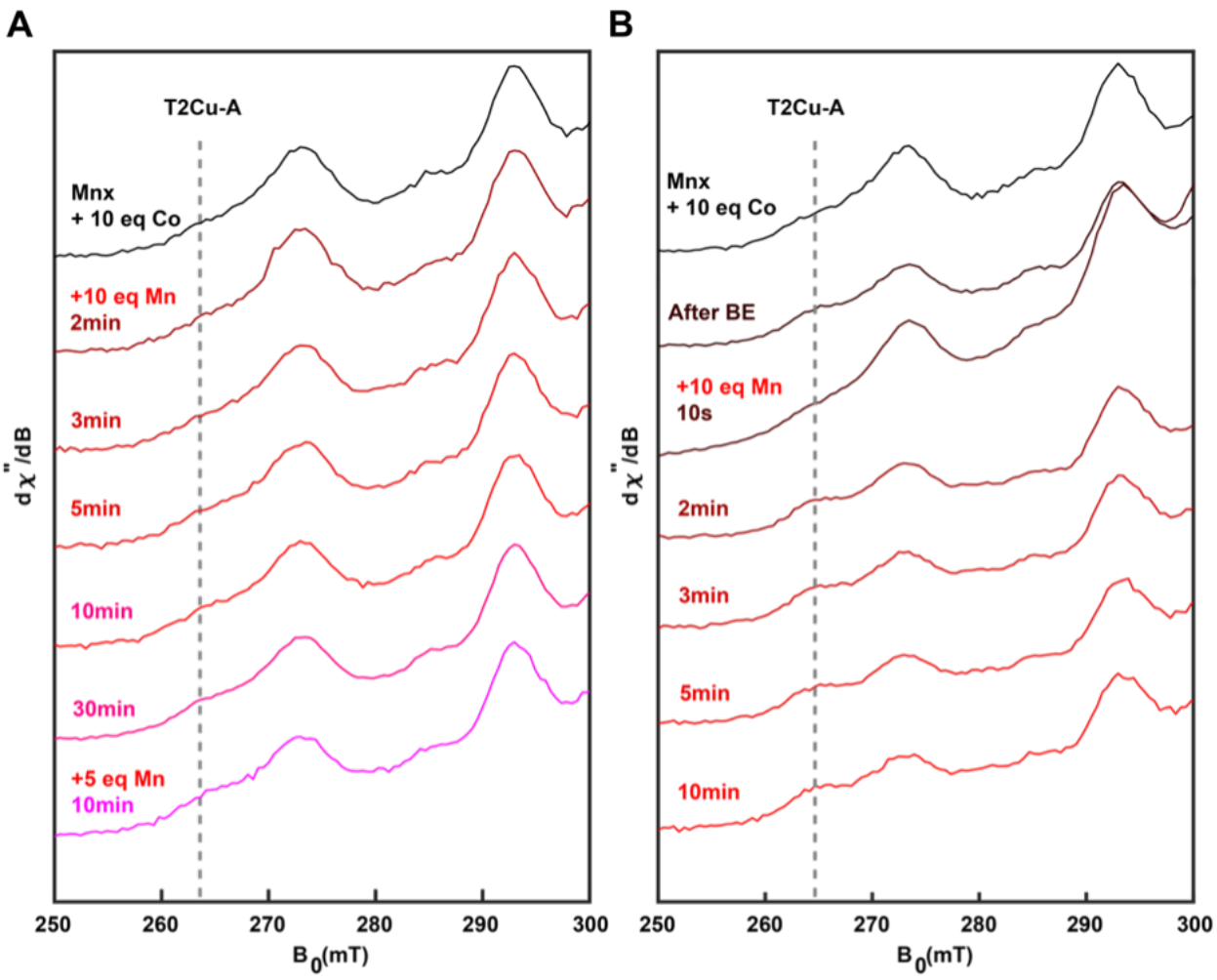

FIGURE 4.12. The zoom-in X band CW EPR of Mnx with 10 equiv. of Co^{2+} and 10 equiv. of Mn^{2+} without BE (A) and with BE (B). BE represents buffer exchange with the HEPES buffer. Experimental parameters: temperature = 15 K; microwave frequency = 9.38 GHz; microwave power = 0.6325 mW (saturating condition for Cu); conversion time = 100 ms; modulation amplitude = 0.8 mT; and modulation frequency = 100 kHz

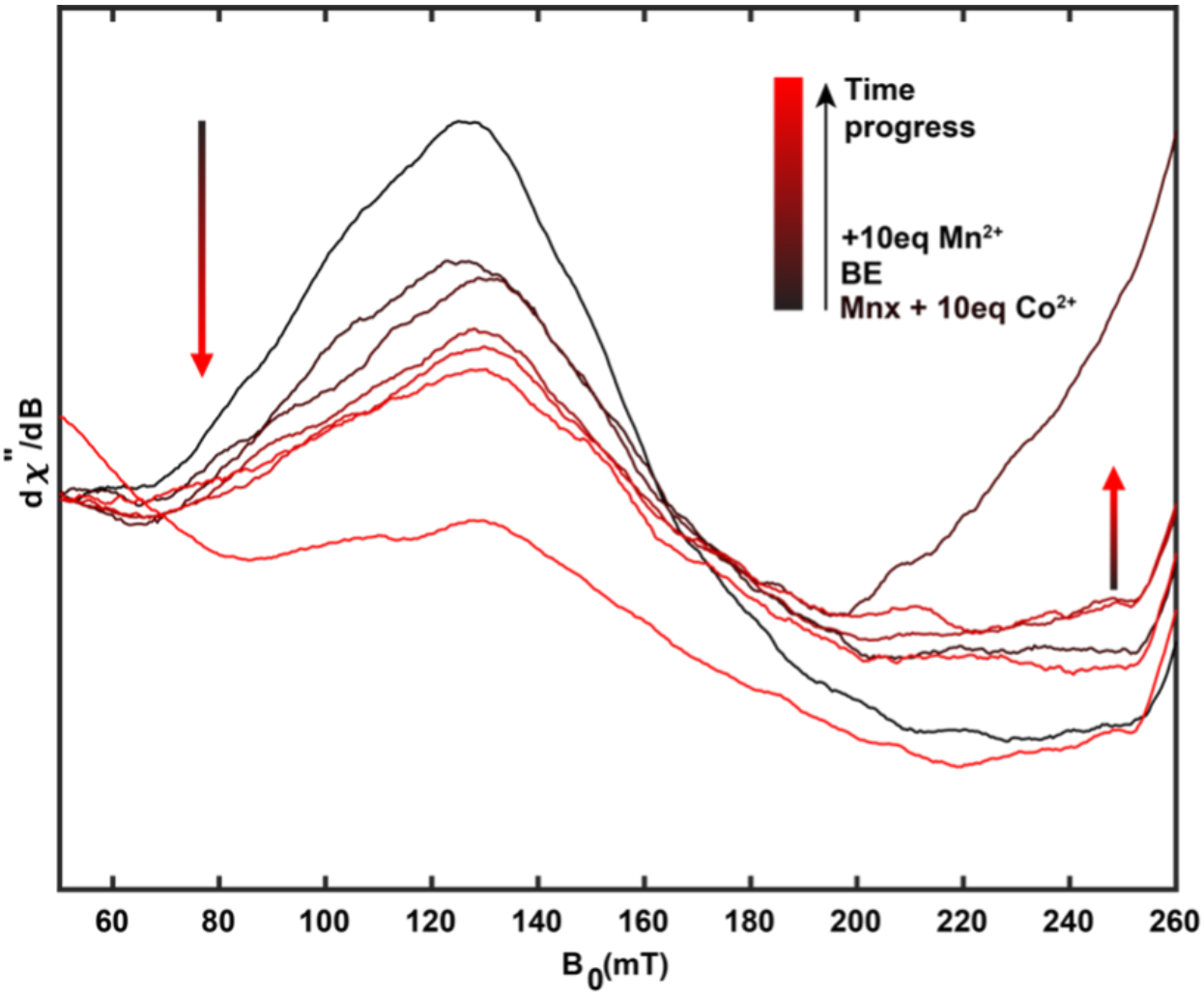

FIGURE 4.13. The zoom-in X-band CW EPR of Mnx with 10 equiv. of Co^{2+} and 10 equiv. of Mn^{2+} with BE. The arrow shows the trend of the peak intensity as the time progresses.

CHAPTER 5

Applications of EPR spectroscopy on inorganic and metalloprotein systems

5.1. Overview

EPR is a highly specific and sensitive tool to investigate the redox active metal centers in the metalloprotein or redox active metal-containing inorganic compound. In Chapter 4, we observed specific loss of the T2Cu copper site in MnxG due to the addition of the first-row transition metal ions via EPR. In this chapter, we will expand the application of EPR in other systems. Section 5.2 will talk about the characterization of the Fe-heme units in an artificial protein analog system while section 5.3 will discuss the determination of the spin state of the FeNO molecule using EPR spectroscopy. Last but not the least, section 5.4 demonstrates how EPR spectroscopy and X-ray crystallography in combination unravels the mystery of inorganic chemistry reactions with different reaction conditions.

5.2. Protein-Embedded Metalloporphyrin Arrays Templated by Circularly Permuted Tobacco Mosaic Virus Coat Proteins

5.2.1. Abstract. Bioenergetic processes in nature have relied on networks of cofactors for harvesting, storing, and transforming the energy from sunlight into chemical bonds. Models mimicking the structural arrangement and functional crosstalk of the cofactor arrays are important tools to understand the basic science of natural systems and to provide guidance for non-natural functional biomaterials. Here, we report an artificial multiheme system based on a circular permutant of the tobacco mosaic virus coat protein (cpTMV). The double disk assembly of cpTMV presents a gap region sandwiched by the two C2-symmetrically related disks. Non-native bis-his coordination sites formed by the mutation of the residues in this gap region were computationally screened and experimentally tested. A cpTMV mutant Q101H was identified to create a circular assembly of 17 protein-embedded hemes. Biophysical characterization using X-ray crystallography, cyclic voltammetry, and electron paramagnetic resonance (EPR) suggested both structural and functional similarity to natural multiheme cytochrome c proteins. This protein framework offers many further engineering opportunities for tuning the redox properties of the cofactors and incorporating non-native components bearing varied porphyrin structures and metal centers. Emulating the electron transfer pathways in nature using a tunable artificial system can contribute to the development of photocatalytic materials and bioelectronics.

The content in this section is in part reproduced from ACS Nano 2021, 15, 8110−8119 doi: https://dx.doi.org/10.1021/acsnano.0c07165 [239]

5.2.2. Introduction. In nature, photosynthetic systems have evolved complex cofactors networks to achieve advanced functions, such as the energy transfer, electron transfer, and chemical conversion steps involved in photon-driven carbon fixation. [240] These systems are key to the success of multi-component protein assemblies that establish and maintain the positions of chromophores, hemes, metal ions, and redox cofactors so that they can function in concert. A number of research groups have endeavored to construct synthetic mimics of these systems, with a particular emphasis on the initial steps of light collection and energy transfer. Polymer, [241] dendrimer, [242] nucleic acid, [243] and protein scaffolds [244] have been reported for this purpose. Lately, Francis lab at UC Berkeley has explored the use of synthetically modified viral capsids, with a focus on tobacco mosaic virus (TMV) coat proteins. [245, 246, 247] This viral capsid-based platform has yielded insight into structure-function relationships found in natural light-harvesting systems and provided design principles for next-generation functional materials for solar energy collection. [248] A key next step in the development of these platforms is the introduction of electron transfer and catalysis functions. The incorporation of heme groups into these scaffolds can provide an important bridge between energy and electron transfer components. [249, 250]

Cytochromes, one of the most prevalent electron transfer proteins, rely on a network of iron protoporphyrin IX hemes and iron–sulfur clusters for their function. [251] Interesting examples of electron transfer and storage complexes in nature are the multiheme proteins that carry electrons across the periplasmic spaces of dissimilatory bacteria, such as Geobacter sulfurreducens [252] and Shewanella oneidensis. [253] A directional electron flow is believed to be achieved through the fine-tuning of redox site potentials within each multiheme cytochrome. [254] Clusters of assorted interacting cytochromes further elongate the length scale of the molecular wire and participate in respiratory chains that require long-range multielectron transport from the cell interior to external redox partners, such as minerals. Mimics of these systems could provide useful components of multielectron catalysis systems.

Herein, we report an artificial multiheme system templated by circularly permuted tobacco mosaic virus capsid proteins (cpTMV) as an electron-transfer model. As previously reported, cpTMV forms a stable double-disk assembly with a central pore (Figure 5.1a). The top and bottom disks each consist of 17 identical monomers, related by C2 symmetry (Figure 5.1b). [245] In this work, a circular assembly of 17 identical, non-native heme-binding pockets were introduced by combining structure-guided design and computational modeling. Functional activity of the protein-embedded heme arrays was suggested by the observation of redox activity.

5.2.3. Summary of the characterization work. Most of the iron atoms involved in electron transfer are axially ligated by two histidine imidazoles or a combination of histidine and methionine side chains. [255] Six optimal histidine mutations were identified using molecular mechanics [256] and an OPLS2005 force field in the Schrödinger Suite version 2016-2. By UV-vis and circular dichroism spectroscopies, Q101H was identified as a stable and strong heme-binding mutation with a six-coordinated low-spin Fe-heme structure motif (Figure 5.1). [257] The structure of cpTMV-Q101H holoprotein was confirmed by the electron density map analysis of X-ray crystallography (Figure 5.2).

5.2.4. EPR characterization of cpTMV-Q101H holoprotein. While the structure of the holoprotein and the active site has been determined with the above characterization, the coordination geometry and electronic structures of the bound hemes are still not directly elucidated. Thus, EPR spectroscopy was performed to investigate the structural and functional properties of the Fe-heme sites.

In the resting state, the cpTMV-Q101H-bound hemes are oxidized, yielding an EPR-detectable Fe(III) species. The continuous-wave (CW) X-band EPR spectra exhibited a single type of heme with the g-values of $[g_z, g_y, g_x] = [3.247, 2.04, 1.24]$ (Figure 5.3). The g-values correspond to a calculated rhombicity of 0.57, which supported the characterization of TMV-bound heme as a rhombic type, six-coordinated low-spin species, as observed in natural cytochromes [258] and designed heme proteins. [257] The slightly larger value of g_z

compared with a typical rhombic type heme, which has the two axial ligands nearly coplanar, suggested a relatively larger dihedral angle between the two histidine planes. [259] The EPR signal was retained at elevated temperature (40 K), showing a relatively slow relaxation rate (Figure 5.4). [260] Chemical reduction of the hemes using sodium dithionite resulted in the disappearance of this signal, indicating a complete conversion from Fe(III) to Fe(II). The reduced hemes can be chemically reoxidized by using potassium ferricyanide, which resulted in the recovery of the EPR signal (Figure 5.3). The redox properties of hemes bound to cpTMV-Q101H were also confirmed by cyclic voltammetry of a protein film, yielding a midpoint reduction potential of -200 mV (vs standard hydrogen electrode).

In this project, the EPR spectrum of cpTMV-Q101H holoprotein is taken to investigate the structure of the Fe-heme sites, which are the active sites of the protein. By comparative studies and theoretical analysis, the hypothetical coordination environment and geometry can be rationalized and proposed. Besides, due to the difference in spin states, EPR spectroscopy provides clear evidence to distinguish Fe(II) and Fe(III), thus monitoring the redox reaction of Fe-heme. Combining with cyclic voltammetry data, a comprehensive redox picture can be illustrated.

5.3. Thionitrite (SNO^-) and Perthionitrite ($SSNO^-$) are Simple Synthons for Nitrosylated Iron Sulfur Clusters

5.3.1. Abstract. S/N crosstalk species derived from the interconnected reactivity of H_2S and NO facilitate the transport of reactive sulfur and nitrogen species in signaling, transport, and regulatory processes. We report here that simple Fe^{2+} ions, such as those that are bioavailable in the labile iron pool (LIP), react with thionitrite (SNO^-) and perthionitrite ($SSNO^-$) to yield the dinitrosyl iron complex $[Fe(NO)_2(S_5)]^-$. In the reaction of $FeCl_2$ with SNO^- we were able to isolate the unstable intermediate hydrosulfido mononitrosyl iron complex $[FeCl_2(NO)^-(SH)]^-$, which was characterized by X-ray crystallography. We also show that $[Fe(NO)_2(S_5)]^-$ is a simple synthon for nitrosylated Fe-S clusters via its reduction with PPh_3 to yield Roussin's Red Salt ($[Fe_2S_2(NO)_4]^{2-}$), which highlights the role of S/N crosstalk species in the assembly of fundamental Fe-S motifs.

The content in this section is in part reproduced from Angew. Chem. Int. Ed. 2022, 61, e202204570 [261]

5.3.2. Introduction. Small gaseous molecules that are endogenously produced and function on molecular targets play essential roles in physiological function. For example, nitric oxide, NO, plays an important role in regulating blood pressure, oxygen delivery and immune functions, [262] and the loss of NO has also been shown as one of the earliest signs for many chronic diseases. [263] Physiological signaling molecules such as CO, NO, and H_2S are also known as gasotransmitters, each being derived from larger biomolecules through enzymatic processes. [264] The reaction between gasotransmitters and related species forms a landscape of intertwined reactive intermediates, or crosstalk species, that are postulated to facilitate different signaling, transport, and regulatory processes. Thionitrous acid (HSNO) is the simplest S/N crosstalk species and is formed from the direct reaction of S-nitrosothiols (RSNO) with H_2S. HSNO is shown to be membrane permeable and facilitates protein transnitrosation via the transport and subsequent generation of NO^+ and HS^- equivalents. [265] Work from Feelisch and co-workers demonstrated that aerobic oxidation of H_2S and NO results in the formation of perthionitrite ($SSNO^-$), which functions as a source of bioavailable sulfane sulfur, polysulfides, and NO. [266]

Gasotransmitter uptake, regulation, and transport is also intertwined with bioinorganic metal centers. For example, NO binds and activates heme in soluble guanylate cyclase to rapidly produce cyclic guanosine monophosphate (cGMP) and generates a physiological response, such as muscle relaxation. [267] Ferric hemoglobin can bind and oxidize hydrosulfide to thiosulfate and iron-bound hydropersulfides, which are crucial reactive sulfur species (RSS) formed in persulfidation signaling pathways. [268] Despite the demonstrated ability of iron systems to interact with NO and H_2S, surprisingly few studies have investigated how metals participate in the generation and interconversion of S/N crosstalk species.

Both SNO^- and $SSNO^-$ can bind to Lewis acidic redox inert metals with potential coordination to S, N, or O. Recent work demonstrated that salt metathesis of redox inert $TpZn(ClO_4)$ (Tp=hydrotris(5-methyl-3-phenyl-pyrazol-1-yl)borate) with $SSNO^-$ efficiently formed $TpZn(\kappa 2\text{-}SSNO)$, which was fully characterized. [269] However, examples of SNO^-

and $SSNO^-$ coordination at biologically relevant redox-active metals remain unsurprisingly elusive, in part due to the redox instability of S/N crosstalk species. As an example of this complexity, reactions of sodium nitroprusside, $Na_2[Fe(CN)_5NO]$ (SNP), with hydrosulfide (HS^-) have been studied for nearly 180 years, [270] but the products remained unknown until recently Wu and co-workers characterized reactive intermediates by NMR (^{17}O, ^{15}N, ^{13}C), UV/Vis, and IR spectroscopy together with DFT calculations to show that SNP reacts with HS^- to form $[Fe(CN)_5(SNO)]^{4-}$, which can subsequently react with HSS^- to form $[Fe(CN)_5(SSNO)]^{4-}$ with a distinct blue color (λ_{max}=570 nm). [271] In addition, HS-mediated nitrite reduction has been observed at a Fe-porphyrin (FeP) system and results in the formation of an FeP-NO complex, which can react with an additional equivalent of HS^- to form a FeP-HSNO species that was characterized by cryospray ESI-TOF MS. [272]

Expanding this coordination chemistry, an attractive hypothesis is that these pools of S/N crosstalk species may also be important synthons in the assembly of fundamental bioinorganic building blocks, particularly those with S and NO motifs. For example, mononitrosyl and dinitrosyl iron complexes (MNICs and DNICs, respectively) are prototypical Fe-NO species that have wide ranging functions including reducing oxidative stress, [273] repairing and/or degrading Fe-S clusters, [274] and signaling via protein S-nitrosation. [275] More broadly, the cellular labile iron pool (LIP), which consists of a chelatable pool of redox-active Fe ions, [276] is key in the formation of Fe-NO species and often proceeds through the initial generation of MNICs followed by subsequent reaction with thiols to generate DNICs. [277] The role of the LIP in sulfur metabolism may also result in formation of S/N crosstalk species, although the fundamental reactions of simple Fe ions with species like SNO^- and $SSNO^-$ remains uninvestigated. Here we report that the simple reaction of SNO^- and $SSNO^-$ with Fe^{2+} generates MNIC and DNIC compounds, as well as NO, hydrosulfide, and persulfide equivalents, all of which highlight the role of S/N crosstalk species in the assembly of fundamental Fe-S motifs.

5.3.3. Synthesis and product characterization. Building from the idea that S/N crosstalk species could react with simple Fe sources, we investigated whether $FeCl_2$ could react directly with [PNP][SSNO]. Reacting $FeCl_2$ with 3 equiv. of [PNP][SSNO] in THF yielded the DNIC [PNP][$Fe(NO)_2(S_5)$] (**1**) with a yield of 61% (Figure 5.5). This synthesis generates undetectable amount of Fe byproducts unlike the prior synthesis of MNIC [PNP][$Fe(CO)^{3-}(NO)$] with S_8. [278] Single crystal X-ray diffraction confirmed the molecular structure of **1** and two NO stretches on the IR spectrum also confirmed the DNIC **1**. [278]

Based on the polysulfide backbone of **1**, we next investigated the reaction of $FeCl_2$ with [PNP][SNO] to determine the reaction outcome when sulfane sulfur sources were removed from the reaction. IR spectra of the product shows that besides the two NO stretches of DNIC **1**, the presence of a new NO stretch indicates the formation of a minor Fe-NO product (**2**).

5.3.4. EPR characterization of the new Fe-NO product. To examine the electronic and magnetic property of the product mixture, EPR spectroscopy was used. Crystalline samples from the reaction between $FeCl_2$ and SNO^- were dissolved in 1:1 toluene/THF and flash frozen in liquid nitrogen. The frozen-solution state EPR spectrum was then recorded at 10 K, as shown in Figure 5.6. Two paramagnetic components were observed, where a major component is an S=1/2 species with g-values=[2.050, 2.027, 2.016] at central field and a minor component at low-field with g≈3.9 is consistent with a high spin S=3/2 species. [279] The major component is assigned to **1**, because the corresponding electronic spin states (low-spin S=1/2 and g-values) match those of **1** previously reported by Tsai et al. [280] Evan's method magnetic susceptibility measurements from crystalline samples from the reaction between $FeCl_2$ and SNO^- showed μ_{eff}=2.10 μB. This μ_{eff} value is slightly higher than that of a pure sample consisting of an S=1/2 system, which is consistent with some incorporation of an S=3/2 product. These data also corroborates the EPR results that both S=1/2 and S=3/2 species were detected from the crystalline sample.

The minor product **2** shown on the EPR spectrum was then confirmed by X-ray crystallography. Complex **2** is a tetrahedral monoanionic Fe complex with a $\tau 4$ value of 0.98, consisting of two anionic chloride, one NO, and one HS^- ligand. The coordination environment of **2** is consistent with an $FeNO_7$ electronic structure using Enemark-Feltham notation. [281] The Fe-N-O bond angle, Fe-NNO and N-O bond lengths, and $\nu_{N\text{-}O}$ in **2** are consistent with other FeIII-NO^- electronic structures, [282] where the triplet NO^- is antiferromagnetically coupled to the high-spin FeIII. Complex **2** is therefore assigned to the S=3/2 species observed in the EPR spectrum (Figure 5.7). We note that **2** is unstable and readily decomposes at room temperature.

In this project, the reactions of Fe^{2+} with SNO^- and $SSNO^-$ generates Fe-NO complexes as reaction intermediates towards dinitrosyl iron complex $[Fe(NO)_2(S_5)]^-$, which helps illustrate the reaction mechanism. EPR spectroscopy provides significant evidence of spin states of the Fe-NO complexes, thus identifying the fact that there are two reaction intermediates present. By comparing the g values with the previous report, the structure of reactive intermediates can be rationalized.

5.3.5. Proposed mechanism of simple Fe^{2+} reaction with [PNP][SNO] and [PNP][SSNO]. With both the observed formation of DNIC **1** from Fe^{2+} and $SSNO^-$ and SNO^-, as well as observation of MNIC **2** from SNO^- we propose a mechanism of this reaction (Figure 5.8. Both $SSNO^-$ and SNO^- initially coordinate to the metal center, followed by rapid homolytic cleavage of the S-N bond to provide a NO ligand and a transient S^{2-} polysulfide in the case of $SSNO^-$ and a thiyl radical and **2** in the case of SNO^-. For SNO^-, subsequent reaction with NO and polysulfides formed through SNO^- disproportionation would lead to formation of **1**. Similarly, for $SSNO^-$, the released polysulfide after initial reaction with Fe^{2+} can result in further polysulfide formation and NO generation, both of which are required to form **1**.

5.4. Reactions of Thianthrene and 10-Phenylphenothiazine with the Lewis Acids–Titanium Tetrachloride, Titanium Tetrabromide, Tin(IV) Tetrachloride, or Antimony(V) Pentachloride: The Competition between Coordination and Oxidation

5.4.1. Abstract. The oxidation of thianthrene and 10-phenylphenothiazine into cation radicals has been examined using redox-active Lewis acids. The reaction of titanium(IV) tetrachloride or titanium(IV) tetrabromide with thianthrene in toluene produces thiantherene-Ti_2 coordination complex while the reaction of antimony(V) pentachloride with thianthrene generates isolated cation radicals, which both yield strong rhombic-type EPR signal. The reaction of 10-phenylphenothiazine with titanium(IV) tetrachloride and tin(IV) tetrachloride in toluene solution resulted in the formation of crystalline paramagnetic (10-phenylphenothiazine$^{\cdot+}$)(Ti(μ-Cl)$_3$Cl$_6^-$) and crystalline paramagnetic (10-phenylphenothiazine$^{\cdot+}$)($SnCl_5^-$), which both give EPR spectra with unresolved hyperfine couplings, unlike the EPR spectra of the solution.

The content in this section is in part reproduced from Inorg. Chem. 2023, 62, 14055−14063 doi: https://doi.org/10.1021/acs.inorgchem.3c02079 [283]

5.4.2. Introduction. Cation radicals are important reactive intermediates in many oxidation reaction mechanisms. [284, 285, 286, 287, 288] While most of the cation radicals exist only within the short time course of the reaction, some of them can be isolated in the crystalline form, such as Magic Blue, a commercially available one-electron oxidizing reagent. [289, 290, 291, 292, 293] Previous publication from the Balch lab discovered that oxidation of triphenylamine with different cations yields different products. With $TiCl_4$, $TiBr_4$, or $SnCl_4$, the crystalline product contained the cation radical of N,N,N',N'-tetraphenyl-1,4-benzenediamine, while oxidation with $SbCl_5$ produced the cation radical of N,N,N',N'-tetraphenylbenzidine. [294] Inspired by this, here we report the products obtained by oxidation of thiantherene and its derivative, 10-phenylphenothiazine, with the Lewis acid oxidants, $TiCl_4$, $TiBr_4$, or $SnCl_4$ and $SbCl_5$ (Figure 5.15. The thiantherene cation radical is important one-electron oxidizer in many inorganic, organometallic and organic chemistry reactions [291, 292, 295, 296, 297, 298, 299, 300] and also plays important role in battery development [301, 302]. 10-Phenylphenothiazine, on the other hand, plays important roles in in the field of optics [303, 304, 305] and medicine [306].

5.4.3. Results. This result part includes only part of the X-ray crystallography results and the reaction details but focus mostly on the EPR spectroscopy results of the product. For the full view of the reaction details, please refer to the original paper.

Reactions with Thiantherene. The synthetic work is summarized in Figure 5.16.

Reaction of Thiantherene with Titanium(IV) Tetrachloride. The reaction of thianthrene with titanium(IV) tetrachloride in toluene solution produces a rich maroon/ purple color that lightened to dark red over the course of several hours. This toluene solution shows an EPR spectrum. As shown in Figure 5.9, a quintet is centered at the magnetic field position of 332.7 mT ($g_{iso} = 2.0084$) with a hyperfine splitting of 1.2 G (3.4 MHz). This quintet feature with a peak intensity ratio of 1:4:6:4:1 is likely due to the hyperfine coupling to four equivalent protons on the two aromatic rings in thianthrene. A similar EPR signal was observed

previously for the thianthrene cation radical in solution. [307,308] Thus, titanium(IV) tetrachloride can oxidize thianthrene to its cation radical. The reaction crystalline product has been confirmed as (**1**)(μ- thianthrene)Ti_2(μ-Cl_2)Cl_6 by single crystal X-ray crystallography, a Ti_2(μ-Cl_2)Cl_6 complex with an unusual bridging coordinating thiantherene ligand. This product shows a weak EPR signal similar to that of the reaction solution (Figure 5.9). Similar results are seen with the product (**2**) from the oxidation reaction of thianthrene with titanium(IV) bromide.

Reaction of Thiantherene with Antimony(V) Pentachloride. The product obtained from the reaction of antimony(V) pentachloride with thianthrene depends upon the solvent used for the reaction. Addition of a toluene solution of antimony(V) pentachloride to a toluene solution of thianthrene produces a violet solution from which black crystals of (**3**) (thianthrene$^{\cdot+}$)$_2$(Sb_2(μ-Cl)$_2$$Cl_6^{2-}$)·($SbCl_3$) appeared within 20 min. The structure of these crystals consists of three components in the crystal: the almost planar thianthrene cation radical, the dianion (Sb_2(μ-Cl)$_2$$Cl_6^{2-}$), and a molecule of $SbCl_3$. The EPR spectrum of a polycrystalline sample of (thianthrene$^{\cdot+}$)$_2$(Sb_2(μ-Cl)$_2$$Cl_6^{2-}$)·($SbCl_3$) is shown in Figure 5.10. Unlike the EPR spectrum of the thianthrene cation radical in solution (Figure Figure 5.9), the EPR spectrum of this polycrystalline sample does not reveal resolved ^{1}H hyperfine splitting within the observed rhombic powder pattern, with g values = 2.0138, 2.0087, and 2.0036. Similar rhombic spectra have been reported previously for salts containing (thianthrene$^{\cdot+}$). [309,310,311,312] Although dimerization of (thianthrene$^{\cdot+}$) can result in the formation of a diamagnetic complex, at room temperature, the spin coupling is weak and usually not sufficient to cause a loss of the EPR spectrum. Generally, upon cooling, the EPR signal has been found to diminish in intensity. [310]

On the other hand, addition of an acetonitrile solution of antimony(V) pentachloride to an acetonitrile solution of thianthrene produces purple crystalline blocks of (**4**) (thianthrene$^{\cdot+}$)($SbCl_6^-$), which consists of planar (thianthrene$^{\cdot+}$) cation radicals and octahedral ($SbCl_6^-$) ions. The EPR spectrum of a polycrystalline sample of (**4**) (thianthrene$^{\cdot+}$)($SbCl_6^-$)

at room temperature is shown in Figure 5.11. Like the EPR spectrum of the polycrystalline sample of (**3**), a rhombic powder pattern is observed for this polycrystalline sample. While g values remain similar, there is a larger line-broadening effect in (**3**) than that in (**4**), which is likely due to the dimerization of (thianthrene$^{\cdot+}$) in (**3**), as is mentioned above. The EPR spectrum resembles that of the red violet solid "thianthrene pentachloroantimonate" obtained from mixing chloroform solutions of thianthrene and antimony pentachloride. [307,308] The spectrum in Figure 5.11 also resembles the EPR spectrum reported above for (**3**).

Reactions with 10-Phenylphenothiazine. The synthetic work is summarized in Figure 5.16.

Reaction of 10-Phenylphenothiazine with Titanium- (IV) Tetrachloride. Treatment of a toluene solution of 10- phenylphenothiazine with titanium(IV) tetrachloride produces a reddish brown solution. The EPR spectrum of this solution is shown in Figure 5.12. The EPR spectrum is centered at a magnetic field position of ∼333.07 mT (corresponding to the g_{iso} = 2.0057) and consists of a triplet with a ^{14}N hyperfine splitting of 7 G (∼19.6 MHz) and an additional small splitting of 2 G (5.6 MHz) arising from 1H hyperfine coupling. The simulation of the EPR spectrum using the parameters previously obtained for the 10-phenylphenothiazine cation radical [313] but with a greater linewidth is shown in the black trace in Figure 5.12. The larger linewidth observed in our spectrum probably was caused by the high concentration of our solution producing interactions between cation radicals.

The crystal structure of the product, (**5**) (10-phenylphenothiazine$^{\cdot+}$)(Ti(μ-Cl)$_3$Cl$_6^-$), consists of planar 10-phenylphenothiazine cation radical, with the phenyl ring perpendicular to the plane, and (Ti(μ-Cl)$_3$Cl$_6^-$) anion. The EPR spectrum of a polycrystalline sample of (**5**) is shown in Figure 5.13. Compared to the EPR spectrum of the 10-phenylphenothiazine cation radical in solution, ^{14}N hyperfine is not well resolved and the EPR spectrum displays an axial pattern with g(perpendicular) = 2.0055 and g(parallel) = 2.0025. The small splitting at g(perpendicular) is assigned to a ^{1}H hyperfine interaction.

Reaction of 10-Phenylphenothiazine with Tin(IV) Tetrachloride. Addition of a solution of tin(IV) tetrachloride in toluene to a toluene solution of 10-phenylphenothiazine produces

(**6**)

(10-phenylphenothiazine$^{\cdot+}$)($SnCl_5^-$), consisting of individual trigonal bipyramidal ($SnCl_5^-$) anions and (10-phenylphenothiazine$^{\cdot+}$) radical cations. A polycrystalline sample of (**6**) produces a single line EPR spectrum with a center magnetic field of 333.04 mT (corresponding to $g_{iso} = 2.0060$), which is shown in Figure 5.14.

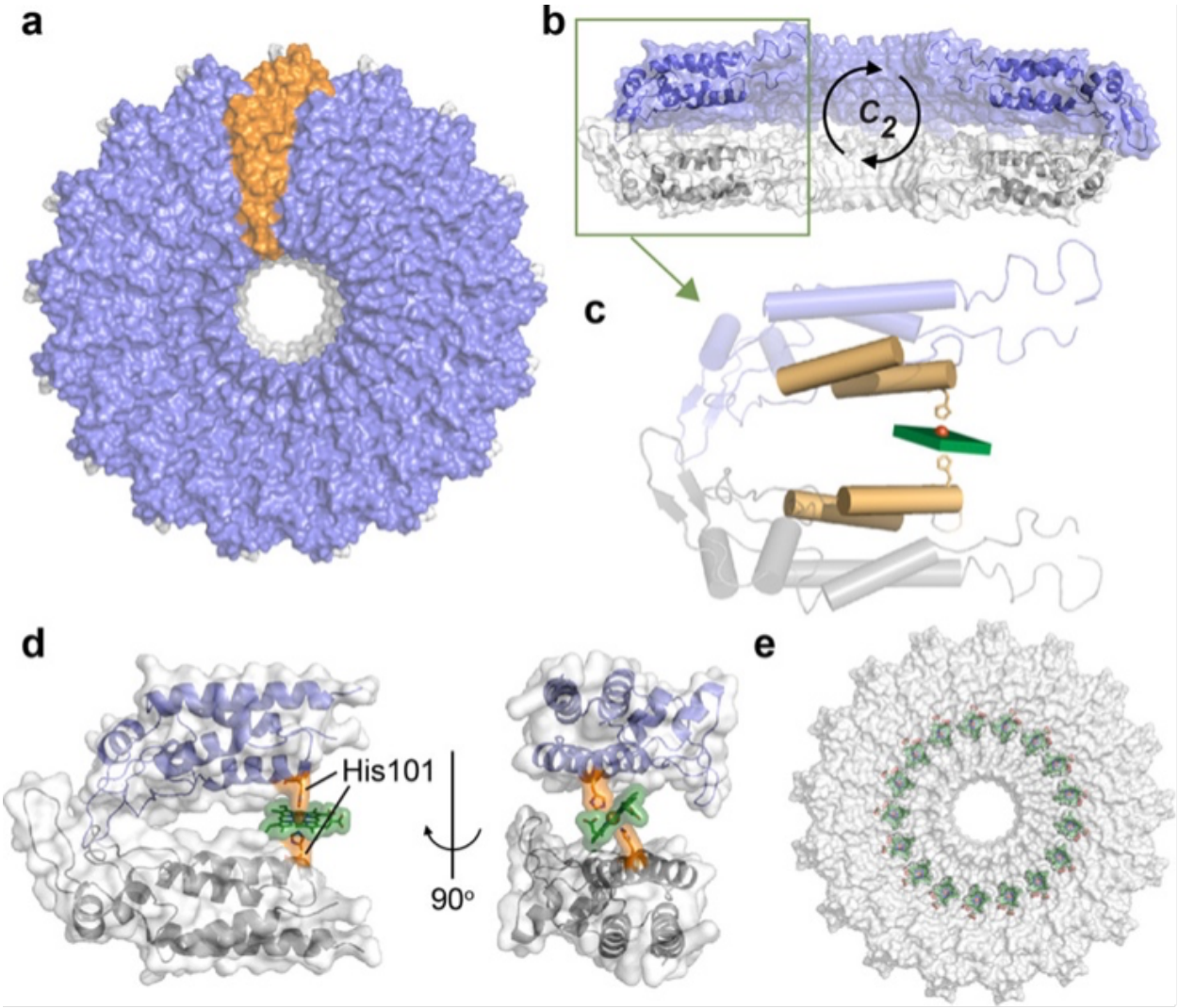

FIGURE 5.1. Design of heme binding pockets in TMV. A circular permutant of Tobacco Mosaic Virus capsid protein (cpTMV) forms a stable double-disk assembly. (a) Each disk consists of 17 identical monomers, as shown in the top-down view of cpTMV assembly, with one monomer highlighted in orange. (b) The top disk and the bottom disk are related by C2-symmetry, creating a hydrated cavity region between them. (c) Four α-helices from a top–bottom monomer pair, illustrated as pale yellow cylinders, present structural features similar to heme-binding motifs found in natural and designed heme proteins. (d) A modeled heme binding pocket displays a histidine mutation (orange), providing axial ligands to coordinate iron porphyrins (green). (e) Installation of the designed binding pockets into all top–bottom pairs yields a 17-heme system fully embedded within the protein scaffold.

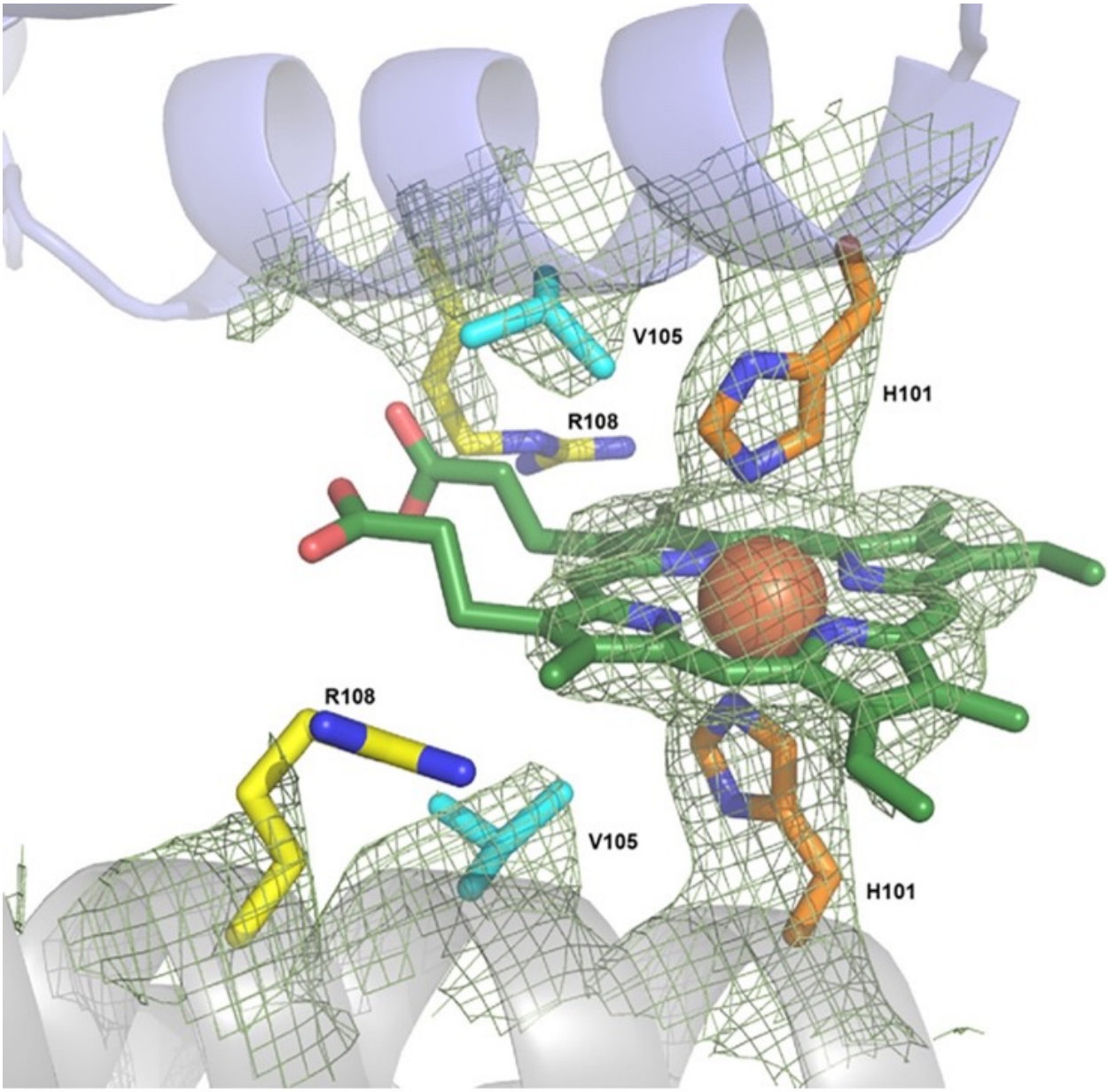

FIGURE 5.2. Crystal structure of cpTMV-Q101H holoprotein. The binding of heme with two axial histidine residues (labeled H101) was observed in the 2mFO-DFC map contoured at the 1.2σ level (shown as mesh line).

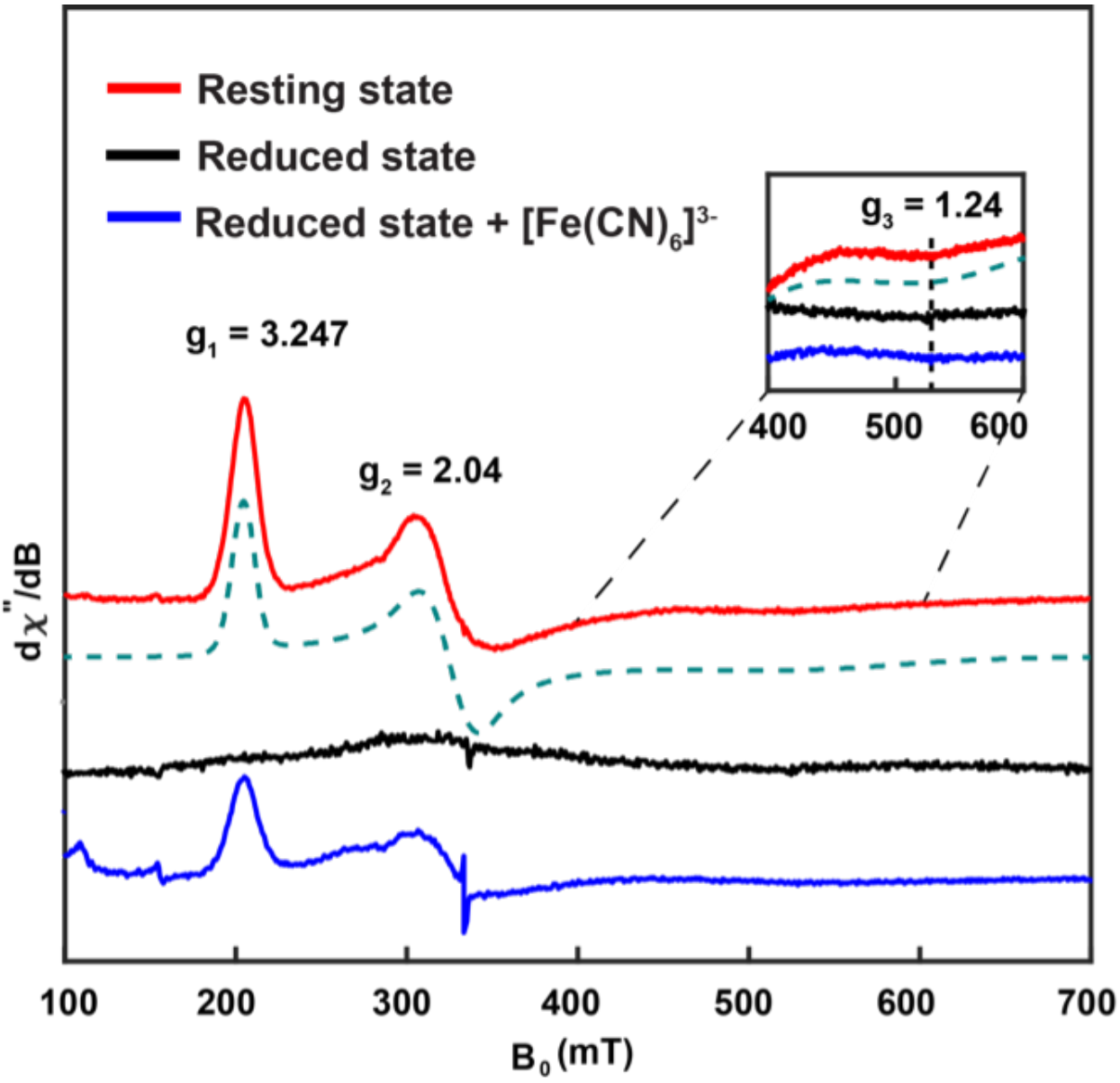

FIGURE 5.3. X-band EPR spectra of heme sites bound to cpTMV-Q101H in their resting ferric states (red) were recorded. The inset shows an expansion of the regions from 400 mT to 600 mT. Experimental parameters: temperature = 15 K; microwave frequency = 9.38 GHz; microwave power = 2 mW (no saturation); conversion time = 100 ms; modulation amplitude = 0.8 mT; and modulation frequency = 100 kHz. The simulated spectra (green dashed line) gave the rhombic g = [3.247, 2.04, 1.24]. Reduction of the heme with sodium dithionite reduced all signals, as shown in the black trace. The signal was recovered by reoxidation with potassium ferricyanide (blue).

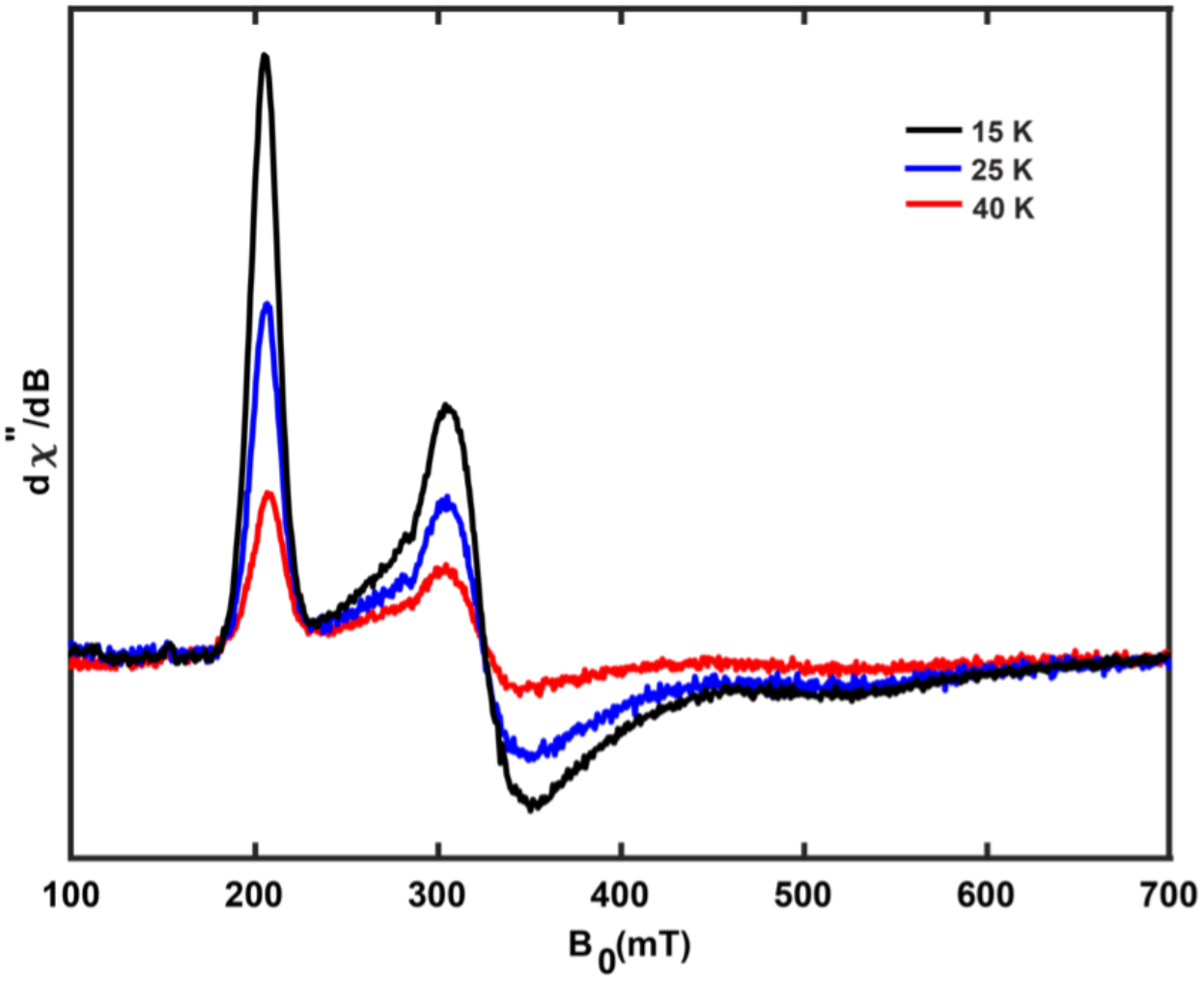

FIGURE 5.4. Temperature dependent EPR spectra. X-band CW EPR spectra of hemes bound to cpTMV-Q101H in their resting ferric states were recorded at 15 K (black line), 25 K (blue line) and 40 K (red line). The spectral features were retained with an intensity decrease of the peaks as temperature increased.Experimental parameters: temperature = 15 K; microwave frequency = 9.38 GHz; microwave power = 2 mW (no saturation); conversion time = 100 ms; modulation amplitude = 0.8 mT; and modulation frequency = 100 kHz.

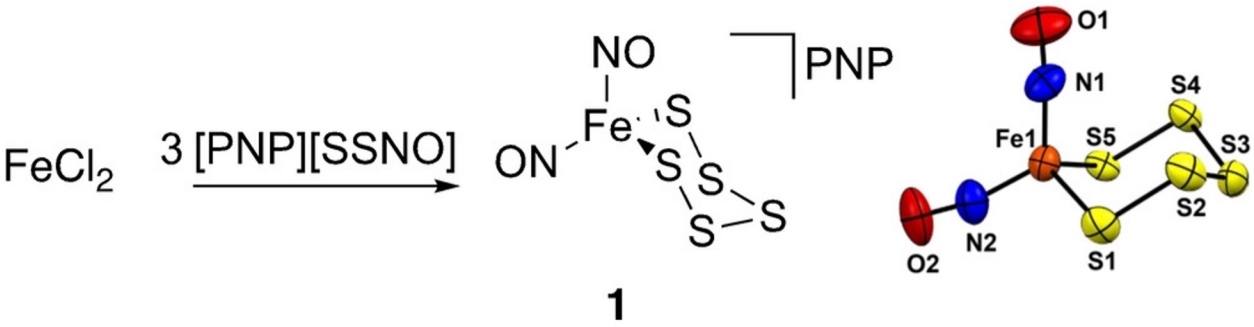

FIGURE 5.5. Synthesis of complex 1 from $FeCl_2$ and [PNP][SSNO]. Solid-state structure of $[Fe(NO)_2(S_5)]^-$ in 1. Ellipsoids are shown at 50% probability levels. Blue, red, orange, and yellow ellipsoids represent N, O, Fe, and S atoms, respectively. The $[PNP]^+$ cation is omitted for clarity.

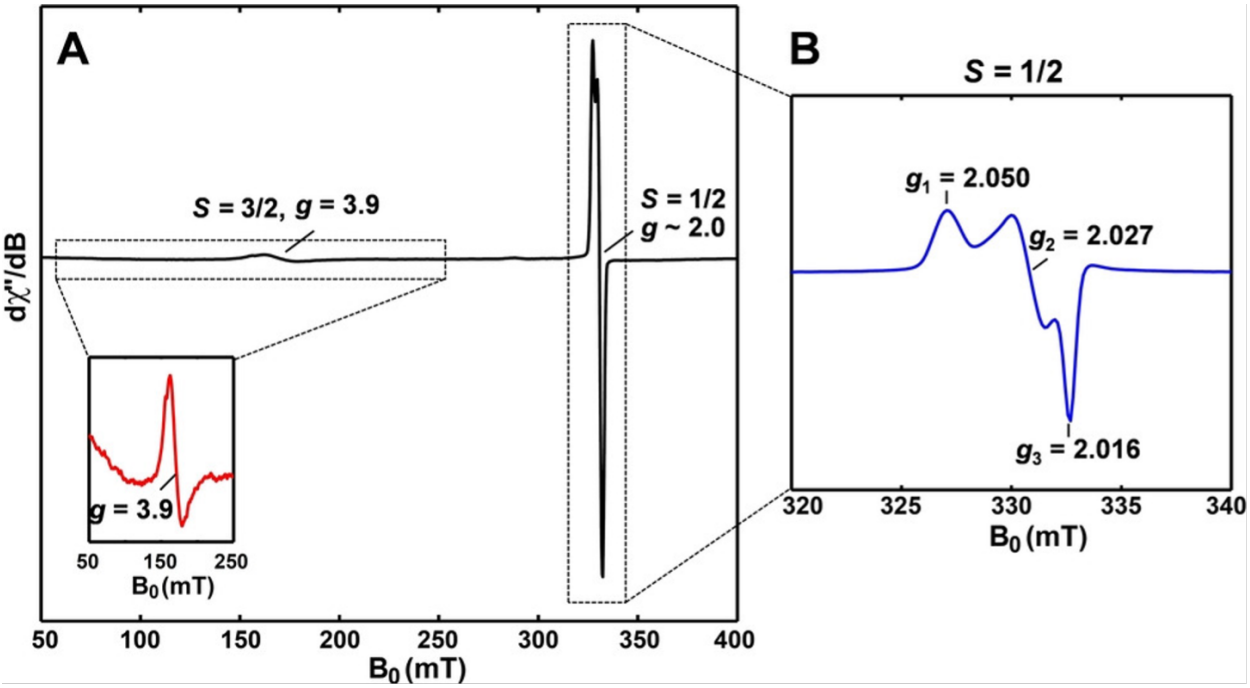

FIGURE 5.6. X-band (9.38 GHz) continuous-wave (CW) EPR spectra (10 K) of frozen-solution crystalline samples from the reaction between $FeCl_2$ and SNO^- in 1:1 toluene/THF. A) A full-spectrum shows both S=3/2 and S=1/2 signals recorded at 10 K, with 6.325 mW microwave power (non-saturating for S=3/2 signal). B) A non-saturating signal for the S=1/2 species obtained by recording the spectrum at 10 K using a much lower microwave power (0.0006325 mW).

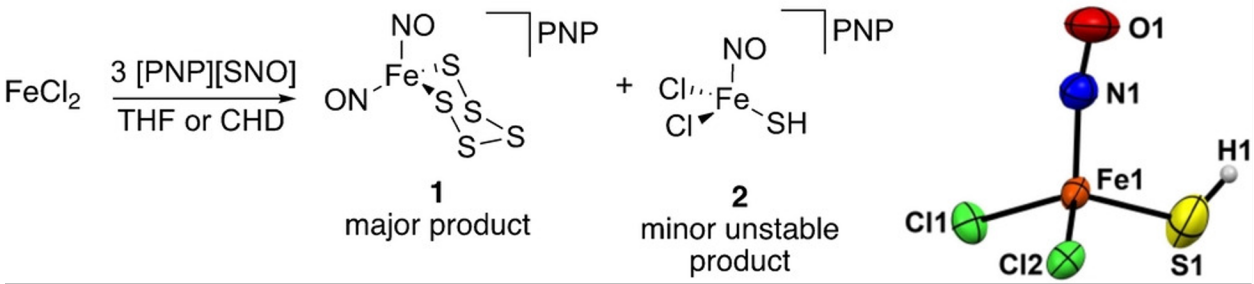

FIGURE 5.7. Products isolated from the reaction of $FeCl_2$ and [PNP][SNO], including the solid state structure of $[Fe(NO)(SH)Cl_2]^-$ in 2. Ellipsoids are shown at 50% probability levels. White, blue, red, green, orange and yellow ellipsoids represent H, N, O, Cl, Fe and S atoms, respectively. The $[PNP]^+$ cation is omitted for clarity.

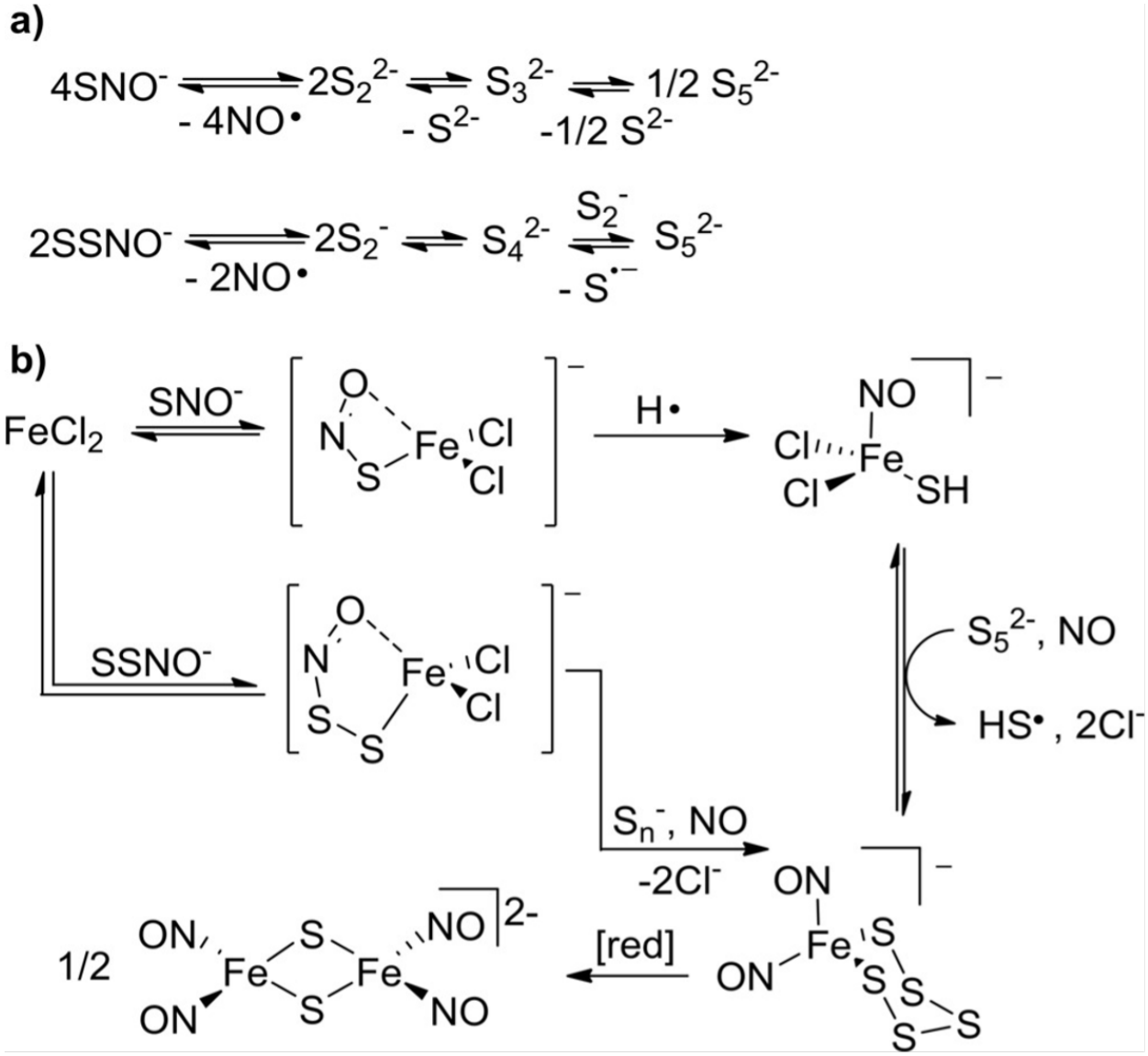

FIGURE 5.8. a) Equilibria showing the formation of polysulfides and NO from $SSNO^-$ and SNO^-. b) Proposed mechanism for the formation of complexes 1, 2, and 3 from SNO^- or $SSNO^-$ and $FeCl_2$.

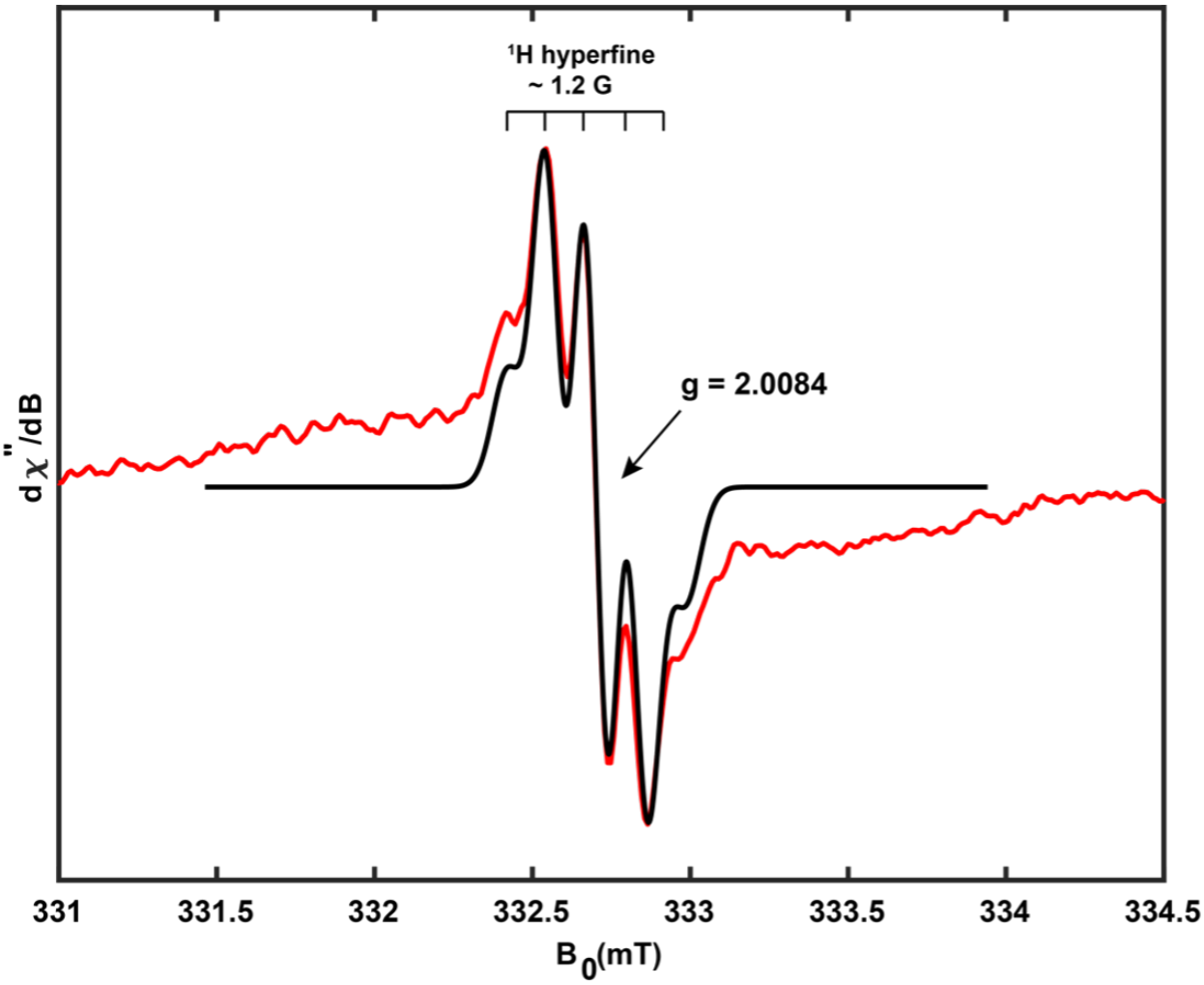

FIGURE 5.9. EPR spectrum of a toluene solution of titanium(IV) tetrachloride and thianthrene at room temperature. In black, the simulated spectrum using identical isotropic hyperfine parameters: A(o-H, ring 1) = A(o-H, ring 2) = A(p-H, ring 1) = A(p-H, ring 2) = 0.12 mT and a simulated linewidth of 0.1 mT.

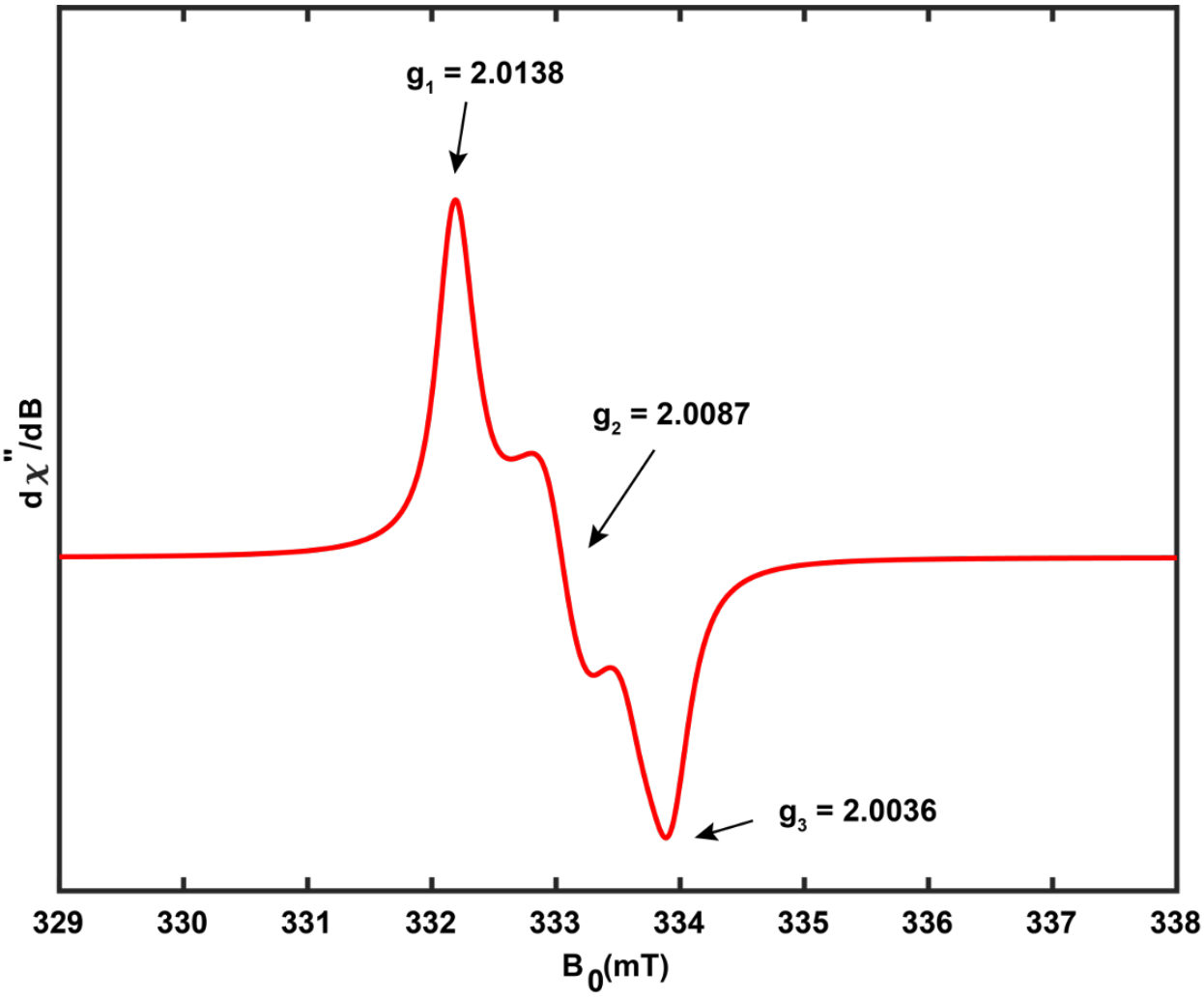

FIGURE 5.10. EPR spectrum of a powder of crystalline (**3**) (thianthrene$^{\cdot+}$)$_2$(Sb$_2$(μ-Cl)$_2$Cl$_6^{2-}$)·(SbCl$_3$).

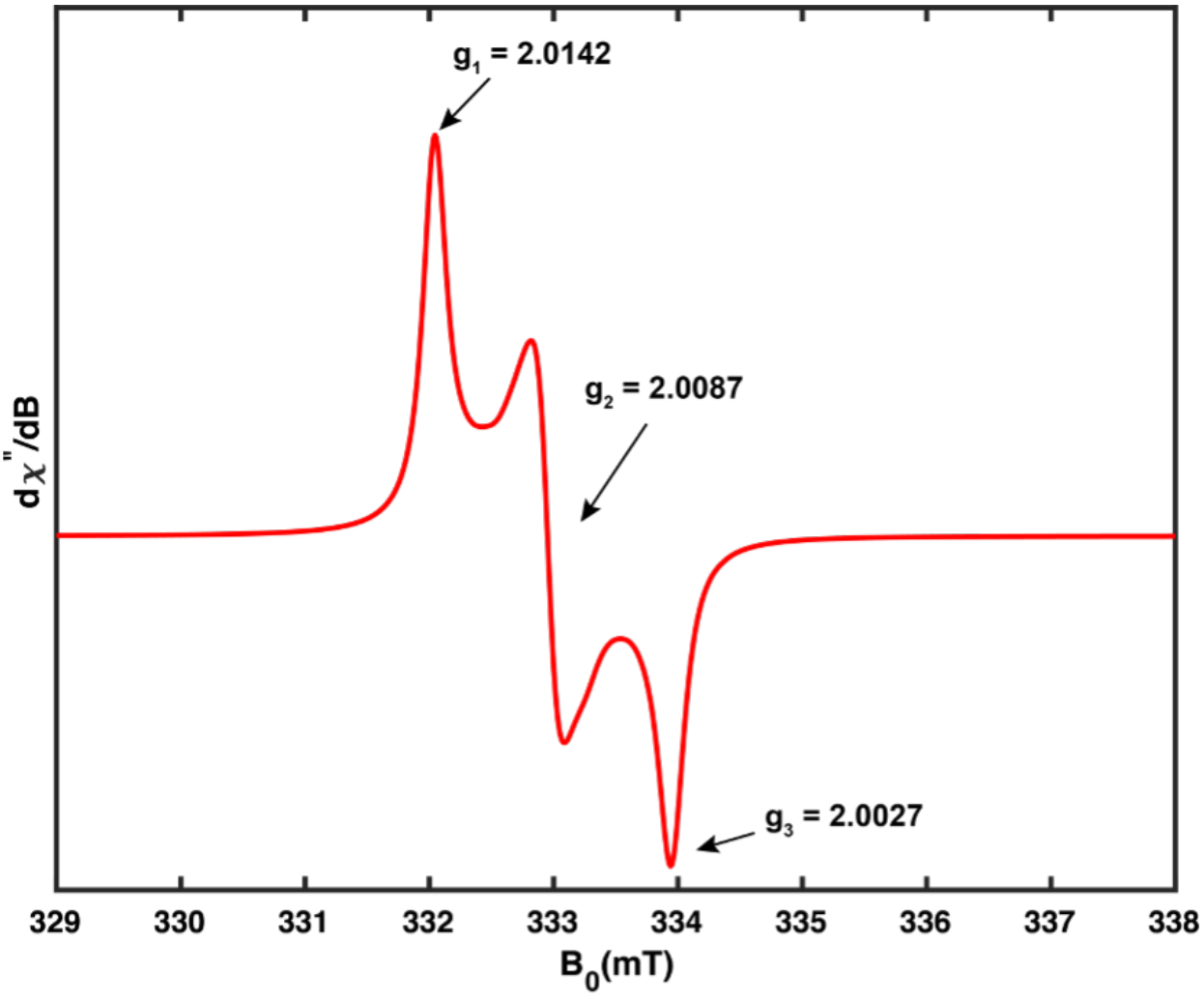

FIGURE 5.11. EPR spectrum of a polycrystalline sample of (**4**) (thianthrene$^{\cdot+}$)($SbCl_6^-$).

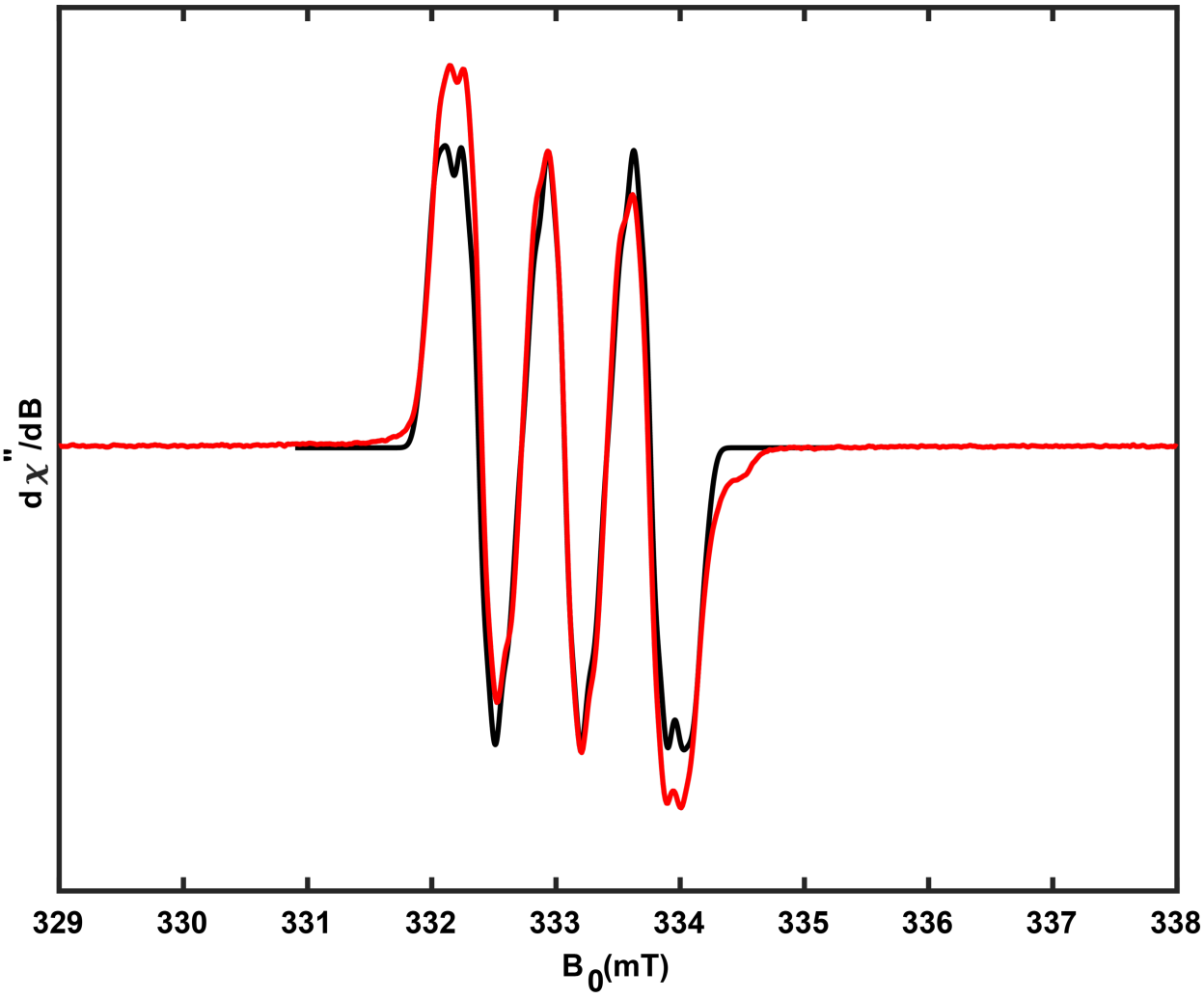

FIGURE 5.12. In red, the experimental EPR spectrum of a solution of 10-phenylphenothiazine and titanium tetrachloride in toluene solution. In black, the simulated spectrum using the isotropic hyperfine parameters from reference [314]: A(N), 0.695; A(1-H), 0.090; A(2-H) 0.022; A(3-H),0.215; A(4-H), 0.090; A(o-H), 0.033; A(m-H), 0.022; A(p-H), 0.012 mT and a simulation linewidth of 0.1 mT.

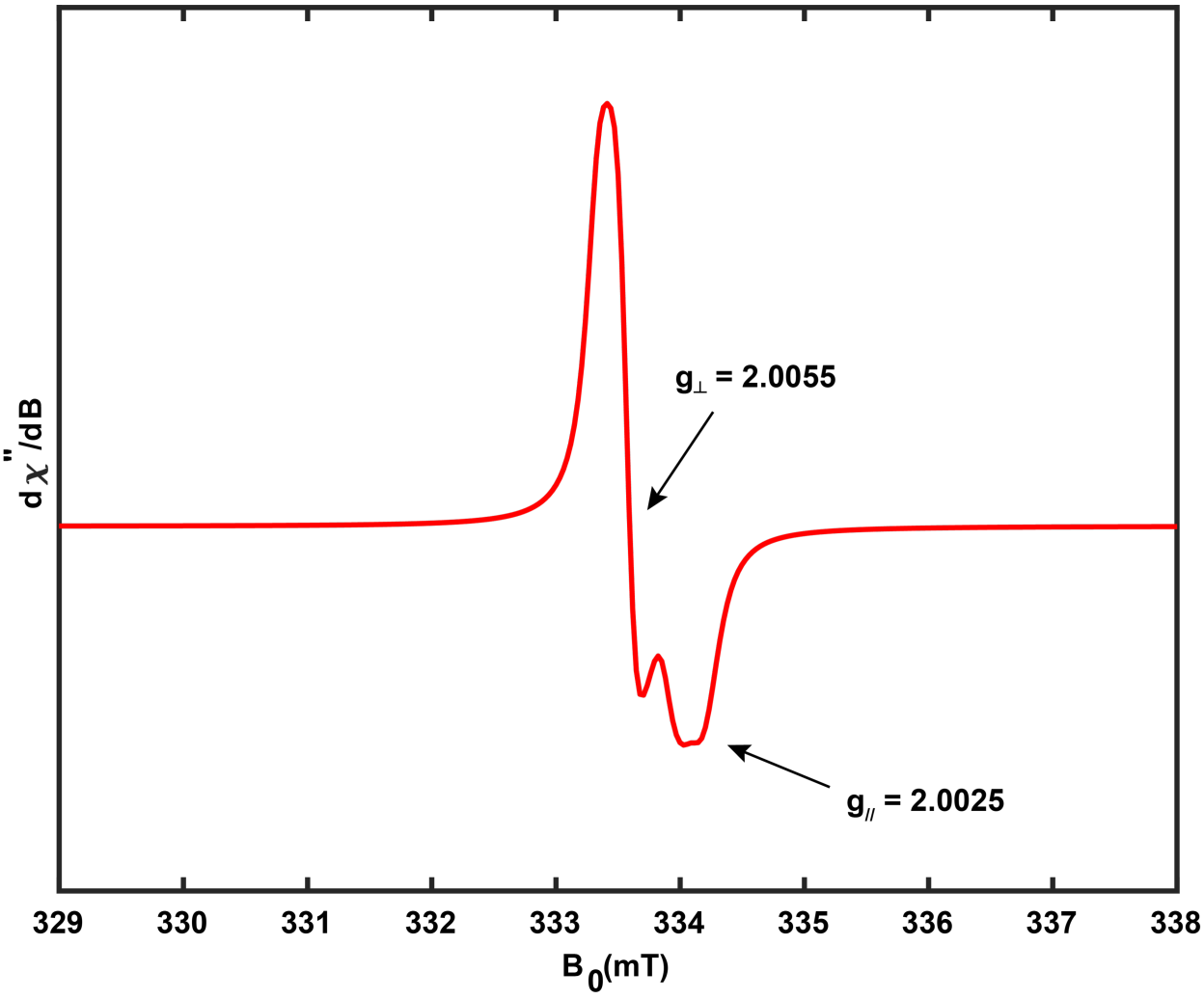

FIGURE 5.13. EPR spectrum of polycrystalline (**5**) (10-phenylphenothiazine$^{\cdot+}$)(Ti(μ-Cl)$_3$Cl$_6^-$).

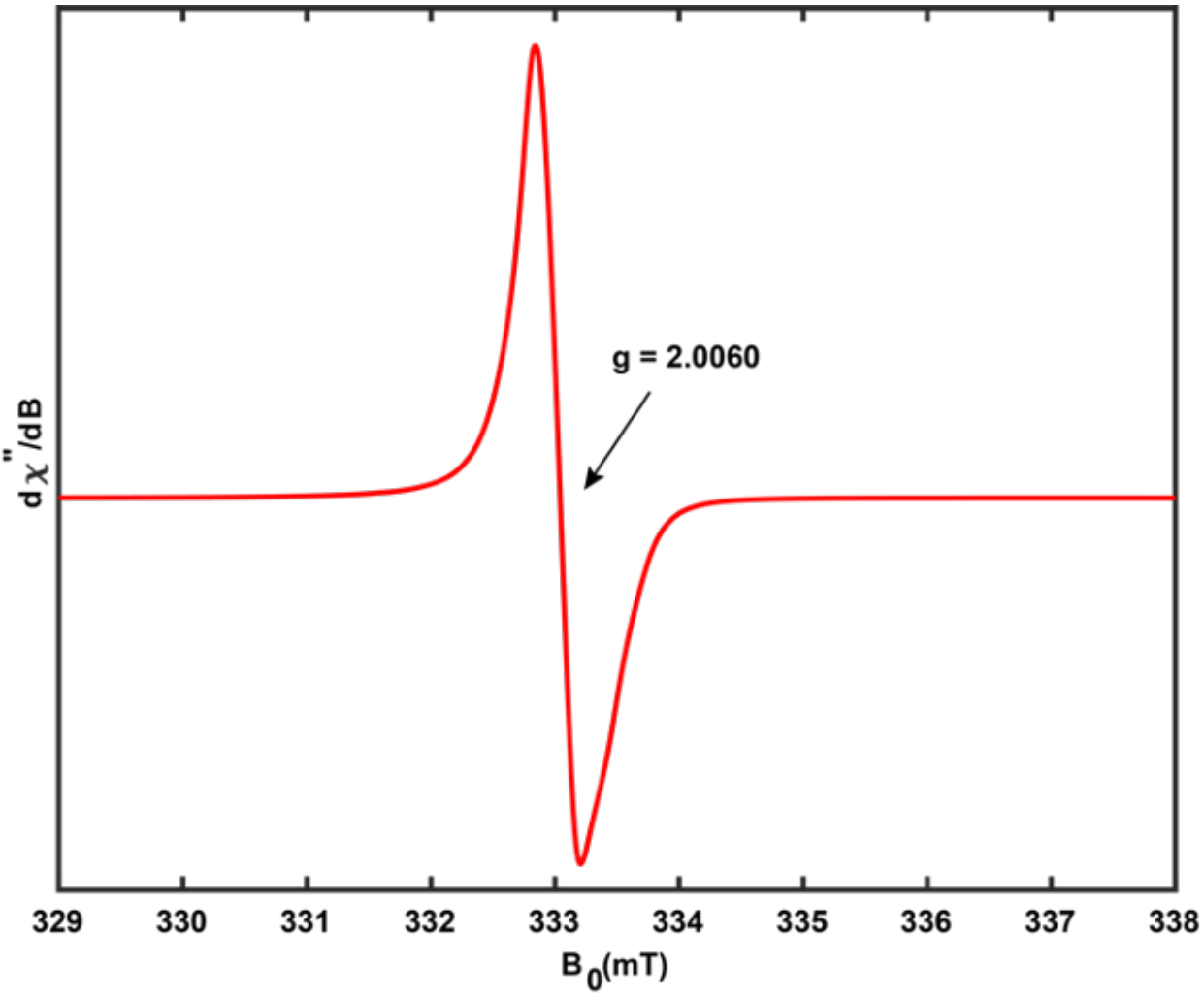

FIGURE 5.14. EPR spectrum of polycrystalline (**6**) (10-phenylphenothiazine$^{\cdot+}$)($SnCl_5^-$).

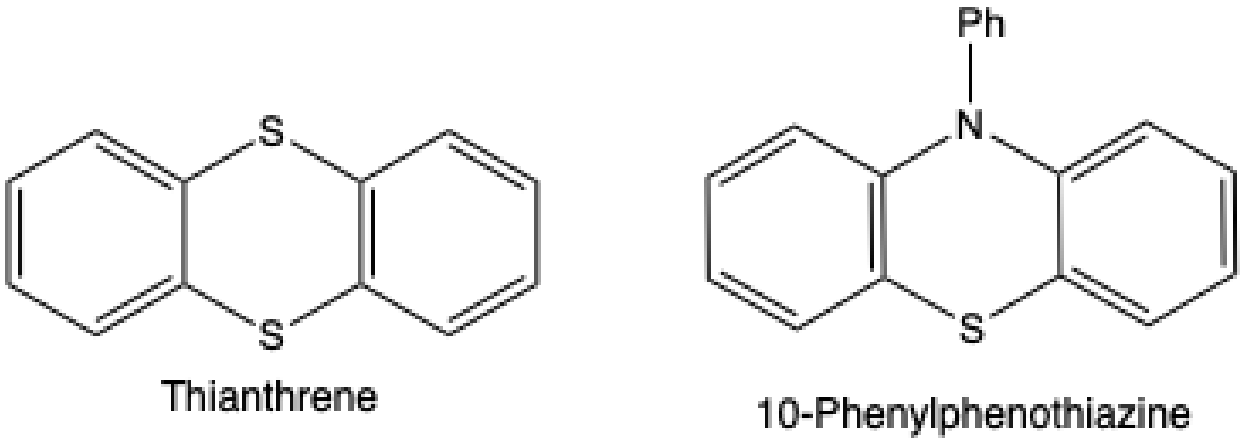

FIGURE 5.15. Structures of the heterocycles: thianthrene and 10-phenylphenothiazine

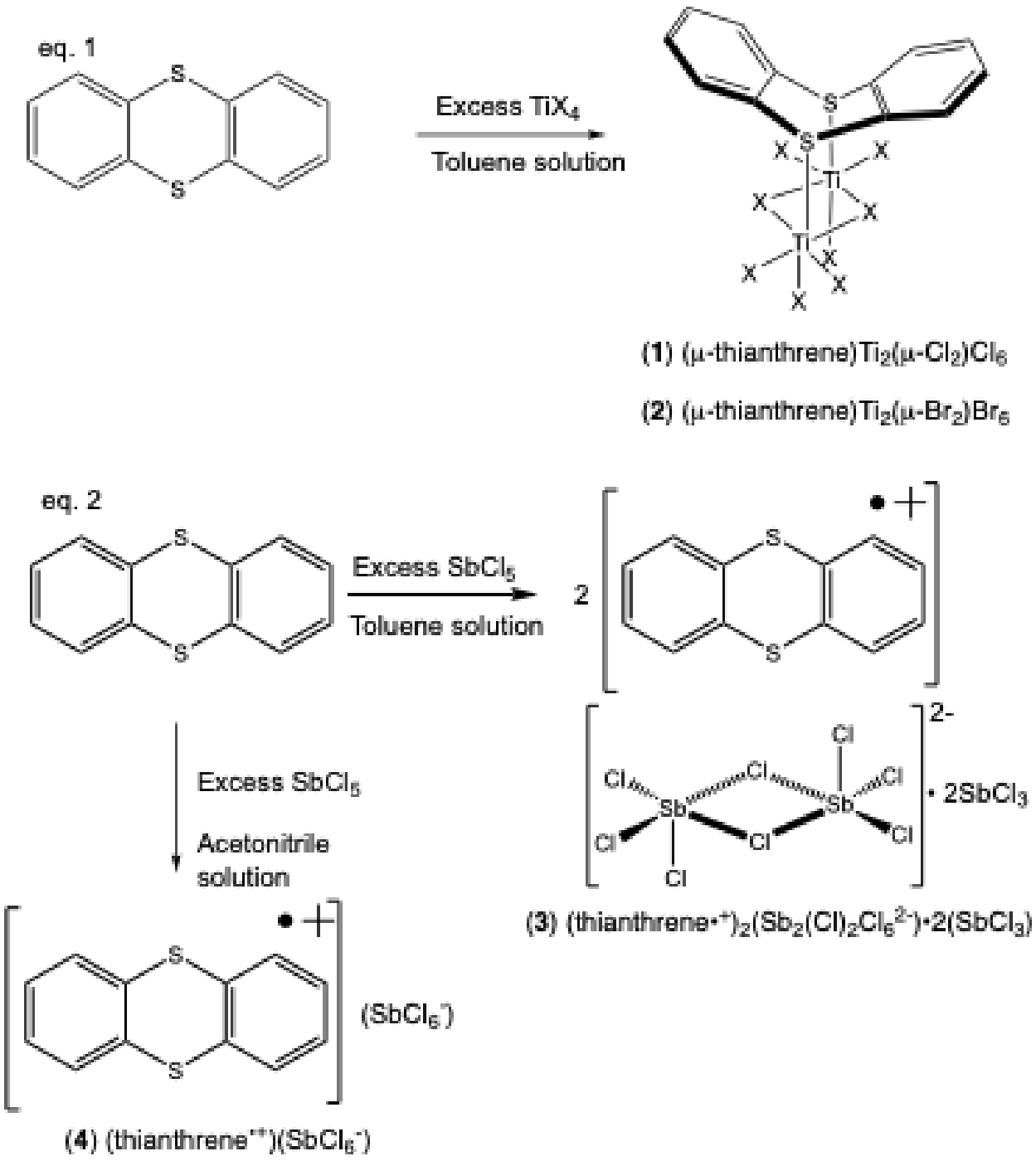

FIGURE 5.16. Crystalline products from thianthrene reactions.

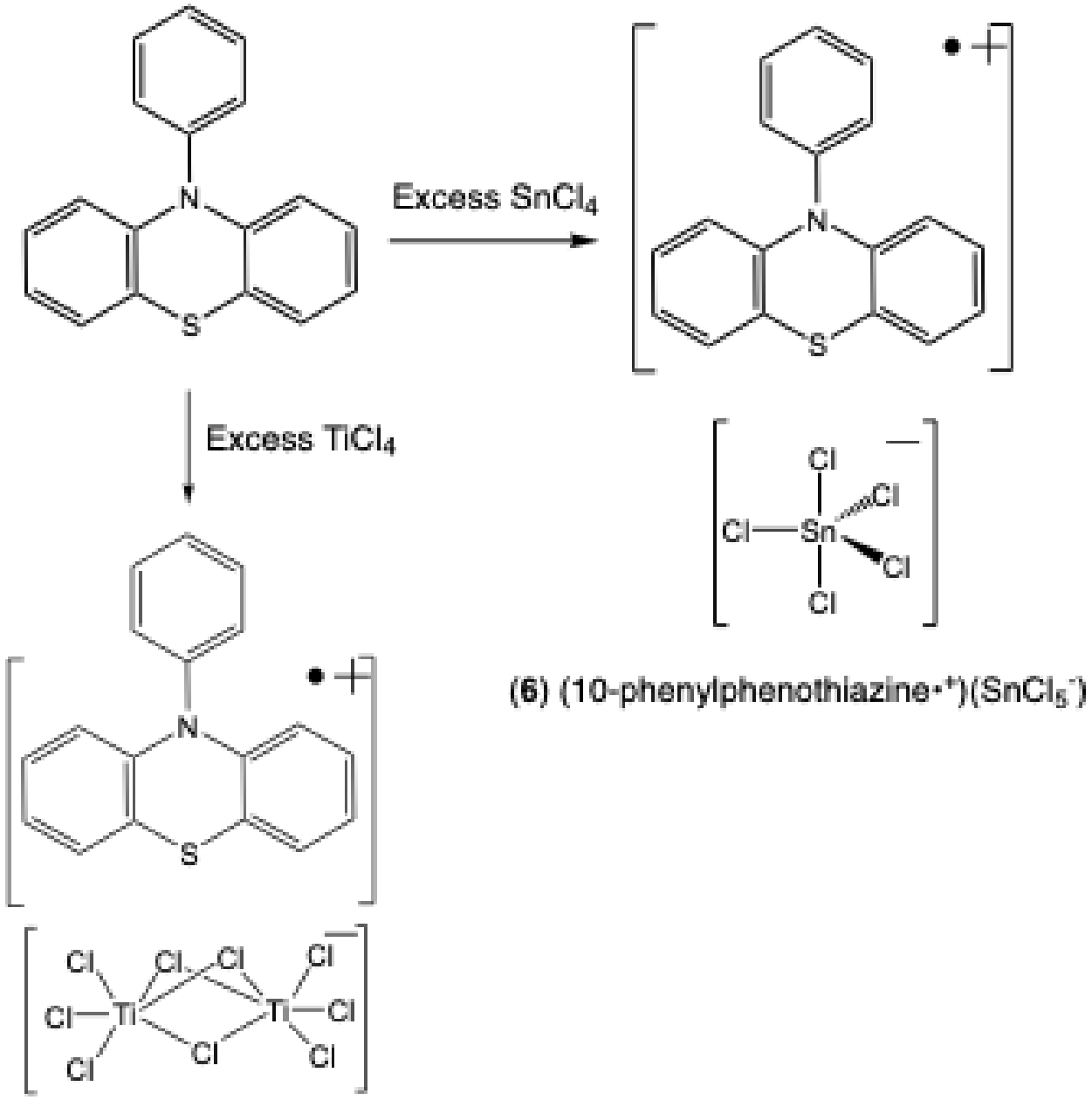

FIGURE 5.17. Crystalline products from 10-phenylphenothiazine reactions in toluene solution

Bibliography

[1] Nathan S. Lewis and Daniel G. Nocera. Powering the planet: Chemical challenges in solar energy utilization. *Proceedings of the National Academy of Sciences of the United States of America*, 103:15729–15735, 2006.

[2] Bryan M. Hunter, Harry B. Gray, and Astrid M. Müller. Earth-abundant heterogeneous water oxidation catalysts. *Chemical Reviews*, 116:14120–14136, 11 2016.

[3] N. S. Lewis, G. Crabtree, A. J. Nozik, M. R. Wasielewski, P. Alivisatos, H. Kung, J. Tsao, E. Chandler, W. Walukiewicz, M. Spitler, R. Ellingson, R. Overend, J. Mazer, M. Gress, J. Horwitz, C. Ashton, B. Herndon, L. Shapard, and R. M. Nault. Basic Research Needs for Solar Energy Utilization. Report of the Basic Energy Sciences Workshop on Solar Energy Utilization, April 18-21, 2005, 4 2005.

[4] David J. Vinyard, Gennady M. Ananyev, and G. Charles Dismukes. Photosystem II: The reaction center of oxygenic photosynthesis. *Annual Review of Biochemistry*, 82:577–606, 2013.

[5] Harry B. Gray. Powering the planet with solar fuel. *Nature Chemistry*, 1:7, 2009.

[6] P. M. Wood. The potential diagram for oxygen at pH 7. *Biochemical Journal*, 253:287–289, 1988.

[7] Fang Song, Lichen Bai, Aliki Moysiadou, Seunghwa Lee, Chao Hu, Laurent Liardet, and Xile Hu. Transition metal oxides as electrocatalysts for the oxygen evolution reaction in alkaline solutions: An application-inspired renaissance. *Journal of the American Chemical Society*, 140:7748–7759, 6 2018.

[8] Maowen Xu, Lingbin Kong, Wenjia Zhou, and Hulin Li. Hydrothermal Synthesis and Pseudocapacitance Properties of α-MnO_2 Hollow Spheres and Hollow Urchins. *The Journal of Physical Chemistry C*, 111:19141–19147, 12 2007.

[9] Marcelo Carmo, David L. Fritz, Jürgen Mergel, and Detlef Stolten. A comprehensive review on pem water electrolysis. *International Journal of Hydrogen Energy*, 38:4901–4934, 4 2013.

[10] Anthony Harriman, Ingrid J. Pickering, John M. Thomas, and Paul A. Christensen. Metal oxides as heterogeneous catalysts for oxygen evolution under photochemical conditions. *Journal of the Chemical Society, Faraday Transactions 1: Physical Chemistry in Condensed Phases*, 84:2795, 1988.

[11] Xueming Chen, Guohua Chen, and Po Lock Yue. Stable Ti/IrO_x-Sb_2O_5-SnO_2 Anode for O_2 Evolution with Low Ir Content. *The Journal of Physical Chemistry B*, 105(20):4623–4628, 2001.

[12] James D. Blakemore, Nathan D. Schley, Gerard W. Olack, Christopher D. Incarvito, Gary W. Brudvig, and Robert H. Crabtree. Anodic deposition of a robust iridium-based water-oxidation catalyst from organometallic precursors. *Chem. Sci.*, 2:94–98, 2011.

[13] Christine Minke, Michel Suermann, Boris Bensmann, and Richard Hanke-Rauschenbach. Is iridium demand a potential bottleneck in the realization of large-scale pem water electrolysis? *International Journal of Hydrogen Energy*, 46(46):23581–23590, 2021.

[14] M. Pourbaix, H. Zhang, and A. Pourbaix. Presentation of an atlas of chemical and electrochemical equilibria in the precence of a gaseous phase. *Materials Science Forum*, 251-254:143–148, 10 1997.

[15] AKIRA FUJISHIMA and KENICHI HONDA. Electrochemical photolysis of water at a semiconductor electrode. *Nature*, 238:37–38, 7 1972.

[16] Mathieu S. Prévot and Kevin Sivula. Photoelectrochemical tandem cells for solar water splitting. *The Journal of Physical Chemistry C*, 117:17879–17893, 9 2013.

[17] Aron Walsh, Yanfa Yan, Muhammad N. Huda, Mowafak M. Al-Jassim, and Su-Huai Wei. Band Edge Electronic Structure of $BiVO_4$: Elucidating the Role of the Bi s and V d Orbitals. *Chemistry of Materials*, 21:547–551, 2 2009.

[18] J. E. Turner, M. Hendewerk, J. Parmeter, D. Neiman, and G. A. Somorjai. The characterization of doped iron oxide electrodes for the photodissociation of water: Stability, optical, and electronic properties. *Journal of The Electrochemical Society*, 131:1777–1783, 8 1984.

[19] Jialei Du, Zuofeng Chen, Shengrong Ye, Benjamin J. Wiley, and Thomas J. Meyer. Copper as a robust and transparent electrocatalyst for water oxidation. *Angewandte Chemie International Edition*, 54:2073–2078, 2 2015.

[20] Shengsheng Cui, Xiang Liu, Zijun Sun, and Pingwu Du. Noble metal-free copper hydroxide as an active and robust electrocatalyst for water oxidation at weakly basic pH. *ACS Sustainable Chemistry & Engineering*, 4:2593–2600, 5 2016.

[21] Chaoran Jiang, Savio J. A. Moniz, Majeda Khraisheh, and Junwang Tang. Earth-Abundant Oxygen Evolution Catalysts Coupled onto ZnO Nanowire Arrays for Efficient Photoelectrochemical Water Cleavage. *Chemistry - A European Journal*, 20:12954–12961, 9 2014.

[22] Jin-Yue Li, Xing-Long Wu, Xiao-Hua Zhang, Hong-Yan Lü, Guang Wang, Jin-Zhi Guo, Fang Wan, and Rong-Shun Wang. Romanechite-structured $Na_{0.31}MnO_{1.9}$ nanofibers as high-performance cathode material for a sodium-ion battery. *Chemical Communications*, 51:14848–14851, 2015.

[23] P. Oliva, J. Leonardi, J.F. Laurent, C. Delmas, J.J. Braconnier, M. Figlarz, F. Fievet, and A.de Guibert. Review of the structure and the electrochemistry of nickel hydroxides and oxy-hydroxides. *Journal of Power Sources*, 8:229–255, 1 1982.

[24] Matthew W. Kanan and Daniel G. Nocera. In situ formation of an oxygen-evolving catalyst in neutral water containing phosphate and co^{2+}. *Science*, 321:1072–1075, 8 2008.

[25] J. Gregory McAlpin, Yogesh Surendranath, Mircea Dincă, Troy A. Stich, Sebastian A. Stoian, William H. Casey, Daniel G. Nocera, and R. David Britt. EPR Evidence for Co(IV) Species Produced During Water Oxidation at Neutral pH. *Journal of the American Chemical Society*, 132:6882–6883, 5 2010.

[26] Marcel Risch, Katharina Klingan, Franziska Ringleb, Petko Chernev, Ivelina Zaharieva, Anna Fischer, and Holger Dau. Water Oxidation by Electrodeposited Cobalt Oxides—Role of Anions and Redox-Inert Cations in Structure and Function of the Amorphous Catalyst. *ChemSusChem*, 5:542–549, 3 2012.

[27] Michael E.G. Lyons and Michael P. Brandon. The Oxygen Evolution Reaction on Passive Oxide Covered Transition Metal Electrodes in Alkaline Solution Part II - Cobalt. *International Journal of Electrochemical Science*, 3:1425–1462, 12 2008.

[28] Matthew W. Kanan, Junko Yano, Yogesh Surendranath, Mircea Dincă, Vittal K. Yachandra, and Daniel G. Nocera. Structure and valency of a cobalt-phosphate water oxidation catalyst determined by in situ x-ray spectroscopy. *Journal of the American Chemical Society*, 132:13692–13701, 10 2010.

[29] Arti Dangwal Pandey, Chunjiang Jia, Wolfgang Schmidt, Matteo Leoni, Manfred Schwickardi, Ferdi Schüth, and Claudia Weidenthaler. Size-Controlled Synthesis and Microstructure Investigation of Co_3O_4 Nanoparticles for Low-Temperature CO Oxidation. *The Journal of Physical Chemistry C*, 116:19405–19412, 9 2012.

[30] James D. Blakemore, Harry B. Gray, Jay R. Winkler, and Astrid M. Müller. Co_3O_4 Nanoparticle Water-Oxidation Catalysts Made by Pulsed-Laser Ablation in Liquids. *ACS Catalysis*, 3:2497–2500, 11 2013.

[31] Marek Grzelczak, Jinshui Zhang, Johannes Pfrommer, Jürgen Hartmann, Matthias Driess, Markus Antonietti, and Xinchen Wang. Electro- and Photochemical Water Oxidation on Ligand-free Co_3O_4 Nanoparticles with Tunable Sizes. *ACS Catalysis*, 3:383–388, 3 2013.

[32] Graeme P. Gardner, Yong Bok Go, David M. Robinson, Paul F. Smith, Joke Hadermann, Artem Abakumov, Martha Greenblatt, and G. Charles Dismukes. Structural Requirements in Lithium Cobalt Oxides for the Catalytic Oxidation of Water. *Angewandte Chemie International Edition*, 51:1616–1619, 2 2012.

[33] Fang Song and Xile Hu. Ultrathin Cobalt–Manganese Layered Double Hydroxide Is an Efficient Oxygen Evolution Catalyst. *Journal of the American Chemical Society*, 136:16481–16484, 11 2014.

[34] Roger Buick. When did oxygenic photosynthesis evolve. *Philosophical Transactions of the Royal Society B: Biological Sciences*, 363:2731–2743, 8 2008.

[35] Nathan Nelson and Adam Ben-Shem. The complex architecture of oxygenic photosynthesis. *Nature Reviews Molecular Cell Biology*, 5:971–982, 12 2004.

[36] Donald A. Bryant and Niels-Ulrik Frigaard. Prokaryotic photosynthesis and phototrophy illuminated. *Trends in Microbiology*, 14:488–496, 11 2006.

[37] M. Wiechen, M. M. Najafpour, S. I. Allakhverdiev, and L. Spiccia. Water oxidation catalysis by manganese oxides: learning from evolution. *Energy & Environmental Science*, 7:2203, 2014.

[38] Donald R. Ort, Charles F. Yocum, and Iris F. Heichel, editors. *Electron Transfer and Energy Transduction in Photosynthesis: An Overview*, pages 1–9. Springer Netherlands, Dordrecht, 1996.

[39] Yasufumi Umena, Keisuke Kawakami, Jian Ren Shen, and Nobuo Kamiya. Crystal structure of oxygen-evolving photosystem II at a resolution of 1.9Å. *Nature*, 473:55–60, 2011.

[40] Jeffrey M. Peloquin and R.David Britt. EPR/ENDOR characterization of the physical and electronic structure of the OEC Mn cluster. *Biochimica et Biophysica Acta (BBA) - Bioenergetics*, 1503:96–111, 1 2001.

[41] Holger Dau, Lucia Iuzzolino, and Jens Dittmer. The tetra-manganese complex of photosystem II during its redox cycle – X-ray absorption results and mechanistic implications. *Biochimica et Biophysica Acta (BBA) - Bioenergetics*, 1503:24–39, 1 2001.

[42] John H Robblee, Roehl M Cinco, and Vittal K Yachandra. X-ray spectroscopy-based structure of the Mn cluster and mechanism of photosynthetic oxygen evolution. *Biochimica et Biophysica Acta (BBA) - Bioenergetics*, 1503:7–23, 1 2001.

[43] R.David Britt, Kristy A Campbell, Jeffrey M Peloquin, M.Lane Gilchrist, Constantino P Aznar, Michelle M Dicus, John Robblee, and Johannes Messinger. Recent pulsed EPR studies of the Photosystem II oxygen-evolving complex: implications as to water oxidation mechanisms. *Biochimica et Biophysica Acta (BBA) - Bioenergetics*, 1655:158–171, 4 2004.

[44] Catherine Berthomieu and Rainer Hienerwadel. Vibrational spectroscopy to study the properties of redox-active tyrosines in photosystem II and other proteins. *Biochimica et Biophysica Acta (BBA) - Bioenergetics*, 1707:51–66, 2 2005.

[45] Takumi Noguchi and Miwa Sugiura. Structure of an Active Water Molecule in the Water-Oxidizing Complex of Photosystem II As Studied by FTIR Spectroscopy. *Biochemistry*, 39:10943–10949, 9 2000.

[46] Warwick Hillier and Tom Wydrzynski. Substrate water interactions within the Photosystem II oxygen evolving complex. *Physical Chemistry Chemical Physics*, 6:4882, 2004.

[47] Per E. M. Siegbahn. Mechanisms of metalloenzymes studied by quantum chemical methods. *Quarterly Reviews of Biophysics*, 36:91–145, 2 2003.

[48] Holger Dau and Michael Haumann. Eight steps preceding O–O bond formation in oxygenic photosynthesis—A basic reaction cycle of the Photosystem II manganese complex. *Biochimica et Biophysica Acta (BBA) - Bioenergetics*, 1767:472–483, 6 2007.

[49] Thomas J. Meyer, My Hang V. Huynh, and H. Holden Thorp. The Possible Role of Proton-Coupled Electron Transfer (PCET) in Water Oxidation by Photosystem II. *Angewandte Chemie International Edition*, 46:5284–5304, 7 2007.

[50] Bessel Kok, Bliss Forbush, and Marion McGloin. Cooperation of charges in photosynthetic o_2 evolution-i. a linear four step mechanism. *Photochemistry and Photobiology*, 11:457–475, 6 1970.

[51] R. J. Debus, B. A. Barry, I. Sithole, Gerald T. Babcock, and L. McIntosh. Directed mutagenesis indicates that the donor to P680+ in photosystem II is tyrosine-161 of the D1 polypeptide. *Biochemistry*, 27:9071–9074, 12 1988.

[52] David A. Marchiori, Richard J. Debus, and R. David Britt. Pulse EPR Spectroscopic Characterization of the S3 State of the Oxygen-Evolving Complex of Photosystem II Isolated from Synechocystis. *Biochemistry*, 59:4864–4872, 12 2020.

[53] Heui Beom Lee, Angela A. Shiau, Paul H. Oyala, David A. Marchiori, Sheraz Gul, Ruchira Chatterjee, Junko Yano, R. David Britt, and Theodor Agapie. Tetranuclear [$MnIIIMn_3IVO_4$] Complexes as Spectroscopic Models of the S2 State of the Oxygen Evolving Complex in Photosystem II. *Journal of the American Chemical Society*, 140:17175–17187, 12 2018.

[54] David M. Sherman. The electronic structures of manganese oxide minerals. *American Mineralogist*, 69(7-8):788–799, 08 1984.

[55] M. Morita, C. Iwakura, and H. Tamura. The anodic characteristics of manganese dioxide electrodes prepared by thermal decomposition of manganese nitrate. *Electrochimica Acta*, 22:325–328, 4 1977.

[56] Feng Jiao and Heinz Frei. Nanostructured manganese oxide clusters supported on mesoporous silica as efficient oxygen-evolving catalysts. *Chemical Communications*, 46:2920, 2010.

[57] Blaise A. Pinaud, Zhebo Chen, David N. Abram, and Thomas F. Jaramillo. Thin Films of Sodium Birnessite-Type MnO_2 : Optical Properties, Electronic Band Structure, and Solar Photoelectrochemistry. *The Journal of Physical Chemistry C*, 115:11830–11838, 6 2011.

[58] Mathias Wiechen, Ivelina Zaharieva, Holger Dau, and Philipp Kurz. Layered manganese oxides for water-oxidation: alkaline earth cations influence catalytic activity in a photosystem II-like fashion. *Chemical Science*, 3:2330, 2012.

[59] Ivelina Zaharieva, Petko Chernev, Marcel Risch, Katharina Klingan, Mike Kohlhoff, Anna Fischer, and Holger Dau. Electrosynthesis, functional, and structural characterization of a water-oxidizing manganese oxide. *Energy & Environmental Science*, 5:7081, 2012.

[60] Mohammad Mahdi Najafpour, Mohsen Kompany-Zareh, Ali Zahraei, Davood Jafarian Sedigh, Hugues Jaccard, Maryam Khoshkam, R. David Britt, and William H. Casey. Mechanism, decomposition pathway and new evidence for self-healing of manganese oxides as efficient water oxidizing catalysts: new insights. *Dalton Transactions*, 42:14603, 2013.

[61] Bhim Prasad Kafle. *Introduction to nanomaterials and application of UV–Visible spectroscopy for their characterization*, pages 147–198. Elsevier, 2020.

[62] Guohong Qiu, Hui Huang, Saminda Dharmarathna, Evan Benbow, Lisa Stafford, and Steven L. Suib. Hydrothermal synthesis of manganese oxide nanomaterials and their catalytic and electrochemical properties. *Chemistry of Materials*, 23:3892–3901, 9 2011.

[63] Yu-Xin Miao, Li-Hui Ren, Lei Shi, and Wen-Cui Li. Hydrothermal synthesis of manganese oxide nanorods as a highly active support for gold nanoparticles in co oxidation and their stability at low temperature. *RSC Advances*, 5:62732–62738, 2015.

[64] M.A. Yewale, A.A. Jadhavar, R.A. Kadam, N.B. Velhal, Umesh T. Nakate, A.M. Teli, J.C. Shin, L.N. Nguyen, D.K. Shin, and N.K. Kaushik. Hydrothermal synthesis of manganese oxide (Mn_3O_4) with granule-like morphology for supercapacitor application. *Ceramics International*, 48:29429–29437, 10 2022.

[65] Shifeng Hong, Shuo Jin, Yue Deng, Regina Garcia-Mendez, Keun il Kim, Nyalaliska Utomo, and Lynden A. Archer. Efficient scalable hydrothermal synthesis of mno_2 with controlled polymorphs and morphologies for enhanced battery cathodes. *ACS Energy Letters*, 8:1744–1751, 4 2023.

[66] A.J. Bard, L.R. Faulkner, and H.S. White. *Electrochemical Methods: Fundamentals and Applications*. Wiley, 2022.

[67] Michael Huynh, D. Kwabena Bediako, Yi Liu, and Daniel G. Nocera. Nucleation and growth mechanisms of an electrodeposited manganese oxide oxygen evolution catalyst. *The Journal of Physical Chemistry C*, 118:17142–17152, 7 2014.

[68] Lizhi Tao, Troy A. Stich, Hugues Jaccard, R. David Britt, and William H. Casey. *Manganese-Oxide Solids as Water-Oxidation Electrocatalysts: The Effect of Intercalating Cations*, pages 135–153. ACS Symposium Series eBooks, 1 2015.

[69] R.G. Bates and J.B. MacAskill. Standard potential of the silver-silver chloride electrode. *Pure and Applied Chemistry*, 50:1701–1706, 1 1978.

[70] Michael Huynh, D Kwabena Bediako, and Daniel G Nocera. A functionally stable manganese oxide oxygen evolution catalyst in acid. *Journal of the American Chemical Society*, 136:6002–6010, 4 2014.

[71] C. Augello and H. Liu. *Surface modification of magnesium by functional polymer coatings for neural applications*, pages 335–353. Elsevier, 2015.

[72] G. Helen Annal Therese and P. Vishnu Kamath. Electrochemical synthesis of $lamno_3$ coatings on conducting substrates. *Chemistry of Materials*, 10:3364–3367, 11 1998.

[73] Elena Kalinina and Elena Pikalova. Opportunities, challenges and prospects for electrodeposition of thin-film functional layers in solid oxide fuel cell technology. *Materials*, 14:5584, 9 2021.

[74] Tirukoti Mounika, Shiddappa L. Belagali, and K.T. Vadiraj. Manganese oxide nanoparticles synthesis route, characterization and optical properties. *Materials Today: Proceedings*, 75:72–76, 2023.

[75] R. M. McKenzie. The synthesis of birnessite, cryptomelane, and some other oxides and hydroxides of manganese. *Mineralogical Magazine*, 38:493–502, 12 1971.

[76] Mohammad Mahdi Najafpour and Atefeh Nemati Moghaddam. Nano-sized manganese oxide: a proposed catalyst for water oxidation in the reaction of some manganese complexes and cerium(IV) ammonium nitrate. *Dalton Transactions*, 41:10292, 2012.

[77] Alexander R. Parent, Robert H. Crabtree, and Gary W. Brudvig. Comparison of primary oxidants for water-oxidation catalysis. *Chem. Soc. Rev.*, 42:2247–2252, 2013.

[78] Ravi Pokhrel, McKenna K. Goetz, Sarah E. Shaner, Xiaoxia Wu, and Shannon S. Stahl. The "best catalyst" for water oxidation depends on the oxidation method employed: A case study of manganese oxides. *Journal of the American Chemical Society*, 137:8384–8387, 7 2015.

[79] Alejandra Ramírez, Philipp Hillebrand, Diana Stellmach, Matthias M. May, Peter Bogdanoff, and Sebastian Fiechter. Evaluation of MnO_x, Mn_2O_3, and Mn_3O_4 Electrodeposited Films for the Oxygen Evolution Reaction of Water. *The Journal of Physical Chemistry C*, 118:14073–14081, 7 2014.

[80] Moritz Kölbach, Sebastian Fiechter, Roel van de Krol, and Peter Bogdanoff. Evaluation of electrodeposited α-Mn_2O_3 as a catalyst for the oxygen evolution reaction. *Catalysis Today*, 290:2–9, 7 2017.

[81] Lizhi Tao, Troy A. Stich, Cristina N. Butterfield, Christine A. Romano, Thomas G. Spiro, Bradley M. Tebo, William H. Casey, and R. David Britt. Mn(II) Binding and Subsequent Oxidation by the Multicopper Oxidase MnxG Investigated by Electron Paramagnetic Resonance Spectroscopy. *Journal of the American Chemical Society*, 137:10563–10575, 8 2015.

[82] Michael Huynh, Chenyang Shi, Simon J. L. Billinge, and Daniel G. Nocera. Nature of activated manganese oxide for oxygen evolution. *Journal of the American Chemical Society*, 137:14887–14904, 12 2015.

[83] Siavash Iravani. Green synthesis of metal nanoparticles using plants. *Green Chemistry*, 13:2638, 2011.

[84] Asmaa Mohamed El Shafey. Green synthesis of metal and metal oxide nanoparticles from plant leaf extracts and their applications: A review. *Green Processing and Synthesis*, 9:304–339, 6 2020.

[85] Muhammad Noman, Temoor Ahmed, Usman Ijaz, Muhammad Shahid, Muhammad Mudassir Nazir, Azizullah, Jason C. White, Dayong Li, and Fengming Song. Bio-functionalized manganese nanoparticles suppress fusarium wilt in watermelon (citrullus lanatus l.) by infection disruption, host defense response potentiation, and soil microbial community modulation. *Small*, 19, 1 2023.

[86] Mitchell H. Wright, Saad M. Farooqui, Alan R. White, and Anthony C. Greene. Production of manganese oxide nanoparticles by shewanella species. *Applied and Environmental Microbiology*, 82:5402–5409, 9 2016.

[87] Jin Liu, Liandong Feng, and Yuzhou Wu. Enzymatically synthesised MnO_2 nanoparticles for efficient near-infrared photothermal therapy and dual-responsive magnetic resonance imaging. *Nanoscale*, 13:11093–11103, 2021.

[88] Mohsen Safaei and Ayoub Moghadam. Optimization of the synthesis of novel alginate-manganese oxide bionanocomposite by taguchi design as antimicrobial dental impression material. *Materials Today Communications*, 31:103698, 6 2022.

[89] Karolina M. Furgal, Rikke L. Meyer, and Kai Bester. Removing selected steroid hormones, biocides and pharmaceuticals from water by means of biogenic manganese oxide nanoparticles in situ at ppb levels. *Chemosphere*, 136:321–326, 10 2015.

[90] Xin Zhang, Kandasamy Saravanakumar, Anbazhagan Sathiyaseelan, and Myeong-Hyeon Wang. Biosynthesis, characterization, antibacterial activities of manganese nanoparticles using arcopilus globulus and their efficiency in degradation of bisphenol a. *Inorganic Chemistry Communications*, 141:109521, 7 2022.

[91] Bipinchandra K. Salunke, Shailesh S. Sawant, Sang-Ill Lee, and Beom Soo Kim. Comparative study of MnO_2 nanoparticle synthesis by marine bacterium Saccharophagus degradans and yeast Saccharomyces cerevisiae. *Applied Microbiology and Biotechnology*, 99:5419–5427, 7 2015.

[92] Debasish Borah, Jayashree Rout, Debika Gogoi, Narendra Nath Ghosh, and Chira R. Bhattacharjee. Composition controllable green synthesis of manganese dioxide nanoparticles using an edible freshwater red alga and its photocatalytic activity towards water soluble toxic dyes. *Inorganic Chemistry Communications*, 138:109312, 4 2022.

[93] G. Sivaprakash, K. Mohanrasu, V. Ananthi, M. Jothibasu, Dinh Duc Nguyen, B. Ravindran, Soon Woong Chang, Phuong Nguyen-Tri, Ngoc Han Tran, M. Sudhakar, K. Gurunathan, S. Arokiyaraj, and A. Arun. Biodiesel production from Ulva linza, Ulva tubulosa, Ulva fasciata, Ulva rigida, Ulva reticulate by using Mn_2ZnO_4 heterogenous nanocatalysts. *Fuel*, 255:115744, 11 2019.

[94] Xin Zhang, Anbazhagan Sathiyaseelan, Kumar Vishven Naveen, Yuting Lu, and Myeong-Hyeon Wang. Research progress in green synthesis of manganese and manganese oxide nanoparticles in biomedical and environmental applications – a review. *Chemosphere*, 337:139312, 10 2023.

[95] Kenneth H. Nealson, Bradley M. Tebo, and Reinhardt A. Rosson. *Occurrence and Mechanisms of Microbial Oxidation of Manganese*, pages 279–318. 1988.

[96] H.L. Ehrlich. *Geomicrobiology*. CRC Press, 4 2002.

[97] A.P. Das, L.B. Sukla, N. Pradhan, and S. Nayak. Manganese biomining: A review. *Bioresource Technology*, 102:7381–7387, 8 2011.

[98] J P de Vrind, F C Boogerd, and E W de Vrind-de Jong. Manganese reduction by a marine bacillus species. *Journal of Bacteriology*, 167:30–34, 7 1986.

[99] Elena A. Podorozhko, Vladimir I. Lozinsky, Irena B. Ivshina, Maria S. Kuyukina, Anastasiya B. Krivorutchko, Jim C. Philp, and Colin J. Cunningham. Hydrophobised sawdust as a carrier for immobilisation of the hydrocarbon-oxidizing bacterium rhodococcus ruber. *Bioresource Technology*, 99:2001–2008, 4 2008.

[100] Frederick Archibald. Lactobacillus plantarum, an organism not requiring iron. *FEMS Microbiology Letters*, 19:29–32, 6 1983.

[101] Alastair G. McEwan. New insights into the protective effect of manganese against oxidative stress. *Molecular Microbiology*, 72:812–814, 5 2009.

[102] Hsing-Ju Tseng, Yogitha Srikhanta, Alastair G. McEwan, and Michael P. Jennings. Accumulation of manganese in neisseria gonorrhoeae correlates with resistance to oxidative killing by superoxide anion and is independent of superoxide dismutase activity. *Molecular Microbiology*, 40:1175–1186, 6 2001.

[103] M. J. Daly, E. K. Gaidamakova, V. Y. Matrosova, A. Vasilenko, M. Zhai, A. Venkateswaran, M. Hess, M. V. Omelchenko, H. M. Kostandarithes, K. S. Makarova, L. P. Wackett, J. K. Fredrickson, and D. Ghosal. Accumulation of Mn(II) in Deinococcus radiodurans Facilitates Gamma-Radiation Resistance. *Science*, 306:1025–1028, 11 2004.

[104] Bradley M. Tebo, Hope A. Johnson, James K. McCarthy, and Alexis S. Templeton. Geomicrobiology of manganese(II) oxidation. *Trends in Microbiology*, 13:421–428, 9 2005.

[105] C. R. Anderson, H. A. Johnson, N. Caputo, R. E. Davis, J. W. Torpey, and B. M. Tebo. Mn(II) Oxidation Is Catalyzed by Heme Peroxidases in " Aurantimonas manganoxydans " Strain SI85-9A1 and Erythrobacter sp. Strain SD-21. *Applied and Environmental Microbiology*, 75:4130–4138, 6 2009.

[106] Gregory J. Dick, Justin W. Torpey, Terry J. Beveridge, and Bradley M. Tebo. Direct Identification of a Bacterial Manganese(II) Oxidase, the Multicopper Oxidase MnxG, from Spores of Several Different Marine Bacillus Species. *Applied and Environmental Microbiology*, 74:1527–1534, 3 2008.

[107] Chris Francis, Karen Casciotti, and Bradley Tebo. Localization of Mn(II)-oxidizing activity and the putative multicopper oxidase, MnxG, to the exosporium of the marine Bacillus sp. strain SG-1. *Archives of Microbiology*, 178:450–456, 12 2002.

[108] Edward I. Solomon, David E. Heppner, Esther M. Johnston, Jake W. Ginsbach, Jordi Cirera, Munzarin Qayyum, Matthew T. Kieber-Emmons, Christian H. Kjaergaard, Ryan G. Hadt, and Li Tian. Copper active sites in biology. *Chemical Reviews*, 114:3659–3853, 4 2014.

[109] T. Sakurai and K. Kataoka. Structure and function of type I copper in multicopper oxidases. *Cellular and Molecular Life Sciences*, 64:2642–2656, 10 2007.

[110] C. Mahendra Kumar, U.V. Sathisha, Shylaja Dharmesh, A.G. Appu Rao, and Sridevi A. Singh. Interaction of sesamol (3,4-methylenedioxyphenol) with tyrosinase and its effect on melanin synthesis. *Biochimie*, 93:562–569, 3 2011.

[111] Joe M. McCord and Irwin Fridovich. Superoxide Dismutase. *Journal of Biological Chemistry*, 244:6049–6055, 11 1969.

[112] Carl G. Holmberg, C.-B Laurell, and Poul Gjertsen. Investigations in Serum Copper. II. Isolation of the Copper Containing Protein, and a Description of some of its Properties. *Acta Chemica Scandinavica*, 2:550–556, 1948.

[113] W ZUMFT. Nitric oxide reductases of prokaryotes with emphasis on the respiratory heme-copper oxidase type. *Journal of Inorganic Biochemistry*, 99:194–215, 1 2005.

[114] Zena Leah Harris. *Ceruloplasmin*, pages 77–84. Elsevier, 2019.

[115] TOM BRODY. *INORGANIC NUTRIENTS*, pages 693–878. Elsevier, 1999.

[116] Maike Gräff, Patrick C. F. Buchholz, Marilize Le Roes-Hill, and Jürgen Pleiss. Multicopper oxidases: modular structure, sequence space, and evolutionary relationships. *Proteins: Structure, Function, and Bioinformatics*, 88:1329–1339, 10 2020.

[117] Edward I. Solomon, Uma M. Sundaram, and Timothy E. Machonkin. Multicopper oxidases and oxygenases. *Chemical Reviews*, 96:2563–2606, 1 1996.

[118] Liliana Gianfreda, Feng Xu, and Jean-Marc Bollag. Laccases: A useful group of oxidoreductive enzymes. *Bioremediation Journal*, 3:1–26, 1 1999.

[119] A. I. Yaropolov, O. V. Skorobogat'ko, S. S. Vartanov, and S. D. Varfolomeyev. Laccase. *Applied Biochemistry and Biotechnology*, 49:257–280, 12 1994.

[120] T Sakurai. Anaerobic reactions of Rhus vernicifera laccase and its type-2 copper-depleted derivatives with hexacyanoferrate(II). *Biochemical Journal*, 284:681–685, 6 1992.

[121] Christine Höfer and Dietmar Schlosser. Novel enzymatic oxidation of Mn^{2+} to Mn^{3+} catalyzed by a fungal laccase. *FEBS Letters*, 451:186–190, 5 1999.

[122] Dietmar Schlosser and Christine Höfer. Laccase-Catalyzed Oxidation of Mn^{2+} in the Presence of Natural Mn^{3+} Chelators as a Novel Source of Extracellular H_2O_2 Production and Its Impact on Manganese Peroxidase. *Applied and Environmental Microbiology*, 68:3514–3521, 7 2002.

[123] Paola Giardina, Vincenza Faraco, Cinzia Pezzella, Alessandra Piscitelli, Sophie Vanhulle, and Giovanni Sannia. Laccases: a never-ending story. *Cellular and Molecular Life Sciences*, 67:369–385, 2 2010.

[124] P. L. A. M. Corstjens, J. P. M. de Vrind, T. Goosen, and E. W. de Vrind-de Jong. Identification and molecular analysis of the Leptothrix discophora SS-1 mofA gene, a gene putatively encoding a manganese-oxidizing protein with copper domains. *Geomicrobiology Journal*, 14:91–108, 4 1997.

[125] Kati Geszvain, James K. McCarthy, and Bradley M. Tebo. Elimination of manganese(ii,iii) oxidation in pseudomonas putida gb-1 by a double knockout of two putative multicopper oxidase genes. *Applied and Environmental Microbiology*, 79:357–366, 1 2013.

[126] P. L G. J. Brouwers, E. Vijgenboom. Bacterial Mn^{2+} Oxidizing Systems and Multicopper Oxidases: An Overview of Mechanisms and Functions. *Geomicrobiology Journal*, 17:1–24, 3 2000.

[127] Justin P. Ridge, Marianne Lin, Eloise I. Larsen, Mark Fegan, Alastair G. McEwan, and Lindsay I. Sly. A multicopper oxidase is essential for manganese oxidation and laccase-like activity in Pedomicrobium sp. ACM 3067. *Environmental Microbiology*, 9:944–953, 4 2007.

[128] Lizhi Tao, Troy A. Stich, Shu-Hao Liou, Alexandra V. Soldatova, David A. Delgadillo, Christine A. Romano, Thomas G. Spiro, David B. Goodin, Bradley M. Tebo, William H. Casey, and R. David Britt. Copper binding sites in the manganese-oxidizing mnx protein complex investigated by electron

paramagnetic resonance spectroscopy. *Journal of the American Chemical Society*, 139:8868–8877, 7 2017.

[129] Jeffrey E. Post. Manganese oxide minerals: Crystal structures and economic and environmental significance. *Proceedings of the National Academy of Sciences*, 96:3447–3454, 3 1999.

[130] James J. Morgan. Kinetics of reaction between O_2 and Mn(II) species in aqueous solutions. *Geochimica et Cosmochimica Acta*, 69:35–48, 1 2005.

[131] Cristina N. Butterfield, Alexandra V. Soldatova, Sung-Woo Lee, Thomas G. Spiro, and Bradley M. Tebo. Mn(II,III) oxidation and MnO_2 mineralization by an expressed bacterial multicopper oxidase. *Proceedings of the National Academy of Sciences*, 110:11731–11735, 7 2013.

[132] Chris A. Francis and Bradley M. Tebo. Enzymatic Manganese(II) Oxidation by Metabolically Dormant Spores of Diverse Bacillus Species. *Applied and Environmental Microbiology*, 68:874–880, 2 2002.

[133] Christine A. Romano, Mowei Zhou, Yang Song, Vicki H. Wysocki, Alice C. Dohnalkova, Libor Kovarik, Ljiljana Paša-Tolić, and Bradley M. Tebo. Biogenic manganese oxide nanoparticle formation by a multimeric multicopper oxidase Mnx. *Nature Communications*, 8:746, 9 2017.

[134] Valeriya R. Samygina, Alexey V. Sokolov, Gleb Bourenkov, Maxim V. Petoukhov, Maria O. Pulina, Elena T. Zakharova, Vadim B. Vasilyev, Hans Bartunik, and Dmitri I. Svergun. Ceruloplasmin: Macromolecular assemblies with iron-containing acute phase proteins. *PLoS ONE*, 8:e67145, 7 2013.

[135] Alexandra V. Soldatova, Wen Fu, Christine A. Romano, Lizhi Tao, William H. Casey, R. David Britt, Bradley M. Tebo, and Thomas G. Spiro. Metallo-inhibition of Mnx, a bacterial manganese multicopper oxidase complex. *Journal of Inorganic Biochemistry*, 224:111547, 11 2021.

[136] Alexandra V. Soldatova, Lizhi Tao, Christine A. Romano, Troy A. Stich, William H. Casey, R. David Britt, Bradley M. Tebo, and Thomas G. Spiro. Mn(II) Oxidation by the Multicopper Oxidase Complex Mnx: A Binuclear Activation Mechanism. *Journal of the American Chemical Society*, 139:11369–11380, 8 2017.

[137] Alexandra V. Soldatova, Christine A. Romano, Lizhi Tao, Troy A. Stich, William H. Casey, R. David Britt, Bradley M. Tebo, and Thomas G. Spiro. Mn(II) Oxidation by the Multicopper Oxidase Complex Mnx: A Coordinated Two-Stage Mn(II)/(III) and Mn(III)/(IV) Mechanism. *Journal of the American Chemical Society*, 139:11381–11391, 8 2017.

[138] Lizhi Tao, Troy A. Stich, Alexandra V. Soldatova, Bradley M. Tebo, Thomas G. Spiro, William H. Casey, and R. David Britt. Mn(III) species formed by the multi-copper oxidase MnxG investigated by electron paramagnetic resonance spectroscopy. *JBIC Journal of Biological Inorganic Chemistry*, 23:1093–1104, 10 2018.

[139] George H. Reed and George D. Markham. *EPR of Mn(II) Complexes with Enzymes and Other Proteins*, pages 73–142. Springer US, 1984.

[140] Stefan Stoll and Arthur Schweiger. EasySpin, a comprehensive software package for spectral simulation and analysis in EPR. *Journal of Magnetic Resonance*, 178:42–55, 1 2006.

[141] Stefan Stoll and R. David Britt. General and efficient simulation of pulse EPR spectra. *Physical Chemistry Chemical Physics*, 11:6614, 2009.

[142] Cristina N. Butterfield, Lizhi Tao, Kelly N. Chacón, Thomas G. Spiro, Ninian J. Blackburn, William H. Casey, R. David Britt, and Bradley M. Tebo. Multicopper manganese oxidase accessory proteins bind Cu and heme. *Biochimica et Biophysica Acta (BBA) - Proteins and Proteomics*, 1854:1853–1859, 12 2015.

[143] Gareth R. Eaton, Sandra S. Eaton, David P. Barr, and Ralph T. Weber. *Quantitative EPR*. Springer Vienna, 2010.

[144] Timothy R. Cook, Dilek K. Dogutan, Steven Y. Reece, Yogesh Surendranath, Thomas S. Teets, and Daniel G. Nocera. Solar energy supply and storage for the legacy and nonlegacy worlds. *Chemical Reviews*, 110:6474–6502, 11 2010.

[145] Steven Chu and Arun Majumdar. Opportunities and challenges for a sustainable energy future. *Nature*, 488:294–303, 8 2012.

[146] Melvin. Calvin. The path of carbon in photosynthesis. *Journal of Chemical Education*, 26:639, 12 1949.

[147] Daniel G. Nocera. The artificial leaf. *Accounts of Chemical Research*, 45:767–776, 5 2012.

[148] Nian-Tzu Suen, Sung-Fu Hung, Quan Quan, Nan Zhang, Yi-Jun Xu, and Hao Ming Chen. Electrocatalysis for the oxygen evolution reaction: recent development and future perspectives. *Chemical Society Reviews*, 46:337–365, 2017.

[149] Natalie D. Morris, Masahiro Suzuki, and Thomas E. Mallouk. Kinetics of Electron Transfer and Oxygen Evolution in the Reaction of $[Ru(bpy)_3]^{3+}$ with Colloidal Iridium Oxide. *The Journal of Physical Chemistry A*, 108:9115–9119, 10 2004.

[150] Takaaki Nakagawa, Christopher A. Beasley, and Royce W. Murray. Efficient Electro-Oxidation of Water near Its Reversible Potential by a Mesoporous IrO_x Nanoparticle Film. *The Journal of Physical Chemistry C*, 113:12958–12961, 7 2009.

[151] Charles C. L. McCrory, Suho Jung, Ivonne M. Ferrer, Shawn M. Chatman, Jonas C. Peters, and Thomas F. Jaramillo. Benchmarking hydrogen evolving reaction and oxygen evolving reaction electrocatalysts for solar water splitting devices. *Journal of the American Chemical Society*, 137:4347–4357, 4 2015.

[152] Michael L. Bushneil. *Architecture of the Environment*, volume 303, pages 101–117. Elsevier, 1988.

[153] Ivelina Zaharieva, M. Mahdi Najafpour, Mathias Wiechen, Michael Haumann, Philipp Kurz, and Holger Dau. Synthetic manganese–calcium oxides mimic the water-oxidizing complex of photosynthesis functionally and structurally. *Energy & Environmental Science*, 4:2400, 2011.

[154] Mohammad Mahdi Najafpour, Till Ehrenberg, Mathias Wiechen, and Philipp Kurz. Calcium Manganese(III) Oxides ($CaMn_2O_4{\cdot}H_2O$) as Biomimetic Oxygen-Evolving Catalysts. *Angewandte Chemie International Edition*, 49:2233–2237, 3 2010.

[155] Jack H. Baricuatro, Fadl H. Saadi, Azhar I. Carim, Jesus M. Velazquez, Youn-Geun Kim, and Manuel P. Soriaga. Influence of redox-inactive cations on the structure and electrochemical reactivity of synthetic birnessite, a heterogeneous analog for the oxygen-evolving complex. *The Journal of Physical Chemistry C*, 120:15618–15631, 7 2016.

[156] Ian G. McKendry, Akila C. Thenuwara, Samantha L. Shumlas, Haowei Peng, Yaroslav V. Aulin, Parameswara Rao Chinnam, Eric Borguet, Daniel R. Strongin, and Michael J. Zdilla. Systematic doping of cobalt into layered manganese oxide sheets substantially enhances water oxidation catalysis. *Inorganic Chemistry*, 57:557–564, 1 2018.

[157] John R. Bargar, Bradley M. Tebo, Uwe Bergmann, Samuel M. Webb, Pieter Glatzel, Van Q. Chiu, and Mario Villalobos. Biotic and abiotic products of Mn(II) oxidation by spores of the marine Bacillus sp. strain SG-1. *American Mineralogist*, 90:143–154, 1 2005.

[158] Thomas G. Spiro, John R. Bargar, Garrison Sposito, and Bradley M. Tebo. Bacteriogenic manganese oxides. *Accounts of Chemical Research*, 43:2–9, 1 2010.

[159] Bradley M. Tebo, John R. Bargar, Brian G. Clement, Gregory J. Dick, Karen J. Murray, Dorothy Parker, Rebecca Verity, and Samuel M. Webb. Biogenic manganese oxides: Properties and mechanisms of formation. *Annual Review of Earth and Planetary Sciences*, 32:287–328, 5 2004.

[160] Alexandr N. Simonov, Rosalie K. Hocking, Lizhi Tao, Thomas Gengenbach, Timothy Williams, Xi-Ya Fang, Hannah J. King, Shannon A. Bonke, Dijon A. Hoogeveen, Christine A. Romano, Bradley M. Tebo, Lisandra L. Martin, William H. Casey, and Leone Spiccia. Tunable biogenic manganese oxides. *Chemistry – A European Journal*, 23:13482–13492, 9 2017.

[161] Mario Villalobos, Brandy Toner, John Bargar, and Garrison Sposito. Characterization of the manganese oxide produced by pseudomonas putida strain MnB1. *Geochimica et Cosmochimica Acta*, 67:2649–2662, 7 2003.

[162] Paula Connor, Jona Schuch, Bernhard Kaiser, and Wolfram Jaegermann. The Determination of Electrochemical Active Surface Area and Specific Capacity Revisited for the System MnO_x as an Oxygen Evolution Catalyst. *Zeitschrift für Physikalische Chemie*, 234:979–994, 5 2020.

[163] J. Wong, F. W. Lytle, R. P. Messmer, and D. H. Maylotte. K-edge absorption spectra of selected vanadium compounds. *Physical Review B*, 30:5596–5610, 11 1984.

[164] Seonyi Namgung, Chul-Min Chon, and Giehyeon Lee. Formation of diverse Mn oxides: a review of bio/geochemical processes of Mn oxidation. *Geosciences Journal*, 22:373–381, 4 2018.

[165] Xue Du, Ye Liao, Minyi Ma, Yujuan Wang, Jing Zhang, and Gaihua He. Advance of manganese dioxide-based electrocatalyst for water splitting. *Journal of Solid State Chemistry*, 329:124369, 1 2024.

[166] K. Selvakumar, S.M. Senthil Kumar, R. Thangamuthu, G. Kruthika, and P. Murugan. Development of shape-engineered α-MnO_2 materials as bi-functional catalysts for oxygen evolution reaction and oxygen reduction reaction in alkaline medium. *International Journal of Hydrogen Energy*, 39:21024–21036, 12 2014.

[167] Jeffrey E.; Post, Peter J.; Heaney, Eugene S.; Ilton, and Evert J. Elzinga. The Crystal Structure of Feitknechtite (β-MnOOH) and a new MnOOH Polymorph. *American Mineralogist*, 283:77–80, 1 2023.

[168] A. Manceau, M. A. Marcus, and S. Grangeon. Determination of Mn valence states in mixed-valent manganates by XANES spectroscopy. *American Mineralogist*, 97:816–827, 5 2012.

[169] Yelena Gorlin, Benedikt Lassalle-Kaiser, Jesse D. Benck, Sheraz Gul, Samuel M. Webb, Vittal K. Yachandra, Junko Yano, and Thomas F. Jaramillo. In situ x-ray absorption spectroscopy investigation of a bifunctional manganese oxide catalyst with high activity for electrochemical water oxidation and oxygen reduction. *Journal of the American Chemical Society*, 135:8525–8534, 6 2013.

[170] Jodi L. Junta and Michael F. Hochella. Manganese (II) oxidation at mineral surfaces: A microscopic and spectroscopic study. *Geochimica et Cosmochimica Acta*, 58:4985–4999, 11 1994.

[171] Zamyla Morgan Chan, Daniil A. Kitchaev, Johanna Nelson Weker, Christoph Schnedermann, Kipil Lim, Gerbrand Ceder, William Tumas, Michael F. Toney, and Daniel G. Nocera. Electrochemical trapping of metastable Mn^{3+} ions for activation of MnO_2 oxygen evolution catalysts. *Proceedings of the National Academy of Sciences*, 115:E5261–E5268, 6 2018.

[172] Kristy A. Campbell, Emine Yikilmaz, Christopher V. Grant, Wolfgang Gregor, Anne-Frances Miller, and R. David Britt. Parallel Polarization EPR Characterization of the Mn(III) Center of Oxidized Manganese Superoxide Dismutase. *Journal of the American Chemical Society*, 121:4714–4715, 5 1999.

[173] Kristy A. Campbell. *CW and pulsed EPR studies of photosystem II and manganese-containing complexes*. PhD thesis, University of California-Davis, 1999. Copyright - Database copyright ProQuest

LLC; ProQuest does not claim copyright in the individual underlying works; Last updated - 2023-02-24.

[174] M.P. Hendrich and P.G. Debrunner. Integer-spin electron paramagnetic resonance of iron proteins. *Biophysical Journal*, 56:489–506, 9 1989.

[175] Eckard Münck, Kristene Ksurerus, and Michael P. Hendrich. *[17] Combining Mössbauer spectroscopy with integer spin electron paramagnetic resonance*, volume 227, pages 463–479. Academic Press, 1993.

[176] Donghyuk Jeong, Kyoungsuk Jin, Sung Eun Jerng, Hongmin Seo, Donghun Kim, Seung Hoon Nahm, Sun Hee Kim, and Ki Tae Nam. Mn_5O_8 Nanoparticles as Efficient Water Oxidation Catalysts at Neutral pH. *ACS Catalysis*, 5:4624–4628, 8 2015.

[177] Masaoki Oku, Kichinosuke Hirokawa, and Shigero Ikeda. X-ray photoelectron spectroscopy of manganese—oxygen systems. *Journal of Electron Spectroscopy and Related Phenomena*, 7:465–473, 1 1975.

[178] J. S. Foord, R. B. Jackman, and G. C. Allen. An X-ray photoelectron spectroscopic investigation of the oxidation of manganese. *Philosophical Magazine A*, 49:657–663, 11 1984.

[179] J. C. Carver, G. K. Schweitzer, and Thomas A. Carlson. Use of X-Ray Photoelectron Spectroscopy to Study Bonding in Cr, Mn, Fe, and Co Compounds. *The Journal of Chemical Physics*, 57:973–982, 7 1972.

[180] A. J. Nelson, John G. Reynolds, and Joseph W. Roos. Core-level satellites and outer core-level multiplet splitting in mn model compounds. *Journal of Vacuum Science & Technology A: Vacuum, Surfaces, and Films*, 18:1072–1076, 7 2000.

[181] Yelena Gorlin and Thomas F. Jaramillo. A bifunctional nonprecious metal catalyst for oxygen reduction and water oxidation. *Journal of the American Chemical Society*, 132:13612–13614, 10 2010.

[182] Eugene S. Ilton, Jeffrey E. Post, Peter J. Heaney, Florence T. Ling, and Sebastien N. Kerisit. XPS determination of Mn oxidation states in Mn (hydr)oxides. *Applied Surface Science*, 366:475–485, 3 2016.

[183] José M. Cerrato, Michael F. Hochella, William R. Knocke, Andrea M. Dietrich, and Thomas F. Cromer. Use of XPS to Identify the Oxidation State of Mn in Solid Surfaces of Filtration Media Oxide Samples from Drinking Water Treatment Plants. *Environmental Science & Technology*, 44:5881–5886, 8 2010.

[184] V. R. Galakhov, M. Demeter, S. Bartkowski, M. Neumann, N. A. Ovechkina, E. Z. Kurmaev, N. I. Lobachevskaya, Ya. M. Mukovskii, J. Mitchell, and D. L. Ederer. Mn 3s exchange splitting in mixed-valence manganites. *Physical Review B*, 65:113102, 2 2002.

[185] Jae Hwa Lee, Young Jin Sa, Tae Kyung Kim, Hoi Ri Moon, and Sang Hoon Joo. A transformative route to nanoporous manganese oxides of controlled oxidation states with identical textural properties. *J. Mater. Chem. A*, 2:10435–10443, 2014.

[186] James W Murray, John G Dillard, Rudolf Giovanoli, Harald Moers, and Werner Stumm. Oxidation of Mn(II): Initial mineralogy, oxidation state and ageing. *Geochimica et Cosmochimica Acta*, 49:463–470, 2 1985.

[187] Xiaoyan Han, Yiping Cui, and Haowen Liu. Ce-doped Mn_3O_4 as high-performance anode material for lithium ion batteries. *Journal of Alloys and Compounds*, 814:152348, 1 2020.

[188] Ming Sun, Bang Lan, Ting Lin, Gao Cheng, Fei Ye, Lin Yu, Xiaoling Cheng, and Xiaoying Zheng. Controlled synthesis of nanostructured manganese oxide: crystalline evolution and catalytic activities. *CrystEngComm*, 15:7010, 2013.

[189] M.H. Miles, E.A. Klaus, B.P. Gunn, J.R. Locker, W.E. Serafin, and S. Srinivasan. The oxygen evolution reaction on platinum, iridium, ruthenium and their alloys at 80°C in acid solutions. *Electrochimica Acta*, 23:521–526, 6 1978.

[190] Ermete Antolini. Iridium as catalyst and cocatalyst for oxygen evolution/reduction in acidic polymer electrolyte membrane electrolyzers and fuel cells. *ACS Catalysis*, 4:1426–1440, 5 2014.

[191] Yogesh Surendranath, Daniel A. Lutterman, Yi Liu, and Daniel G. Nocera. Nucleation, growth, and repair of a cobalt-based oxygen evolving catalyst. *Journal of the American Chemical Society*, 134:6326–6336, 4 2012.

[192] Akila C. Thenuwara, Samantha L. Shumlas, Nuwan H. Attanayake, Yaroslav V. Aulin, Ian G. McKendry, Qiao Qiao, Yimei Zhu, Eric Borguet, Michael J. Zdilla, and Daniel R. Strongin. Intercalation of cobalt into the interlayer of birnessite improves oxygen evolution catalysis. *ACS Catalysis*, 6:7739–7743, 11 2016.

[193] Yue Yang, Xingsong Su, Lei Zhang, Peter Kerns, Laura Achola, Veronica Hayes, Rebecca Quardokus, Steven L. Suib, and Jie He. Intercalating MnO_2 Nanosheets With Transition Metal Cations to Enhance Oxygen Evolution. *ChemCatChem*, 11:1689–1700, 3 2019.

[194] Ian G. McKendry, Loveyy J. Mohamad, Akila C. Thenuwara, Tim Marshall, Eric Borguet, Daniel R. Strongin, and Michael J. Zdilla. Synergistic In-Layer Cobalt Doping and Interlayer Iron Intercalation into Layered MnO_2 Produces an Efficient Water Oxidation Electrocatalyst. *ACS Energy Letters*, 3:2280–2285, 9 2018.

[195] G.G. Amatucci, J.M. Tarascon, D. Larcher, and L.C. Klein. Synthesis of electrochemically active $LiCoO_2$ and $LiNiO_2$ at 100 °C. *Solid State Ionics*, 84(3):169–180, 1996.

[196] Santiago J.A. Figueroa, Félix G. Requejo, E.J. Lede, Luciano Lamaita, M. Andrés Peluso, and Jorge E. Sambeth. XANES study of electronic and structural nature of Mn-sites in manganese oxides with catalytic properties. *Catalysis Today*, 107-108:849–855, 10 2005.

[197] Evert J. Elzinga. Reductive Transformation of Birnessite by Aqueous Mn(II). *Environmental Science & Technology*, 45:6366–6372, 8 2011.

[198] Johannes Wandt, Anna Freiberg, Rowena Thomas, Yelena Gorlin, Armin Siebel, Roland Jung, Hubert A. Gasteiger, and Moniek Tromp. Transition metal dissolution and deposition in Li-ion batteries investigated by operando X-ray absorption spectroscopy. *Journal of Materials Chemistry A*, 4:18300–18305, 2016.

[199] Sujit Kumar Ghosh. Diversity in the family of manganese oxides at the nanoscale: From fundamentals to applications. *ACS Omega*, 5:25493–25504, 10 2020.

[200] Brandy Toner, Sirine Fakra, Mario Villalobos, Tony Warwick, and Garrison Sposito. Spatially resolved characterization of biogenic manganese oxide production within a bacterial biofilm. *Applied and Environmental Microbiology*, 71:1300–1310, 3 2005.

[201] Juan Liu, Yixiao Zhang, Qian Gu, Anxu Sheng, and Baogang Zhang. Tunable Mn Oxidation State and Redox Potential of Birnessite Coexisting with Aqueous Mn(II) in Mildly Acidic Environments. *Minerals*, 10:690, 8 2020.

[202] R. Choumane and S. Peulon. Electrodeposited birnessite thin film: An efficient eco-friendly sorbent for removing heavy metals from water. *Colloids and Surfaces A: Physicochemical and Engineering Aspects*, 577:594–603, 9 2019.

[203] Amina Amarray, Sanae El Ghachtouli, Youssef Samih, Mouad Dahbi, and Mohammed Azzi. Enhancement of Cd(II) electrosorption using electrosorption process with manganese oxide nanomaterial electrodeposited. *Desalination*, 521:115307, 1 2022.

[204] S. Mann, N. H. C. Sparks, G. H. E. Scott, and E. W. de Vrind-de Jong. Oxidation of Manganese and Formation of Mn_3O_4 (Hausmannite) by Spore Coats of a Marine Bacillus sp. *Applied and Environmental Microbiology*, 54:2140–2143, 8 1988.

[205] Hui Yin, Yu Liu, Luuk K. Koopal, Xionghan Feng, Shengqi Chu, Mengqiang Zhu, and Fan Liu. High Co-doping promotes the transition of birnessite layer symmetry from orthogonal to hexagonal. *Chemical Geology*, 410:12–20, 9 2015.

[206] Daniel J. Kosman. Multicopper oxidases: a workshop on copper coordination chemistry, electron transfer, and metallophysiology. *JBIC Journal of Biological Inorganic Chemistry*, 15:15–28, 1 2010.

[207] Cara M. Santelli, Samuel M. Webb, Alice C. Dohnalkova, and Colleen M. Hansel. Diversity of Mn oxides produced by Mn(II)-oxidizing fungi. *Geochimica et Cosmochimica Acta*, 75:2762–2776, 5 2011.

[208] Naoyuki Miyata, Yukinori Tani, Keisuke Iwahori, and Mitsuyuki Soma. Enzymatic formation of manganese oxides by an Acremonium-like hyphomycete fungus, strain KR21-2. *FEMS Microbiology Ecology*, 47:101–109, 1 2004.

[209] S.M. Webb. Structural characterization of biogenic Mn oxides produced in seawater by the marine bacillus sp. strain SG-1. *American Mineralogist*, 90:1342–1357, 8 2005.

[210] Mengqiang Zhu, Matthew Ginder-Vogel, Sanjai J. Parikh, Xiong-Han Feng, and Donald L. Sparks. Cation Effects on the Layer Structure of Biogenic Mn-Oxides. *Environmental Science & Technology*, 44:4465–4471, 6 2010.

[211] Ian Saratovsky, Peter G. Wightman, Pablo A. Pastén, Jean-François Gaillard, and Kenneth R. Poeppelmeier. Manganese Oxides: Parallels between Abiotic and Biotic Structures. *Journal of the American Chemical Society*, 128:11188–11198, 8 2006.

[212] Xiong Han Feng, Mengqiang Zhu, Matthew Ginder-Vogel, Chaoying Ni, Sanjai J. Parikh, and Donald L. Sparks. Formation of nano-crystalline todorokite from biogenic Mn oxides. *Geochimica et Cosmochimica Acta*, 74:3232–3245, 6 2010.

[213] Christina K. Remucal and Matthew Ginder-Vogel. A critical review of the reactivity of manganese oxides with organic contaminants. *Environmental Science: Processes & Impacts*, 16:1247, 2014.

[214] William G. Sunda and David J. Kieber. Oxidation of humic substances by manganese oxides yields low-molecular-weight organic substrates. *Nature*, 367:62–64, 1 1994.

[215] Brandon J. Lafferty, Matthew Ginder-Vogel, and Donald L. Sparks. Arsenite oxidation by a poorly crystalline manganese-oxide, stirred-flow experiments. *Environmental Science & Technology*, 44:8460–8466, 11 2010.

[216] Lily Schacht and Matthew Ginder-Vogel. Arsenite depletion by manganese oxides: A case study on the limitations of observed first order rate constants. *Soil Systems*, 2:39, 6 2018.

[217] Alan T. Stone and James J. Morgan. Reduction and dissolution of manganese(III) and manganese(IV) oxides by organics: 2. Survey of the reactivity of organics. *Environmental Science & Technology*, 18:617–624, 8 1984.

[218] Jianing Chang, Yukinori Tani, Hirotaka Naitou, Naoyuki Miyata, Fuyumi Tojo, and Haruhiko Seyama. Zn(II) sequestration by fungal biogenic manganese oxide through enzymatic and abiotic processes. *Chemical Geology*, 383:155–163, 9 2014.

[219] Jianing Chang, Yukinori Tani, Hirotaka Naitou, Naoyuki Miyata, Haruhiko Seyama, and Kazuya Tanaka. Cobalt(II) sequestration on fungal biogenic manganese oxide enhanced by manganese(II) oxidase activity. *Applied Geochemistry*, 37:170–178, 10 2013.

[220] Qianqian Yu, Keiko Sasaki, Kazuya Tanaka, Toshihiko Ohnuki, and Tsuyoshi Hirajima. Structural factors of biogenic birnessite produced by fungus Paraconiothyrium sp. WL-2 strain affecting sorption of Co^{2+}. *Chemical Geology*, 310-311:106–113, 6 2012.

[221] Mario Villalobos, John Bargar, and Garrison Sposito. Mechanisms of Pb(II) Sorption on a Biogenic Manganese Oxide. *Environmental Science & Technology*, 39:569–576, 1 2005.

[222] S. M. Webb, B. M. Tebo, and J. R. Barger. Structural Influences of Sodium and Calcium Ions on the Biogenic Manganese Oxides Produced by the Marine Bacillus Sp., Strain SG-1. *Geomicrobiology Journal*, 22:181–193, 4 2005.

[223] S. M. Webb, J. R. Bargar, and B. M. Tebo. Determination of Uranyl Incorporation into Biogenic Manganese Oxides Using X-ray Absorption Spectroscopy and Scattering. *Physica Scripta*, T115:949, 2005.

[224] Yuanzhi Tang, Samuel M Webb, Emily R Estes, and Colleen M Hansel. Chromium(III) oxidation by biogenic manganese oxides with varying structural ripening. *Environmental science. Processes & impacts*, 16:2127–36, 9 2014.

[225] Brandy Toner, Alain Manceau, Samuel M. Webb, and Garrison Sposito. Zinc sorption to biogenic hexagonal-birnessite particles within a hydrated bacterial biofilm. *Geochimica et Cosmochimica Acta*, 70:27–43, 1 2006.

[226] Wenbo Liu, Nora B. Sutton, Huub H. M. Rijnaarts, and Alette A. M. Langenhoff. Pharmaceutical removal from water with iron- or manganese-based technologies: A review. *Critical Reviews in Environmental Science and Technology*, 46:1584–1621, 10 2016.

[227] Shuji Matsushita, Daisuke Komizo, Linh Thi Thuy Cao, Yoshiteru Aoi, Tomonori Kindaichi, Noriatsu Ozaki, Hiroyuki Imachi, and Akiyoshi Ohashi. Production of biogenic manganese oxides coupled with methane oxidation in a bioreactor for removing metals from wastewater. *Water Research*, 130:224–233, 3 2018.

[228] Tom Hennebel, Bart De Gusseme, Nico Boon, and Willy Verstraete. Biogenic metals in advanced water treatment. *Trends in Biotechnology*, 27:90–98, 2 2009.

[229] Yukinori Tani, Naoyuki Miyata, Maiko Ohashi, Toshihiko Ohnuki, Haruhiko Seyama, Keisuke Iwahori, and Mitsuyuki Soma. Interaction of Inorganic Arsenic with Biogenic Manganese Oxide Produced by a Mn-Oxidizing Fungus, Strain KR21-2. *Environmental Science & Technology*, 38:6618–6624, 12 2004.

[230] Nakharin Therdkiattikul, Thunyalux Ratpukdi, Pinit Kidkhunthod, Narong Chanlek, and Sumana Siripattanakul-Ratpukdi. Manganese-contaminated groundwater treatment by novel bacterial isolates: kinetic study and mechanism analysis using synchrotron-based techniques. *Scientific reports*, 10:13391, 8 2020.

[231] O. W. Duckworth, N. A. Rivera, T. G. Gardner, M. Y. Andrews, C. M. Santelli, and M. L. Polizzotto. Morphology, structure, and metal binding mechanisms of biogenic manganese oxides in a superfund site treatment system. *Environmental Science: Processes & Impacts*, 19:50–58, 2017.

[232] Qianqian Yu, Keiko Sasaki, Kazuya Tanaka, Toshihiko Ohnuki, and Tsuyoshi Hirajima. Zinc sorption during bio-oxidation and precipitation of manganese modifies the layer stacking of biogenic birnessite. *Geomicrobiology Journal*, 30:829–839, 10 2013.

[233] H. IRVING and R. J. P. WILLIAMS. Order of stability of metal complexes. *Nature*, 162:746–747, 11 1948.

[234] R. Bruce Martin. A stability ruler for metal ion complexes. *Journal of Chemical Education*, 64:402, 5 1987.

[235] Carl Frieden. Kinetic aspects of regulation of metabolic processes. *Journal of Biological Chemistry*, 245:5788–5799, 11 1970.

[236] Karen J. Murray, Samuel M. Webb, John R. Bargar, and Bradley M. Tebo. Indirect Oxidation of Co(II) in the Presence of the Marine Mn(II)-Oxidizing Bacterium Bacillus sp. Strain SG-1. *Applied and Environmental Microbiology*, 73:6905–6909, 11 2007.

[237] Anna A. Simanova and Jasquelin Peña. Time-Resolved Investigation of Cobalt Oxidation by Mn(III)-Rich δ-MnO_2 Using Quick X-ray Absorption Spectroscopy. *Environmental Science & Technology*, 49:10867–10876, 9 2015.

[238] Kazuya Tanaka, Qianqian Yu, Keiko Sasaki, and Toshihiko Ohnuki. Cobalt(II) Oxidation by Biogenic Mn Oxide Produced by Pseudomonas sp. Strain NGY-1. *Geomicrobiology Journal*, 30:874–885, 11 2013.

[239] Jing Dai, Gavin J. Knott, Wen Fu, Tiffany W. Lin, Ariel L. Furst, R. David Britt, and Matthew B. Francis. Protein-embedded metalloporphyrin arrays templated by circularly permuted tobacco mosaic virus coat proteins. *ACS Nano*, 15:8110–8119, 5 2021.

[240] Robert. E. Blankenship. *Molecular mechanisms of photosynthesis*. Blackwell Science, 12 2002.

[241] Yifei Jiang and Jason McNeill. Light-harvesting and amplified energy transfer in conjugated polymer nanoparticles. *Chemical reviews*, 117:838–859, 1 2017.

[242] Alex Adronov and Jean M. J. Fréchet. Light-harvesting dendrimers. *Chemical Communications*, pages 1701–1710, 2000.

[243] Palash K. Dutta, Symon Levenberg, Andrey Loskutov, Daniel Jun, Rafael Saer, J. Thomas Beatty, Su Lin, Yan Liu, Neal W. Woodbury, and Hao Yan. A DNA-Directed Light-Harvesting/Reaction Center System. *Journal of the American Chemical Society*, 136:16618–16625, 11 2014.

[244] Heechul Park, Nimrod Heldman, Patrick Rebentrost, Luigi Abbondanza, Alessandro Iagatti, Andrea Alessi, Barbara Patrizi, Mario Salvalaggio, Laura Bussotti, Masoud Mohseni, Filippo Caruso, Hannah C. Johnsen, Roberto Fusco, Paolo Foggi, Petra F. Scudo, Seth Lloyd, and Angela M. Belcher. Enhanced energy transport in genetically engineered excitonic networks. *Nature Materials*, 15:211–216, 2 2016.

[245] Michel T. Dedeo, Karl E. Duderstadt, James M. Berger, and Matthew B. Francis. Nanoscale Protein Assemblies from a Circular Permutant of the Tobacco Mosaic Virus. *Nano Letters*, 10:181–186, 1 2010.

[246] Rebekah A. Miller, Nicholas Stephanopoulos, Jesse M. McFarland, Andrew S. Rosko, Phillip L. Geissler, and Matthew B. Francis. Impact of Assembly State on the Defect Tolerance of TMV-Based Light Harvesting Arrays. *Journal of the American Chemical Society*, 132:6068–6074, 5 2010.

[247] Rebekah A. Miller, Andrew D. Presley, and Matthew B. Francis. Self-Assembling Light-Harvesting Systems from Synthetically Modified Tobacco Mosaic Virus Coat Proteins. *Journal of the American Chemical Society*, 129:3104–3109, 3 2007.

[248] Milan Delor, Jing Dai, Trevor D. Roberts, Julia R. Rogers, Samia M. Hamed, Jeffrey B. Neaton, Phillip L. Geissler, Matthew B. Francis, and Naomi S. Ginsberg. Exploiting chromophore–protein interactions through linker engineering to tune photoinduced dynamics in a biomimetic light-harvesting platform. *Journal of the American Chemical Society*, 140:6278–6287, 5 2018.

[249] M. Akram, A. Dietl, U. Mersdorf, S. Prinz, W. Maalcke, J. Keltjens, C. Ferousi, N. M. de Almeida, J. Reimann, B. Kartal, M. S. M. Jetten, K. Parey, and T. R. M. Barends. A 192-heme electron transfer network in the hydrazine dehydrogenase complex. *Science Advances*, 5:1–8, 4 2019.

[250] Heather M. Jensen, Aaron E. Albers, Konstantin R. Malley, Yuri Y. Londer, Bruce E. Cohen, Brett A. Helms, Peter Weigele, Jay T. Groves, and Caroline M. Ajo-Franklin. Engineering of a synthetic electron conduit in living cells. *Proceedings of the National Academy of Sciences*, 107:19213–19218, 11 2010.

[251] Martin Stillman. Biological inorganic chemistry. structure and reactivity. edited by ivano bertini, harry b. gray, edward i. stiefel and joan s. valentine. *Angewandte Chemie International Edition*, 46:8741–8742, 11 2007.

[252] Telma C. Santos, Marta A. Silva, Leonor Morgado, Joana M. Dantas, and Carlos A. Salgueiro. Diving into the redox properties of geobacter sulfurreducens cytochromes: a model for extracellular electron transfer. *Dalton Transactions*, 44:9335–9344, 2015.

[253] David J. Richardson, Julea N. Butt, Jim K. Fredrickson, John M. Zachara, Liang Shi, Marcus J. Edwards, Gaye White, Nanakow Baiden, Andrew J. Gates, Sophie J. Marritt, and Thomas A. Clarke. The 'porin-cytochrome' model for microbe-to-mineral electron transfer. *Molecular Microbiology*, 85:201–212, 7 2012.

[254] Marian Breuer, Kevin M. Rosso, and Jochen Blumberger. Electron flow in multiheme bacterial cytochromes is a balancing act between heme electronic interaction and redox potentials. *Proceedings of the National Academy of Sciences*, 111:611–616, 1 2014.

[255] Charles J. Reedy and Brian R. Gibney. Heme protein assemblies. *Chemical Reviews*, 104:617–650, 2 2004.

[256] Devleena Shivakumar, Joshua Williams, Yujie Wu, Wolfgang Damm, John Shelley, and Woody Sherman. Prediction of absolute solvation free energies using molecular dynamics free energy perturbation and the opls force field. *Journal of Chemical Theory and Computation*, 6:1509–1519, 5 2010.

[257] M. Fahnenschmidt, R. Bittl, E. Schlodder, W. Haehnel, and W. Lubitz. Characterization of de novo synthesized four-helix bundle proteins with metalloporphyrin cofactors. *Physical Chemistry Chemical Physics*, 3:4082–4090, 2001.

[258] Giorgio Zoppellaro, Kara L. Bren, Amy A. Ensign, Espen Harbitz, Ravinder Kaur, Hans-Petter Hersleth, Ulf Ryde, Lars Hederstedt, and K. Kristoffer Andersson. Review: Studies of ferric heme proteins with highly anisotropic/highly axial low spin (S = 1/2) electron paramagnetic resonance signals with bis-Histidine and histidine-methionine axial iron coordination. *Biopolymers*, 91:1064–1082, 12 2009.

[259] Edward A. Berry and F. Ann Walker. Bis-histidine-coordinated hemes in four-helix bundles: how the geometry of the bundle controls the axial imidazole plane orientations in transmembrane cytochromes of mitochondrial Complexes II and III and related proteins. *JBIC Journal of Biological Inorganic Chemistry*, 13:481–498, 5 2008.

[260] Espen Harbitz and K. Kristoffer Andersson. Cytochrome c-554 from Methylosinus trichosporium OB3b; a Protein That Belongs to the Cytochrome c2 Family and Exhibits a HALS-Type EPR Signal. *PLoS ONE*, 6:e22014, 7 2011.

[261] Tobias J. Sherbow, Wen Fu, Lizhi Tao, Lev N. Zakharov, R. David Britt, and Michael D. Pluth. Thionitrite (sno−) and perthionitrite (ssno−) are simple synthons for nitrosylated iron sulfur clusters. *Angewandte Chemie International Edition*, 61, 7 2022.

[262] Nathan S. Bryan and David J. Lefer. Update on gaseous signaling molecules nitric oxide and hydrogen sulfide: Strategies to capture their functional activity for human therapeutics. *Molecular Pharmacology*, 96:109–114, 7 2019.

[263] K Egashira, T Inou, Y Hirooka, H Kai, M Sugimachi, S Suzuki, T Kuga, Y Urabe, and A Takeshita. Effects of age on endothelium-dependent vasodilation of resistance coronary artery by acetylcholine in humans. *Circulation*, 88:77–81, 7 1993.

[264] Gopi K. Kolluru, Xinggui Shen, Shuai Yuan, and Christopher G. Kevil. Gasotransmitter heterocellular signaling. *Antioxidants & Redox Signaling*, 26:936–960, 6 2017.

[265] Milos R. Filipovic, Jan Lj. Miljkovic, Thomas Nauser, Maksim Royzen, Katharina Klos, Tatyana Shubina, Willem H. Koppenol, Stephen J. Lippard, and Ivana Ivanović-Burmazović. Chemical characterization of the smallest s -nitrosothiol, hsno; cellular cross-talk of h 2 s and s -nitrosothiols. *Journal of the American Chemical Society*, 134:12016–12027, 7 2012.

[266] Miriam M. Cortese-Krott, Gunter G. C. Kuhnle, Alex Dyson, Bernadette O. Fernandez, Marian Grman, Jenna F. DuMond, Mark P. Barrow, George McLeod, Hidehiko Nakagawa, Karol Ondrias, Péter Nagy, S. Bruce King, Joseph E. Saavedra, Larry K. Keefer, Mervyn Singer, Malte Kelm, Anthony R. Butler, and Martin Feelisch. Key bioactive reaction products of the NO/H_2S interaction are S/N-hybrid species, polysulfides, and nitroxyl. *Proceedings of the National Academy of Sciences*, 112:E4651–E4660, 8 2015.

[267] Stephen P.L. Cary, Jonathan A. Winger, Emily R. Derbyshire, and Michael A. Marletta. Nitric oxide signaling: no longer simply on or off. *Trends in Biochemical Sciences*, 31:231–239, 4 2006.

[268] Trever Bostelaar, Victor Vitvitsky, Jacques Kumutima, Brianne E. Lewis, Pramod K. Yadav, Thomas C. Brunold, Milos Filipovic, Nicolai Lehnert, Timothy L. Stemmler, and Ruma Banerjee. Hydrogen sulfide oxidation by myoglobin. *Journal of the American Chemical Society*, 138:8476–8488, 7 2016.

[269] Valiallah Hosseininasab, Jeffery A. Bertke, and Timothy H. Warren. Thionitrite and Perthionitrite in NO Signaling at Zinc. *Angewandte Chemie International Edition*, 60:21184–21188, 9 2021.

[270] L. Playfair. On the nitroprussides, a new class of salts. *Abstracts of the Papers Communicated to the Royal Society of London*, 5:846–847, 12 1851.

[271] Yin Gao, Abouzar Toubaei, Xianqi Kong, and Gang Wu. Solving the 170-year-old mystery about red-violet and blue transient intermediates in the gmelin reaction. *Chemistry - A European Journal*, 21:17172–17177, 11 2015.

[272] Jan Lj. Miljkovic, Isabell Kenkel, Ivana Ivanović-Burmazović, and Milos R. Filipovic. Generation of HNO and HSNO from Nitrite by Heme-Iron-Catalyzed Metabolism with H_2S. *Angewandte Chemie International Edition*, 52:12061–12064, 11 2013.

[273] Sumit Sahni, Jason R. Hickok, and Douglas D. Thomas. Nitric oxide reduces oxidative stress in cancer cells by forming dinitrosyliron complexes. *Nitric Oxide*, 76:37–44, 6 2018.

[274] Ming-Li Tsai, Chih-Chin Tsou, and Wen-Feng Liaw. Dinitrosyl Iron Complexes (DNICs): From Biomimetic Synthesis and Spectroscopic Characterization toward Unveiling the Biological and Catalytic Roles of DNICs. *Accounts of Chemical Research*, 48:1184–1193, 4 2015.

[275] Matthias Boese, Peter I. Mordvintcev, Anatoly F. Vanin, Rudi Busse, and Alexander Mülsch. S-Nitrosation of Serum Albumin by Dinitrosyl-Iron Complex. *Journal of Biological Chemistry*, 270:29244–29249, 12 1995.

[276] Or Kakhlon and Z.Ioav Cabantchik. The labile iron pool: characterization, measurement, and participation in cellular processes1 1this article is part of a series of reviews on "iron and cellular redox status." the full list of papers may be found on the homepage of the journal. *Free Radical Biology and Medicine*, 33:1037–1046, 10 2002.

[277] Daniela R. Truzzi, Nathalia M. Medeiros, Ohara Augusto, and Peter C. Ford. Dinitrosyl Iron Complexes (DNICs). From Spontaneous Assembly to Biological Roles. *Inorganic Chemistry*, 60:15835–15845, 11 2021.

[278] Fu-Te Tsai, Ting-Shen Kuo, and Wen-Feng Liaw. Dinitrosyl Iron Complexes (DNICs) Bearing O-Bound Nitrito Ligand: Reversible Transformation between the Six-Coordinate $\{Fe(NO)_2\}_9[(1\text{-MeIm})_2$ (η 2 -ONO)$Fe(NO)_2$] (g = 2.013) and Four-Coordinate $\{Fe(NO)_2\}_9$ [(1-MeIm)(ONO)$Fe(NO)_2$] (g = 2.03). *Journal of the American Chemical Society*, 131:3426–3427, 3 2009.

[279] Timothy C. Berto, Amy L. Speelman, Sheng Zheng, and Nicolai Lehnert. Mono- and dinuclear non-heme iron–nitrosyl complexes: Models for key intermediates in bacterial nitric oxide reductases. *Coordination Chemistry Reviews*, 257:244–259, 1 2013.

[280] Ming-Li Tsai, Chiao-Chun Chen, I-Jui Hsu, Shyue-Chu Ke, Chung-Hung Hsieh, Kuo-An Chiang, Gene-Hsiang Lee, Yu Wang, Jin-Ming Chen, Jyh-Fu Lee, and Wen-Feng Liaw. Photochemistry of the dinitrosyl iron complex $[S_5Fe(NO)_2]^-$ leading to reversible formation of $[S_5Fe(\mu\text{-}S)_2FeS_5]^{2-}$: spectroscopic characterization of species relevant to the nitric oxide modification and repair of [2Fe-2S] ferredoxins. *Inorganic chemistry*, 43:5159–67, 8 2004.

[281] J.H. Enemark and R.D. Feltham. Principles of structure, bonding, and reactivity for metal nitrosyl complexes. *Coordination Chemistry Reviews*, 13:339–406, 9 1974.

[282] Martin Keilwerth, Johannes Hohenberger, Frank W Heinemann, Jörg Sutter, Andreas Scheurer, Huayi Fang, Eckhard Bill, Frank Neese, Shengfa Ye, and Karsten Meyer. A Series of Iron Nitrosyl Complexes {Fe-NO} and a Fleeting {Fe-NO} Intermediate en Route to a Metalacyclic Iron Nitrosoalkane. *Journal of the American Chemical Society*, 141:17217–17235, 10 2019.

[283] Mrittika Roy, Wen Fu, Lilia M. Baldauf, James C. Fettinger, R. David Britt, and Alan L. Balch. Reactions of Thianthrene and 10-Phenylphenothiazine with the Lewis Acids Titanium Tetrachloride, Titanium Tetrabromide, Tin(IV) Tetrachloride, or Antimony(V) Pentachloride: The Competition between Coordination and Oxidation. *Inorganic Chemistry*, 62:14055–14063, 8 2023.

[284] Jay K. Kochi. *Electron-transfer Oxidation*, pages 849–889. Elsevier, 1991.

[285] Abdelaziz Houmam. Electron transfer initiated reactions: Bond formation and bond dissociation. *Chemical Reviews*, 108:2180–2237, 7 2008.

[286] Rajendra Rathore and Jay K. Kochi. *Donor/acceptor organizations and the electron-transfer paradigm for organic reactivity*, pages 193–318. 2000.

[287] Vernon D. Parker. Reaction pathways of the cation radicals of aromatic compounds related to the anthracenes. *Accounts of Chemical Research*, 17:243–250, 7 1984.

[288] Ulla Svanholm, Ole Hammerich, and Vernon D. Parker. Kinetics and mechanisms of the reactions of organic cation radicals and dications. ii. anisylation of thianthrene cation radical. *Journal of the American Chemical Society*, 97:101–106, 1 1975.

[289] Jiayu Wang, Kuan Liu, Lanchao Ma, and Xiaowei Zhan. Triarylamine: Versatile platform for organic, dye-sensitized, and perovskite solar cells. *Chemical Reviews*, 116:14675–14725, 12 2016.

[290] Marat R. Talipov, Mohammad M. Hossain, Anitha Boddeda, Khushabu Thakur, and Rajendra Rathore. A search for blues brothers: X-ray crystallographic/spectroscopic characterization of the tetraarylbenzidine cation radical as a product of aging of solid magic blue. *Organic & Biomolecular Chemistry*, 14:2961–2968, 2016.

[291] Neil G. Connelly and William E. Geiger. Chemical redox agents for organometallic chemistry. *Chemical Reviews*, 96:877–910, 1 1996.

[292] Alan L. Balch, Charles R. Cornman, Lechoslaw Latos-Grazynski, and Marilyn M. Olmstead. Characterization of five- and six-coordinate iron(III) complexes of N-methylporphyrins. *Journal of the American Chemical Society*, 112:7552–7558, 10 1990.

[293] Darin D. DuMez and James M. Mayer. Synthesis and Characterization of Rhenium(VI) cis-Dioxo Complexes and Examination of Their Redox Chemistry. *Inorganic Chemistry*, 37:445–453, 2 1998.

[294] Mrittika Roy, Jeffrey H. Walton, James C. Fettinger, and Alan L. Balch. Direct crystallization of diamine radical cations: Carbon-nitrogen bond formation from the reaction of triphenylamine with $ticl_4$, $tibr_4$, or $sncl_4$ versus carbon-carbon bond formation with $sbcl_5$. *Chemistry – A European Journal*, 28, 3 2022.

[295] Florian Berger, Matthew B. Plutschack, Julian Riegger, Wanwan Yu, Samira Speicher, Matthew Ho, Nils Frank, and Tobias Ritter. Site-selective and versatile aromatic C-H functionalization by thianthrenation. *Nature*, 567:223–228, 3 2019.

[296] Beatrice Lansbergen, Paola Granatino, and Tobias Ritter. Site-selective c–h alkylation of complex arenes by a two-step aryl thianthrenation-reductive alkylation sequence. *Journal of the American Chemical Society*, 143:7909–7914, 6 2021.

[297] Junting Chen, Jiakun Li, Matthew B. Plutschack, Florian Berger, and Tobias Ritter. Regio- and stereoselective thianthrenation of olefins to access versatile alkenyl electrophiles. *Angewandte Chemie International Edition*, 59:5616–5620, 3 2020.

[298] Y. Murata and H. J. Shine. Ion radicals. XVIII. Reactions of thianthrenium perchlorate and thianthrenium trichlorodiiodide. *The Journal of Organic Chemistry*, 34:3368–3372, 11 1969.

[299] Huan Meng, Ming-Shang Liu, and Wei Shu. Organothianthrenium salts: synthesis and utilization. *Chemical Science*, 13:13690–13707, 2022.

[300] Paramashivappa Rangappa and Henry J. Shine. An overview of some reactions of thianthrene cation radical. products and mechanisms of their formation. *Journal of Sulfur Chemistry*, 27:617–664, 12 2006.

[301] Samuel I. Etkind, Jeffrey Lopez, Yun Guang Zhu, Jen-Hung Fang, Wen Jie Ong, Yang Shao-Horn, and Timothy M. Swager. Thianthrene-based bipolar redox-active molecules toward symmetric all-organic batteries. *ACS Sustainable Chemistry & Engineering*, 10:11739–11750, 9 2022.

[302] Pedro Luis Arrechea, Kristian B. Knudsen, J. Wayne Mullinax, Justin B. Haskins, Charles W. Bauschlicher, John W. Lawson, and Bryan D. McCloskey. Suppression of Parasitic Chemistry in Li–O_2 Batteries Incorporating Thianthrene-Based Proposed Redox Mediators. *ACS Applied Energy Materials*, 3:8812–8821, 9 2020.

[303] Roberto Grisorio, Bart Roose, Silvia Colella, Andrea Listorti, Gian Paolo Suranna, and Antonio Abate. Molecular tailoring of phenothiazine-based hole-transporting materials for high-performing perovskite solar cells. *ACS Energy Letters*, 2:1029–1034, 5 2017.

[304] Huanle Chen, Weifei Fu, Chuyi Huang, Zhongqiang Zhang, Shuixing Li, Feizhi Ding, Minmin Shi, Chang-Zhi Li, Alex K.-Y. Jen, and Hongzheng Chen. Molecular engineered hole-extraction materials to enable dopant-free, efficient p-i-n perovskite solar cells. *Advanced Energy Materials*, 7, 9 2017.

[305] Fei Zhang, Shirong Wang, Hongwei Zhu, Xicheng Liu, Hongli Liu, Xianggao Li, Yin Xiao, Shaik Mohammed Zakeeruddin, and Michael Grätzel. Impact of peripheral groups on phenothiazine-based hole-transporting materials for perovskite solar cells. *ACS Energy Letters*, 3:1145–1152, 5 2018.

[306] Philip Seeman. Atypical antipsychotics: Mechanism of action. *The Canadian Journal of Psychiatry*, 47:27–38, 2 2002.

[307] E. A. C. Lucken. 1,4-dithiinium radical-cations. *Journal of the Chemical Society (Resumed)*, page 4963, 1962.

[308] Minoru Kinoshita. The electron spin resonance absorption of the complex of thianthrene with antimony pentachloride. *Bulletin of the Chemical Society of Japan*, 35:1137–1140, 7 1962.

[309] Hans Bock, Andreas Rauschenbach, Christian Näther, Markus Kleine, and Zdenek Havlas. Thianthren-radikalkation-tetrachloroaluminat. *Chemische Berichte*, 127:2043–2049, 10 1994.

[310] Johannes Beck, Thomas Bredow, and Rachmat Triandi Tjahjanto. Thianthrene radical cation hexafluorophosphate. *Zeitschrift für Naturforschung B*, 64:145–152, 2 2009.

[311] Peter Rapta, Lars Kress, Philippe Hapiot, and Lothar Dunsch. Dimerization of thianthrene radical cations as studied by in situ ESR and UV-Vis-NIR voltammetry at different temperatures. *Physical Chemistry Chemical Physics*, 4:4181–4185, 8 2002.

[312] José-Vicente Folgado, Hermenegildo García, Vicente Martí, and Mercedes Esplá. ESR study of thianthrenium radical cation within acid zeolites. *Tetrahedron*, 53:4947–4956, 3 1997.

[313] David Clarke, Bruce C. Gilbert, and Peter Hanson. Heterocyclic free radicals. part v. an electron spin resonance investigation of the cation-radicals of 10-phenylphenoxazine and 10-phenylphenothiazine. *Journal of the Chemical Society, Perkin Transactions 2*, page 1078, 1975.

[314] M. De Sorgo, B. Wasserman, and M. Szwarc. Aggregation of salts of thianthrene radical cations. *The Journal of Physical Chemistry*, 76:3468–3471, 11 1972.